Vortex-Induced Vibration of Flexible Cylinders in Time-Varying Flows

by

Themistocles L. Resvanis

MEng Mechanical Engineering, Imperial College London (2008)

Submitted to the Department of Mechanical Engineering
in partial fulfillment of the requirements for the degree of

Doctor of Philosophy

at the

MASSACHUSETTS INSTITUTE OF TECHNOLOGY

September 2014

Author .....
Department of Mechanical Engineering
August 7, 2014

Certified by .....
J. Kim Vandiver
Professor of Mechanical and Ocean Engineering
Thesis Supervisor

Accepted by .....
David E. Hardt
Chairman, Department Committee on Graduate Students

Vortex-Induced Vibration of Flexible Cylinders in Time-Varying Flows

by

Themistocles L. Resvanis

Submitted to the Department of Mechanical Engineering
on August 7, 2014, in partial fulfillment of the
requirements for the degree of
Doctor of Philosophy

Abstract

This thesis investigates two aspects of Vortex-Induced Vibrations (VIV) on long flexible cylinders. The work is split into a minor and major part. The minor part addresses the effect of Reynolds number on flexible cylinder VIV. The major contribution addresses the prediction of VIV under unsteady current excitation or time-varying flows.

The study on the effect of Reynolds number makes extensive use of a recent set of experiments performed by MARINTEK on behalf of SHELL Exploration and Production Co. Three $38m$ long cylinders of different diameters were towed through the ocean basin over a wide range of Reynolds numbers in both uniform and sheared flows. The experimental data showed that the response amplitudes and dimensionless response frequency are strongly influenced by the Reynolds number. Both of these Reynolds effects should be of interest to riser designers that traditionally rely on experimental data obtained at much lower Reynolds numbers.

In this thesis, I propose a dimensionless parameter, γ, that governs whether lock-in under unsteady flow conditions is possible and show that it is useful for determining *a priori* whether the response under unsteady conditions will be similar to the response under steady flows. The unsteady flow parameter, γ, describes the change in flow speed per cycle of cylinder vibration and is defined as:

$$\gamma = \frac{dU/dt}{U} T_n$$

The experimental data necessary to support this work is taken from a set of experiments performed at the State Key Laboratory of Ocean Engineering at Shanghai Jiao Tong University (SJTU), where a $4m$ long flexible cylinder was towed through an ocean basin under carefully selected amounts of acceleration/deceleration. Analysis of the experimental data showed that the response can typically be divided into three regimes based on the γ value:

For very quickly accelerating flows ($\gamma > 0.1$) the cylinder cannot react quickly enough and at most a couple of cycles of small amplitude vibration will be observed.

For moderately accelerating flows ($0.02 < \gamma < 0.1$), the cylinder will typically start

vibrating and can build up a significant response. However, most of the time, the flow will have exited the required synchronization region before the cylinder manages to reach the large amplitudes observed in steady flows.

For very slowly accelerating flows ($\gamma < 0.02$), the flow is changing considerably slower than the cylinder's reaction time and thus, the cylinder has more than enough time to build up its response. Under these conditions, the observed response is qualitatively similar to the response of flexible cylinders in steady flows.

The γ dependence that was identified in the SJTU data is not limited to that specific situation but instead, is a general property of low mass ratio cylinders vibrating in unsteady flows. This is shown by demonstrating how the unsteady flow parameter, γ, can be used to analyze unsteady response data from the aforementioned SHELL tests where the riser models were considerably longer than the SJTU model.

This thesis shows how a single ramp test –where the towing speed is continuously varied in a control manner– may be used to obtain the same information as 10 constant speed tests covering the range of speeds. This can and will significantly reduce the number of runs necessary to completely characterize the VIV response of flexible cylinders and will translate into large cost savings in the future. The thesis closes by describing the differences observed in the VIV response at high mode numbers depending on whether the time-varying flow was accelerating or decelerating. In both situations a 'hysteresis' effect is noted, where the cylinder is found to 'lag behind' preferring to vibrate in the previously excited mode as a result of cylinder lock-in. In accelerating flows, this means that the cylinder will typically be responding one mode lower than it would have in a steady flow. In decelerating flows, the same 'lag' or 'hysteresis' will cause the cylinder to respond one (or more) mode number(s) higher than it would have in a steady flow.

Thesis Supervisor: J. Kim Vandiver
Title: Professor of Mechanical and Ocean Engineering

Acknowledgments

I feel indebted to my thesis supervisor Prof. Kim Vandiver for his support and guidance during my studies at MIT. Working with him on a variety of research topics over the past few years has truly been a pleasure and I wholeheartedly believe that working under his supervision has made me a better engineer.

I also want to acknowledge the other members of my committee. I owe many thanks to Prof. Shixao Fu from Shanghai Jiao Tong University, without his help this thesis would not have been complete. Our collaboration has been fruitful and I hope it can continue in the future. Prof. Michael Triantafyllou has always been very encouraging and his comments have been very helpful when dealing with many of the intricacies of this work. Finally, I must acknowledge Prof. Eduardo Kausel for rekindling my interest in vibrations when I first arrived at the Institute.

I need to thank SHELL International Exploration and Production Co. for allowing me to use their data in my thesis and especially Dr. Vikas Jhingran for making this possible.

My friend, colleague and officemate, Mr. Zhibiao Rao is due many thanks. We have had many useful and interesting discussions over the years, that have greatly helped with the completion of this thesis.

Last but not least, I want to thank my parents, Leonidas and Frances and my siblings, Elli and Koulis. They greatly assisted me while editing this thesis. Furthermore, their support and encouragement during all my years of study has been pivotal to my success.

THIS PAGE INTENTIONALLY LEFT BLANK

Contents

THIS PAGE INTENTIONALLY LEFT BLANK

List of Figures

List of Tables

THIS PAGE INTENTIONALLY LEFT BLANK

Chapter 1

Introduction

Any bluff body exposed to an external flow will experience large forces as a result of the flow separation that occurs downstream of the body. This occurs at most Reynolds numbers of engineering interest. Bodies with circular-cross sections (or other symmetric profiles) are subject to Vortex-Induced Vibrations (VIV), which is a sub-class of the general fluid-structure interaction problem. The flow separation results in a periodic vortex shedding that can cause severe structural failures if the vortex shedding frequencies coincide with the structure's natural frequencies.

The ground work for understanding VIV was only completed during the 19^{th} and 20^{th} century but the phenomenon itself has been observed and has fascinated people for centuries, ranging from the construction of Aeolian harps in antiquity that were used as autonomous musical instruments to the Renaissance era when Leonardo Da Vinci was fascinated with turbulence and eddies shed downstream of a reed on a river bank (Blevins, 1986).

During the 20^{th} century, interest and research on VIV has waxed and waned as different communities/industries identify it as a potential source of severe failures that needs to be researched and better understood:

- The 50's saw some of the first systematic VIV studies and the development of the first VIV suppression devices as a result of a series of failures of large factory smokestacks. (Scruton, 1955)

- This was followed by the nuclear energy industry that also studied the problem while designing heat exchangers and fuel rods. (Chen & Chun, 1976)
- Coastal engineers needed to study the problem in order to understand the forces on submerged piles caused by ocean waves. (Sarpkaya, 1978 and Sumer & Fredsoe, 1988)
- The early 80's saw a lot of work on the VIV of long flexible structures; including cables for towed sonar arrays and mooring lines, related to the expansion into deeper water by the offshore engineering community.
- More recently, the Oil and Gas industry has been the major driver for VIV research on long flexible structures. This is closely tied with the industry's push to deeper water in search of new or previously untapped oil and gas reserves. Many structural components that are used in offshore drilling and production industry are susceptible to VIV caused by the presence of underwater currents. These components include but are not limited to: drilling risers, production risers, free-spans on export pipelines, mooring lines and cables, subsea jumpers and umbilicals.

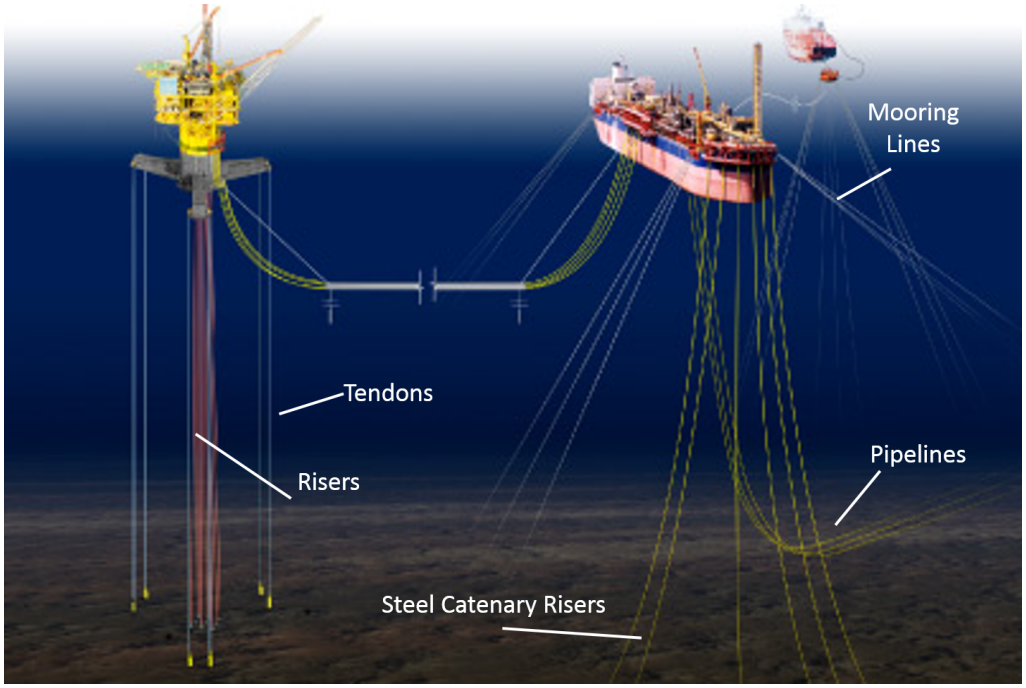

Figure 1-1: Offshore installation showing mooring lines, tendons, risers, SCR and flowlines (rigzone.com, 2014)

As oil and gas exploration and production move into deeper water, the fatigue damage accumulated due to VIV is quickly becoming one of the most critical, if not the most critical, aspect of deepwater riser design. Since many of the aforementioned components are critical components for the smooth operation of a facility and hence a venture's profitability, they are typically designed with very large safety factors. The large safety factors are a result of several issues, some of the most important are:

- Extreme variability in ocean conditions and the engineer's reluctance to design a structure with an operating life of 20-30 years based on environmental (meta-ocean) data that was only collected over the duration of a few months.
- Lack of experimental data and understanding of VIV at the high Reynolds numbers (500,000 to 2,000,000) that is typical of offshore structures. Considering the hundreds of offshore platforms installed and the thousands of risers in use there is a surprisingly small number of high Reynolds numbers model tests.

The latter point is probably one of the reasons why the Oil and Gas industry has continued to fund research on VIV with the emphasis being primarily on understanding the phenomena as it relates to structures of interest rather than over-idealized scenarios. In the long term, this is a winning proposition for the industry because as the community's confidence in understanding VIV increases their designers will be more willing to reduce the safety factors they impose on a given structure, thus considerably reducing costs.

1.1 Scope of the Thesis

This thesis investigates two aspects of Vortex-Induced Vibrations on long flexible cylinders. The work is split into a minor and major part. The minor part addresses the effect of Reynolds number on flexible cylinder VIV. The major contribution addresses the prediction of VIV under unsteady current excitation or time-varying flows.

The study on the effect of Reynolds number makes extensive use of a recent set of experiments performed by MARINTEK on behalf of SHELL Exploration and Pro-

duction Co. Three $38m$ long cylinders of different diameters were towed through the ocean basin over a wide range of Reynolds numbers in both uniform and sheared flows. The experimental data revealed that the response amplitudes and dimensionless response frequency were strongly influenced by the Reynolds number. Both of these Reynolds number effects should be of interest to riser designers that traditionally rely on or make use of experimental data obtained at much lower Reynolds numbers. Identifying the Reynolds number effects on the response of flexible cylinders in steady flows proved critical to explaining other details that were observed in the response. This was necessary before even attempting to compare these results with the VIV response observed in unsteady flows.

The major contribution of the thesis is in the area of VIV in time varying flows. Experimental investigations of VIV on rigid or flexible cylinders, with few exceptions, are usually performed in laboratories, towing tanks or ocean basins under carefully controlled conditions. The typical way of performing such experiments in towing tanks involves mounting the cylinder on a carriage and towing the carriage and cylinder through the tank at a constant speed. For obvious reasons an experimentalist would like to keep constant as many independent variables as possible during an experiment.

The disadvantage is that a typical test matrix will require the testing of the cylinder at many different current speeds in order to achieve a very fine grid of reduced velocities for each natural frequency included in the test matrix. Towing tanks, such as the one at MARINTEK in Trondheim, Norway, which are capable of conducting tests on long flexible cylinders are expensive to operate. It is quite common for VIV experiments to require a few weeks to cover a satisfactory test matrix. This translates into hundreds of thousands of dollars in testing costs. This thesis explores a new method of carrying out VIV tests that can cover the same test matrix in a more efficient manner. This method requires conducting 'ramp tests', in which the carriage speed (or flow velocity) is varied in a carefully controlled way so as to obtain the equivalent of a large number of steady speed tests in a single tow through the tank.

There are two questions that have to be answered first:

- Can VIV achieve lock-in conditions during unsteady flow conditions? If so, what are the requirements or parameters that primarily govern whether lock-in will be observed?

- If lock-in is achieved under unsteady flow conditions will the cylinder response be the same as what is observed under steady flow conditions? The VIV response is typically characterized by the response amplitude and stress (or curvature or strain) and the response frequency.

In this work, I propose a dimensionless parameter, γ, that governs whether lock-in under unsteady flow conditions is possible and show that it is useful for determining *a priori* whether the response under unsteady conditions will be similar to the response under steady current conditions. The experimental data necessary to support this work is taken from a set of experiments performed at the State Key Laboratory of Ocean Engineering at Shanghai Jiao Tong University (SJTU), where a $4m$ long flexible cylinder was towed through an ocean basin under carefully selected amounts of acceleration/deceleration. Further evidence is drawn from a subset of the aforementioned SHELL tests which shows how a single ramp test can be used to extract data equivalent to ten or more individual tests at constant speeds.

1.2 Thesis Outline

This thesis starts by giving a very brief description of some very fundamental concepts of VIV and is immediately followed by Chapter 3 which describes the two experimental datasets used in this work.

Chapter 4 includes the analysis of the first of these. The $38m$ SHELL dataset, showed that the response amplitude and the dimensionless response frequency of flexible cylinders are significantly influenced by the Reynolds number. In the Reynolds number range between 5,000 through 200,000, the response amplitude increases while at the same time the dimensionless response frequency decreases. The Reynolds number effects on the response amplitude are shown to be a direct consequence of the

effect that Reynolds number has on the lift coefficient. Both effects identified have serious implications for riser design.

Chapter 5 outlines a method by which both Reynolds number effects identified in Chapter 4 may easily be incorporated into commonly used VIV prediction programs that currently do not incorporate any Reynolds number dependence for their hydrodynamic coefficient databases. The chapter closes by describing the importance that correctly modelling the two Reynolds number effects can have on the predicted stresses and damage rates.

Chapter 6 shows that even though the In-Line (IL) motion is relatively small it can induce large stresses and even larger damage rates due to the higher response frequency in that direction. Despite the large IL stresses, an analysis of the damage rates at every position around the circumference of the cylinder's cross-section showed that the most damaging location around the cross-section almost always coincides with the Cross-Flow (CF) directions. In any case, this chapter reaches the important conclusion that the CF and IL damage rates as well as their most damaging vector-combination are always of the same order of magnitude reaffirming the community's belief that a conservative design that only models the CF vibration is sufficient to characterize the fatigue life of an offshore riser.

The thesis continues with its main contribution which is the investigation and analysis of VIV in time-varying or unsteady flows. Chapter 7 introduces the unsteady flow parameter, γ, a dimensionless parameter that describes the change in flow speed in a single cycle of cylinder vibration. Chapter 8 describes the analysis of the SJTU dataset that included tests with slowly and quickly accelerating flows. The chapter shows that the unsteady flow parameter, γ, is well suited in characterizing the response of flexible cylinders in time-varying flows. Similar to steady flow VIV, the current speed still has be within a specific band of values (synchronization region), but the response can typically be divided into three regimes based on the γ value:

- For very quickly accelerating flows ($\gamma > 0.1$), i.e., more than 10% speed variation per cycle) the cylinder cannot react quickly enough and at most a couple of cycles of small amplitude vibration will be observed.

- For moderately accelerating flows ($0.02 < \gamma < 0.1$) the cylinder will typically start vibrating and can build up a significant response amplitude. However, most of the time the flow will have exited the required synchronization region before the cylinder manages to reach the maximum amplitudes observed in steady flows.

- For very slowly accelerating flows ($\gamma < 0.02$), i.e., less than 2% speed variation per cycle) the flow is changing considerably slower than the cylinder's reaction time and thus the cylinder has more than enough time to build up its response.

This thesis shows that the VIV response of flexible cylinders in time-varying flows is qualitatively similar to the response of flexible cylinders in steady flows and can often be larger than what is observed in a typical VIV test matrix where cylinders are tested at predetermined speeds believed to be close to the speed that will cause the greatest response. The larger response amplitudes observed in slowly time-varying flows are the result of allowing the cylinder to 'choose' the fluid speed at which it will respond the most vigorously instead of limiting it to a few specific speeds.

This, in turn, is one of the most compelling reasons to use 'ramp tests' or slowly-varying flows for future VIV model testing. Designers are typically interested in the most damaging response not one that is believed to be close to the most damaging. Another reason to introduce 'ramps' in VIV model testing is to explore the transition between multiple modes in a single run through the basin or towing tank.

Chapter 9 shows how a single ramp test may be used to obtain the same information as ten constant speed tests. This can and will significantly reduce the number of runs necessary to completely characterize the VIV response of flexible cylinders and will translate into considerable cost savings in the future. The chapter closes by describing the differences observed in the VIV response at high mode numbers depending on whether the time-varying flow was accelerating or decelerating. In both situations a 'hysteresis' effect is noted, where the cylinder is found to 'lag behind' preferring to vibrate in the previously excited mode as a result of cylinder lock-in. In accelerating flows, this means that the cylinder will typically be responding one mode

lower than it would have in a steady flow. In decelerating flows, the same 'lag' or 'hysteresis' will cause the cylinder to respond one (or more) mode number(s) higher than it would have in a steady flow.

Chapter 10 offers suggestions for future model tests using ramps. Specifically, 'ramp tests' are designed in a way that will keep the γ value constant throughout the test. This is complemented by a discussion on issues that will result due to 'mode overlap' or closely spaced natural frequencies.

The thesis closes by summarizing the most important conclusions identified in this work and provides recommendations for future work that could further our understanding of VIV in time-varying flows.

Chapter 2

Background VIV

Over the past decades there has been a lot of research focusing on VIV and the general vortex shedding process behind stationary cylinders. This has been accompanied by detailed investigations in order to understand what happens to the boundary layers as the fluid flows around the cross-section. Reviewing every contribution to the field of VIV on rigid and flexible structures is not within the scope of this thesis. This has already been done by established and experienced researchers and the reader is referred to the very thorough review papers by Sarpkaya (1979, 2004), Bearman (1984), Williamson & Govardhan (2004, 2008) and the books by Blevins (1986) and Summer & Fredsoe (2006) to list but a few.

Despite the extensive research studies, both experimental and numerical, it is important for the reader to understand there is no complete analytical solution to the vortex shedding process despite some of the most famous fluid mechanics researchers having attempted the problem, including Stokes, Oseen, Lamb and Blahsius. The solution would require solving the full set of the Navier-Stokes equations and this is further complicated by the fact that the body can move inside the stream. Researchers as far back as the early 80's assumed that computing power will eventually enable us to solve the Navier-Stokes equations but more than 30 years later and after a huge increase in computing power, Computational Fluid Dynamics (CFD) is still seeing limited use in VIV prediction and is mostly limited to optimizing the design of suppression devices or for the most fundamental of problems at low Reynolds

numbers.

Typical riser design requires predicting VIV under a multitude of ocean conditions, often thousands of different current profiles will be used to characterize the meta-ocean statistics of a given location, for each individual riser. Additionally, the design process is often iterative and has to be repeated several times which makes any attempts at using CFD for actual riser design prohibitively expensive.

The vast amount of experimental work has been essential in providing insight to the VIV problem, to the point where engineers can quite confidently (albeit with large safety factors) design a tubular member that will not fail due to VIV. Bearman (1984) points out that "Progress on (these) practical engineering problems has been made possible through the understanding gained from fundamental studies".

All structural dynamics problems involve an excitation source and the structure's response to this force. Identifying the source and understanding the behavior of the structure's response are necessary steps in gaining insight that can be useful in design recommendations or VIV suppression/mitigation strategies. The following sections will provide the reader with a very brief background to some fundamental concepts of VIV, just enough, so that the remainder of the thesis makes sense to someone not yet familiar with many of the intricacies of VIV.

2.1 Vortex Shedding

Flow around a rigid cylindrical structure (or any other bluff body) is characterized by flow separation at all but the smallest of Reynolds numbers. Flow separation occurs when the boundary layer thickness increases suddenly and separates from the surface leading to large areas of flow recirculation.

Figure 2-1 shows the form that the recirculation or flow-separation behind a stationary cylinder takes as a function of Reynolds number. For any Reynolds number larger than ~ 40, the flow separation is characterized by the shedding of vortices. It should be pointed out that the flow is very two-dimensional, with the vortices being shed in a coherent vortex sheet, up until a Reynolds number of approximately

$200,000 - 500,000$ where the two-dimensionality breaks down and strong three dimensional effects are observed, in what is known as the drag crisis regime.

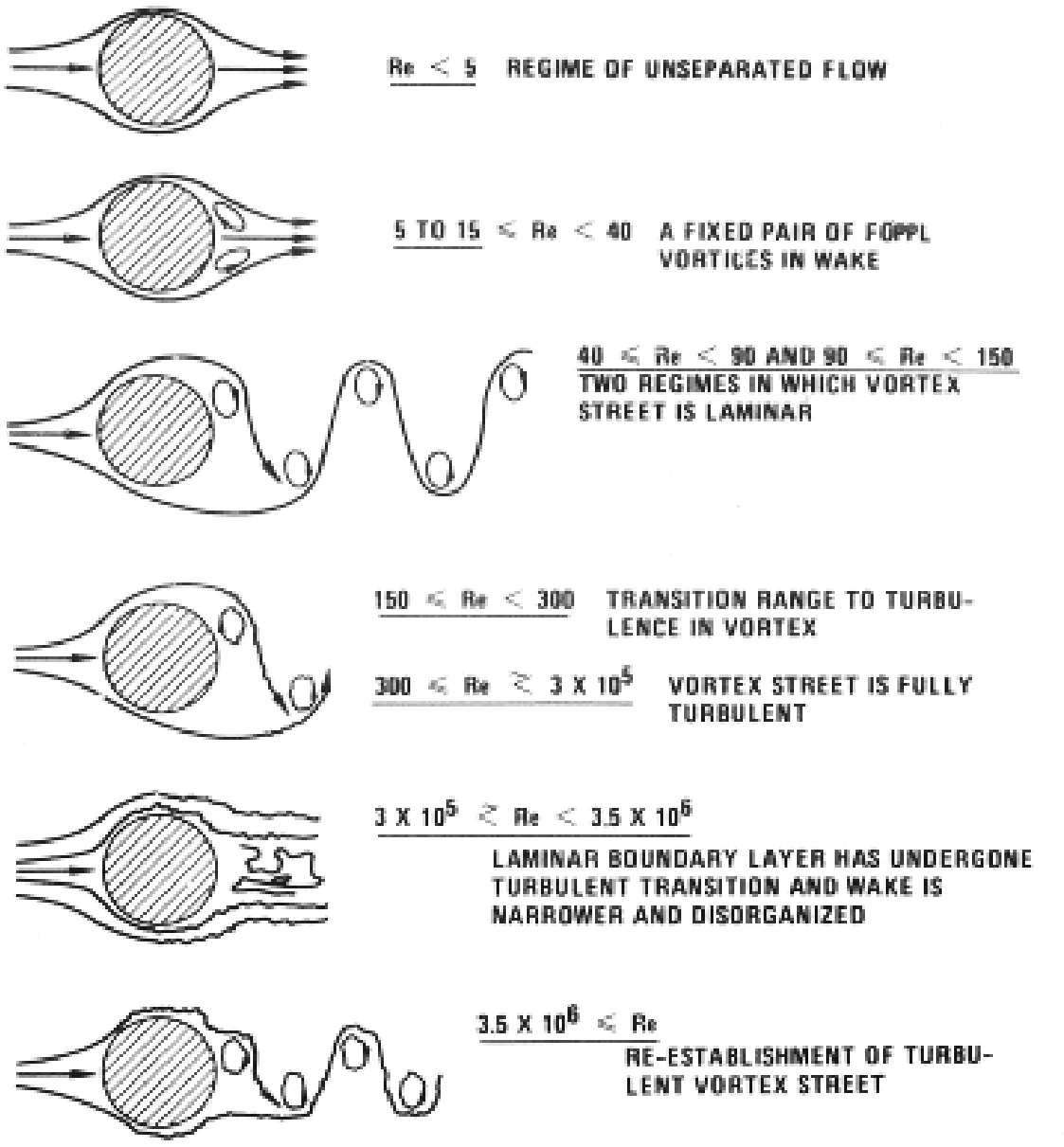

Figure 2-1: Flow separation and vortex shedding behind a stationary cylinder (Blevins, 1986).

Theodore von Karmann was among the first researchers to study these periodically shed vortices giving his name to the instantly recognizable "von Karman Vortex Street". Figure 2-2 is a photograph of a von Karmann vortex street clearly showing the periodicity in the wake.

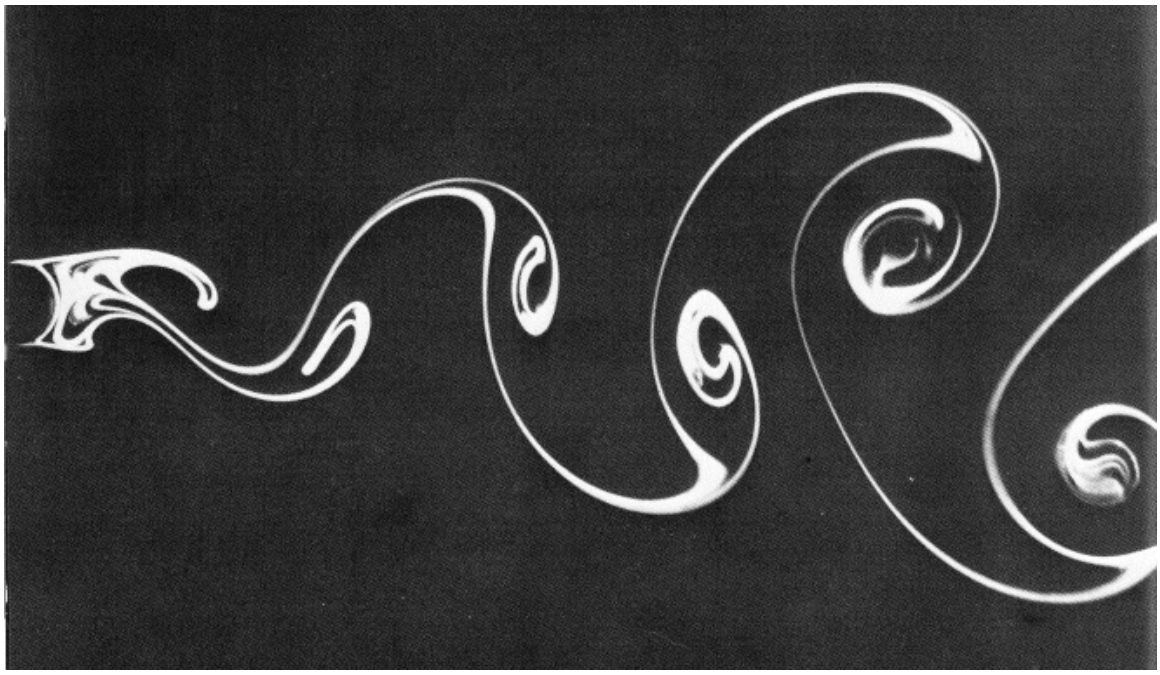

Figure 2-2: Vortex street behind a stationary cylinder (Van Dyke, 1982).

The frequency of the shed vortices behind a STATIONARY cylinder is given by the *Strouhal relationship* shown below. U is the velocity of the free stream, D is the cylinder's diameter and St is an experimentally measured constant of proportionality known as the Strouhal number.

$$f_{vortex\ shedding} = St\frac{U}{D} \tag{2.1}$$

Even though the exact form of the shed vortices and the size of the wake depend on the Reynolds number, the Strouhal number remains surprisingly constant over a large range of Reynolds numbers. Figure 2-3 shows the experimentally measured Strouhal number from a large number of experiments.

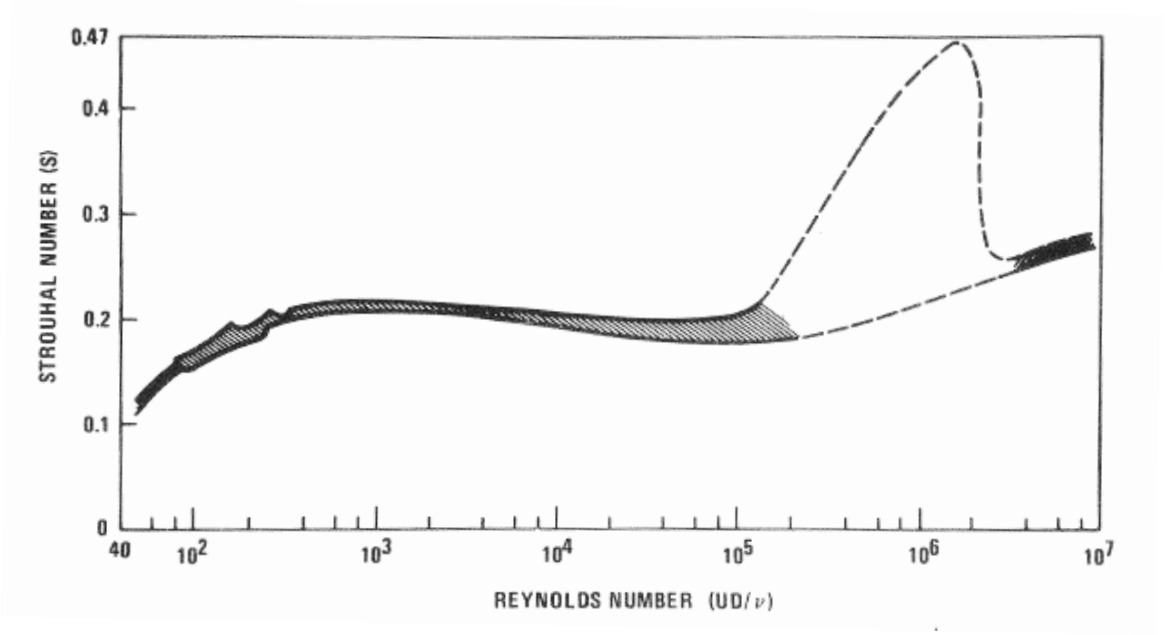

Figure 2-3: Strouhal number as a function or Reynolds number (Blevins, 1986)

Every time a vortex is being formed and shed, the large amounts of vorticity lead to local regions of low pressure on the cylinder's surface. Because vortices are being shed alternately from both sides of the cylinder these regions of low pressure will also exist on alternate sides. This will lead to a 'lift force', primarily, in the cross-flow direction that has the same periodicity as the shed vortices.

2.2 Elastically Mounted Rigid Cylinders

If the cylinder was free to move instead of being held fixed in space, one would expect that the presence of a periodic forcing will quickly lead to strong vibrations.

Understanding the behavior of flexible structures undergoing VIV is much more straightforward if one starts with the simpler case of a spring-mounted rigid cylinder. This elastically mounted cylinder, which can now respond to the vorticity in the downstream wake, has a single natural frequency given by the square root of the ratio of the spring stiffness to the system's mass. The mass term has to include the physical mass of the cylinders (and contents) as well as the mass of the accelerated

fluid (surrounding) when the cylinder starts moving, which is known as the added mass.

This simplified scenario of an elastically mounted cylinder is one of the building blocks of VIV and has been the focus of many studies and to this day continues to fascinate some researchers. Figure 2-4 is very typical of the response of a spring-mounted cylinder exposed to a cross flow. The top portion of the figure shows the ratio of the Shedding Frequency f_s to the natural frequency f_n as a function of the reduced velocity, $V_r = \frac{U}{f_n D}$. The lower portion of the figure shows how the response amplitude, A_y, non-dimensionalized by the diameter, D, varies as a function of the reduced velocity.

The first observation that one can make is that the width of the resonance is much larger than one would expect at such low levels of damping. Examining the ratio of $\frac{f_s}{f_n}$ gives some clues as to what is happening: Instead of the vortex shedding frequency increasing with the increasing velocity (or V_r) as one would expect from the Strouhal Relationship it remains roughly constant and equal to the natural frequency during most of the resonance. This is one of the quintessential features of VIV and is termed lock-in, synchronization or wake-capture. As soon as the cylinder starts moving the vortex shedding process becomes 'easier', with the shed vortices being stronger and with greater spanwise coherence and most importantly the vortices are being shed at a frequency very close to the cylinder's natural frequency instead of the frequency dictated be the Strouhal relationship.

The entire phenomenon is due to the fact that the cylinder's added mass starts decreasing immediately after the resonance. This results in an increase of the structure's natural frequency which will be closer to the shedding frequency thus allowing the resonant conditions to continue.

The lock-in bandwidth or synchronization region was found to increase with increasing response amplitude by Bearman & Obasaju (1982). It was later discovered that the mass ratio is critical to determining the lock-in bandwidth, with low-mass ratio cylinders having considerably larger lock-in bands than their high mass ratio counterparts. The mass ratio is defined as the ratio of the cylinder's mass to the ratio

of displaced fluid due to a solid cylinder of the same outer diameter:

$$m^* = \frac{m}{\frac{1}{4}\pi\rho_{fluid}D^2}$$

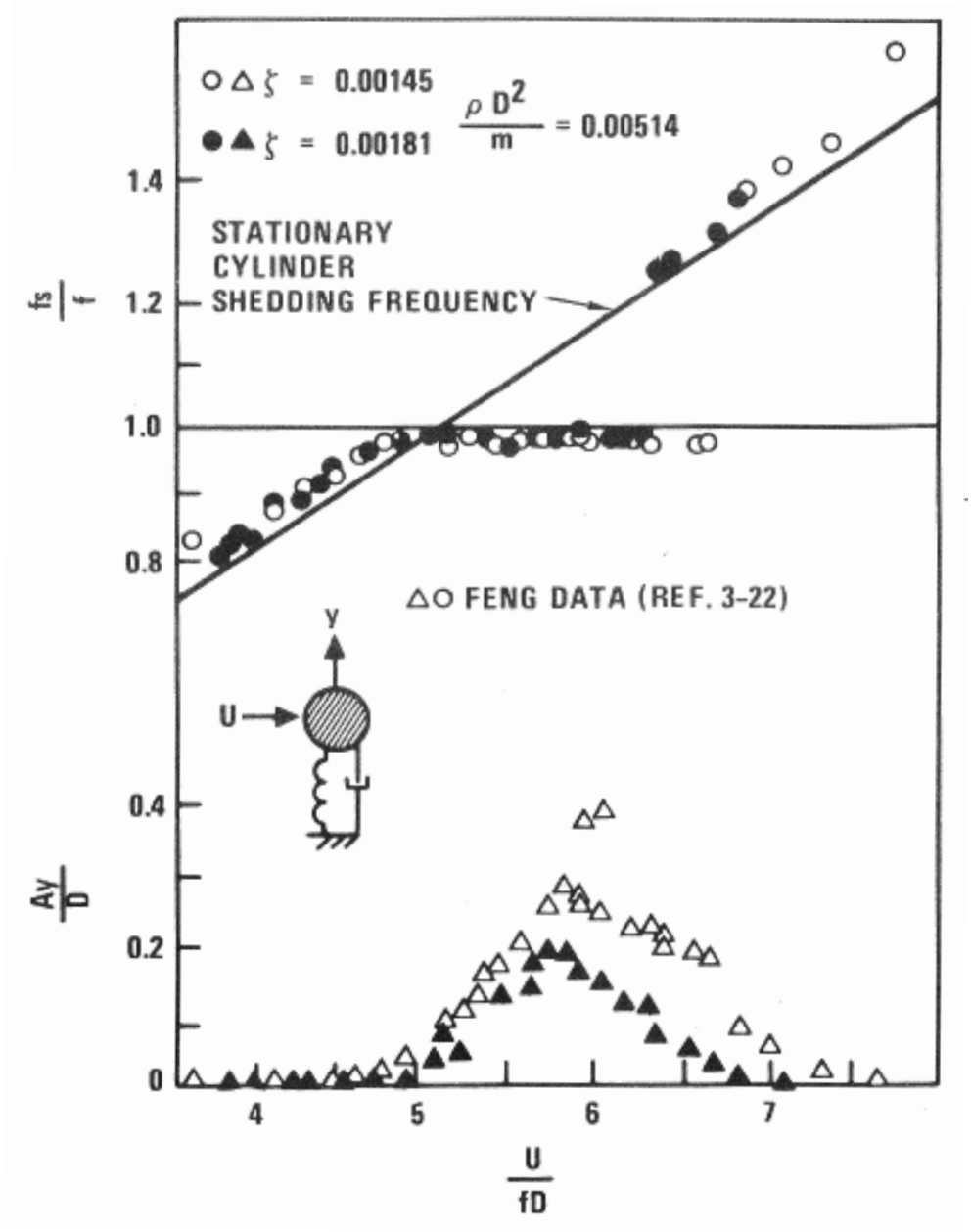

Figure 2-4: Response of a spring mounted rigid cylinder (Blevins, 1986)

Anyone familiar with basic vibration theory will recognize that a periodic forcing at the structure's resonant frequency will cause a very large response that is only limited by the amount of damping present. Figure 2-4 shows that the resonant amplitude at $V_r \sim 6$ is actually not that large considering the very small amount of damping present $\zeta \sim 0.2\%$ (typical of many lightly damped structures). In fact, studies have shown that reducing the damping even further would not lead to a considerably larger response. This reveals one of the most interesting non-linear features of VIV, namely, that these systems have limit-cycles which prevent the response from increasing indefinitely at resonant conditions. This is best explained by the non-linear dependence of the lift-coefficient on the response amplitude shown in Figure 2-5.

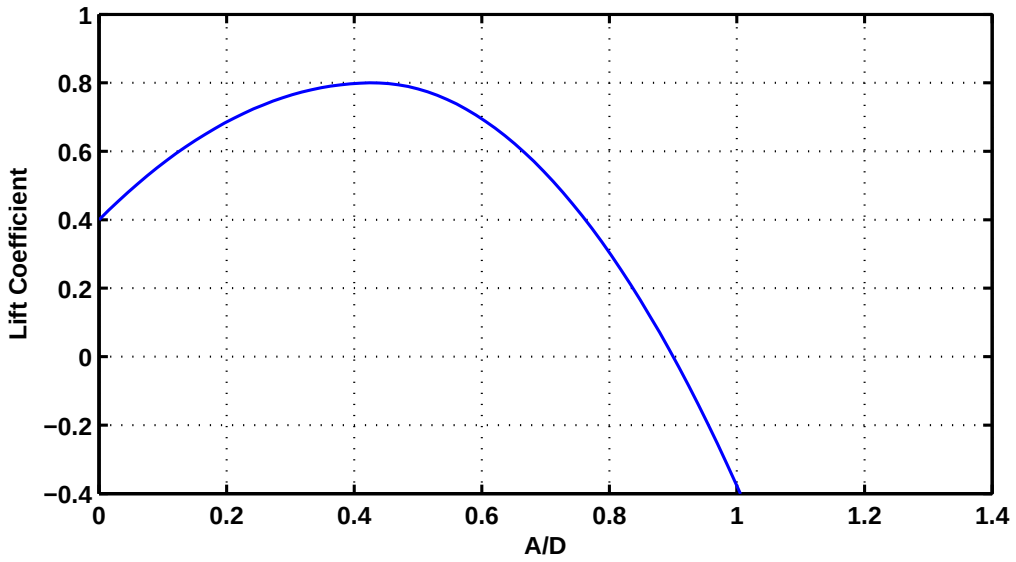

Figure 2-5: Lift coefficient (C_L) vs. A/D curve at a specific dimensionless response frequency

This nonlinear relationship is characterized by the fact that, at small amplitudes, the lift coefficient is positive and increases with increasing response amplitude up until a certain point after which the lift coefficient decreases. Eventually, the lift coefficient becomes negative, which implies that instead of energy flowing from the fluid into the structure, the opposite actually occurs: Energy flows from the structure to the fluid in

order to limit the response. The maximum response amplitude due to VIV can depend on many things such as aspect ratio, end conditions, surface roughness, damping, etc., which makes comparisons among different datasets quite tricky. The general rule of thumb is that the largest response amplitude will be roughly one diameter. This is also the reason why the response amplitude is typically non-dimensionalized by dividing by the cylinder's diameter.

As previously mentioned, elastically mounted rigid cylinders have been studied extensively and many interesting features of the response can now be explained by the behavior of the wake and the pattern of the shed vortices. This was only made possible with the development of flow visualization techniques such as Particle Image Velocimetry. The reason that these intricacies will not be expanded on further in this thesis, is because many of the unique response characteristics (response branches etc.) are not observed on flexible cylinder VIV and furthermore it is not yet clear if many of the unique wake patterns observed will survive or be relevant at the higher Reynolds numbers that are typically of interest to offshore engineers.

2.3 VIV of Flexible Cylinders

The vortex induced vibration of flexible cylinders shares many common features with the response of elastically mounted cylinders which makes analyzing and understanding their response substantially simpler. Indeed many of the commonly used VIV prediction tools use experimental data obtained from rigid cylinders combined with a strip-theory approach to model the response of a flexible structure.

Triantafyllou et al. (2003) studied the response of a pinned-pinned flexible beam which could vibrate both perpendicular to, as well as in-line to the flow. The upper portion of Figure 2-6 shows the Cross-Flow (CF) and the In-Line (IL) response amplitudes as a function of the reduced velocity (V_r). The lower portion of the figure shows the cylinder trajectories at a few selected values of reduced velocity.

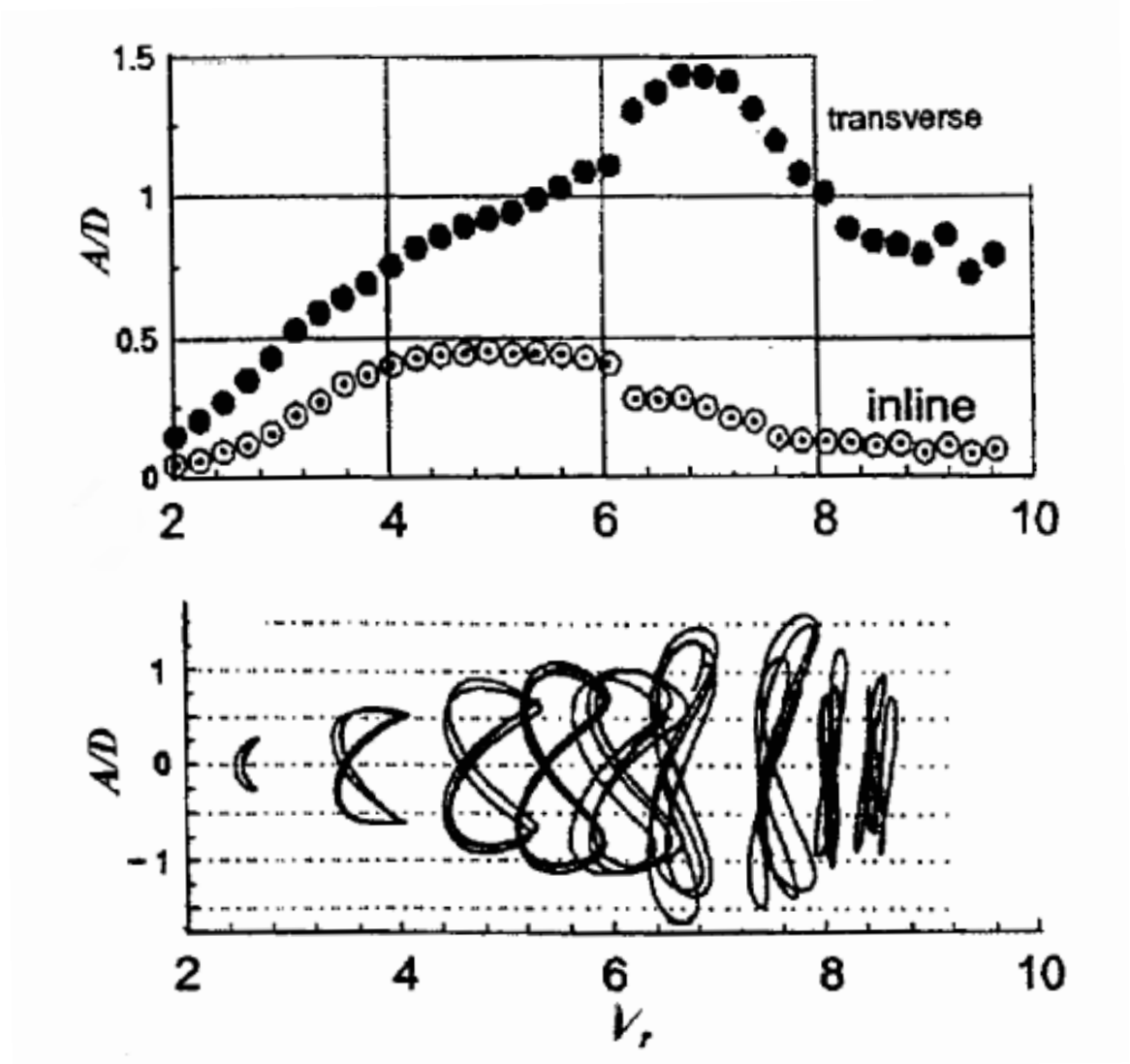

Figure 2-6: Transverse (CF) and Inline (IL) response of a flexible cylinder as a function of reduced velocity (Sarpkaya, 2004 (originally Triantafyllou et al., 2003))

VIV on flexible cylinders tends to be much more damaging because unlike an elastically mounted cylinder (i.e., a spring mounted rigid body) which only has one natural frequency (or two if IL motion is permitted) a continuous structure will have an infinite number of natural frequencies each one corresponding to a different mode shape for the structure. The presence of infinitely many resonances means that it is susceptible to large amplitude vibrations at a huge range of current velocities unlike the elastically mounted rigid cylinder which was susceptible to VIV at a specific current velocity and a small band around it, known as the synchronization region. One

can gain a lot of insight into a flexible cylinder VIV problem if he can conceptually treat every normal mode and associated natural frequency as an individual elastically mounted cylinder responding to the flow conditions.

However, there are also many differences or challenges with VIV on flexible cylinders, some of these are associated with the spatial variation of a given mode's response and others are directly related to the variability in the ocean environment. The current velocity along the cylinder length need not be constant, in fact this is extremely rare in the actual ocean environment where there can be substantial difference in current strength and direction as a function of depth associated with the existence of thermoclines and loop-currents.

This spatial variation is demonstrated with the schematic in Figure 2-7, showing an idealized current profile and regions along the riser that could be sources of excitation and other regions that will act as sources of hydrodynamic damping.

These spatial variations when combined with the fact that natural frequencies and modes are closely spaced gives rise to many interesting problems. Vandiver (1985, 1993) identified a method to predict lock-in and the location of the power-in or excitation region under linearly sheared currents. This was achieved by balancing the power into the structure with the power dissipated through damping.

The Lake Seneca and Miami I and II field experiments demonstrated the concept of 'mode competition' which is the possibility of having two different sources of VIV at different frequencies if they are spatially separated by a large enough distance. The same tests demonstrated the existence of mode-switching where the response at a given location can jump from mode to mode as time progresses. This is a direct result of closely spaced natural frequencies and current speeds that can excite a number of neighboring modes after the lock-in or synchronization bands are taken into account (Swithenbank, 2007).

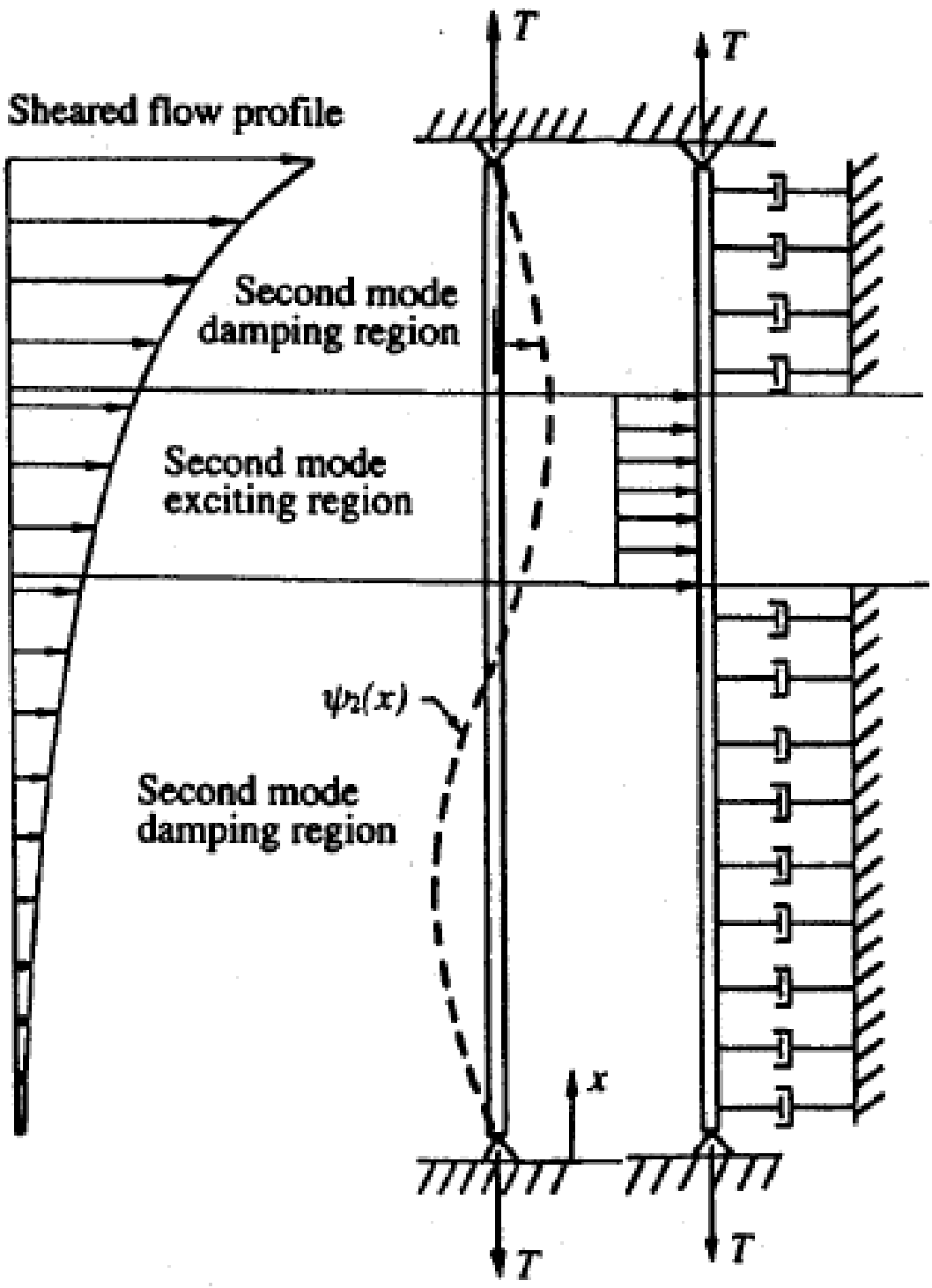

Figure 2-7: Power flow model for a flexible cylinder (Vandiver, 1993).

Kim et al. (1985, 1986) were among the first to comment on the existence of travelling waves in the VIV response of very long cables. These were later observed and confirmed by Vandiver et al. (2009) and Marcollo et al. (2007) in the Lake Seneca and Miami I and II tests where the dense instrumentation even allowed the calculation of wave propagation speeds. These travelling waves were also associated with large amounts of response at higher harmonics (3X, 5X) which are a considerable source of fatigue damage (Vandiver, 2006).

Considerable efforts have been made in recent years to try and improve cable and riser VIV prediction software that is being used extensively in the offshore industry. This is often done in conjunction with the model testing of flexible cylinders in a towing tank or the ocean environment. As our understanding of cable and riser dynamics improves and as new phenomena are observed, efforts are made to incorporate such findings or to improve the quality of the predictions. Recent examples of this are Mukundan et al. (2010), Resvanis & Vandiver (2011) and Campbel & Slocum (2013).e

Recent efforts have concentrated on benchmarking all three of the most commonly used VIV prediction packages (VIVA, VIVANA & SHEAR7) against the same experimental datasets. This is an industry wide initiative led by DEEPSTAR in order to assess the inherent modeling differences of the three software packages. The experimental datasets included:

- NDP $38m$ high mode number tests donated by the Norwegian Deepwater Program (a $38m$ long cylinder tested at MARINTEK)
- The Miami I and II tests donated by DEEPSTAR (a $700ft$ long riser model tested in the ocean, offshore Miami)
- The ExxonMobil $10m$ rotating rig tests donated by Exxon (a $10m$ long cylinder tested at MARINTEK)

The project's aim was to study how inherently conservative each software package was by comparing carefully collected experimental data with predictions. The experimental data was intentionally expanded to include three different datasets, because

it had been observed that a software package that produces good predictions against a specific dataset does not necessarily produce good predictions for another. The idea was to compare each VIV prediction package against a very large number of tests from different model tests and thus get a more 'global' perspective on how conservative a given prediction package is, as well as, the extent of the scatter of its predictions.

These studies indicated that the extent of the scatter is one of the most important factors in choosing just how large the necessary safety factor will be in order to guarantee a given probability of failure. (Fontaine et al. (2011, 2013) and Tognarelli et al. (2013)).

Chapter 3

Description of Experiments

3.1 The 38m SHELL Experiments

The 38m SHELL experiments were conducted in the spring of 2011 at MARINTEK's ocean basin on behalf of SHELL International Exploration and Production Co. The experiment involved towing three densely instrumented flexible cylinders, of different diameters, in uniform and sheared currents. The full test matrix included more than 430 runs which tested the effects of fairings, strakes, staggered buoyancy and marine growth on riser response in uniform and linearly sheared currents. An interesting feature of this data set was the very large range of Reynolds numbers covered while testing the three different pipes. Towing velocities ranged from $0.25m/s$ to $3.45m/s$ which correspond to Reynolds number range from 5,000 to 220,000. More details on the experimental set-up can be found in Lie et al.(2012). The properties of the three different pipes are summarized in Table 3.1. (MARINTEK, 2011)

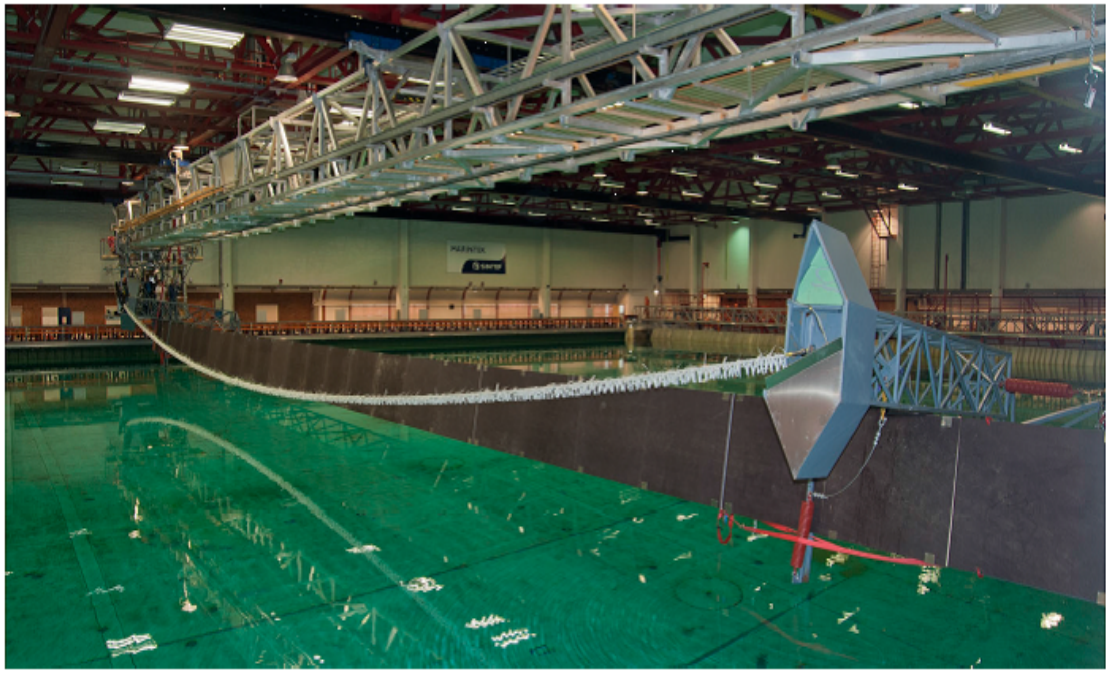

Figure 3-1: The 12mm diameter riser model covered in ribbon fairings. The model is shown mounted on the carriage before it is submerged

Table 3.1: The 38m SHELL Tests Pipe Properties

	Pipe 1	Pipe 2	Pipe 3
Length	38 m	38 m	38 m
Outer Diameter (Hydrodynamic Dia.)	12 mm	30 mm	80 mm
Optical Diameter (Strength Diameter)	10 mm	27 mm	27 mm
Inner Diameter	(solid rod)	21mm	21mm
EI	16.1 Nm^2	572.3 Nm^2	572.3 Nm^2
E	3.27x10$^{10}N/m^2$	3.46x10$^{10}N/m^2$	3.46x10$^{10}N/m^2$
Mass in air(with contents)	0.197 kg/m	1.088 kg/m	5.708 kg/m
Mass in water(with contents)	0.078 kg/m	0.579 kg/m	0.937 kg/m
Mass ratio	1.74	1.54	1.14

The smallest cylinder, Pipe 1, was instrumented with 52 fiber optic Bragg strain gauges measuring pipe curvature in each of the Cross-Flow (CF) and In-Line (IL) directions. The optical fiber was located at a distance of $5mm$ from the neutral axis and was covered by a silicon sheet $1mm$ thick. The medium and large diameter cylinders, Pipes 2 & 3 respectively, had curvature (strain) measured at 30 different locations along the length and accelerations at 22 points in both the CF and IL directions. All sensors were sampled at a frequency of 1200Hz. The largest diameter pipe was simply the medium sized pipe with a clam-like plastic shell, $25mm$ thick, surrounding it. For the medium and large pipes, the curvature was measured at a distance of $13.5mm$ from the neutral axis and the fiber optic cable was then covered by a silicon sheet $1.5mm$ thick. Data will also be drawn from a set of runs where the largest diameter pipe was covered in P40 sandpaper in order to alter its surface roughness.

Damping tests conducted in air for all three pipes yielded structural damping ratios of $\sim 0.5 - 0.7\%$ of critical damping.

The SHELL tests also included some 'ramp tests', where the pipes were exposed to uniform flows while the carriage and cylinder were accelerated or decelerated in linear and quadratic manners. Of the approximately 430 runs in the test matrix, approximately 15 were of the ramp type and all the remaining were at constant speed. These 'ramp tests' were tests of opportunity which led to the development of the γ parameter. Once its importance was understood, a new set of model tests were planned which allowed for a systematic evaluation of VIV as a function of γ. These tests were conducted at the ocean basin in the State Key Laboratory at Shanghai Jiao Tong University.

3.2 Shanghai Jiao Tong University Tests (SJTU Tests)

Unlike the SHELL ramp tests, the time-varying tests at the State Key Laboratory of Ocean Engineering at SJTU were designed from the very beginning to explore the influence of γ on lock-in and VIV. As such, they cover a much larger range of flow accelerations. These tests were the result of an ongoing collaboration between Prof. Shixiao Fu's research group at SJTU and Prof. Kim Vandiver's research group at MIT. These tests were conducted at the ocean basin in the State Key Laboratory during the summer of 2012.

The flexible cylinder tested was 4m in length and was made using a wire cable for the core with a composite layer which encased the Fiber Optic Bragg strain gauges surrounding the core. The entire structure was then covered in a thin layer of rubber shrink tubing. Table 3.2 lists the most important physical properties of the riser model constructed at SJTU. The axial and bending stiffness were determined after subjecting a section of the riser model to tensile and three-point bending tests, respectively. More details can be found in Appendix D.

Table 3.2: The SJTU riser model properties

Model Length	4 m
Outer Diameter	24 mm
Mass in air	0.69 kg/m
Mass ratio	1.53
Bending Stiffness EI	10.5 Nm^2
Axial Stiffness EA	6.67x$10^5 N$
Pretension	500 N

There were a total of four fiber optic cables embedded in the composite layer of the cylinder; two in each of the CF and IL directions. The CF direction had 7 measurement locations whereas the IL direction had 11. The strains were recorded at a sampling frequency of 250 Hz. Damping tests in air showed that the structural

damping ratio was 1.5% of critical damping.

The cylinder was mounted on the *Forced Oscillation Apparatus* that was designed by Prof. Shixiao Fu (Fu et al., 2013). Figures 3-2 & 3-3 show the riser model mounted on the carriage. The relatively short track length of the experimental apparatus was the largest limitation in the design of the test matrix. The short track length meant that it would not be feasible to start a ramp test at zero velocity and reach the target velocity before reaching the end of the track while accelerating at rate that would allow us to observe VIV and lock-in. The way around this limitation was to program the carriage to start at zero speed and immediately jump to a speed close to the target speed and then accelerate or decelerate at the desired rate through the target speed.

The original test matrix was designed to excite the 3^{rd} and 4^{th} modes under many different accelerations and decelerations. In order to excite the 3^{rd} and 4^{th} modes the carriage would have to be towed at speeds of approximately 1.4 and 2.3 m/s assuming a dimensionless response frequency of 0.15. In practice, the cylinder was tension dominated and the initial pretension was set to $\sim 500N$. During the tests, the large drag forces resulted in tensions that were comparable or larger than the initial pretension. The increased overall tension affected the cylinder's natural frequencies which resulted in the natural frequencies 'tracking' the speed and always being excited at modes 2-3 independent of whether the towing speeds were centered around 1.4 or $2.3m/s$.

There were a total of 27 ramp tests around the 'target speed' of $1.4m/s$ with accelerations ranging from 0.002 to $1.119m/s^2$. In addition to these, 28 further ramp tests were performed around the 'target speed' of $2.3m/s$ with accelerations ranging from 0.032 to $1.403m/s^2$. The test matrix also included multiple runs at constant speeds which would serve as a baseline to compare to the data extracted from the ramp tests. Table 3.3 lists the acceleration and the associated γ for all the ramp tests performed at SJTU that are included in this thesis.

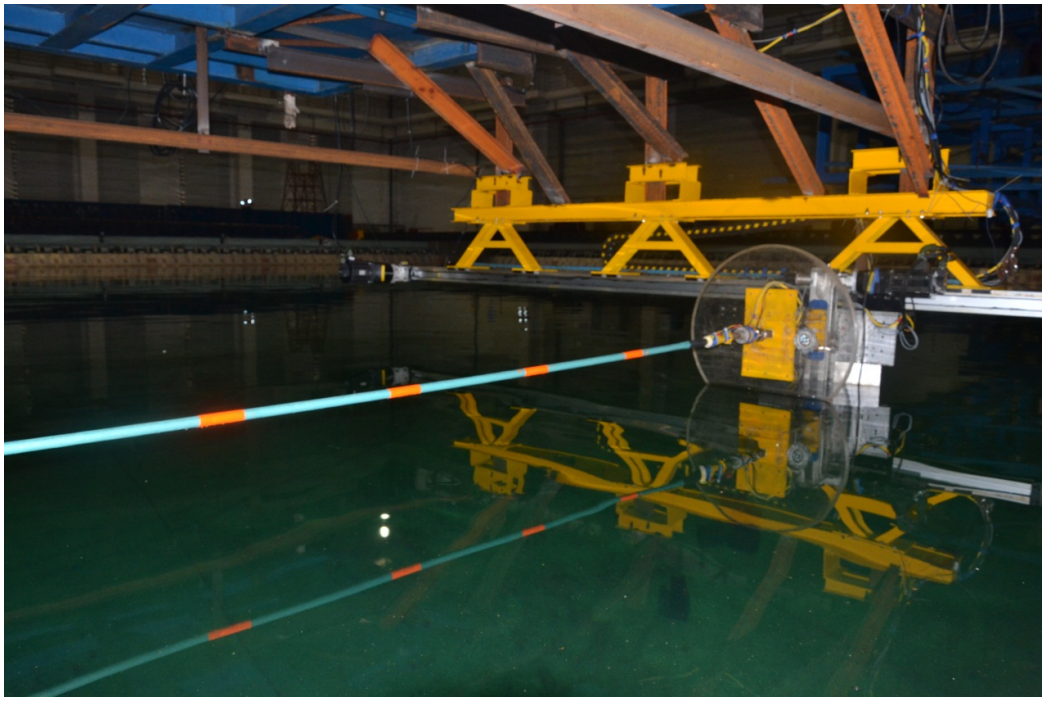

Figure 3-2: The SJTU riser model before it was submerged in the ocean basin

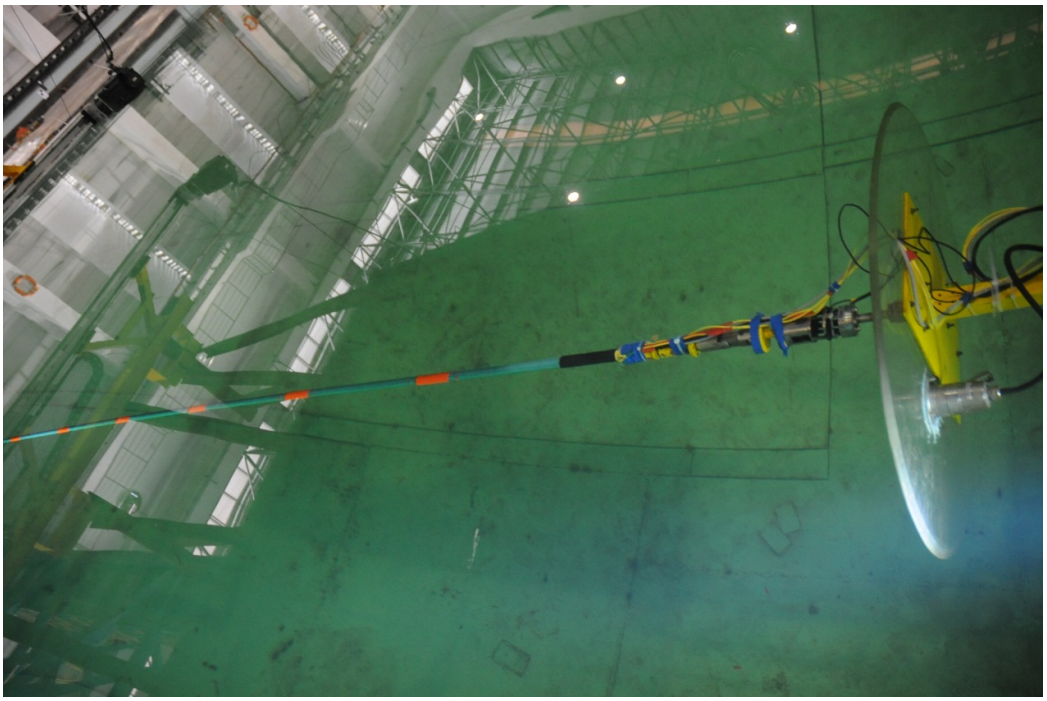

Figure 3-3: End connection (Model, Clamp, Universal Coupling, Force Transducer, End Plate)

Table 3.3: Ramp tests performed at SJTU

tests around 1.4 m/s			tests around 2.3 m/s		
Test #	acceleration (m/s^2)	γ	Test #	acceleration (m/s^2)	γ
1a	1.119	0.105	19a	1.402	0.035
2a	0.499	0.040	19b	1.400	0.037
2b	0.505	0.042	19c	1.395	0.036
2c	0.496	0.043	19d	1.402	0.036
2d	0.492	0.039	20a	0.866	0.018
3a	0.311	0.025	21a	0.646	0.018
4a	0.230	0.016	21b	0.670	0.017
5a	0.166	0.012	21c	0.669	0.019
5b	0.168	0.012	21d	0.655	0.018
5c	0.166	0.013	22a	0.464	0.013
5d	0.173	0.013	23a	0.354	0.008
7a	0.115	0.009	25a	0.240	0.006
8a	0.087	0.007	25b	0.249	0.006
9a	0.074	0.005	25c	0.249	0.006
10a	0.068	0.005	25d	0.259	0.007
10b	0.059	0.004	26a	0.202	0.005
10c	0.059	0.004	27a	0.172	0.004
10d	0.059	0.004	28a	0.123	0.003
11a	0.046	0.003	29a	0.072	0.002
12a	0.044	0.003	29b	0.077	0.002
13a	0.039	0.003	29c	0.093	0.002
14a	0.034	0.002	29d	0.073	0.002
15a	0.023	0.002	30a	0.069	0.002
16a	0.016	0.001	31a	0.046	0.001
17a	0.014	0.001	31b	0.050	0.001
18a	0.002	0.000	31c	0.046	0.001
142a1	steady flow	0	31d	0.032	0.001
142a2	steady flow	0	231a	steady flow	0
142b	steady flow	0	231b	steady flow	0
142c	steady flow	0	231c	steady flow	0

Chapters 4 through 6 make used of the steady flow data from the $38m$ SHELL dataset. The same dataset includes some unsteady flow cases or 'ramp tests' that are presented in Chapter 9. The SJTU data is presented in Chapter 8.

Chapter 4

Reynolds Number Effects on the VIV of Flexible Cylinders

The Reynolds number, Re, is a very important dimensionless parameter in most fluid dynamics problems including VIV.

$$Re = \frac{UD}{\nu}$$

Recently, independent studies by Govardhan & Williamson (2006) and Klamo et al. (2005) have shown that the Reynolds number is an extremely important parameter when analyzing the response amplitude of rigid cylinders undergoing VIV in laboratory experiments. Both studies demonstrate that the mass ratio does not influence the peak response amplitude whereas there is a strong dependence on the Reynolds number - with the peak response amplitude increasing with the Reynolds number in the range 500 $<Re<$12,000.

Despite being an important factor that governs the behavior of VIV, it has been very hard to study the effect of Reynolds number on the VIV response of flexible risers. Most of the high Reynolds number data remains the proprietary information of the oil and gas companies that funded the experiments, and only a few published datasets are available to researchers. Furthermore, when attempting to compile enough data so as to span a reasonable Reynolds number range, one inevitably runs into the problem

of comparing data from many different systems with different dynamic properties, instrumentation procedures, etc.

To date, the most comprehensive study of the Reynolds number effects on flexible cylinders is the work of Swithenbank et al. (2008) who compiled and organized the A/D vs. Re number data from ten different datasets including laboratory and field experiments.

This thesis includes attempts to build on the past work by using data from recent experiments on flexible pipes where the Reynolds number range spans three orders of magnitude. The aim of this chapter is to reveal the trends that exist between the Reynolds number and some of the most important VIV response parameters (dimensionless response frequency, Cross-Flow (CF) & In-Line (IL) amplitudes and drag coefficient C_d). All the flexible cylinder data that are presented in this chapter are from the $38m$ long SHELL tests at MARINTEK.

4.1 Effect of Reynolds Number on the Response of Elastically Mounted Rigid Cylinders

Govardhan & Williamson (2006) and Klamo et al. (2005) independently showed that the Reynolds number influences the peak response of a rigid cylinder free to vibrate in a cross-flow. After accounting for the Reynolds number dependence both authors were able to show excellent correlation between peak response amplitudes with their respective damping parameters. The authors clearly demonstrated that the response amplitude depends on the Reynolds number and some form of the damping parameter. Vandiver (2012) reviewed the history of the various forms of damping parameters, including the two used by Govardhan & Williamson and by Klamo et al. He explains the shortcomings of all previous damping parameters used in the study of VIV and then introduces a new damping parameter c^*, which is defined below.

$$c^* = \frac{2c\omega}{\rho U^2}$$

By far the most interesting result to follow from his analysis, is that a very simple relationship is shown to exist between the lift coefficient, C_L the dimensionless response amplitude, A^*, and the damping parameter, c^*, as shown in Equation 4.1:

$$C_L = A^* c^* \tag{4.1}$$

The key points from this analysis are repeated here because they not only provide great insight into the VIV problem but also help explain the strong Reynolds number dependence that Govardhan & Williamson (2006) and Klamo et al. (2005) discovered and will be shown to exist with flexible cylinder data later on in this chapter.
Starting with the equation of motion for a rigid, spring-mounted cylinder exposed to a cross flow,

$$m\ddot{y} + c\dot{y} + ky = \frac{1}{2} C_F \rho U^2 D \sin(\omega t + \phi) = \frac{1}{2} C_F \rho U^2 D \sin\omega t \cos\phi + \cos\omega t \sin\phi$$

and after substituting $y = A\sin(\omega t)$ for the response amplitude, the resulting equation can be separated into two equations. The first describes the dynamic equilibrium between the stiffness and inertial terms:

$$(k - m\omega^2)A = \frac{1}{2} C_F \rho U^2 D \cos\phi$$

The second equation describes the equilibrium between the damping force and the lift force:

$$c\omega A = \frac{1}{2} C_F \rho U^2 D \sin\phi$$

After rearranging this equation, the relationship shown in Equation 4.1 is obtained for the lift coefficient:

$$A^* \equiv A/D = \frac{\rho U^2}{2c\omega} C_F \sin\phi = \frac{1}{c^*} C_F \sin\phi = \frac{C_L}{c^*}$$

It is a well-known fact that the Reynolds number influences the lift coefficient of stationary cylinders (Norberg, 2003). Klamo et al. (2005) and Govardhan & Williamson (2006) showed that dimensionless response amplitude, A^*, is very dependent on Reynolds number for spring-mounted, rigid cylinders. However, Equation 4.1 makes it clear that the Reynolds number effect on A^* for rigid oscillating cylinders is entirely embodied in the lift coefficient, because c^* is composed only of parameters that have no Reynolds number dependence.

At this point Equation 4.1 becomes extremely useful, because it allows the calculation of the lift coefficient from quantities that both Govardhan & Williamson (2006) and Klamo et al. (2005) measured in their experiments. Namely, for every damping value tested, there is a corresponding peak A^* achieved by the vibrating cylinder. After calculating the c^* corresponding to each damping value it is then straightforward to calculate the C_L using Equation 4.1.

Doing so, one creates curves of C_L vs A^*, at the specific value of reduced velocity (V_r) that A^* was recorded at. This was done with the data used in Govardhan & Williamson (2006) and Klamo et al. (2005) and the C_L versus A^* curves that were created are shown in Figures 4-1 and 4-2 respectively.

The keen observer will notice that even though the shape of the curves is very similar, the C_L values are quite different. This is due to differences in experimental setups such as aspect ratio, end plates etc. Despite this, it is very obvious that in these Reynolds number ranges, increasing the Reynolds number of the flow will lead to an increase of the magnitude of the lift coefficient.

The Reynolds number effect on the response amplitude, A/D, is best explained through the effect that Reynolds number has on the lift coefficient. The purpose of the next section is to show that a similar dependence of A/D on Reynolds number may be observed in the VIV response of flexible cylinders after analyzing the $38m$ SHELL data.

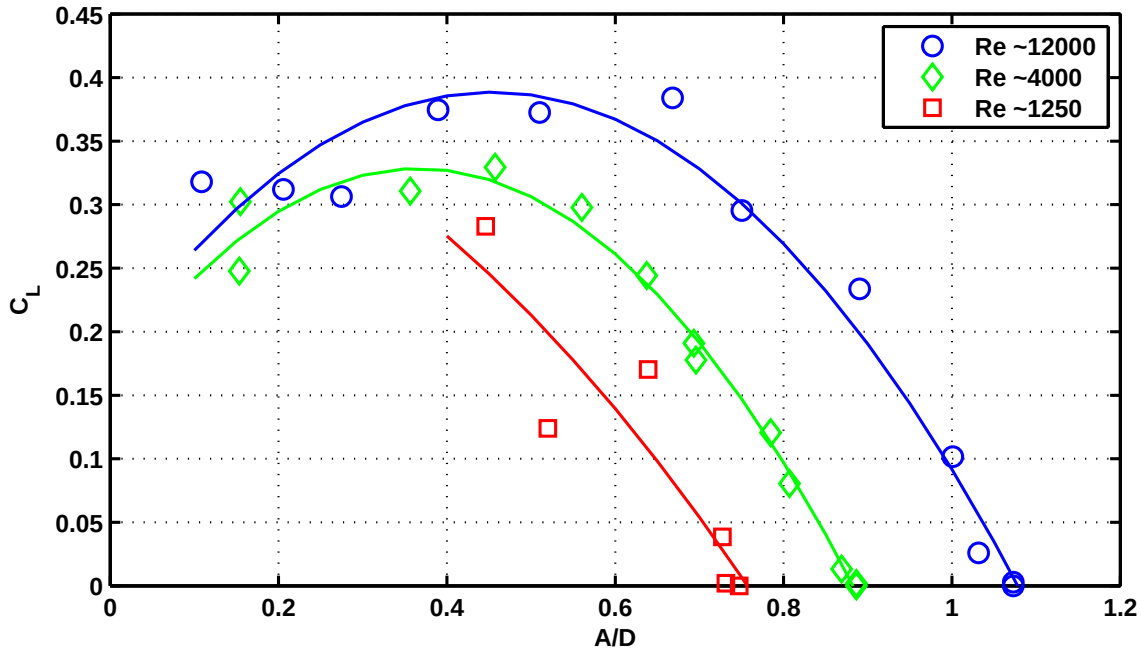

Figure 4-1: C_L vs. A/D constructed using data from Govardhan & Williamson

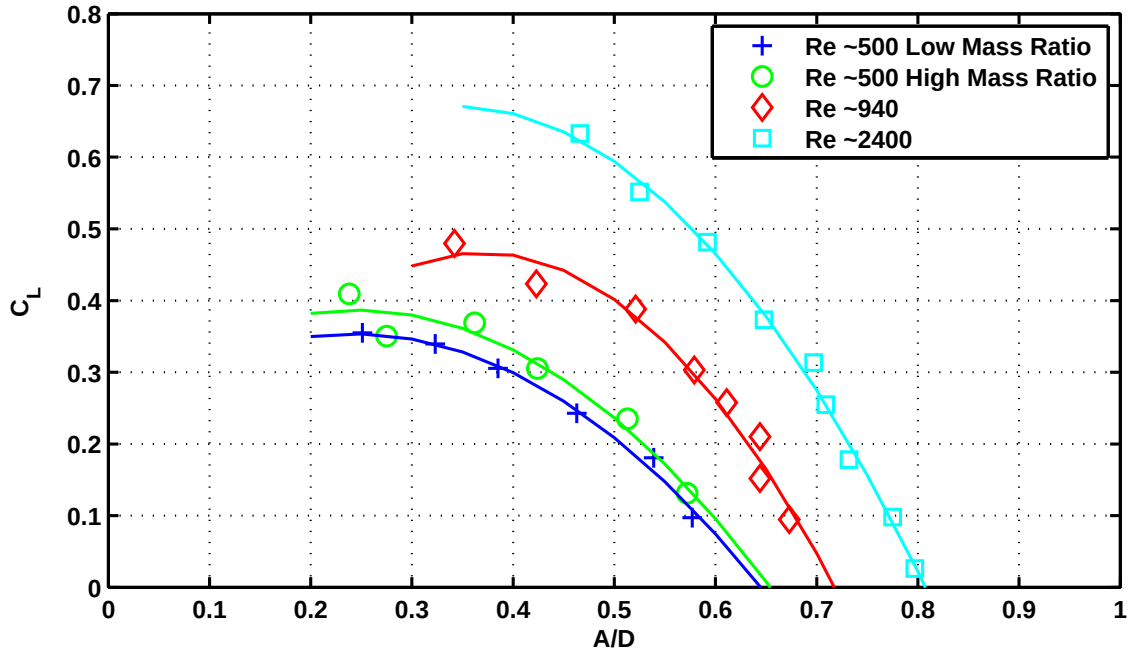

Figure 4-2: C_L vs. A/D constructed using data from Klamo et al.

4.2 Analysis

The variables under investigation are:

4.2.1 The Dimensionless Response Frequency

$$f^* = \frac{f_{response} D}{U}$$

The dimensionless response frequency for each test was calculated by identifying the resonant frequency, $f_{response}$, from the response spectra of several curvature sensors within the power-in region. In a similar way that the Strouhal number is the constant of proportionality that relates the frequency of the shed vortices behind a STATIONARY cylinder with the upstream current speed, the dimensionless response frequency, f^*, relates the response frequency of a vibrating cylinder with the upstream current speed.

Analysis of the recorded data revealed the strong presence of higher harmonics in most of the test cases. All of the time-series data used in this chapter were band-pass filtered around the dominant CF or IL frequencies often denoted as 1X or 2X respectively. Thus, the higher harmonics (3X, 4X and 5X) are excluded from the data shown in remainder of the chapter unless it is otherwise explicitly stated.

4.2.2 Response Amplitude

For the medium and large sized pipes, the amplitude at every accelerometer location was determined after integrating the accelerometer time history in the frequency domain. For the smallest pipe, the response amplitude was determined after reconstructing the displacement response based on the measured curvature and identifying the mode weights. In all cases, once the response amplitude, $y(x/L, t)$, was known, the spatial mean of the Root Mean Square (RMS) values in time, $\overline{\sigma_{A/D}}$, was calculated according to:

$$\overline{\sigma_{A/D}} = \frac{\sum_{i=1}^{N} \sigma_{A/D}}{N} = \frac{\sum_{i=1}^{N} \sqrt{\frac{1}{M} \sum_{j=1}^{M} (y_j(t) - \bar{y})_i^2}}{ND}$$

Where N is the number of sensors and M is the number of samples in the time history under consideration. $y_j(t)$ and $\bar{y}$ are respectively the instantaneous amplitude and the mean value in time at a specific sensor.

Even though the above parameter is useful when looking at data from uniform flow tests, it should not be used with response data from sheared flow tests. Sheared flow tests usually have large response amplitudes within the power-in region but the response outside the power-in region is considerably smaller. Therefore averaging the response amplitude over the entire riser length is not appropriate. Instead, the maximum RMS value, $\sigma_{A/D}^{MAX}$, along the length is a more appropriate metric.

$$\sigma_{A/D}^{MAX} \equiv \max[\sigma_{A/D}|_{i=1}, \sigma_{A/D}|_{i=2}, ..., \sigma_{A/D}|_{i=N}]$$

To account for the possibility that the maximum response occurs at a location which falls between two measurement locations, a modal reconstruction along the lines of Lie & Kaasen (2006) was performed for each test case. Figure 4-3 contains an example of a typical response reconstruction.

Figure 4-3 is a typical example of the response of a riser in a sheared flow. The test is number 3112, which involved towing the medium sized cylinder, Pipe 2 ($D = 0.03m$) in a sheared current with a maximum speed of $1.5m/s$ at $x/L = 0$. The maximum Reynolds number is $\sim 40,900$, but the Reynolds number corresponding to the power-in region will be somewhat smaller. The blue stars indicate the measured quantities, while the continuous green curves represent the modal reconstruction. The maximum response is on the high velocity end of the riser, but the location of the power-in region is not immediately apparent.

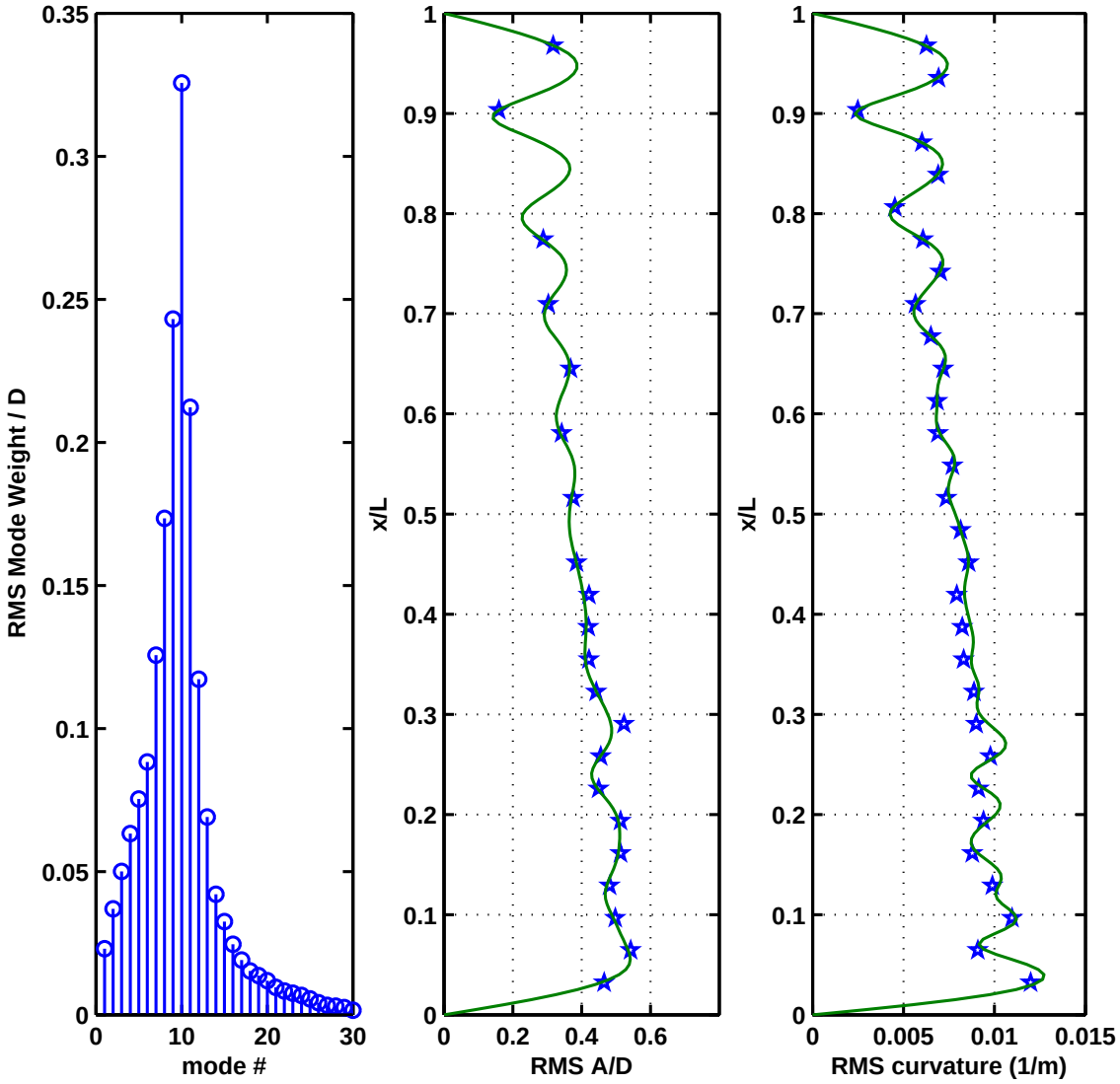

Figure 4-3: Modal reconstruction of CF response for Test 3112 (sheared flow with max. velocity of $1.5m/s$ at $x/L = 0$)

4.2.3 Drag Coefficient

The drag coefficient along the length of the pipe was estimated based on the method outlined in Jhingran et al. (2008). The key points are repeated below. Starting with the equation of motion in the In-Line, direction:

$$(m(x) + m_a(x,\omega))\frac{\partial^2 y}{\partial t^2} + c(x)\frac{\partial y}{\partial t} + EI(x)\frac{\partial^4 y}{\partial x^4} - T(x)\frac{\partial^2 y}{\partial x^2} = F(x,t)$$

Taking the temporal mean,($\overline{\ \ ^t}$), makes all zero-mean terms vanish. If EI is neglected for a tension dominated riser, the above formula simplifies to:

$$-T(x)\overline{\frac{\partial^2 y}{\partial x^2}^t} = \overline{F(x,t)^t}$$

The forcing term on the right-hand-side is simply the mean drag force per unit length, which can be expressed as:

$$F(x) = \frac{1}{2}C_D(x)\rho D U(x)^2$$

Substituting and rearranging yields the mean drag coefficient C_D at a specific location, x:

$$C_D(x) = \frac{4T(x)\overline{\frac{\partial^2 y}{\partial x^2}^t}}{\rho D U(x)^2}$$

It is important to emphasize that all these quantities are calculated locally (i.e., at a specific sensor, located at a distance x from the end) and as such the drag coefficient will vary considerably along the length of the riser. This is demonstrated in Figure 4-4. The plot shows the drag coefficient C_D at every curvature sensor along the riser. The data presented in this plot is typical of the data used to create Figure 4-10, where all the test cases (Pipe 3 and Pipe 3 Rough) and all the sensor data have been included.

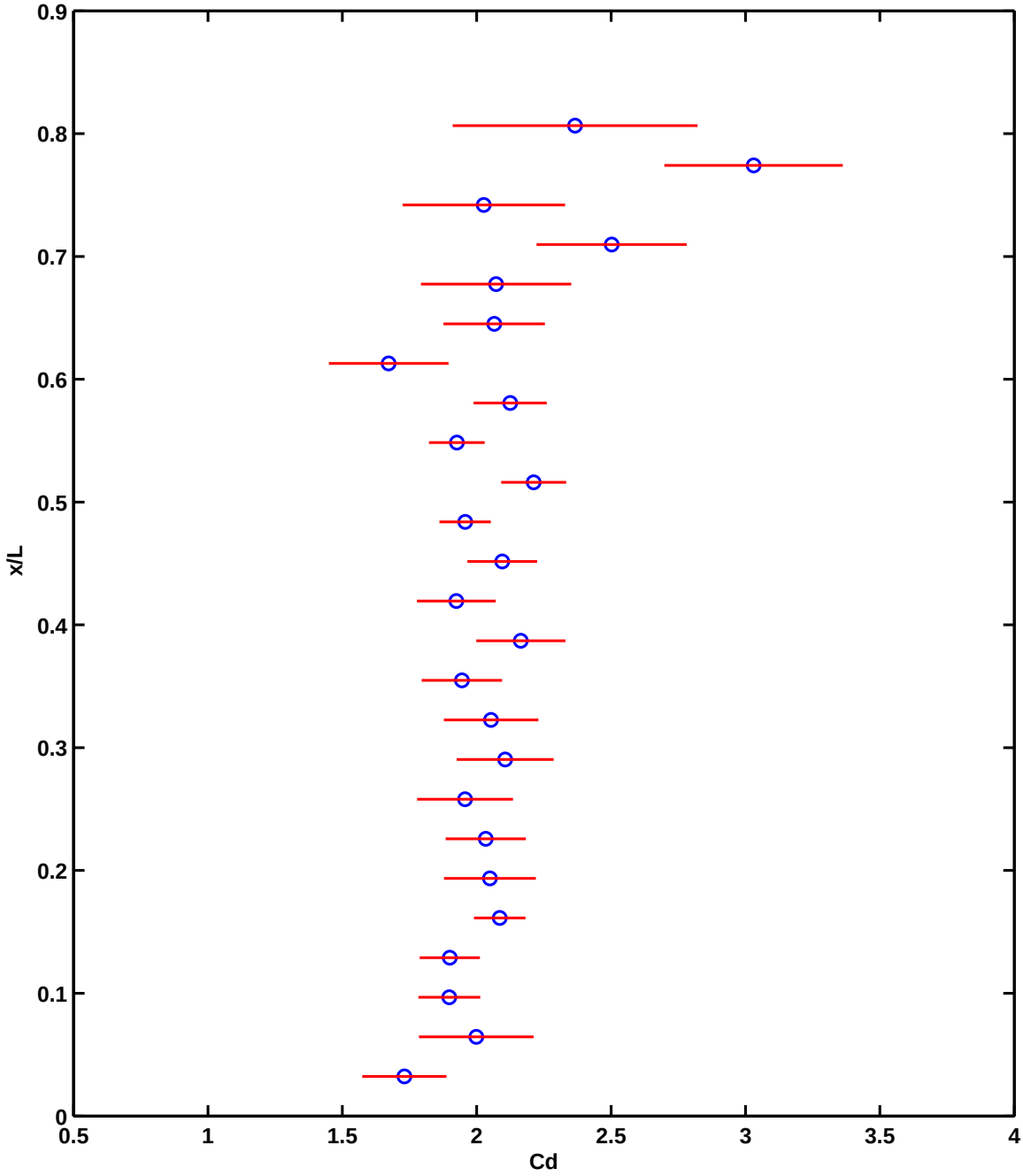

Figure 4-4: Drag coefficient as a function of x/L for Test 3112. The red lines indicate the uncertainty in the C_D calculation at every measurement location

4.2.4 Power-In Location

The power-in region is traditionally defined as the region along the length of the pipe where the wake is well correlated with the riser motion.

In uniform flow tests when the pipe is responding at low mode numbers, the power-in region extends over the entire riser length. Since the entire pipe is exposed to the same current, determining the corresponding Reynolds number for such a case is straightforward.

The same cannot be said for sheared flows. Here, the current varies along the pipe length and, as such, the Reynolds number varies from 0 on one end to $\frac{U_{max}D}{\nu}$ on the high velocity end. The question that then arises is: what is the appropriate Reynolds number for such a case?

Choosing the Reynolds number that corresponds to the location of the power-in region seems like a sensible choice. Identifying the power-in region in sheared flows is still a matter of current research, yet one can try to use previous experimental evidence to approximately identify this region.

VIV experiments on flexible cylinders in sheared and non-uniform currents, such as the Lake Seneca tests, the Miami II tests, the $38m$ NDP tests as well as the current SHELL tests typically show that the largest strains are always near the high velocity end and the response decays as you move toward the low velocity end (see Figure 4-3).

The exact location of the power-in region will eventually depend on which mode (of all the potentially excited modes) ends up dominating the response. In this work, it will be assumed that the power-in region is approximately centered at a distance x/L=0.25 away from the high velocity end. Accordingly, the Reynolds number for the sheared flow cases, to be used in the comparisons later on, will be 25% smaller than the maximum Reynolds number which is always at x/L=0.

The trends between the response amplitude and the Reynolds number for the sheared flow cases are not very sensitive to the precise location at which the Reynolds number is computed, which in this work is at x/L=0.25. If a slightly larger or smaller

Reynolds number had been chosen the data on a plot of A/D vs. Re would simply shift slightly to the right or left respectively and all trends in the plots of A/D vs. Re would appear the same.

4.3 Results

Table 4.1 summarizes some of the key results from the tests. The Reynolds number reported for the sheared flow tests is the value corresponding to what is believed to be the power-in region and not the maximum Reynolds number on the riser.

Table 4.1: Range of values for all test cases under review

	Reynolds number	Mode #	$\overline{\sigma_{A/D}}$	$\sigma_{A/D}^{MAX}$	$n\zeta$
Pipe 1 Unif.	$4.9 \times 10^3 - 3.76 \times 10^4$	10 - 26	0.32 - 0.52	0.47 - 0.84	0.07 - 0.18
Pipe 1 Shear	$4.1 \times 10^3 - 2.54 \times 10^4$	9 - 30	0.26 - 0.36	0.39 - 0.49	
Pipe 2 Unif.	$6.6 \times 10^3 - 6.8 \times 10^4$	3 -11	0.30 - 0.57	0.42 - 0.83	0.02 - 0.08
Pipe 2 Shear	$6.2 \times 10^3 - 5.9 \times 10^4$	3 - 13	0.27 - 0.47	0.36 - 0.71	
Pipe 3 Unif.	$3.6 \times 10^4 - 1.3 \times 10^5$	2 - 7	0.39 - 0.64	0.54 - 0.91	0.01 - 0.05
Pipe 3 Shear	$2.7 \times 10^4 - 1.6 \times 10^5$	2 - 8	0.36 - 0.62	0.49 - 0.81	
Rough Unif.	$1.8 \times 10^4 - 1.2 \times 10^5$	2 - 7	0.31 - 0.48	0.46 - 0.73	0.01 - 0.05
Rough Shear	$4.9 \times 10^4 - 1.5 \times 10^5$	4 - 11	0.31 - 0.40	0.39 - 0.50	

Figure 4-5 shows how the response amplitude of the medium sized cylinder (Pipe 2) varied as a function of Reynolds number. The plot shows the spatial mean ($\overline{\sigma_{A/D}}$) and maximum ($\sigma_{A/D}^{MAX}$) in both the CF and IL amplitudes for all the uniform flow cases. The influence that Reynolds number has on the response data is clearly visible, with the response amplitude in both CF and IL directions increasing as the Reynolds number is increased.

If one assumes that the power-in region for uniform flows covers the entire riser length, then there is no hydrodynamic damping present, and the only damping present in the system is the structural/hysteretic damping which is the same for all cases.

Since all other factors are the same, the scatter can be attributed to variations in reduced velocity. This is further reinforced by the fact that at the larger Reynolds numbers (and hence higher velocities and higher excited mode numbers) the scatter is smaller. At high mode numbers the natural frequencies are spaced much closer than at low mode numbers, which means that there is a higher probability that the selected constant towing speed will coincide or be very close to that mode's critical reduced velocity.

Figure 4-6 shows how the dimensionless response frequency,f^*, determined from the uniform flow tests, varied as a function of the Reynolds number. Looking at the bare cylinder data, it is obvious that the dim. response frequency decreases as the Reynolds number increases. A best fit, through all of the bare pipe data (i.e., excluding the roughened pipe) presented in Figure 4-6 in the Reynolds range investigated is:

$$f^* = -0.0065 \ln Re + 0.21 \tag{4.2}$$

Figure 4-7 shows the spatial mean RMS amplitude, $\overline{\sigma_{A/D}}$, in the CF and IL directions for all the pipes tested in this experiment. The figure also shows the best fit from Swithenbank et al. (2008).

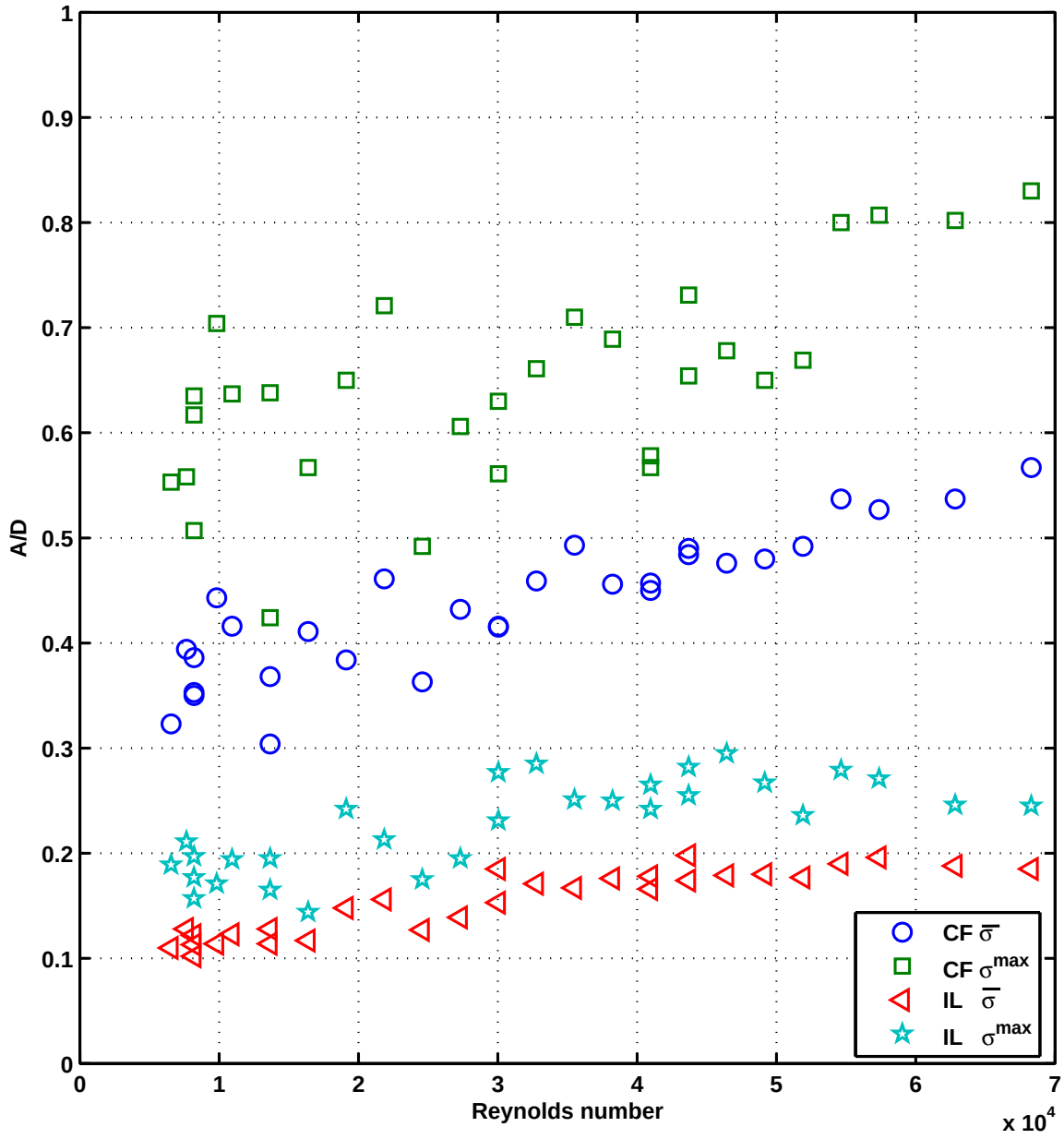

Figure 4-5: Response amplitude (A/D) vs. Reynolds number for Pipe 2 in uniform flows

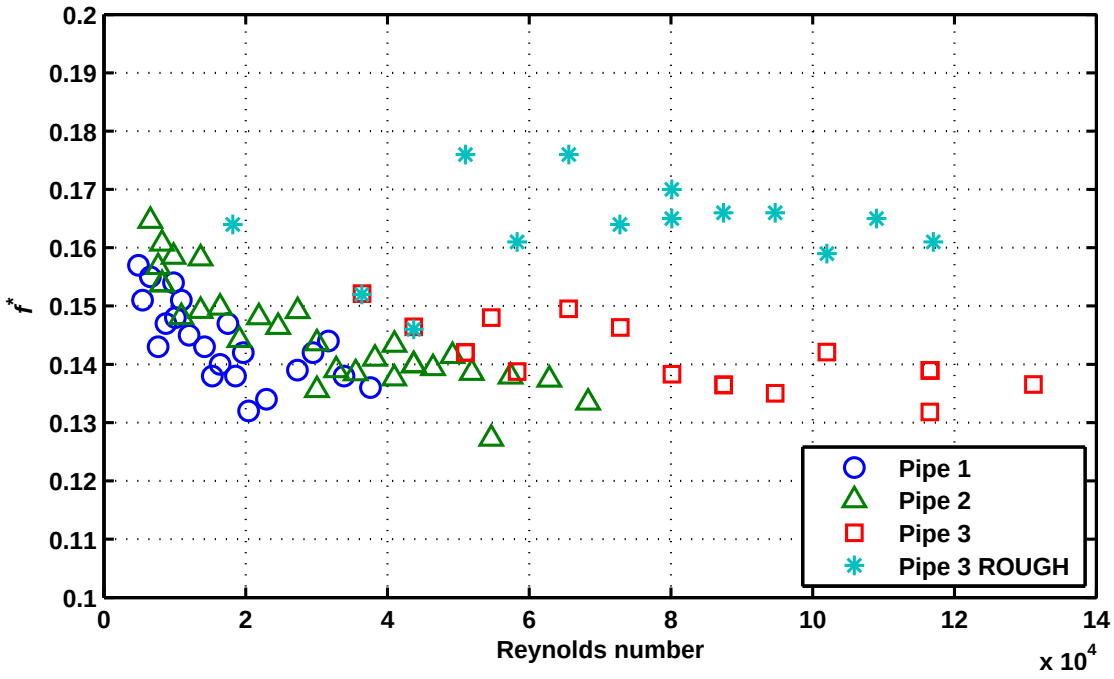

Figure 4-6: Dimensionless response frequency vs. Reynolds number from uniform flow tests

The first thing to point out here is the peculiar behavior seen in the CF response of Pipe 1. Initially, the response amplitudes are large but at Reynolds numbers greater than 17,000-18,000 the response amplitude starts decreasing rapidly. This behavior was very puzzling in the beginning and was initially attributed to a strong travelling response and a shift from strong standing wave to travelling wave response in Resvanis et al. (2012). Follow-up investigations by MARINTEK (2012), showed that at large towing speeds the drag induced very large deflections (sag) on the small riser model (pipe 1). This in turn meant that the flow was no longer normally incident on the pipe and this was especially true of the two ends of the model. The variation in incident current meant that only a portion of the cylinder was available for power-input to the model with considerable portions now contributing to damping which in turn greatly limited the response amplitude.

The relatively large scatter in the CF RMS A/D values of Pipe 3 is due to the fact that the responding modes are much lower (3-7) and a lot of the variability can be attributed to reduced velocity effects.

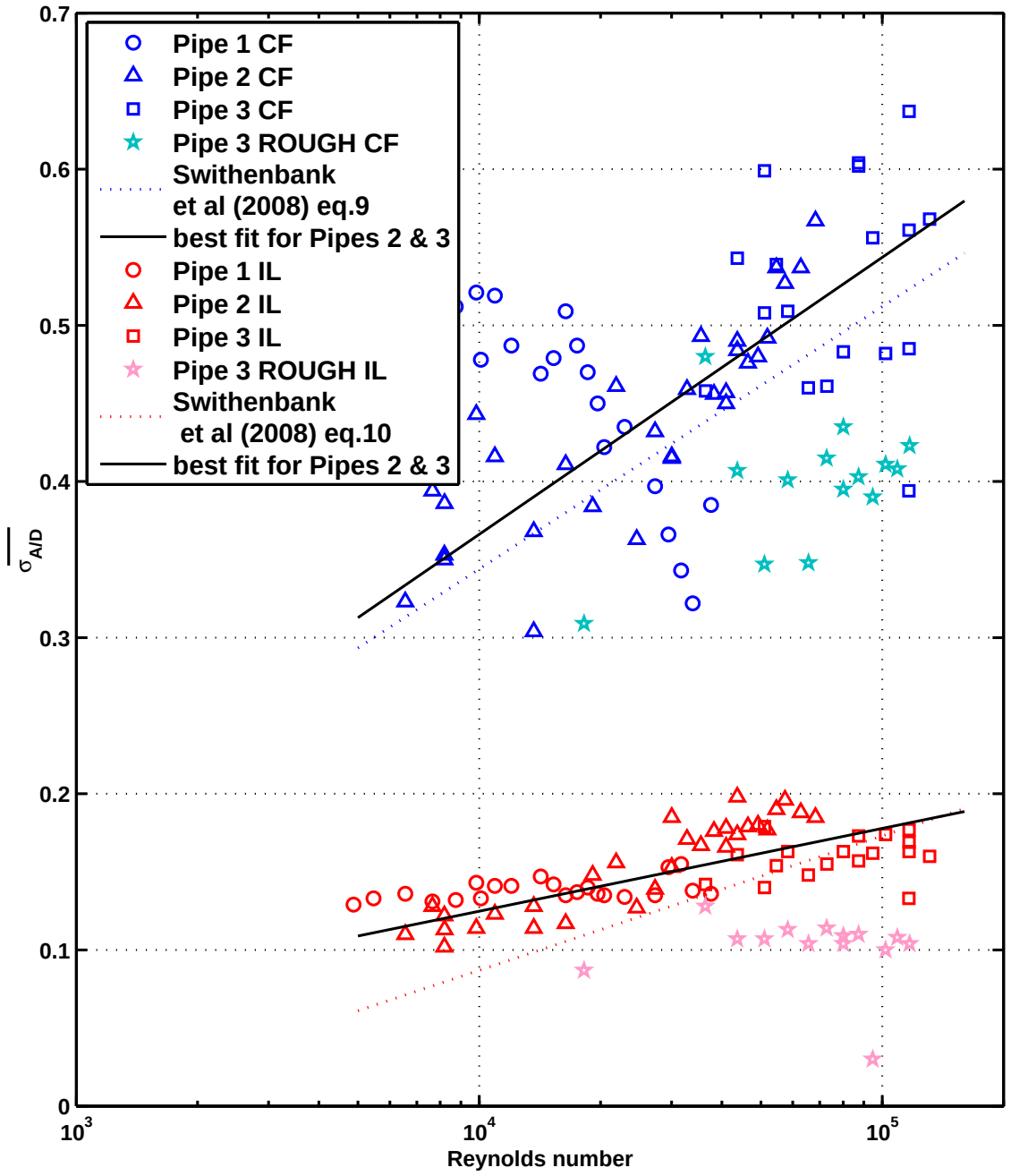

Figure 4-7: Spatial mean RMS amplitude, ($\overline{\sigma_{A/D}}$) vs. Reynolds number for the CF and IL directions in uniform flows

The best fits through the bare Pipe 2 and Pipe 3 data for the CF and IL direction are:

$$\text{CF direction:} \qquad \overline{\sigma_{A/D}} = 0.077 \ln Re - 0.343 \tag{4.3}$$

$$\text{IL direction:} \qquad \overline{\sigma_{A/D}} = 0.023 \ln Re - 0.087 \tag{4.4}$$

In Figure 4-8, note how the maximum RMS response amplitudes, $\sigma_{A/D}^{MAX}$, for the sheared cases are always smaller than the uniform flow cases. This happens because under sheared flow conditions the power-in length is limited to a small portion of the riser and the remaining sections provide hydrodynamic damping. As a result, the sheared flow cases always have higher damping values than their corresponding uniform flow cases. The increased damping will in turn limit the maximum resonant amplitude.

The best fit through the data for the CF direction is:

$$\text{CF direction:} \qquad \sigma_{A/D}^{MAX} = 0.077 \ln Re - 0.343 \tag{4.5}$$

Once again, the roughened pipe data was not included when calculating this fit and neither was the Pipe 1.

Figure 4-9 shows the spatial mean (spanwise averaged) drag coefficient, C_D, along the riser length calculated from the uniform flow cases.

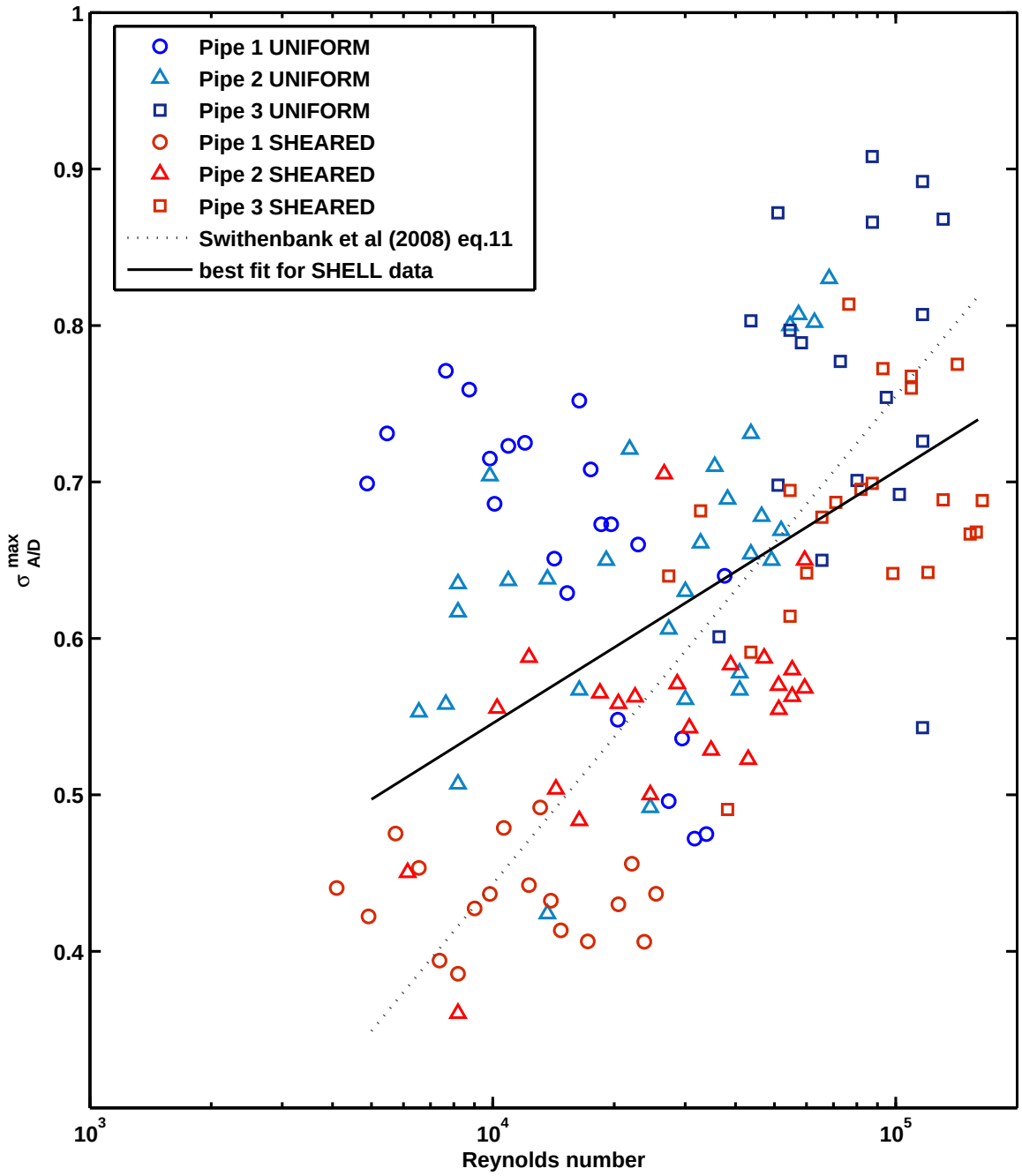

Figure 4-8: Cross-flow $\sigma_{A/D}^{MAX}$ vs. Reynolds number for uniform and sheared flows

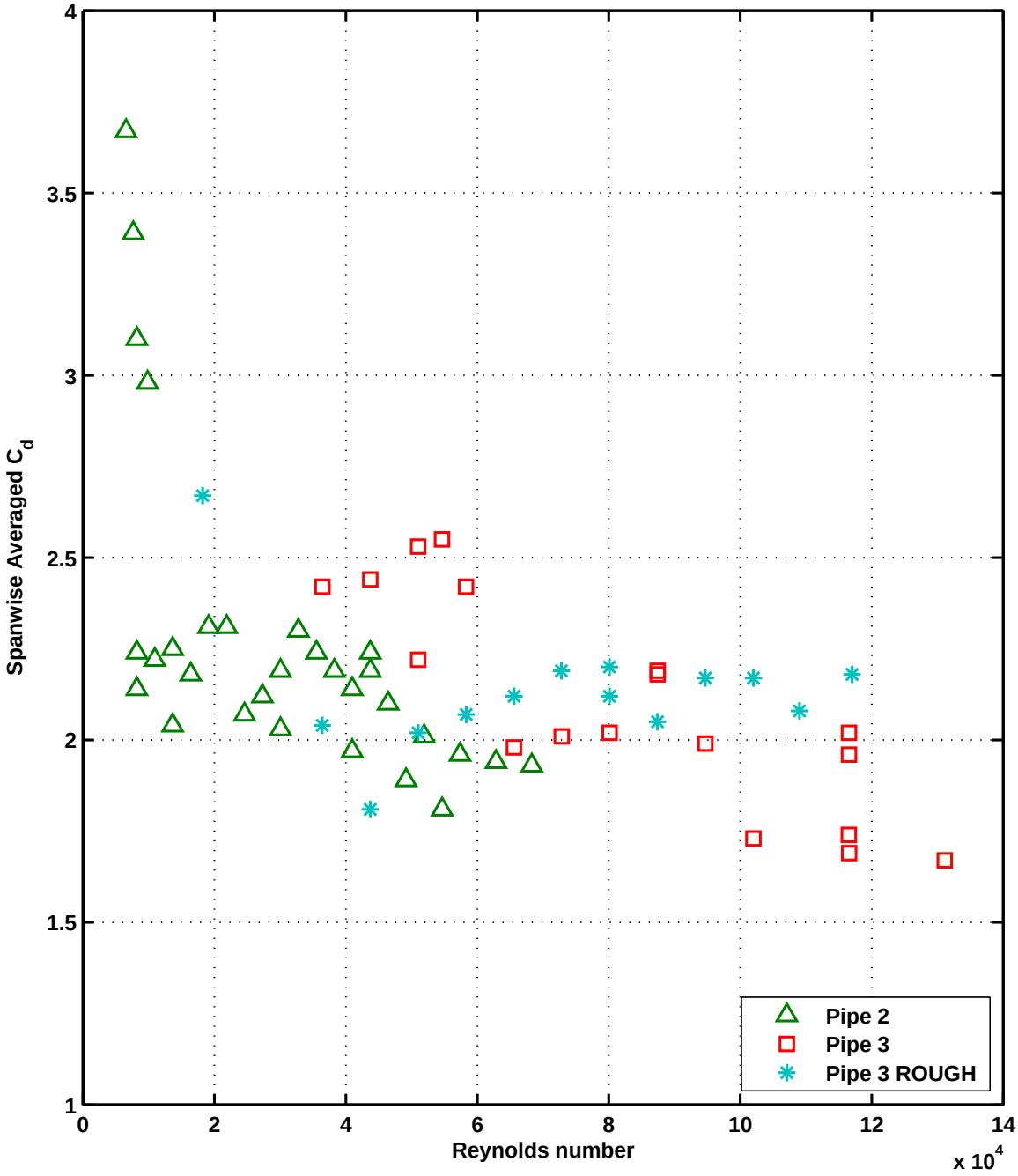

Figure 4-9: Spanwise averaged C_D vs. Reynolds number for uniform tests

Little emphasis has been placed until this point on the results of the roughened cylinder; it has been included here to demonstrate how profoundly the surface roughness can alter the response characteristics. The roughened cylinder results are directly comparable with the large diameter (Pipe 3) results since all other properties (aspect ratio, Re, etc) are the same. From Figure 4-6 it is apparent that the dimensionless response frequency is considerably larger for the rough pipe, whereas Figure 4-7 reveals that the response amplitude in both CF and IL directions is significantly smaller than its bare cylinder counterpart.

Figure 4-10 shows the drag coefficient at **every location** along the riser as a function of the Reynolds number at that location. Only the data corresponding to the largest diameter pipe with and without the rough surface finish has been included. The surface roughness caused by the attached sandpaper was applied in order to create a more turbulent boundary layer thus mimicking a flow at even higher larger Reynolds numbers than was attainable with the largest diameter pipe.

At a given Reynolds number the variation in C_D is due to the A/D dependence, especially obvious when looking at the uniform flow results, which show a lot of scatter consistent with the variation in C_D seen at the nodes or anti-nodes of a strong standing wave response. At Reynolds numbers smaller than 10^5 there is a lot of overlap in the C_D values shown. As Reynolds number increases, well into the drag crisis region, the C_D for the smooth pipe starts decreasing whereas the C_D for the roughened pipe is considerably larger.

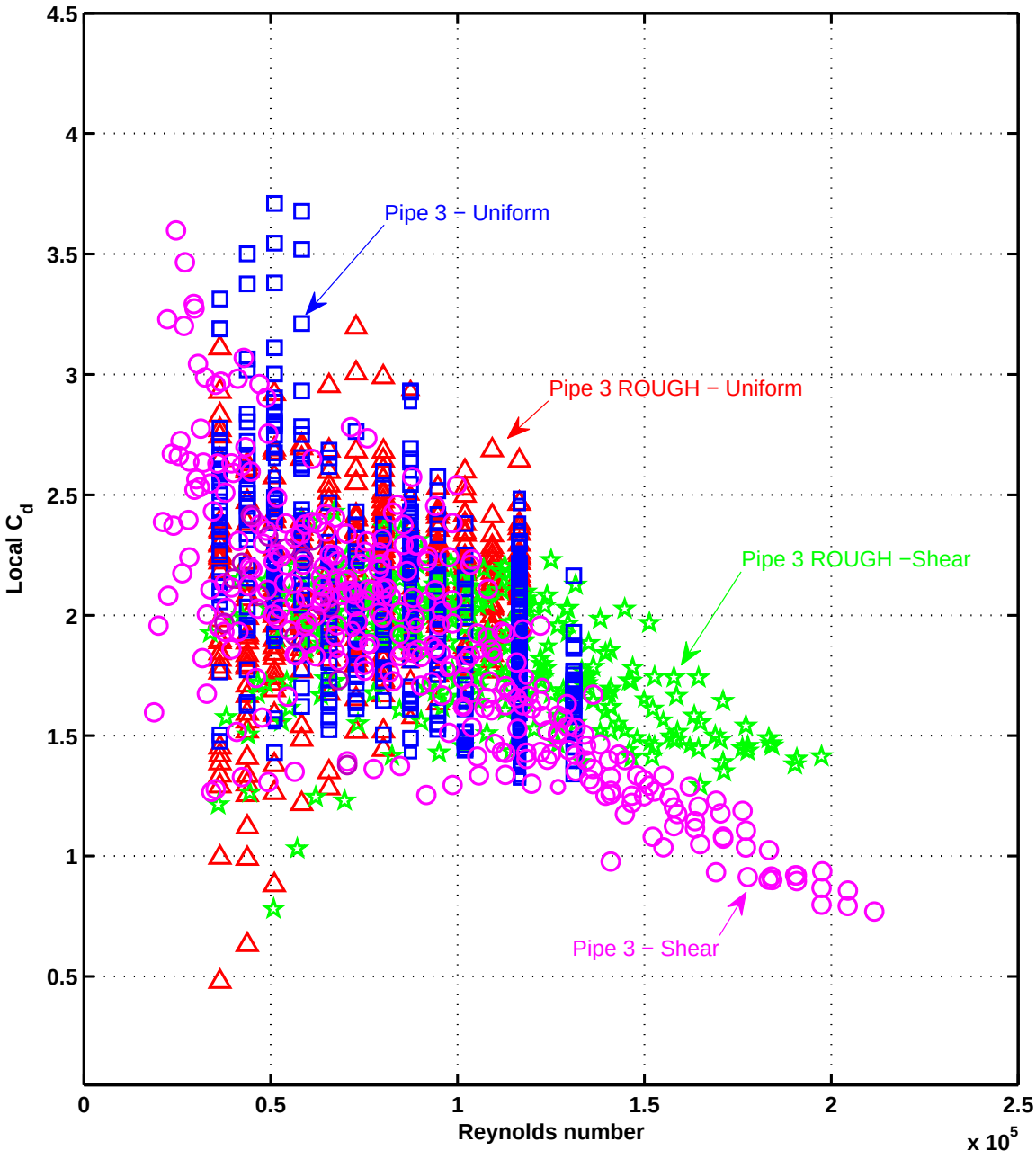

Figure 4-10: Local drag coefficient, C_D, vs. Reynolds number for Pipe 3 (smooth and rough) in uniform and sheared flows

4.4 Chapter Summary

The first part of this chapter provides an explanation for the strong influence of Reynolds number on the response of spring-mounted rigid cylinders vibrating freely in a cross-flow. This is attributed to the effects that Reynolds number has on the lift coefficient, demonstrated here, using the experimental data from Govardhan & Williamson (2006) and Klamo et al. (2005).

The most interesting result from the analysis of the SHELL 38m long data, is the clearly demonstrated effect that increasing Reynolds number has on the response amplitude of flexible cylinders. The trend identified is in good agreement with what has been previously reported for flexible cylinders and there are strong similarities with the effect of Reynolds number on rigid cylinders. For elastically mounted rigid cylinders vibrating in a cross flow, this work shows that the lift coefficient increases as the Reynolds number is increased. The same should hold true for the lift coefficient of flexible risers and should be the main cause of the increasing response amplitude as a function of Reynolds number in the range tested.

Many of the factors that influence the response of rigid cylinders are also important for the response of flexible cylinders. A lot of the scatter seen in the plotted results- in this work and in previous studies- can be attributed to variations of these parameters between experiments. The most notable are damping, reduced velocity, aspect ratio and responding mode number as well as surface roughness.

The dimensionless response frequency for a vibrating riser decreases as the Reynolds number is increased, approaching a limiting value between 0.13 and 0.14 at Reynolds numbers up to 1.4×10^5. This is a very interesting result because Strouhal number data from stationary cylinders in the same Reynolds number range show that it remains roughly constant at $\sim 0.18 - 0.2$ from $Re \sim 500$ until the drag crisis region around $Re \sim 2 \times 10^5$. This has important implications for riser designers, since a lower Dim. Response Freq. at a given Reynolds number will typically mean a lower excited mode and hence smaller strains and stresses for a given current speed.

Further experimental evidence, at even higher Reynolds numbers, is necessary to

see if this limiting value will hold even beyond the drag crisis regime.

Later on in this thesis, many comparisons of the VIV response in steady and unsteady flows will be shown. It would have been impossible to explain differences between these if the Reynolds number effects not been sorted out beforehand, for it would have been too difficult to distinguish which response characteristics were due to the unsteady nature of the oncoming flow and which were due to the Reynolds number.

THIS PAGE INTENTIONALLY LEFT BLANK

Chapter 5

Incorporating Reynolds Number Effects in VIV Prediction Programs

The main aim of this chapter is to propose a methodology for the incorporation of a Reynolds number dependent lift coefficient (C_L) curve into a VIV response prediction program like SHEAR7 (Vandiver et al., 2012). The SHEAR7 predictions are then compared with experimental data from the recent SHELL 38m tests which showed strong Reynolds number effects.

SHEAR7 is a semi-empirical VIV prediction program that is capable of predicting the response (amplitude, stress, frequency and mode) and the associated damage rates for a given current profile. It uses experimentally measured fluid coefficient data from CF forced vibration tests at a single Reynolds number and then applies an approach similar to strip-theory to predict the response of a long flexible riser. The C_L curves currently used in SHEAR7 do not currently account for Reynolds number.

The proposed methodology to incorporate Reynolds number effects in VIV predictions is shown to produce good results in the Reynolds number range between 5,000 and ~70,000. It should not be used outside this range until further experimental evidence is collected to confirm its validity beyond this range.

5.1 Effect of Reynolds on C_L vs. A/D curves

Govardhan & Williamson (2006) and Klamo et al. (2005) independently showed that the Reynolds number influences the peak response of a rigid cylinder free to vibrate in a cross-flow. Both groups clearly demonstrated that the response amplitude depends on the Reynolds number and some form of damping parameter. The relationship identified by Govardhan & Williamson is shown in Equation 5.1.

$$A^* = (1 - 2.2\alpha + 0.30\alpha^2)\log(0.41Re^{0.36}) = (1 - 2.2\alpha + 0.30\alpha^2)f(Re) \tag{5.1}$$

Equation 5.1 consists of two terms, the first describes the amplitude's dependence on the mass-damping parameter, α, and the second term, $f(Re)$, describes the amplitude's dependence on the Reynolds number.

Even though both groups investigated the response as a function of the Reynolds number they did not show the effect that Reynolds number might have on the lift coefficient. Vandiver (2012) shows how the various forms of the damping parameter proposed through the years are related to each other and, most importantly, how casting the damping in the correct dimensionless form of c^*, allows one to calculate the lift coefficient using only the response amplitude and damping through the relationship $C_L = A^*c^*$. Using this relationship, it has been possible to show that the Reynolds number greatly affects the lift coefficient. It is for this reason that the amplitude of both rigid and flexible cylinders increases as a function of the Reynolds number.

Figure 5-1 plots Govardhan & Williamson's data of dimensionless response amplitude, $A*$ vs. α, their mass-damping parameter, in the same way they present it in their publication. At a given value of mass-damping parameter, the Reynolds number dependence of the response amplitude is clearly visible.

This can then easily be converted into curves of dimensionless response amplitude, A^*, vs. damping parameter, c^*, using the conversion factors calculated by Vandiver (2012), namely that

$$c^* = \alpha 4\pi^3 \frac{f_n D}{U}\frac{fD}{U} \approx \alpha 3.59$$

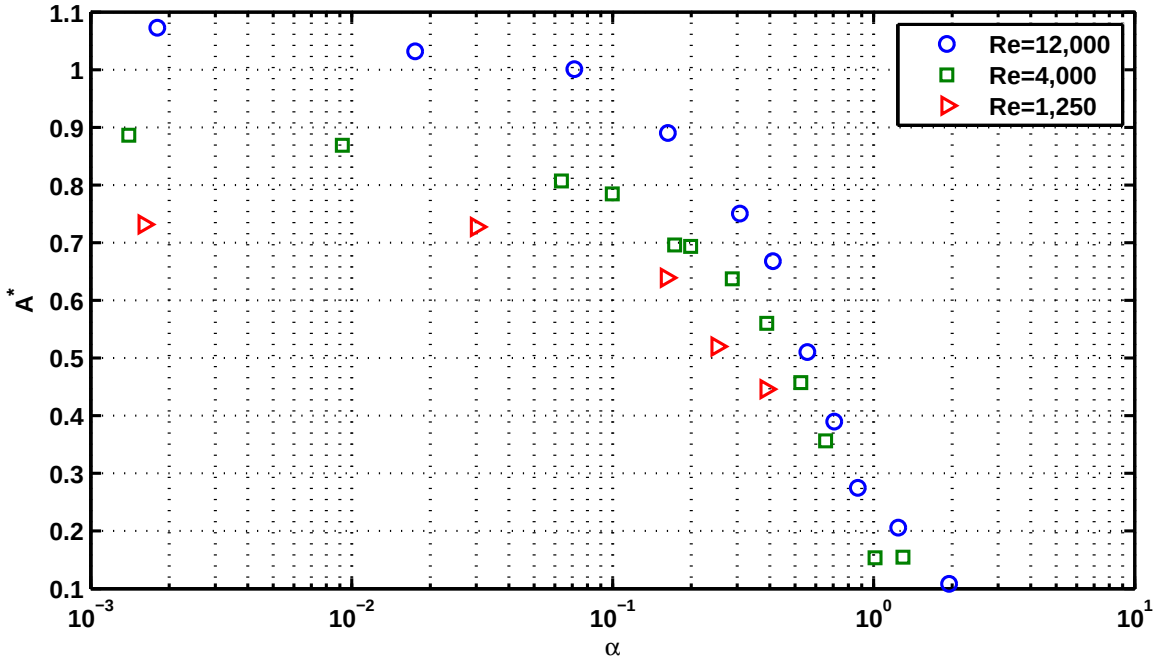

Figure 5-1: Response amplitude,A^* vs. α, the mass-damping parameter

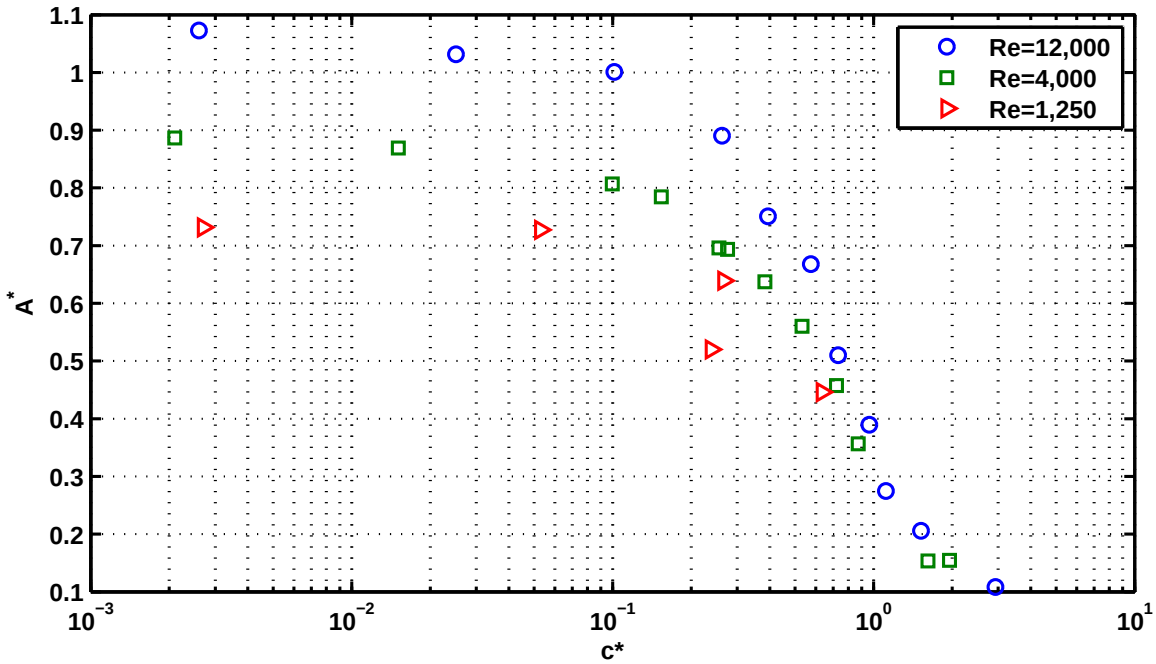

Figure 5-2: Response amplitude,A^* vs. c^*, the damping parameter

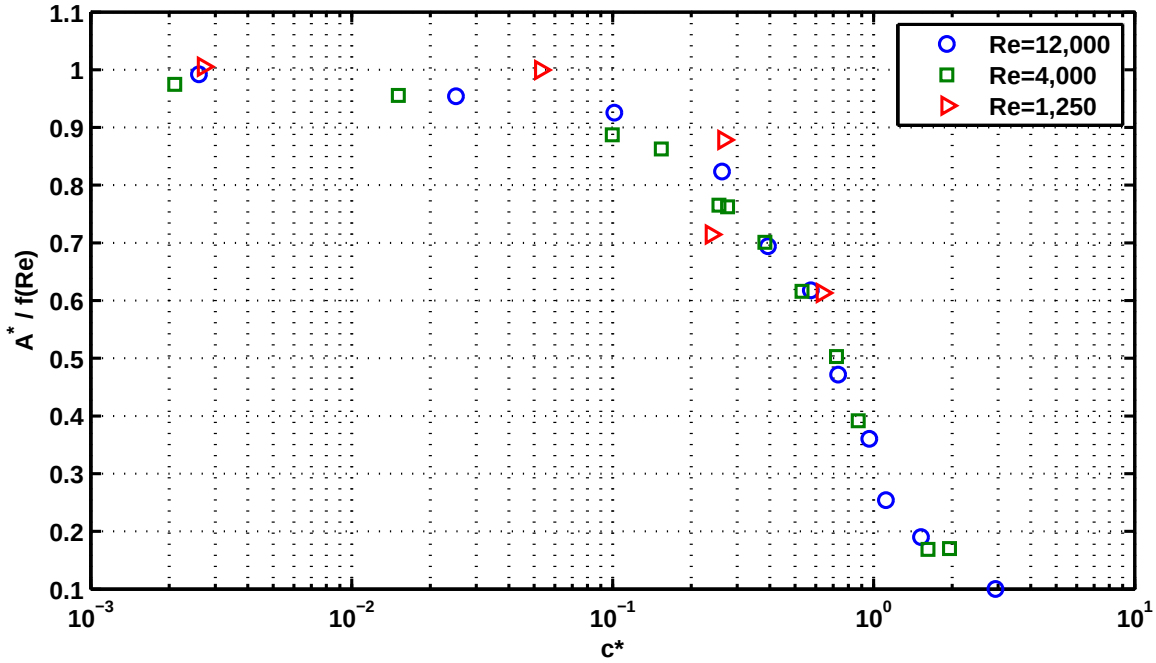

Figure 5-3: $A^*/f(Re)$ vs. c^*

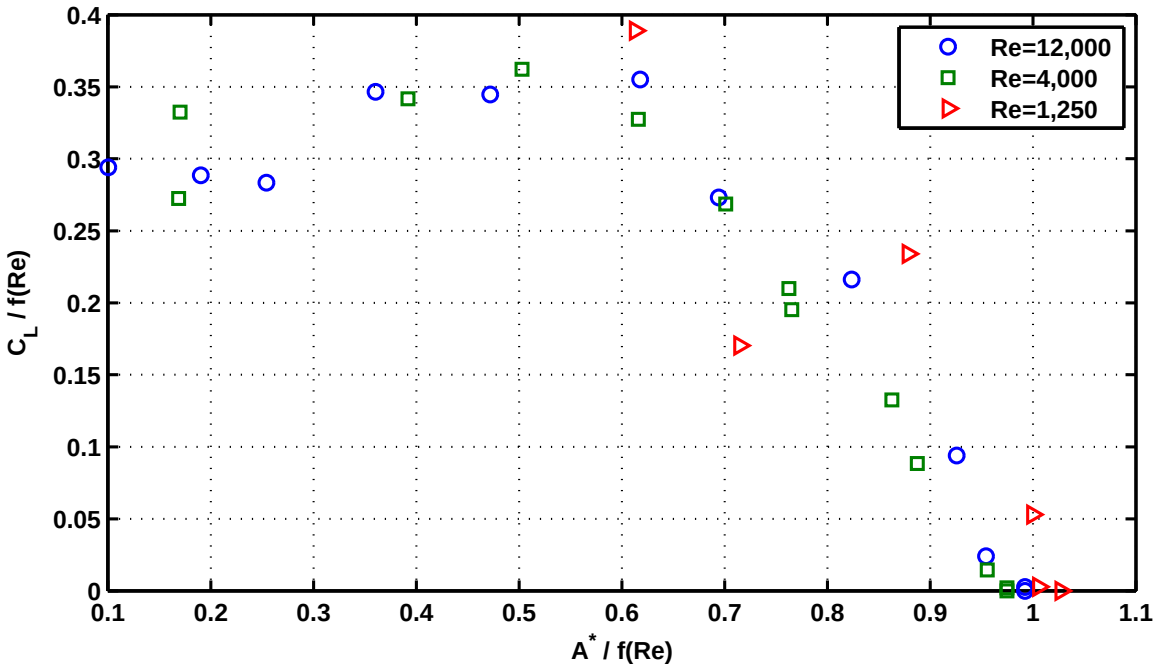

Figure 5-4: $C_L/f(Re)$ vs. $A^*/f(Re)$

Figure 5-2 shows the same data shown in Figure 5-1, but now the data is plotted as A^* vs. c^* instead of α, the Williamson mass damping parameter.

If the A^* values shown in Figure 5-2 are divided by the Reynolds number factor, $f(Re)$, in Equation 5.1, the three curves on the previous plot collapse onto a single curve of $A^*/f(Re)$ vs. c^*, as shown in Figure 5-3.

Recalling that $A^*c^* = C_L$ leads to: $\frac{A^*}{f(Re)}c^* = \frac{C_L}{f(Re)}$ since c^* does not depend on the Reynolds number.

This means that the curve in Figure 5-3 contains all the information necessary to calculate a lift coefficient vs. amplitude curve with all Reynolds number effects removed. Figure 5-4 shows how the three curves of lift coefficient, C_L, vs. A^*, can collapse onto a single line after the Reynolds number effects have been removed. (Note that if the Re number dependence had not been removed the figured would look like Figure 4-1)

It stands to reason that if one can collapse multiple different C_L vs. A/D curves onto a single curve by removing the Reynolds number effects then one could also proceed in the converse direction. That is, one can start modifying a single C_L vs. A/D curve by multiplying both axes with the Reynolds number function, $f(Re)$, in order to introduce the Reynolds number effects. The next section will show how making these changes to the C_L data used in SHEAR7 results in response predictions that are Reynolds number dependent and are similar to the response observed in the SHELL tests.

5.2 Incorporating Reynolds Number Dependent C_L Curves Into SHEAR7

Now that the effect of Reynolds number on C_L has been demonstrated all that remains is to start modifying the SHEAR7 lift coefficient curve to incorporate the Reynolds number effects documented.

In SHEAR7, lift curves are defined by a set of four numbers. The procedure

to incorporate the Reynolds number effects into the lift curve is straightforward and requires multiplying each value defining the lift curve with a factor equal to $f(Re) = \log(0.41\, Re^{0.36})$ from Equation 5.1 in the beginning of this chapter.

SHEAR7 allows users to input their own lift coefficient curves in terms of C_L vs. A/D the remainder of this chapter will only deal with one commonly used curve and it's modification to incorporate Reynolds number effects. The chosen curve is referred to as CL-table-2 and is defined by defined by [0.9, 0.43, 0.8, 0.4 at fdim=1]. Table 5.1 below lists how these values have to be modified at a few different Reynolds numbers. Figure 5-5 shows what the modified lift coefficient curves have to look like in order to model the uniform flow tests on the $30mm$ diameter cylinder from the $38m$ SHELL dataset. The original C_L curve is shown with black data points, and all lift coefficient curves have been drawn at the same value of reduced velocity (or fdim=1).

Table 5.1: Parameters for defining the Reynolds number adjusted C_L curves in SHEAR7

Re number	$f(Re)$	aCL0	aCLmax	CLmax	CLa0
5,000	0.944	0.850	0.406	0.755	0.380
7,150	1.000	0.9	0.43	0.8	0.4
10,000	1.053	0.948	0.453	0.842	0.421
20,000	1.161	1.045	0.499	0.929	0.464
...	...	...	...	...	...
70,000	1.357	1.221	0.584	1.086	0.543

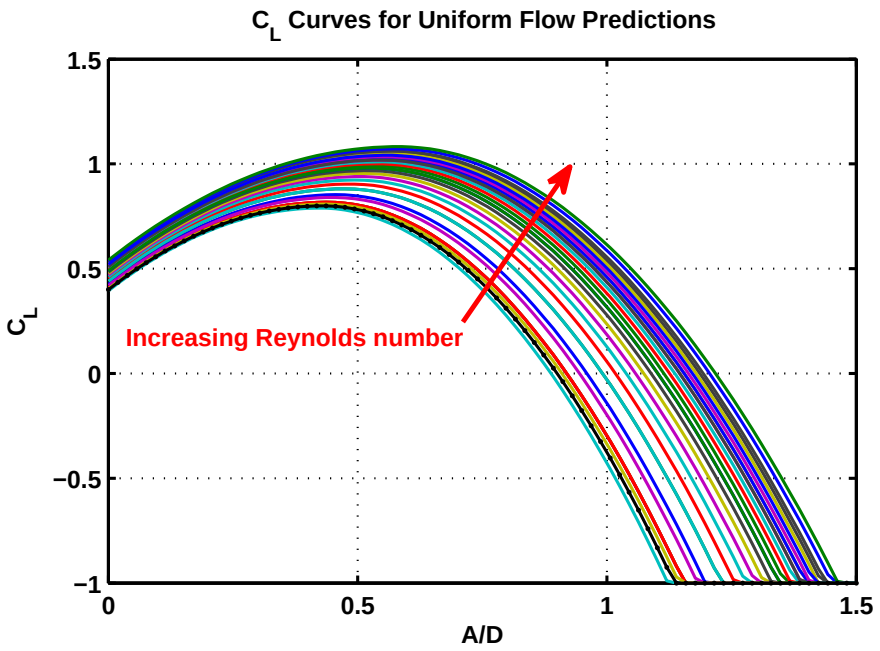

Figure 5-5: $C_L(Re)$ vs. A/D at fdim=1, the black data points correspond to the original CL-table-2 at fdim=1

For uniform flows the choice of Reynolds number is trivial since the entire riser is exposed to the same current and hence the Reynolds number does not vary along the length of the riser. The same cannot be said, however, for linearly sheared current profiles; here the Reynolds number varies from the maximum value on one end to zero on the other end. Using the Reynolds number corresponding to the location of the Power-In region would be a sensible choice. Experimental measurements and CFD calculations usually place the center of the Power-In region at a distance of approximately 0.25 to 0.30 x/L from the high-speed end of the riser. For the sheared flow cases shown in this chapter the corresponding Reynolds number was approximated by $Re = 0.75\,Re(x/L = 0)$ (i.e, 75% of the Reynolds number on the high speed end of the model).

The following sections will compare measurements and predictions using the standard lift coefficient tables as well as the Reynolds number adjusted C_L curves. The dimensionless response frequency, which is referred to as 'Strouhal number' in SHEAR7, is originally kept fixed at the recommended value of 0.18 and is later allowed to vary as a function of Reynolds number according to the Equation 4.2.

5.3 SHEAR7 Predictions and Comparisons With Measurements From the $38m$ SHELL Experiments

5.3.1 Response Amplitude

The SHEAR7 predictions presented in the following section are based on the original CL-table-2 and modified versions of these tables that account for the Reynolds number as described in the previous section. CL-table-2, is based on the experimental data collected by Gopalkrisnan (1993) and allows the lift coefficient to be a function of reduced velocity as well as the A/D response. This results in predictions that are much closer to the measurements (i.e., the spatial mean agrees well with the measurements) but roughly the same number of points will be over and under-predicted.

Allowing SHEAR7 to use these Reynolds number adjusted CL curves has a profound effect on the predicted A/D response as demonstrated in Figure 5-6. The upper plot shows the maximum amplitude anywhere along the cylinder and the lower plot shows the spanwise averaged mean amplitude as function of the Reynolds number.

The measured data is shown with red stars and it is quite clear that the A/D value depends on Reynolds number (at $Re \sim 9,000$ the A/D is approximately 0.6 and at $Re \sim 70,000$ the A/D has reached 0.9). The green rectangular data points show the SHEAR7 predictions if the traditional C_L curve is used. The blue data points correspond to the SHEAR7 predictions using C_L curves that depend on Reynolds number (as shown in Figure 5-5). These Reynolds number adjusted predictions are much closer to the measured values and show the same trend for A/D as a function of Re number as the measurements. The standard CL-table-2 prediction shows some variation due to V_r (dimensionless frequency effects) but otherwise the A/D values predicted across the Reynolds number range are fairly constant around 0.6.

Figure 5-7 is similar to Figure 5-6 but compares the measured values of the sheared flow tests with the traditional SHEAR7 and the Reynolds number adjusted SHEAR7 predictions. The Reynolds number adjusted SHEAR7 predictions are slightly closer to the measured values, especially at Reynolds number values above 20,000.

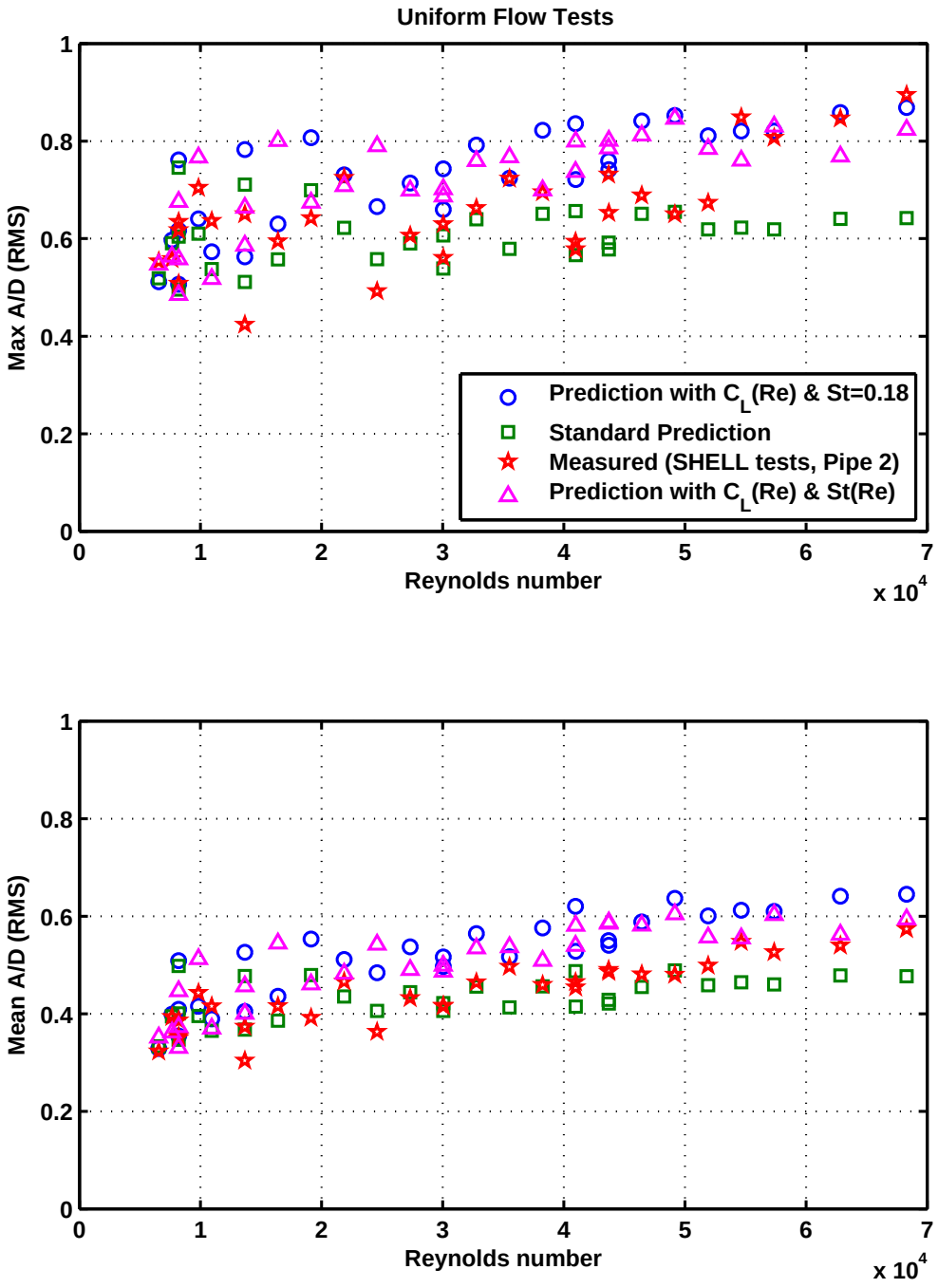

Figure 5-6: Predicted and measured A/D vs. Re for the $30mm$ diameter cylinder exposed to uniform currents

Both Figures 5-6 & 5-7 also show predictions that allowed **both** the lift coefficient **and** the Strouhal number to vary as a function of the Reynolds number. The figures show that modeling the Reynolds number dependence of the Strouhal number does not produce significant differences in uniform flows but does in fact improve the predictions in sheared flows.

The primary difference between modeling sheared and uniform flows is the importance that hydrodynamic damping will have in the first case. Unlike a cylinder exposed to a uniform flow where practically the entire pipe length is available for power-input, a cylinder vibrating in response to a sheared current will have a relatively short power-in region (approx. 30% of the total length). This means that the remaining $\sim 70\%$ will have to contribute to the hydrodynamic damping.

Looking back at Figures 5-6 & 5-7 with the predictions using CL-table-2 it is clear that the sheared flow predictions are under-predicting the measured response. This could be for two reasons, either the lift coefficient data being used is not large enough, or the hydrodynamic damping model implemented is assuming that there will be a lot more damping than what actually exists.

Because the uniform flow predictions were very close to the measured values, one could conclude that the lift coefficient data being used is appropriate. This only leaves the hydrodynamic damping as the most likely culprit for some of the under-predictions in sheared flows. The difference between the measured and predicted response suggests that the damping coefficients and model currently implemented in SHEAR7 are overestimating the amount of hydrodynamic damping present at these Reynolds numbers.

5.3.2 Stresses

Figures 5-8 & 5-9 are typical scatter plots of *predicted stress* vs. *measured stress*. Each data point corresponds to a certain location along the riser (30 sensors in the CF direction) for a specific test. In such scatter plots, any points lying above the solid black equality line have been over-predicted (i.e., conservative prediction) whereas any points located below the line have been under-predicted. The low speed, low mode

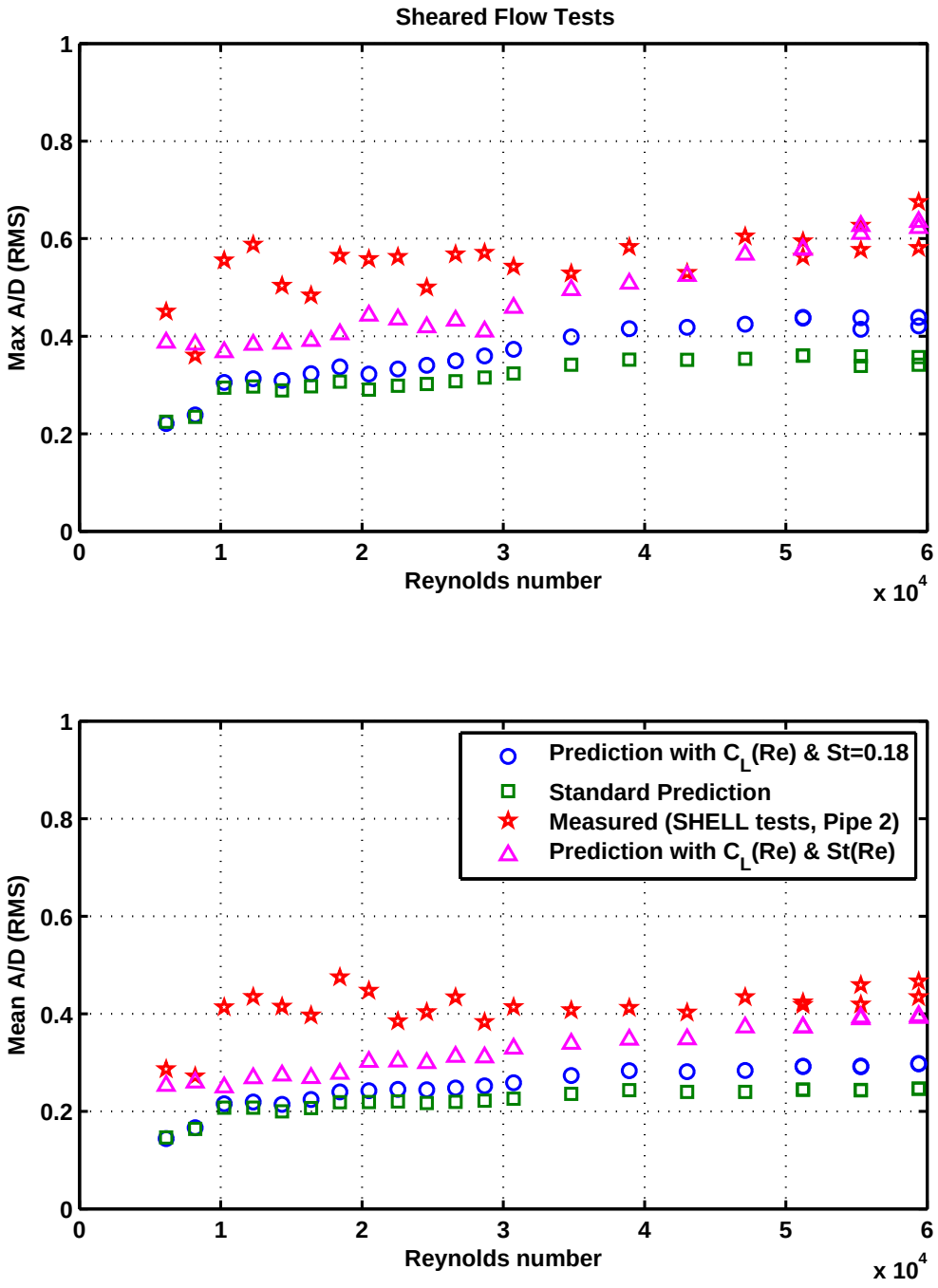

Figure 5-7: Predicted and measured A/D vs. Re for the $30mm$ cylinder exposed to sheared currents

number and **low Reynolds** number cases are typically located on the **lower left** whereas the high speed, high mode number and **high Reynolds** number cases are located on the **upper right** portion of the equality line.

Figure 5-8 compares the SHEAR7 predicted stresses with the 1X measured values for the $30mm$ diameter cylinder (Pipe 2) in sheared and uniform flows. The red data points are from predictions where the Lift coefficient was a function of Reynolds number whereas the green data points are from predictions using the standard CL-table-2. As expected, the cluster of points lies approximately on top of the equality line, with roughly the same number of points being over and under-predicted.

In both cases, the predictions have used a fixed $St = 0.18$ and this figure only illustrates the effect of using a Reynolds number dependent lift coefficient, C_L, in VIV predictions. Allowing the lift coefficient to be a function of the Reynolds number results in slightly more conservative predictions at high Reynolds numbers; there is a noticeable difference between the red and green data points on the right hand side portion of the plot. On the contrary, the red and green data points on the lower left portion of the plot are virtually identical since these correspond to low Reynolds number cases where $f(Re)$ is approximately 1.

In Figure 5-9 the red data points are based on predictions that allow the lift coefficient to be a function of the Reynolds number but the Strouhal number is kept fixed at 0.18 (this is the same data shown in red color in Figure 5-8). These predictions are now compared to the blue data points which are predictions using both a Reynolds number dependent lift coefficient and a Strouhal number. The most obvious difference is that the blue predictions are closer to the equality line than the red colored predictions. This effect is much more pronounced on right hand side of the plot which corresponds to the high Reynolds number cases.

The difference in the predicted stresses after allowing the Strouhal number to be a function of Reynolds is best explained by comparing the fixed Strouhal value of 0.18 with the relationship identified in Chapter 4. This is shown in Figure 5-10, where the difference between the blue line representing the curve fit for the dimensionless response freq. (Equation 4.2) and the dashed red line, which is constant at $St = 0.18$,

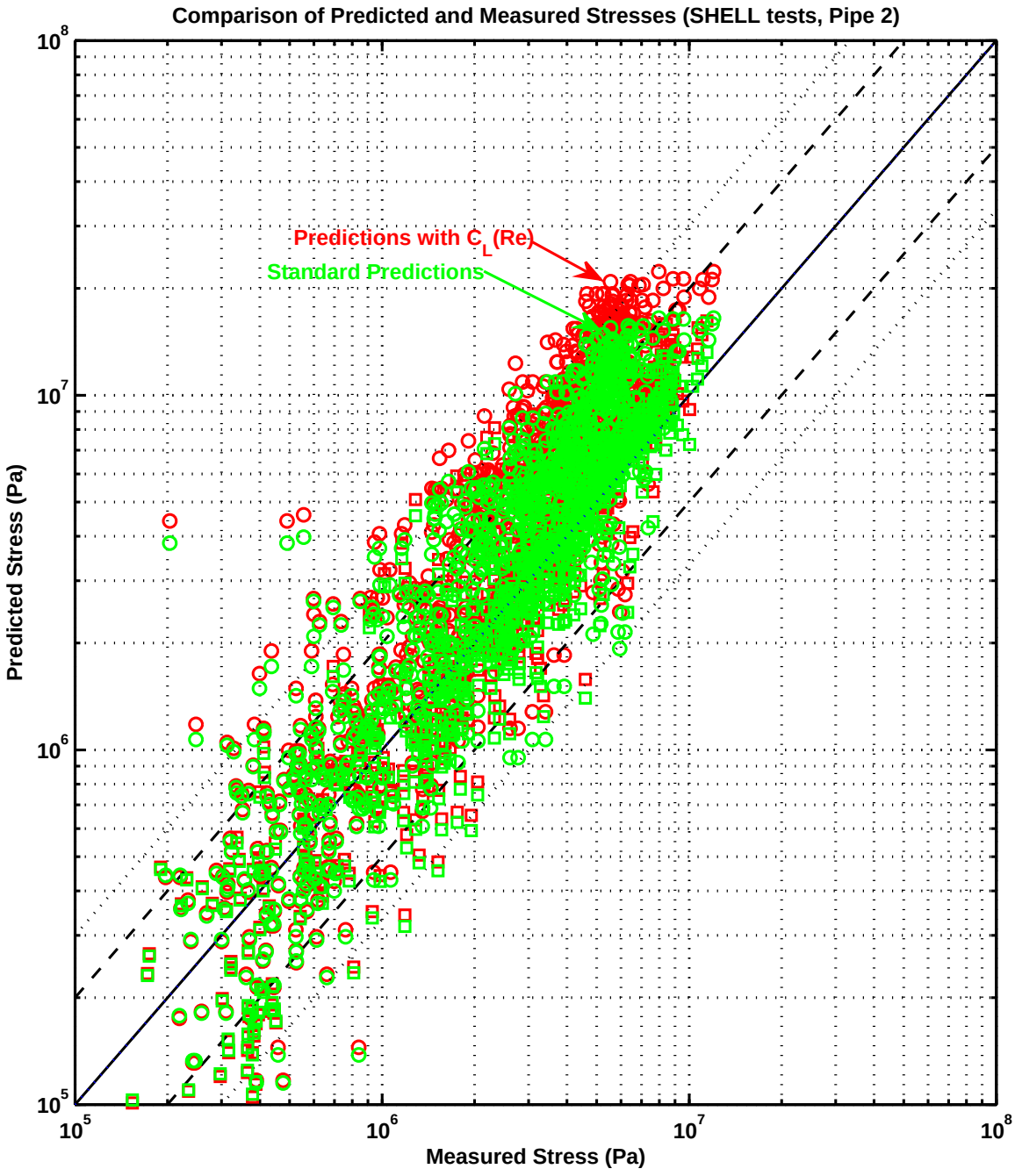

Figure 5-8: Predicted vs. Measured Stress

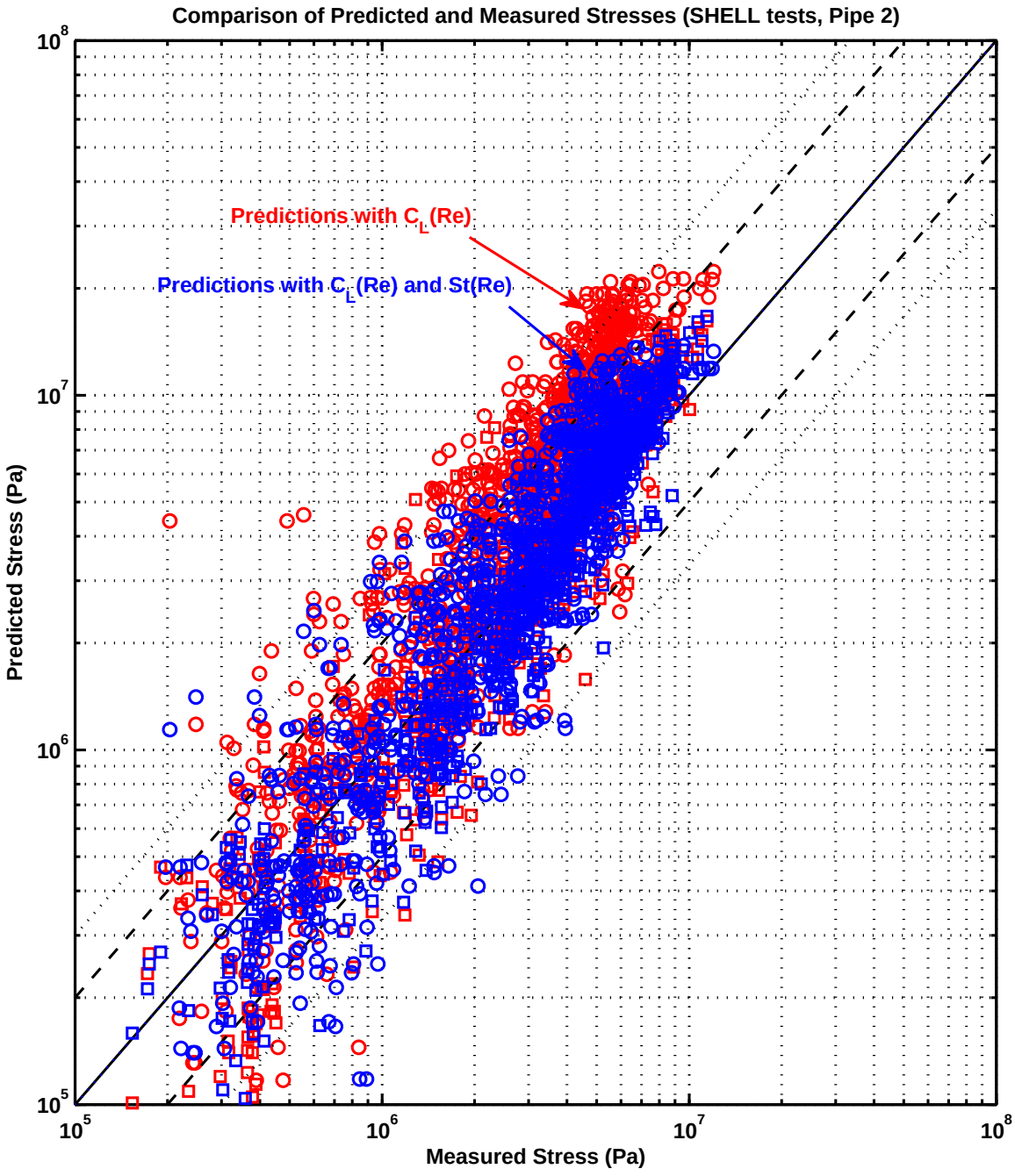

Figure 5-9: Predicted vs. Measured Stress

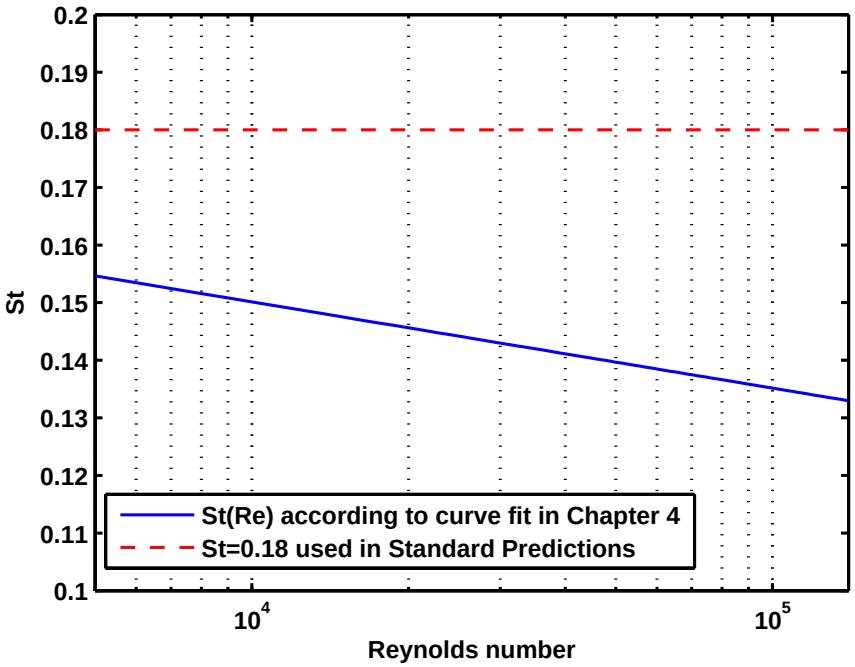

Figure 5-10: Strouhal number vs. Reynolds number based on the fit presented in Chapter 4. Dashed red line $St = 0.18$ is the SHEAR7 recommended value.

increases with Reynolds number. This means that predictions using $St(Re)$ will have a considerably smaller response frequency at larger Reynolds numbers.

The smaller predicted response frequency will excite a mode with a smaller wavenumber and therefore it is very reasonable that the predicted stresses were smaller at high Reynolds numbers since the predicted stresses are a function of both amplitude and wavenumber:

$$\sigma = E\varepsilon = EA\frac{OD}{2}k^2$$

The Damage Rates calculated in SHEAR7 will be influenced twofold since they are a function of both the response frequency and the predicted stresses.

5.4 Chapter Summary

A procedure was demonstrated through which VIV prediction software can be easily adjusted to account for Reynolds number effects on the lift coefficient and dimensionless response frequency (equivalent Strouhal number for vibrating cylinders). This results in SHEAR7 predictions of response amplitudes that are much closer to measured values in the SHELL tests and show similar trends as the Reynolds number increases. More specifically:

1. Allowing the lift coefficient to be a function of the Reynolds number:
    - Has a pronounced effect on the predicted response amplitudes.
    - Increases the predicted stresses at higher Reynolds numbers.
2. Allowing the dimensionless response frequency number to be a function of Reynolds number:
    - Has very small effects on the predicted response amplitudes in uniform flows but can improve sheared flow predictions.
    - Tends to decrease the magnitude of predicted stresses at higher Reynolds number.

Even though incorporating a Reynolds number dependent lift coefficient doesn't have a dramatic effect on the predicted stresses (and hence damage rates) it is worthwhile because accurately calculating the A/D response allows more accurate damping calculations since the still water damping term depends on A/D.

Drag coefficients are also amplitude dependent as shown by Vandiver (1983). Therefore a more accurate prediction of the response amplitude will also improve the accuracy of the drag calculations in these Reynolds number ranges.

It is important to note that the Reynolds number factor identified by Govardhan and Williamson was determined from laboratory data in the range $1,250 < Re < 12,000$. In this chapter it was shown that the same relationship produces very good results at least up to $Re \sim 70,000$ when modelling the SHELL tests but under no

circumstances should one expect that the same Reynolds number factor will be valid at even higher Reynolds numbers or in the drag crisis regime.

THIS PAGE INTENTIONALLY LEFT BLANK

Chapter 6

Fatigue Damage due to Combined Cross-Flow and In-Line Motion

The objective of this chapter is to evaluate and compare the contribution to the damage rate that results from the cross-flow and in-line vibration on the flexible cylinders used in the 38m long SHELL tests.

In this section, a framework is presented for determining the worst possible combination of Cross-Flow (CF) and In-Line (IL) damage. Specifically, I wish to determine the position on the circumference of the cylinder's cross-section that will experience the most severe loading due to the simultaneous motion in both CF and IL directions. The analysis shows that the damage due to the IL motion is comparable to that of the CF motion, and that their combined effect results in a damage rate of the same order of magnitude as the pure CF signal and is usually situated at a position on the circumference of the cross-section that is very close to or coincides with the CF direction.

6.1 Need for Rainflow-Counting

It is conceivable that due to the complicated motion of the cylinder while undergoing VIV, the most damaging location on the circumference of the cross-section would not coincide with the CF or IL directions but rather at some angle between the two.

In this chapter the stresses and damage rates are calculated at 24 positions (i=1,2...,24) around the circumference of the cross-section as shown in Figure 6-1. This is done at every sensor location along the pipe length.

At each circumferential position, the stress time-history, $\vec{\sigma_{\theta i}}$, is given by the appropriate vector addition of the CF and IL stress signals, and respectively, shown in Equation 6.1:

$$\vec{\sigma_{\theta i}}(t) = \vec{\sigma_{CF}}(t)\cos\theta_i + \vec{\sigma_{IL}}(t)\sin\theta_i \tag{6.1}$$

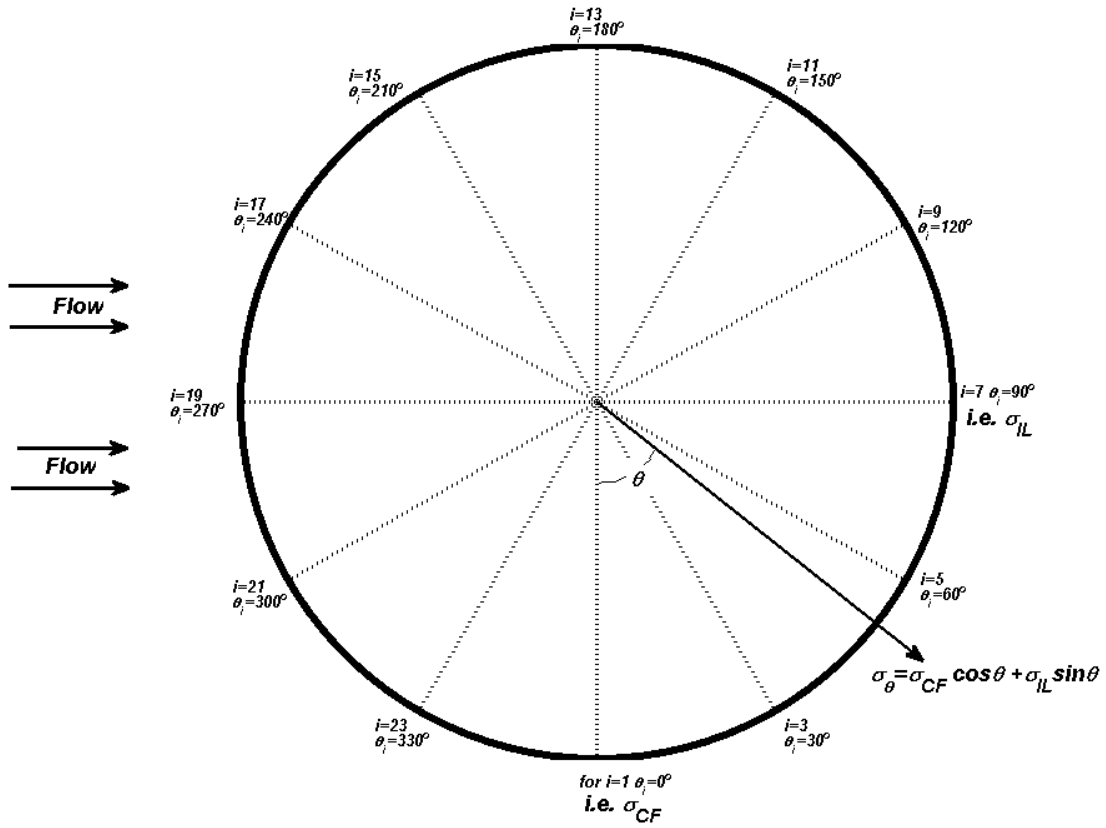

Figure 6-1: Cylinder cross-section showing the combination of $\vec{\sigma_{CF}}$ and $\vec{\sigma_{IL}}$ at some arbitrary angle θ_i

Figure 6-2 shows the results of this vector addition and the resulting stress time-histories at the angles corresponding to $\theta = 0$(i.e. CF), $\theta = 30$, $\theta = 60$ & $\theta = 90(i.e. IL)$. This is done at every angle, θ_i, and each stress time-history is subsequently rain-flow counted and the most damaging position/angle is chosen as the combined stress or combined damage for each one of the 30 locations along the length of the pipe where the CF and IL strain gauges are located.

The idea is based on the analysis presented by Tognarelli et al. (2004), the main difference being that in this work every stress time-history is rain-flow counted whereas Tognarelli et al. first calculated a damage index based on the RMS stresses for both the CF and IL directions and their respective response frequencies and only then applied the coordinate transformation similar to Equation 6.1 to their RMS quantities.

Estimating the fatigue life (or Damage Rate) for a perfectly sinusoidal stress time history is straightforward since the analytic equations are straightforward to derive. Similarly, if the stress time-history is narrow banded Gaussian once again the analytic expressions for Damage Rate can be derived as shown in Crandall & Mark (1963). If the signal contains multiple frequencies and the response amplitude varies significantly, one has no other choice except to revert to cycle-counting to obtain the relevant stress amplitude statistics.

Each plot in Figure 6-2 also lists the rainflow-counted damage rate and it shown that at this axial position along the cylinder ($x/L \sim 0.06$), the most damaging location around the cross-section was at $\sim 30^o$. The WAFO toolbox (WAFO-Group, 2006) was used to carry out the rain-flow counting of each stress time-history.

Since fatigue properties were not available for the exact composite material that the flexible cylinder was made of, all fatigue calculations assumed that it was made of steel with an S-N curve defined according to the DNV-F curve (i.e., $\log(a) = 11.378$ and $m = 3.0$, Det Norske Veritas (2010)).

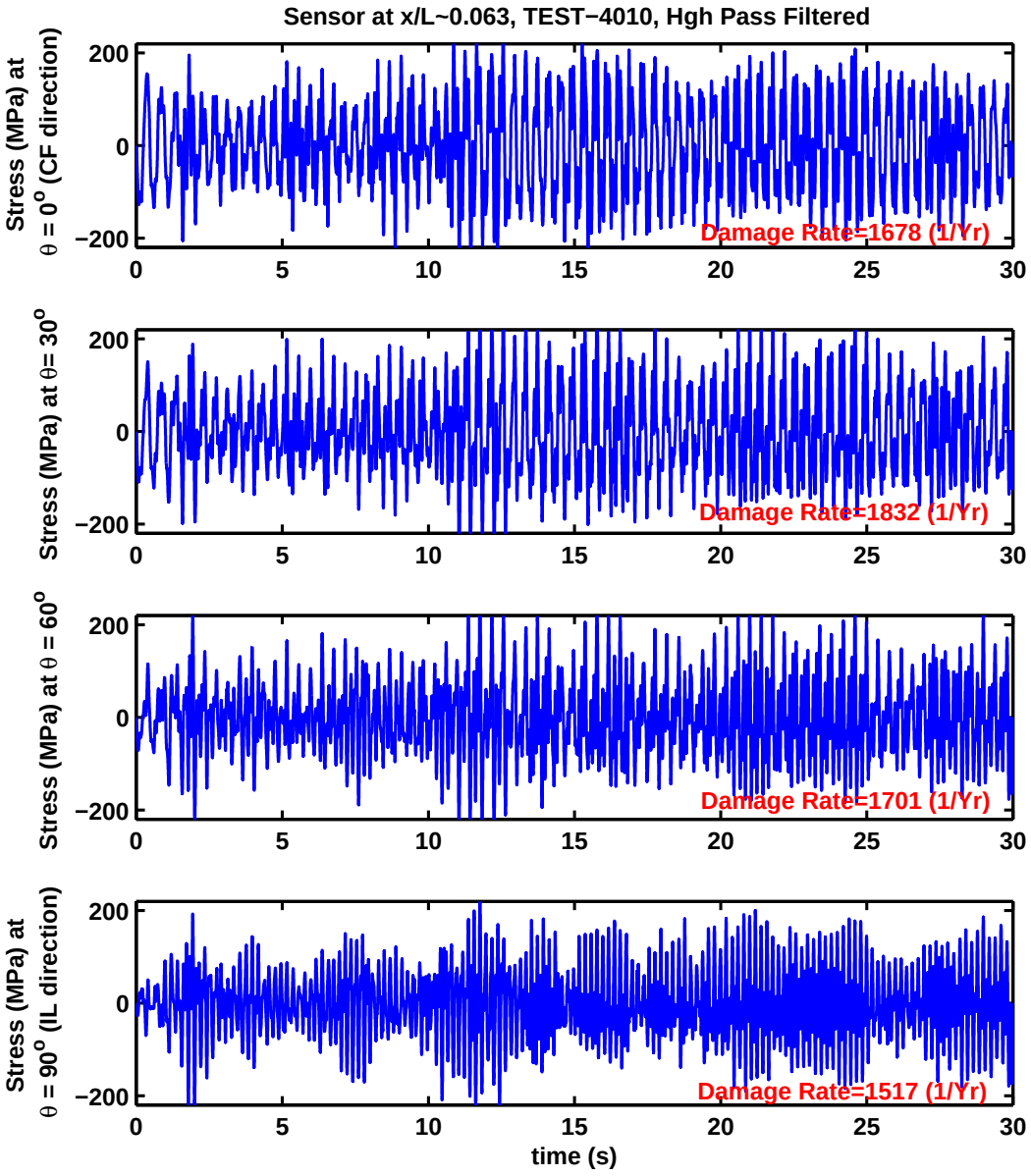

Figure 6-2: The stress time-histories at four different locations: $\theta = 0$(i.e. CF), $\theta = 30$, $\theta = 60$ & $\theta = 90(i.e. IL)$ around the circumference of the cross-section at a position $x/L \sim 0.06$ along the cylinder length (The Damage Rates listed in this figure were calculated using the DNV-F2 curve instead of the DNV-F curve used in the remainder of the chapter)

Figure 6-3 shows the response of the fully bare pipe under a uniform flow of $1.4m/s$. The top plot shows the CF and IL displacements as calculated by the modal reconstructions. Observe that even though the IL response amplitude is much smaller, there are certain locations where the IL stresses are of comparable magnitude with the CF stresses! This happens because even though the IL response amplitude is significantly smaller than the CF amplitude, the IL wavenumber is much greater than the CF wavenumber due to the approximately two times higher response frequency. The relationship between stresses and amplitude for a flexural wave on a beam is shown in Equation 6.2. Here, σ is the bending stress, E is the Young's Modulus, ε is the bending related strain, A is the response amplitude at a specific time, $OD/2$ is the distance from the neutral axis at which the stresses/strains were measured ($13.5mm$) and k is the wavenumber.

$$\sigma = E\varepsilon = EA\frac{OD}{2}k^2 \tag{6.2}$$

Figure 6-3 also shows the damage rate along the length of the pipe. Each location has two data-points corresponding to the damage rates as calculated from the CF and IL stress time-histories and a third data-point corresponding to the damage rate from the most damaging combination of the CF and IL stress time histories according to Equation 6.1. The last plot shows the angle around the circumference of the cross-section at which the most damaging combination of CF and IL occurred. With a few exceptions the combined damage rate at most sensor locations coincides with the CF direction.

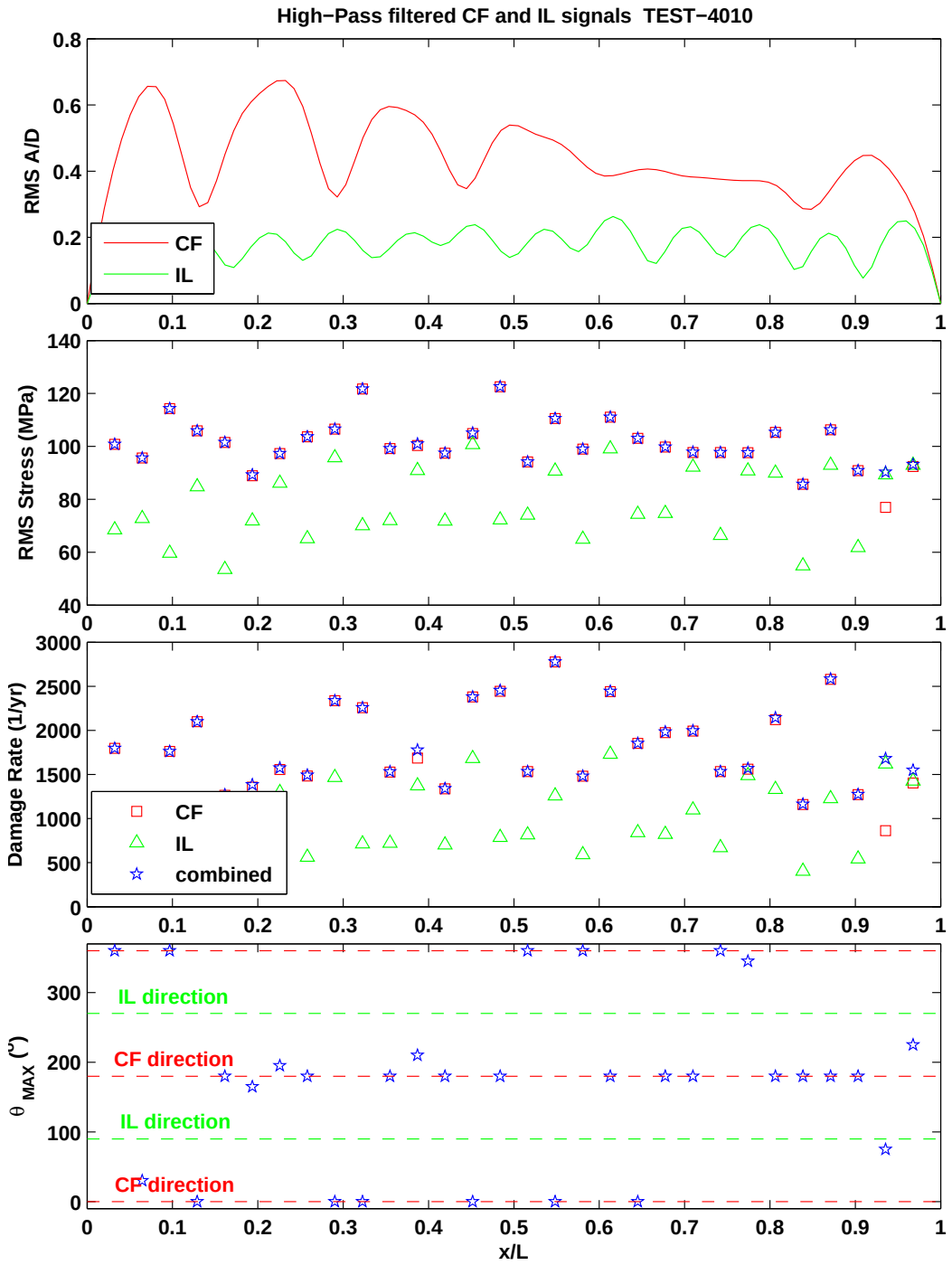

Figure 6-3: VIV Response under uniform flow conditions of $1.4m/s$ (Test 4010) **Top:** CF and IL RMS response amplitude 2^{nd} **from top:** CF and IL RMS stresses (MPa) and the largest combination of the signals in both directions 3^{rd} **from top:** CF and IL damage rates ($1/yr$) and the most damaging combination of the signals in both directions **Bottom:** Angle around the circumference of the cross-section where the most damaging combination of CF and IL damage occurs

6.2 Results and Discussion

Figure 6-4a shows the maximum damage rate along the pipe span as a function of towing speed for the uniform flow tests for the $80mm$ diameter cylinder (Pipe 3). For each flow speed there are three damage rate values: those corresponding to the CF and IL directions as well as the most damaging combination of the two. Similarly, Figure 6-4b shows the maximum damage rates for the sheared flow tests with Pipe 3. For both uniform and sheared flow tests it is shown that the IL damage rate is of the same order of magnitude as the CF. The worst possible combination of the two coincides or is virtually identical to the CF damage calculation suggesting that the most damaging position on the circumference tends to be at or very close to the CF direction (this was also demonstrated for a specific test in the last plot of Figure 6-3).

The stress signals used for plotting Figures 6-4a & 6-4b contained large amounts of higher harmonics (3X and 5X for the CF and 4X for the IL directions) as is typically observed in high mode number model testing. Figures 6-5a & 6-5b show what would happen if the CF and IL signals had been band-pass filtered around the 1X and 2X frequencies respectively. Now, there are a few cases where the worst possible damage calculation around the cross-section coincides with the IL signal/direction. This happens because the CF signal no longer includes the 3X and 5X components which greatly affect the damage rate of the CF signal.

The aim of this section was not to dismiss the importance of IL motion, to the contrary, the intention was to carefully measure the fatigue caused by the IL motion and demonstrate experimentally that the worst possible damage accumulated anywhere around the cross-section is generally in the cross-flow direction. If one conservatively designs for Cross-Flow VIV, then one should be confident that they have also accounted for the worst possible combination of CF and IL VIV. This is especially interesting in light of the recent DEEPSTAR Factor of Safety papers (Fontaine et al. 2011, 2013), where experimentally measured CF damage rates were compared with results from VIV response prediction software that, to date, only account for CF VIV.

To further support the observation that the CF and IL damage rates are of similar magnitudes and that the CF direction tends to be the position around the cross-section that experiences the most severe loading, the same analysis was repeated for the $30mm$ diameter cylinder (Pipe 2). Figures 6-6 & 6-7 show the CF, IL and combined damage rates for the $30mm$ diameter cylinder. The trends and observations are virtually identical to those reported earlier and are not discussed further.

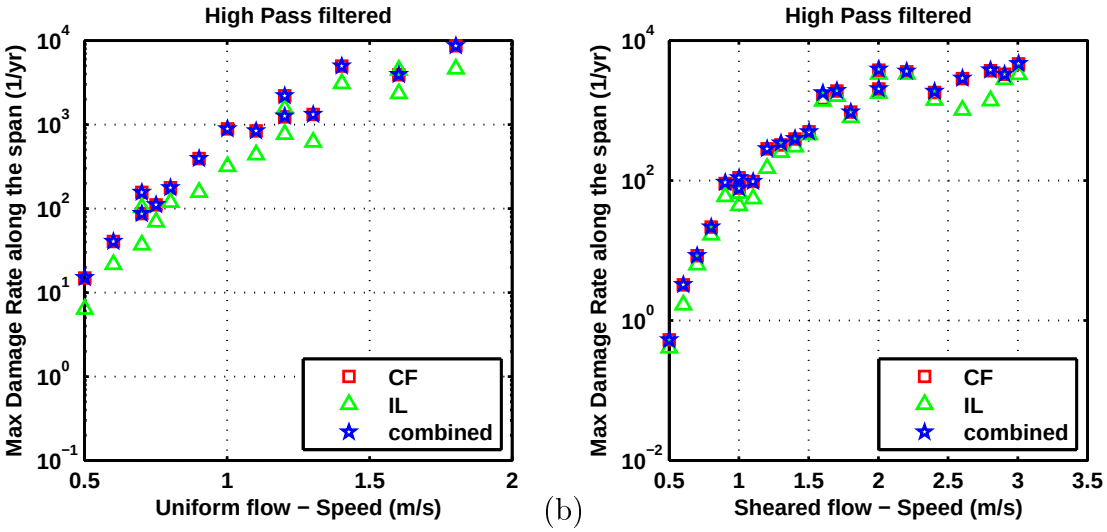

Figure 6-4: Maximum Damage Rate $(1/yr)$ vs. towing speed (m/s) in uniform flows (a) and sheared flows (b) for PIPE 3. Data shown **includes** all higher harmonics

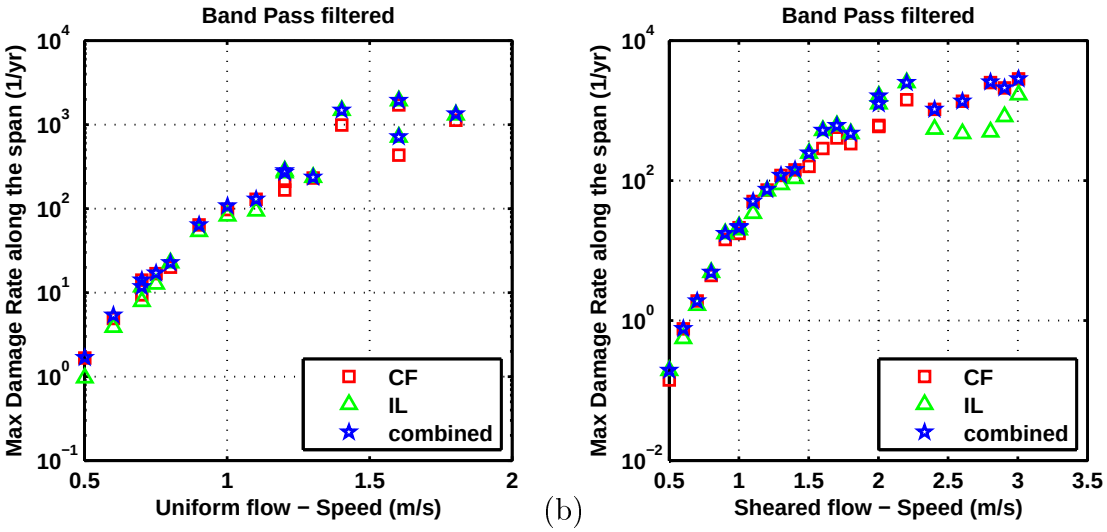

Figure 6-5: Maximum Damage Rate $(1/yr)$ vs. towing speed (m/s) in uniform flows (a) and sheared flows (b) for PIPE 3. Data shown **excludes** all higher harmonics

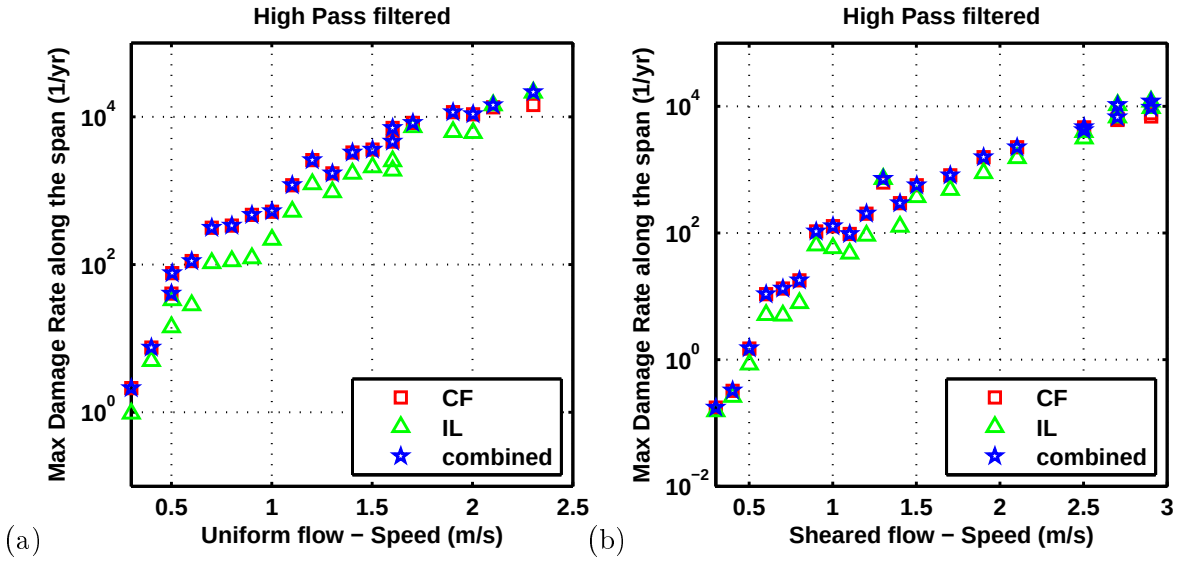

Figure 6-6: Maximum Damage Rate $(1/yr)$ vs. towing speed (m/s) in uniform flows (a) and sheared flows (b) for PIPE 2. Data shown **includes** all higher harmonics

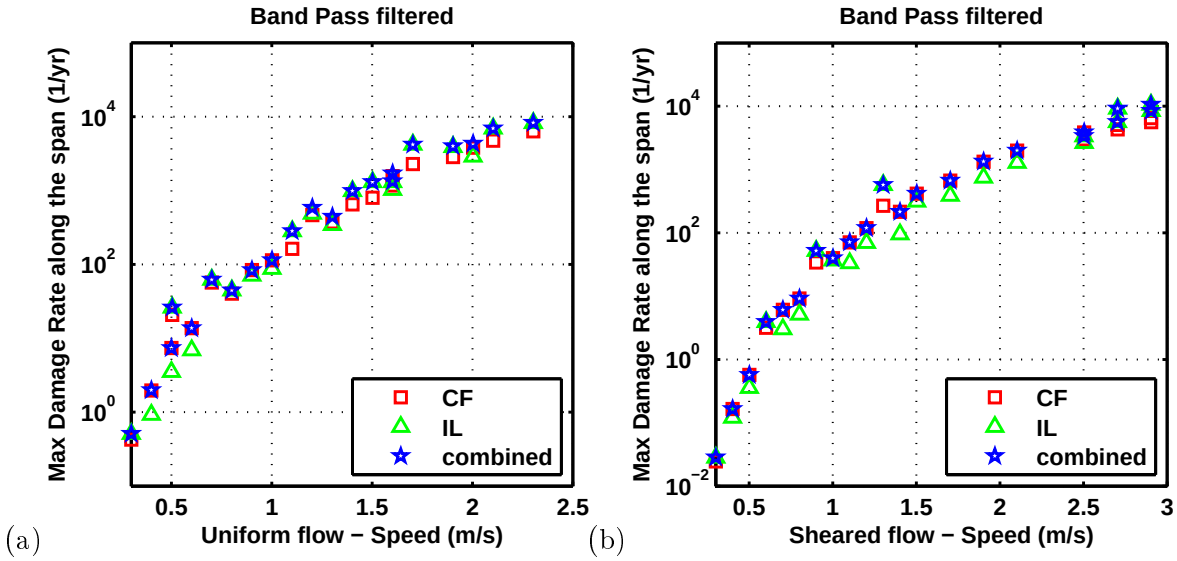

Figure 6-7: Maximum Damage Rate $(1/yr)$ vs. towing speed (m/s) in uniform flows (a) and sheared flows (b) for PIPE 2. Data shown **excludes** all higher harmonics

Chapter 7

VIV in Time-Varying Flows

There is an industry wide need to be able to predict VIV in unsteady flows. These unsteady flows can take many forms depending on the mechanism that causes them:

- One example is the oscillatory flow that exists near the free surface in the presence of ocean waves.
- Oscillatory flow could also result from the heave or surge motion of an offshore platform which will in turn cause any Steel Catenary Riser (SCR) or umbilical connected to it to also move with the platform.
- The ebb and flow of tides will also result in unsteady flows that tend to behave like slowly accelerating or decelerating flows.

Additionally, model testing long flexible cylinders for VIV in large ocean basins can often be extremely expensive by the time a satisfactory test matrix is covered. There is a real need to develop more cost effective ways to conduct VIV model tests. In this thesis, a slowly time-varying flow is shown to be a more efficient substitute to a test matrix of many discrete constant velocity tests.

This was the primary motivation for experimenting with ramp tests. A 'ramp test' is very similar to the conventional way of testing cylinders for VIV but instead of keeping the carriage speed (or the flume) constant it is accelerated or decelerated during the course of a single test. There are two questions that have to be answered first:

- Can a cylinder experience VIV 'lock-in' during transients or unsteady flow conditions?

- If lock-in is observed, is the cylinder's response similar to the response observed under lock-in in steady flow conditions?

One of the principal contributions of this thesis is the identification and experimental verification of a dimensionless parameter that may be used to predict when a cylinder in an unsteady flow will exhibit similar response characteristics to VIV in steady flows.

7.1 Prior Work on VIV in Unsteady Flows

Even though ocean currents are usually unsteady and can vary slowly or quickly in time depending on geographic location and environmental conditions, surprisingly little research has been carried out regarding the possibility of VIV in time-varying flows.

Most efforts have concentrated on the VIV response of rigid cylinders in oscillatory flows. The primary motivation was to study the response of cylinders and piles in oscillating flows created by free surface waves. The most notable of all researchers is Sarpkaya (1978, 1979 & 1986) with his extensive research program –spanning many years– studying both forces on fixed cylinders exposed to oscillatory flows as well as the dynamic response of elastically mounted cylinders exposed to oscillatory flows.

Summer & Fredsoe (1988) also studied oscillatory flow VIV on rigid cylinders. More recently, Liao (2002) and Fu et al. (2013, 2014) studied oscillatory flow VIV on flexible cylinders primarily motivated by the motion of Steel Catenary Risers (SCR) and the fatigue at the touch-down point. Contrary to Sarpkaya, who used a U-shaped water tunnel and oscillated the flow around the cylinder, the other authors created an oscillatory flow by mounting the cylinder on specially designed forced motion apparatuses that were capable of 'towing' the cylinders with a prescribed oscillatory motion through still water.

All the aforementioned oscillatory flow experiments have in common that there is

no mean flow. This in turn means that the cylinder will be forced to cross its own wake. That is, immediately following the first half-oscillation of the test, as soon as the cylinder starts its return-leg, it will be forced to travel through the very wake it created during the outbound-leg, and the process will continue indefinitely. At very large Keulegan-Carpenter numbers (KC), where the flow oscillation period is large, this will probably not be a major issue since there will be sufficient time for the vorticity to diffuse. At low KC numbers, the vorticity will not have enough time to diffuse, and inevitably the situation starts looking more like Wake-Induced Vibration instead of the expected VIV.

Fei (1995) conducted wind tunnel experiments on a flexible cylinder vibrating in its first mode. The main objective was to study whether turbulence could disrupt VIV and what happened to the response during strong wind gusts. Fei found that free-stream turbulence up to 10% did not significantly affect the amplitude of vibration of the cylinder. His tests showed that sudden gusts can disrupt VIV and he chose the cylinder 'rise time' and the gust's 'duration of visit' as the critical timescales that characterize the problem.

Unlike Fei, who primarily focused on the effects of wind gusts and turbulence, Frederic & Laneville (2002) studied the response of a flexible cylinder vibrating in its first mode in slowly varying oscillatory flow created in a wind tunnel. Their goal was to study the "response of the cylinder as the periodic variation of the flow imposes a periodic entry and exit of the synchronization range (at the onset and at the exit of synchronization)". They found that given sufficient time the cylinder could reach amplitudes similar to those observed in steady flow tests, however their cylinder's response was heavily modulated.

Both of these studies looked at the vibration of flexible cylinders in air instead of water and as such their mass ratios were much larger than the range of mass ratios ($m^* = [1 - 2]$) of the cylinders analyzed in this thesis and are of primary interest to the Oil and Gas industries. The much larger mass ratio meant that the 'rise time' was on the order of many tens of cycles, this was visible after examining the time-histories in the published material.

In stark contrast to tests performed in air, tests with low mass ratio cylinders –usually performed in water– have a rise time that is much smaller, typically between 4-10 cycles. Appendix C shows that in the SJTU tests the rise time, defined as the time required to reach the maximum response, was only 4 or 5 cycles.

7.2 The Unsteady Flow Parameter, γ

This work introduces a dimensionless parameter, γ, that governs the extent to which VIV and lock-in is possible under unsteady flow conditions. The VIV problem is governed by the incident current (flow velocity). It is the free stream that determines the response, as such, the parameter chosen should be one that describes the change in current velocity in a given amount of time. In this thesis, the parameter is formed by the product of the natural period of vibration for the n^{th} mode, T_n , and the ratio of the instantaneous flow acceleration, $\frac{\partial U}{\partial t}$, to the current velocity necessary to excite the same mode, U_n , as shown in equation 7.1.

$$\gamma = \frac{\frac{\partial U}{\partial t}}{U_n} T_n \tag{7.1}$$

The physical meaning of this parameter, can be thought of as being **the fractional change in flow velocity (or current speed) observed during one cycle of vibration**. One would expect that as γ decreases, the VIV response will approach steady state conditions. As γ increases, steady state behavior becomes increasingly less likely. An alternative is to think of this as a ratio of two time scales, the first is the timescale that describes the changes in current speed compared with a timescale that is critical to the structural response, the natural period of vibration. Another timescale that is important to the structural response, and could have been used, is the 'rise time' to maximum amplitude. In mechanical vibrations the 'rise time' is typically defined as the time required to reach some fraction (e.g., 95%) of the steady state vibration amplitude. This is typically several periods long and Appendix C shows that it will depend on the cylinder mass ratio and damping present. It was not used in this thesis because even though the experimental evidence available included

four different cylinders or riser models, the mass ratio and damping ratio of all four was very similar and as such it would not be possible to discern the influence of these two parameters.

7.3 Dimensional Analysis

Sarpkaya (2004) presents a set of dimensionless parameters that govern the transverse oscillations of a cylinder in time varying flow. He begins the analysis by listing the following physical properties of the system: the fluid density, ρ_f, dynamic viscosity, μ, the ambient flow velocity, U, the cylinder's diameter, D, the cylinder's length, L, spring stiffness, k, the surface roughness, k_s , the structural damping ratio, ζ, the cylinder's mass, m, the mean shear, $\frac{\partial U}{\partial y}$, the cylinder's taper, $\frac{\partial D}{\partial y}$, the characteristic turbulence intensity, ϵ_t, the integral length scales of the ambient flow, I_{ils}, and the Schewe parameters, S_p, which typically include all the physical properties of the system that are not easily controllable or quantifiable. These could include end effects, three-dimensional effects on a primarily two-dimensional body, blockage ratio, secondary vibrations of the structure and its supports etc. He proceeds to form the following groups in which he defines the dimensionless response amplitude A/D, as the dependent dimensionless group.

$$A/D = f(\zeta, \frac{\rho_f U D}{\mu_f}, \frac{L}{D}, \frac{4m}{\rho_f \pi L D^2}, \frac{D}{U}\sqrt{\frac{k}{m}}, \frac{D}{U_o^2}\frac{\partial U}{\partial t}, \frac{D}{U}\frac{\partial U}{\partial y}, \frac{\partial D}{\partial y}, \epsilon_t, \frac{k_s}{D}, \frac{I_{ils}}{D}, S_p)$$

Where:

$\frac{\rho_f U D}{\mu_f}$ is the Reynolds number

$\frac{L}{D}$ is the cylinder's aspect ratio

$\frac{4m}{\rho_f \pi L D^2}$ is the mass ratio

$\frac{D}{U}\sqrt{\frac{k}{m}}$ is the reciprocal of the reduced velocity (based on the nat. freq in air)

$\frac{D}{U_o^2}\frac{\partial U}{\partial t}$ is the ratio of the local acceleration to the convective acceleration

$\frac{D}{U}\frac{\partial U}{\partial y}$ is the shear parameter

$\frac{\partial D}{\partial y}$ characterizes the cylinder's taper

S_p are the Schewe parameters

The dimensional analysis produces a group of independent dimensionless parameters which are fixed in number, but are not unique. One may find many more equally valid sets by making simple combinations of members of the first set one finds. Whereas Sarpkaya settled upon $\frac{D}{U_o^2}\frac{\partial U}{\partial t}$ as a group which characterizes the change in flow velocity, the equally valid parameter γ may be found by multiplying Sarpkaya's unsteady flow parameter by the reduced velocity based on the natural frequency as shown here:

$$\gamma = (\frac{D}{U_o^2}\frac{\partial U}{\partial t})(\frac{U}{D}\sqrt{\frac{m}{k}})2\pi \tag{7.2}$$

Where a factor of 2π has to be included to convert the natural frequency from radians per second into the natural frequency in Hz.

7.4 Comments on the γ Parameter

Appendix C shows that in the SJTU tests the 'rise time' to approach the maximum response is of the order of a few cycles, typically 4 or 5 cycles. This quick rise time observed on low mass ratio cylinders is extremely important in explaining why it is possible to observe a VIV response in time-varying or unsteady flows. This section includes some simple calculations that will compare the duration of the excitation with the minimum number of cycles necessary to approach maximum response amplitudes in order to show that under large accelerations (large γ) there simply is not enough time for the cylinder to reach its maximum response.

Assuming that the lock-in bandwidth or synchronization region is $U_n \pm 20\%$, where U_n is the velocity to excite mode n, the γ parameter can be rewritten as:

$$\gamma = \frac{\frac{\partial U}{\partial t}}{U_n} T_n \approx \frac{\frac{\Delta U}{\Delta t}}{U_n} T_n = \frac{\frac{1.2U_n - 0.8U_n}{\Delta t}}{U_n} T_n = \frac{2}{5}\frac{T_n}{\Delta t}$$

Duration of the excitation force:

$$\frac{\Delta t}{T_n} = \frac{2}{5}\frac{1}{\gamma}$$

Which is the time required to 'traverse' the entire synchronization region if the flow is accelerating or decelerating linearly. This is also the duration of the excitation force in a constant acceleration flow measured in cycles of vibration! Keeping in mind that a low-mass ratio cylinder experiencing VIV needs at least 4 to 5 cycles to approach its maximum response amplitude, one can compare the excitation duration (expressed in cycles) with this minimum number of cycles and try to determine if there is enough time for the response to 'build up'.

This is demonstrated with the schematic shown in Figure 7-1 which shows the duration of the excitation force measured in CYCLES as a function of γ for an

unsteady flow of constant acceleration.

In an unsteady flow with $\gamma = 0.4$, the excitation will only last 1 cycle, therefore it would be impossible for a system to respond and achieve high amplitude vibration (keeping in mind that it requires a minimum of 4 cycles to build up its response). On the other hand, in an unsteady flow with $\gamma = 0.02$ the force will be acting for ~ 20 cycles which is several times longer than the 4 cycles that cylinder needs to reach maximum amplitudes and therefore it is very likely that the VIV response will be similar to what is observed in steady flows.

The exact γ values that determine the response in unsteady flows are not yet known, and analysis of the experimental results in the following chapters will help define the different response regions.

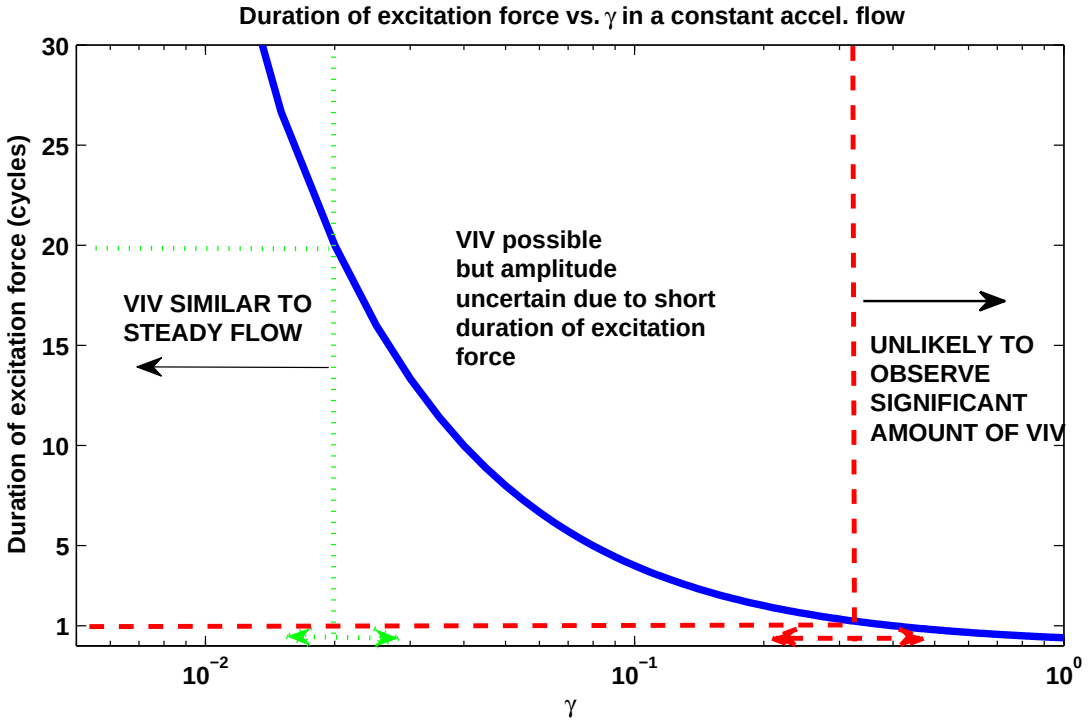

Figure 7-1: Duration of the excitation force measured in cycles for different values of γ in unsteady flows of constant acceleration

Chapter 8

Results From the Time-Varying Tests at SJTU

This chapter presents the results from the time-varying tests (ramp tests) performed at the State Key Laboratory of Ocean Engineering at the Shanghai Jiao Tong University (SJTU). The main objective is to demonstrate that the γ parameter is well suited to predicting whether the response during a time-varying test is similar to that observed in steady flows. It will be shown that results extracted from slowly varying ramps (i.e., small γ) match well with their steady flow counterparts but results extracted from quickly varying ramps do not compare well because the excitation duration is shorter than the time necessary for the structure to 'build-up' its response.

This chapter begins by showing what the VIV response in a steady flow test at SJTU looked like. This will serve as a baseline for comparisons when, and if, a VIV response is observed in the time-varying flows or 'ramp tests'. This is immediately followed by the analysis of the VIV response in a slowly accelerating test. The primary intention of presenting the data in this sequence is to convince the reader of the good qualitative agreement between the VIV response in slowly varying flows with the response observed in steady flows.

The chapter closes by presenting the results from the entire test matrix investigated at SJTU in an abridged form and by showing how these results can be used to classify the VIV response in time-varying flows using the unsteady flow parameter, γ.

8.1 A Constant Speed Test (or Baseline Test)

It is instructive to begin with a constant speed test and to review some traditional data processing techniques used by the VIV community. It will be shown that these standard tools have certain shortcomings when it comes to analyzing transient data. Figure 8-1 shows the speed of the carriage for test-142b. Because of the relatively short track length in the experimental setup, the test duration is short, only allowing the carriage to move at a constant speed for approximately 2 seconds. Nonetheless, the response frequency was 9.77Hz which meant that even this short time section was long enough to observe approximately ~ 20 cycles.

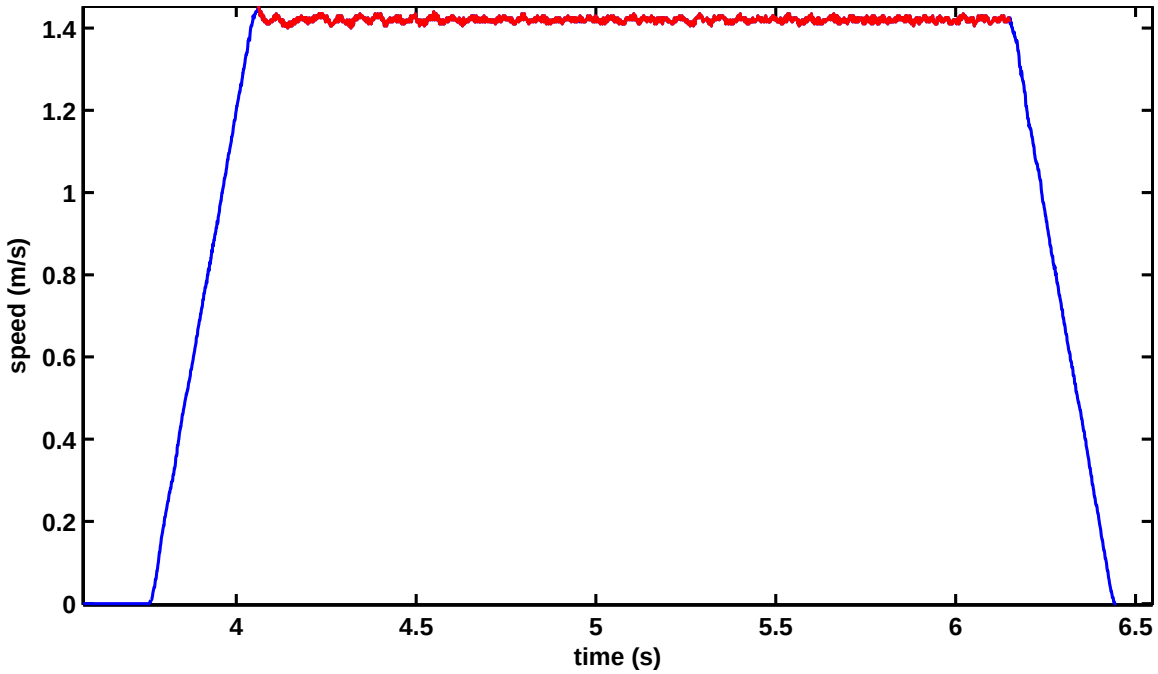

Figure 8-1: Towing Speed vs. Time for Test-142b

It is fairly standard practice in conventional, constant speed tests to dismiss the first $5-15\%$ and the final $5-10\%$ of the time record in an attempt to exclude transient effects. The remaining time-history can then be used as an approximate steady state sample for data extraction and further analysis. An alternative approach calls for identifying the statistically stationary portions of the time history and only using those time sections. This can be extremely challenging in practice especially when

dealing with flexible cylinders with multiple sensors because what seems to be a statistically stationary time section at a specific sensor location may not appear stationary at another sensor or location. These issues are addressed in detail in Appendix A.

Figure 8-2 shows the response spectra from CF and IL sensors located at the middle of the $4m$ long flexible cylinder. Because of the short record length the spectra have quite poor spectral resolution. The upper two plots are computed using conventional spectral analysis, based on the Fast Fourier Transform (FFT). The lower two plots show the spectra generated from the same time-history, but using the Maximum Entropy Method (MEM) which results in much better spectral resolution. The CF spectrum shows a peak at approximately $\sim$ 10Hz which corresponds to the 1X VIV frequency but also shows significant response at the 2X, 3X and 4X higher harmonics which is common on flexible cylinders. The IL spectrum shows a lot of energy at the 2X peak but little anywhere else.

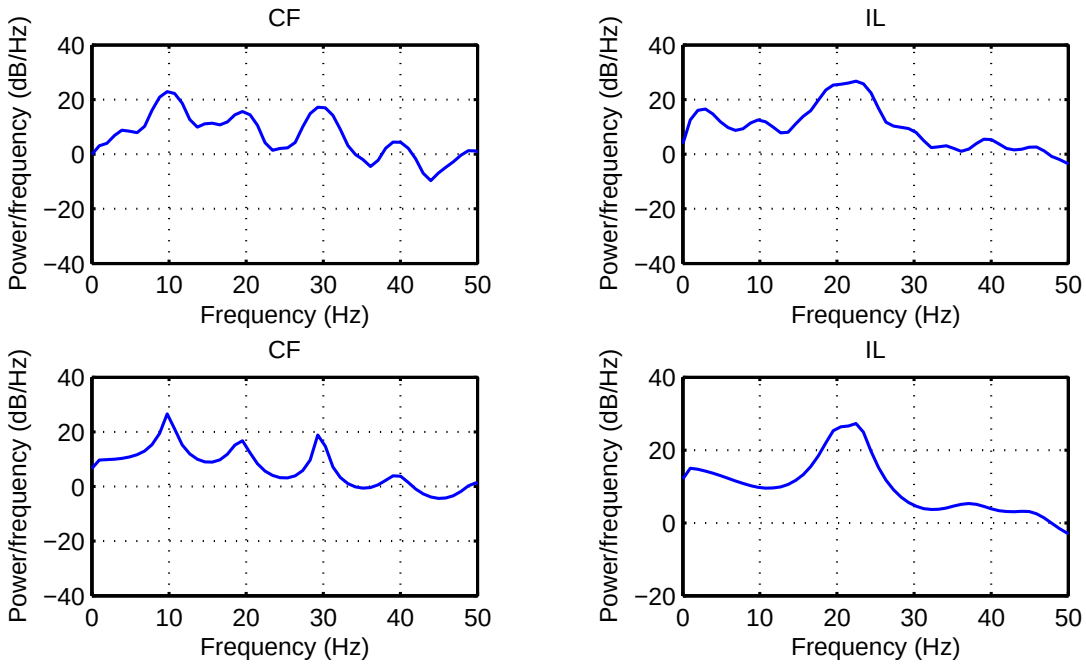

Figure 8-2: Power Spectral Density (PSD spectra) for the CF and IL directions (test-142b) **Top row:** computed using the FFT **Bottom row:** computed using the MEM

Due to the presence of the higher harmonics most subsequent analysis will use data

that has been band-pass filtered around the 1X frequency or the 2X frequency for the CF and IL directions respectively.

Figure 8-3 is a contour plot showing the CF strain as a function of time along the cylinder's span. As expected, since these are low mode number tests, standing waves are observed in the CF direction. It is interesting to note that the maximum response amplitude varies with time and that the time instant when the largest amplitude is observed in the CF direction does not coincide with the time instants that maximum IL response occurs (not shown).

It is much easier to identify the resonant mode through a modal reconstruction in the manner described by Lie & Kassen (2006). Figure 8-4 shows the results of such a modal analysis in the CF direction using the entire available time history. The figure shows the mode weights (modal participation factors) where it is quite clear that the response is dominated by mode 3. The star-shaped data points are the measured curvatures at the 7 different locations along the cylinder whereas the solid line is the curvature along the cylinder that results from the modal reconstruction. The dimensionless response amplitude along the cylinder is also obtained from the modal reconstruction.

Finally, Figure 8-5 shows the cylinder trajectories at three different locations along the cylinder span. The simultaneous vibration in the CF and IL direction means that the cross-section dances around in easily identifiable patterns that depend on the magnitude of the CF and IL vibrations and most importantly the phase between the two motions (Dahl, 2008).

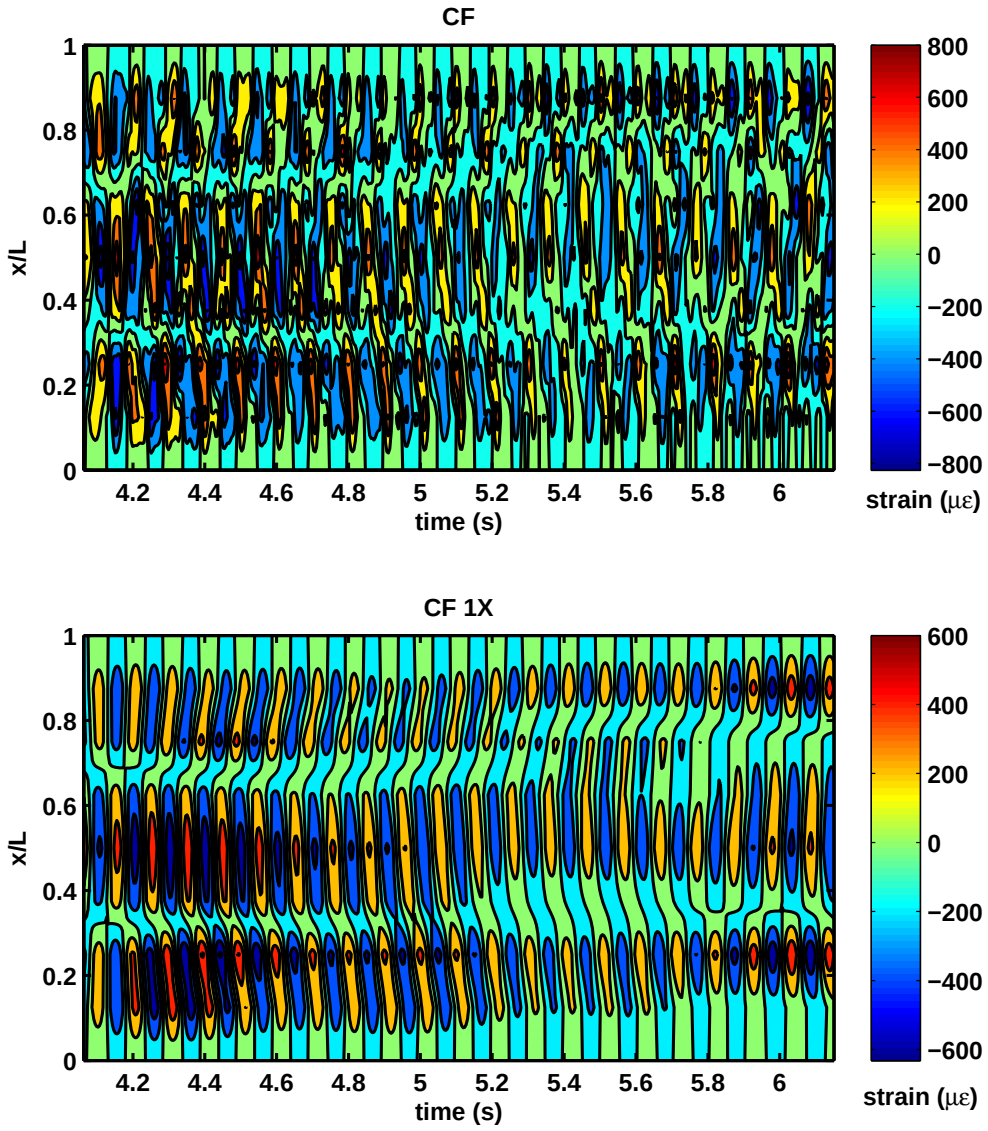

Figure 8-3: Contour plot of CF strain ($\mu\varepsilon$) as a function of time and position along the cylinder for Test-142b. The upper plot **includes** all higher harmonics. The lower has been **filtered** to show the 1X frequency component only

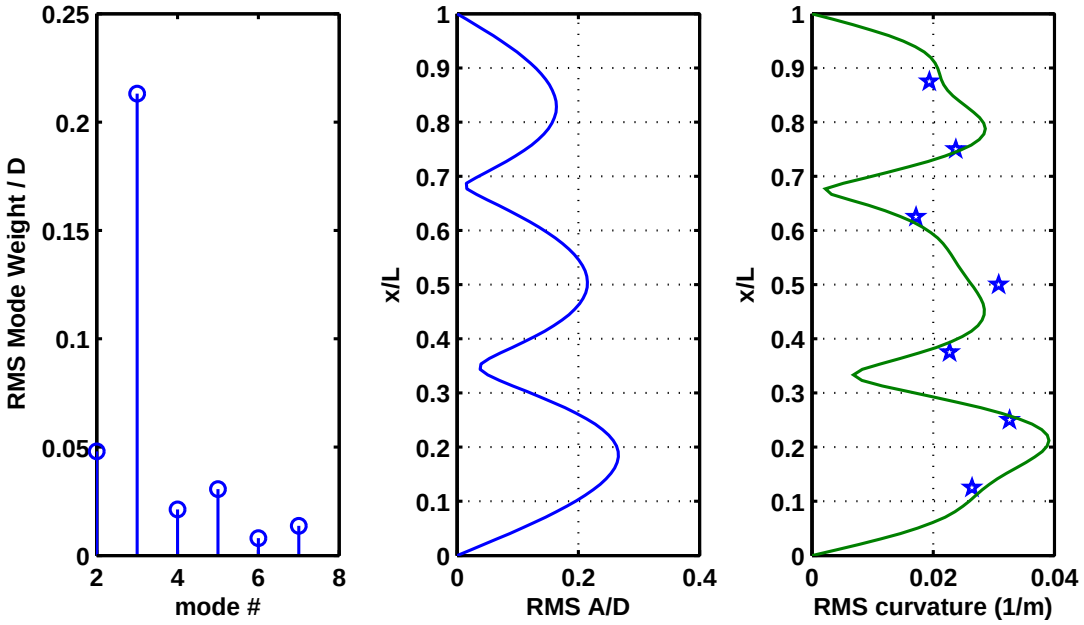

Figure 8-4: Modal Reconstruction in the CF direction for Test-142b:
Far left: RMS mode weights, **Middle:** the reconstructed CF response amplitude,
Far right: the reconstructed curvature (solid line) and the measured curvature (star shaped data points)

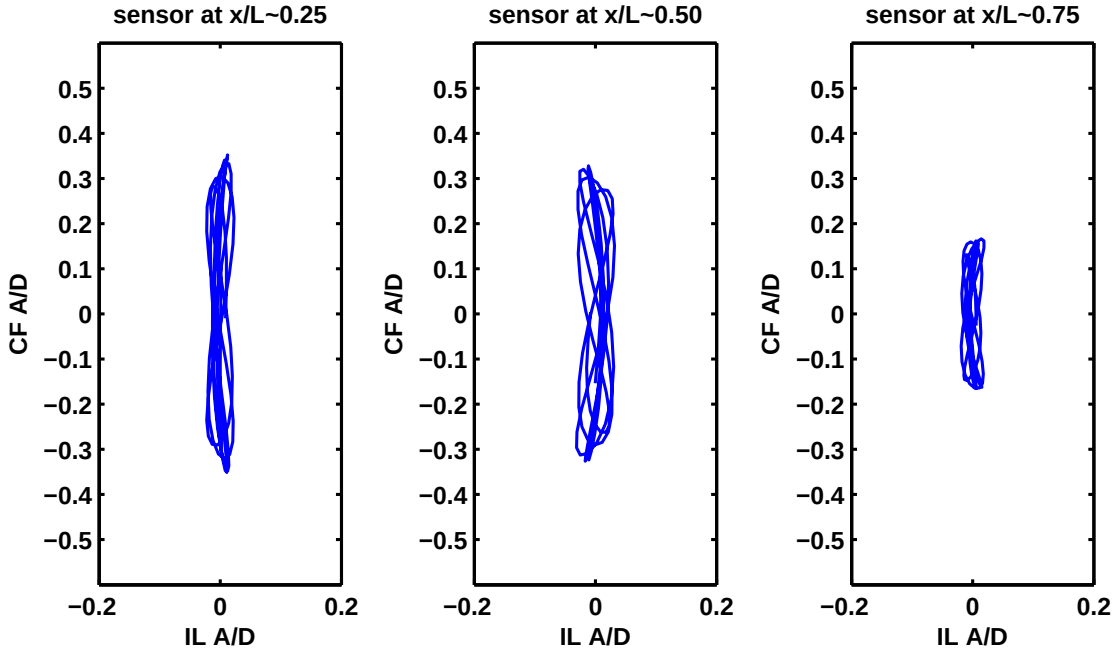

Figure 8-5: Cylinder trajectories at three different locations for Test-142b

8.2 A Typical Ramp Test (Slowly Accelerating)

The objective once again is to study the cylinder response at a velocity of $1.4m/s$ which should excite the 3^{rd} mode. However, instead of keeping the velocity constant like the previous example in Section 8.1, the 'ramp tests' involved towing the cylinder through the 'target velocity' of $1.4m/s$ under varying amounts of acceleration, Test-8a was one such example and is shown in Figure 8-6. The figure shows towing velocity as a function of time and is very characteristic of the ramp tests performed at SJTU.

In the central portion of the ramp shown in Figure 8-6, the acceleration is approximately $0.083m/s^2$, which corresponds to a γ value of approximately 0.006. In other words, in every vortex shedding period the flow is changing by $\sim 0.6\%$ which is quite small and quasi steady state behavior might occur.

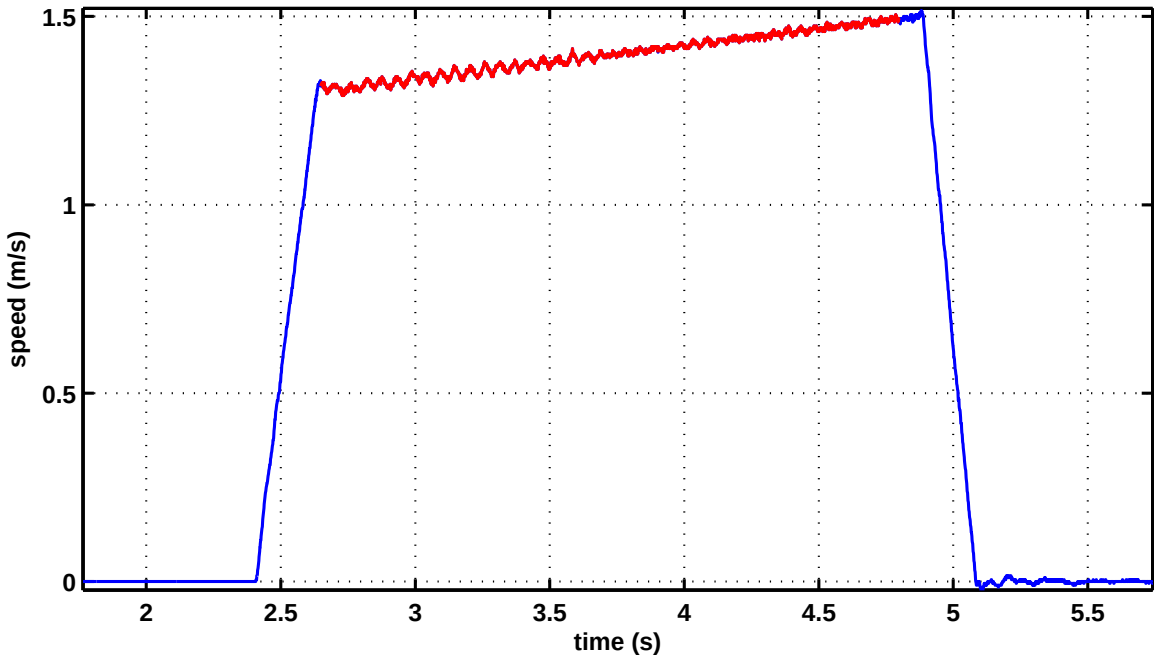

Figure 8-6: Towing speed vs. Time for Test-8a

In general, one is still interested in measuring the same response quantities as would typically be obtained from a constant speed test. These typically are the response frequency, the dominant responding mode, the RMS amplitude along the pipe span, the RMS strain, mean drag coefficients, etc.

At this point, it is important to remember that since the speed is changing the cylinder may or may not lock-in unless the conditions are favorable. If it does lock-in, it is highly unlikely that it will lock-in for the entire duration of the test. For this reason the data analysis should not be performed on the entire test but instead only on the section of the time-record corresponding to the strongest VIV response. In order to capture the unsteady behavior, all response statistics, like the RMS dimensionless amplitude, etc. are computed from within a 'moving window' which passes through the entire data record, the equations are given below.

A typical window length that was used, was one corresponding to 5 periods ($j = 5$), with the shedding frequency determined using the instantaneous flow speed and a Strouhal number of 0.16.

$$T_{vortex}(t) = \frac{1}{f_{vortex}(t)} = \frac{D}{U(t)St} \tag{8.1}$$

The moving or running mean can be defined as:

$$\text{Continuous: } \mu_x(t) = \frac{1}{T(t)} \int_{t-\frac{T}{2}}^{t+\frac{T}{2}} x(\tau) d\tau \text{ with } T(t) = jT_{vortex}(t)$$

$$\text{Discrete: } \mu_x(k\Delta t) = \frac{1}{N(t)} \sum_{l=k-\frac{N}{2}}^{k+\frac{N}{2}} x(l\Delta\tau) \text{ with } N(t) = T(t)\Delta f = jT_{vortex}(t)\Delta f$$

where Δf and Δt are the sampling frequency (Hz) and the sampling interval (s) respectively.

Similarly, the moving or running Root Mean Square (RMS) can be defined as:

$$\text{Continuous: } \sigma_x(t) = \sqrt{\frac{1}{T(t)} \int_{t-\frac{T}{2}}^{t+\frac{T}{2}} (x(\tau) - \mu_x)^2 d\tau} \text{ with } T(t) = jT_{vortex}(t) \tag{8.2}$$

$$\text{Discrete: } \sigma_x(k\Delta t) = \sqrt{\frac{1}{N(t)} \sum_{l=k-\frac{N}{2}}^{k+\frac{N}{2}} (x(l\Delta\tau) - \mu_x)^2} \text{ with } N(t) = T(t)\Delta f = jT_{vortex}(t)\Delta f \tag{8.3}$$

Finally, the kurtosis (or 4^{th} moment) can be defined as:

$$\text{Continuous:}\kappa_x(t) = \frac{1}{T(t)} \int_{t-\frac{T}{2}}^{t+\frac{T}{2}} (x(\tau) - \mu_x)^4 d\tau \text{ with } T(t) = jT_{vortex}(t) \tag{8.4}$$

$$\text{Discrete: } \kappa_x(k\Delta t) = \frac{1}{N(t)} \sum_{l=k-\frac{N}{2}}^{k+\frac{N}{2}} (x(l\Delta\tau) - \mu_x)^4 \text{ with } N(t) = T(t)\Delta f = jT_{vortex}(t)\Delta f \tag{8.5}$$

The kurtosis is included here because it is well-suited in distinguishing a sinusoidal response, which will have a kurtosis of 1.5 from a broadband Gaussian response for which the kurtosis would be equal to 3.0. (Kaasen et al., 2000)

Figure 8-7 shows how the moving RMS strain varied with time during the slowly accelerating portion of the ramp test. The plot of *strain* vs. *time* includes four different lines: the heavy blue line is the total CF strain, the green line corresponds to the 1X band pass filtered signal, the red line corresponds to the 3X band pass filtered signal and finally the dashed line is the sum of the 1X and 3X filtered signals. By comparing the solid blue line and the dashed blue line and noticing that their differences are small, one can confirm that indeed the 1X and 3X frequencies are the main components of the raw signal and most of the energy is associated with these two frequencies.

The CF strain peaks just after the 3^{rd} second. It is interesting to note that at the same time, the kurtosis approached a value of 1.5 which would indicate a purely sinusoidal signal.

Figure 8-8 is a contour plot showing the CF strain at every position along the cylinder as a function of time, with the red and blue colors corresponding to tensile and compressive bending strains respectively. The nearly vertical lines indicate a standing wave response very similar to the steady flow case shown earlier. Note that the figure indicates the magnitude and location of the anti-nodes change slightly during the test, but consistently remain dominated by the third mode; recall that this was also observed in the steady speed test. The figure shows that the response is strongest around the 3^{rd} second which agrees with the data shown in Figure 8-7.

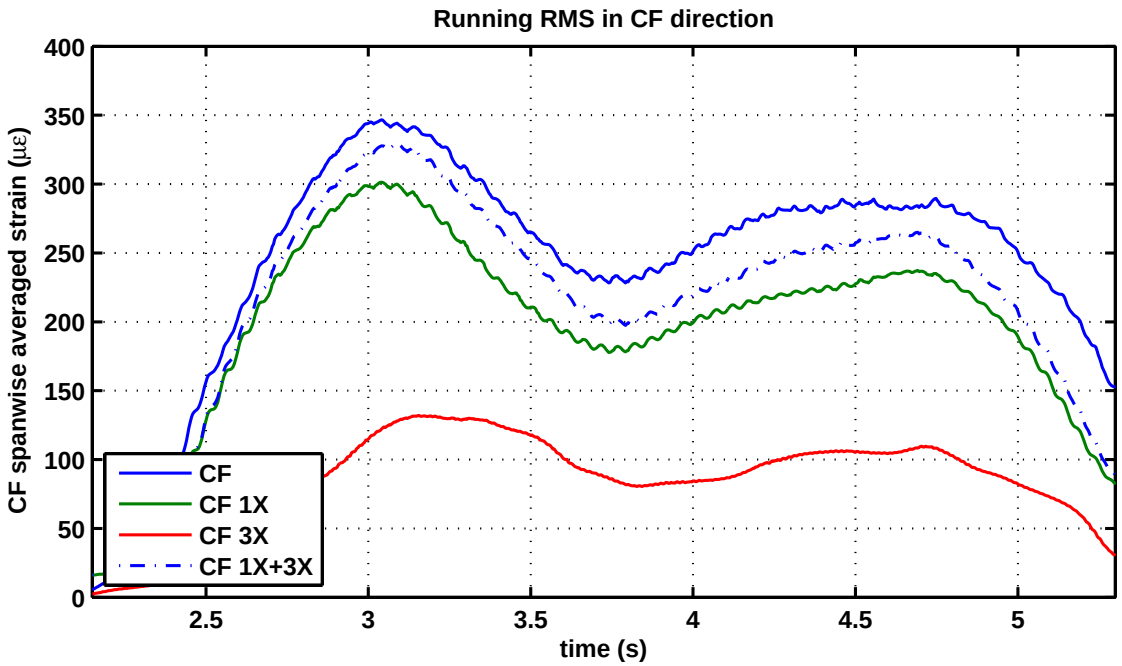

Figure 8-7: CF RMS Strain ($\mu\varepsilon$) vs. time for Test-8a calculated using the moving window

Figure 8-9 shows the modal reconstruction of a short time record, equivalent to 5 cycles or $\sim$ 0.5 seconds, centered on the 3 second mark. Like the steady flow case, the 3^{rd} mode dominates the response and the calculated response amplitude and curvature are very similar to what is shown in Figure 8-4, with the slight difference that this case had a larger non-resonant contribution from the second mode.

Figure 8-10 shows the cylinder trajectories observed during the ramp test. These are qualitatively very similar to what was observed in steady flows shown in Figure 8-5. The main reason for showing all these response details from the unsteady flow test and comparing them to the response details at constant speed (that was shown in the beginning of this chapter) is to convince the reader that when the rate of change of speed is slow it will result in a VIV response with very similar characteristics to what is observed in steady flows.

The procedure described in this sections was used to analyze all the different 'ramp tests' that were part of the SJTU dataset.

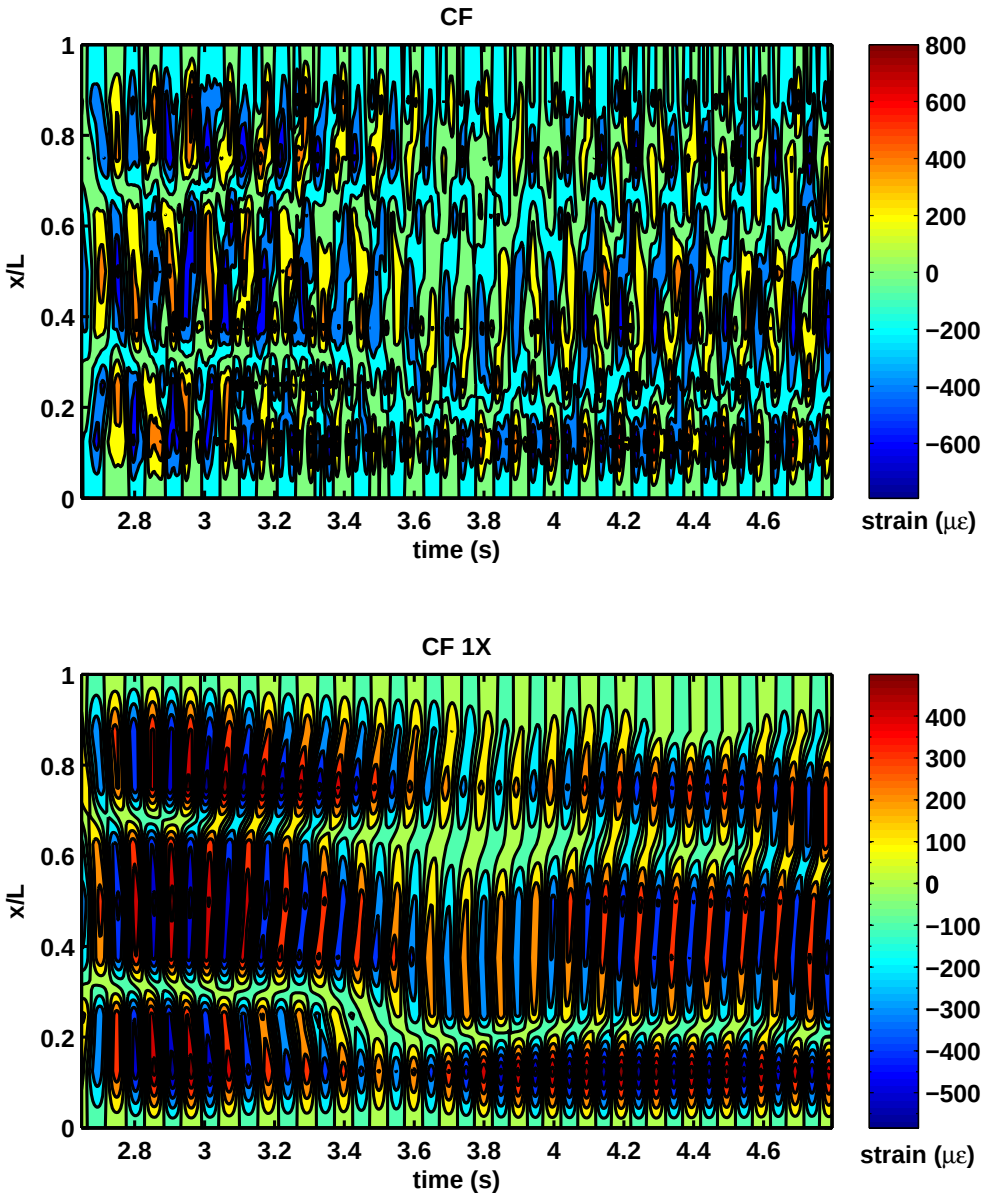

Figure 8-8: Contour plot of CF strain ($\mu\varepsilon$) as a function of time and position along the cylinder for Test-8a. The upper plot **includes** all higher harmonics. The lower has been **filtered** to show the 1X frequency component only

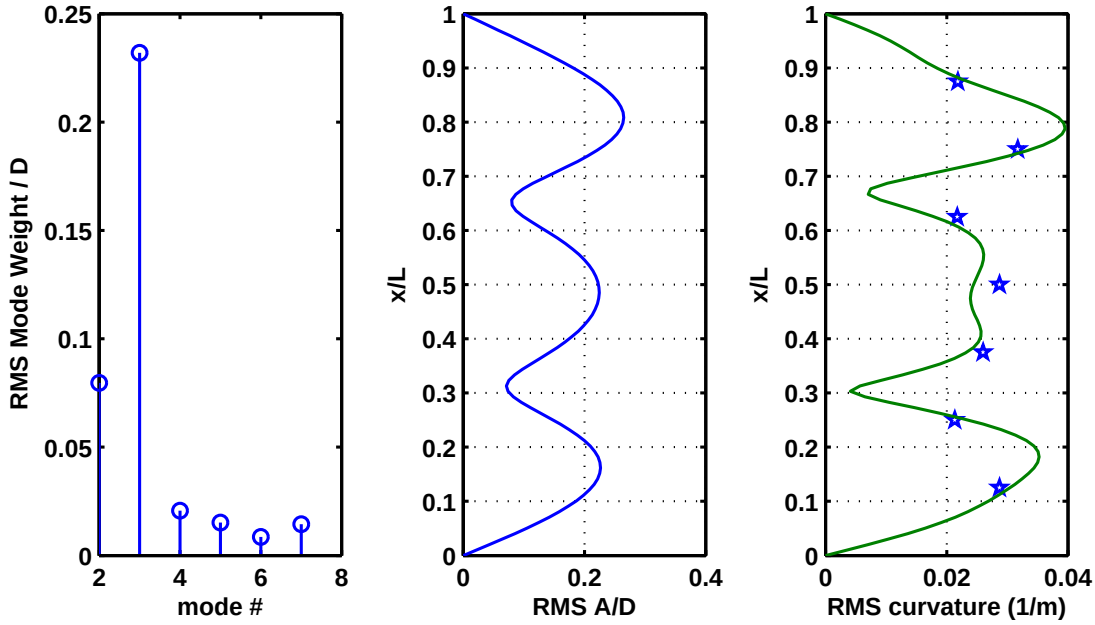

Figure 8-9: Modal Reconstruction in the CF direction for Test-8a
Far left: RMS mode weights, **Middle:** the reconstructed CF response amplitude, **Far right:** the reconstructed curvature (solid line) and the measured curvature (star shaped data points)

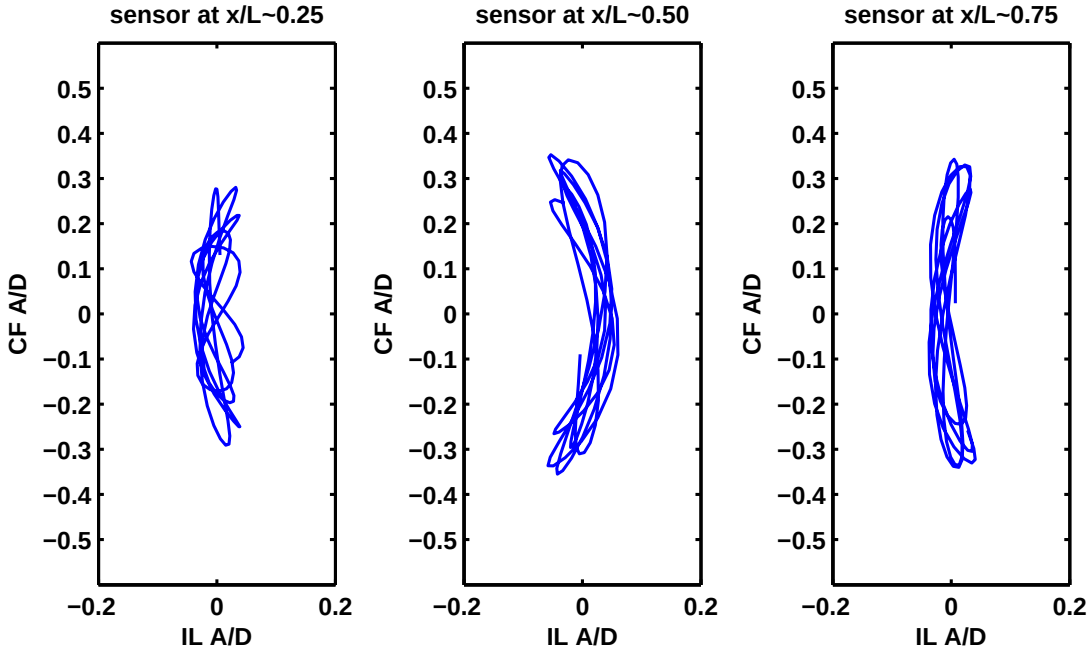

Figure 8-10: Trajectories at three different locations for Test-8a

8.3 A Quickly Accelerating Ramp Test (Large γ)

In the previous section it was shown that results from a slowly varying unsteady test (or 'ramp test') agree well with the steady speed test results. However, it will be instructive to see how the cylinder will respond under stronger accelerations and how this will affect the observed response.

Figure 8-11 shows one of the strongest ramps in the entire SJTU data corresponding to Test-1a. The carriage ramps through both of the 'target speeds' of interest (i.e. 1.4 and $2.3m/s$), which are indicated on the graph with the red lines.

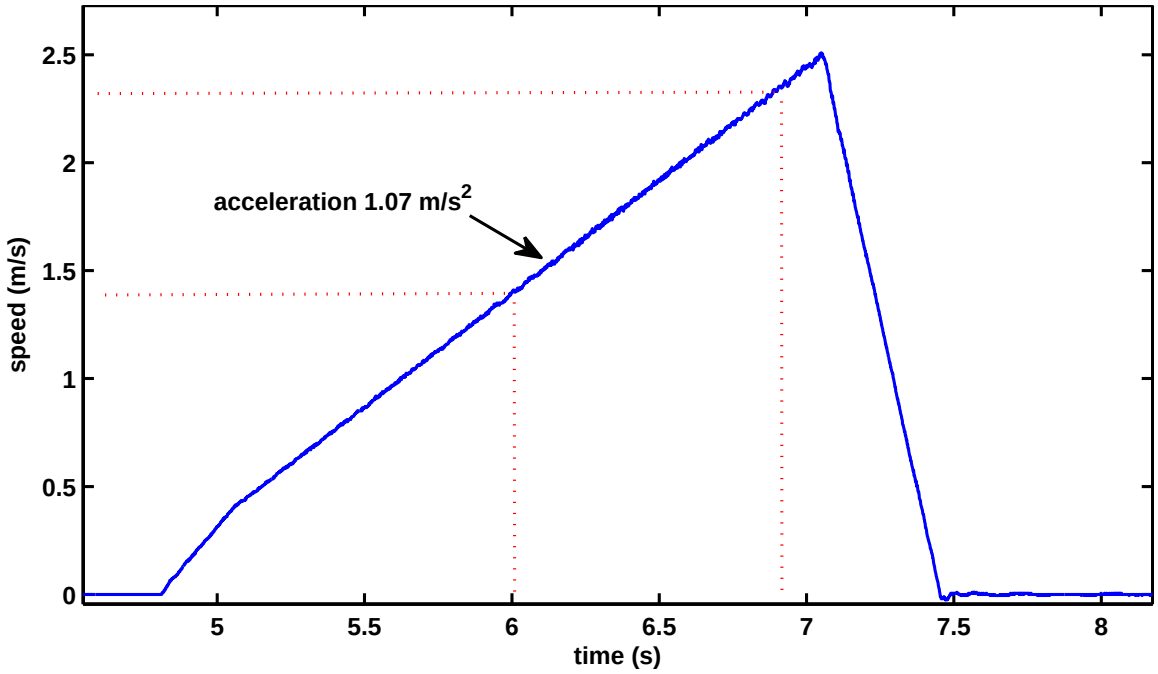

Figure 8-11: Towing speed vs. Time for Test-1a

Even though the acceleration is constant in this portion of the ramp there are two different γ values; one for each combination of mode/frequency and towing speed:

$$\gamma = \frac{1.07m/s^2}{1.4m/s}\frac{1}{9.77Hz} \approx 0.08 \tag{8.6}$$

$$\gamma = \frac{1.07m/s^2}{2.3m/s}\frac{1}{16.6Hz} \approx 0.03 \tag{8.7}$$

Figure 8-12 shows the CF strain along the span as a function of time for Test-1a. The top-most plot shows the CF strain as recorded with no filtering. The distance

between troughs and peaks is an indication of the response frequency which is observed to start off very low and increases throughout the duration of the ramp. It is hard to distinguish exactly what is happening around the 6 and 6.8 second marks, which are of interest, because the plot's scale is governed by the high amplitude response at the end of the test.

Since the response frequencies are known it was possible to band-pass filter the recorded strain data around each of the two frequencies and see if the cylinder actually vibrated and locked-in during the predicted time-instances. The middle plot in Figure 8-12, shows the CF strain after the data was band-pass filtered around 9.77Hz. It is immediately obvious that there is some response at this frequency before and after the 6^{th} second. The bottom plot shows the CF strain after it has been band-pass filtered around 16.6HZ, and once again it is clear that the pipe is also responding at the second frequency from approximately 6.8 seconds until the end of the test.

Even though there is a discernible CF response around the 6^{th} second it only lasts 5-6 cycles. In this short amount of time the pipe has to start building-up its response and eventually decay as the velocity increases to the point that it is outside the synchronization region. Figure 8-13 compares the CF RMS amplitude and curvatures extracted from the ramp test for a time window that lasts 5 cycles centered on the 6^{th} second. When these results are compared to the response envelopes from the steady flow tests (green-gray areas) it is clear that they do not agree well. This should not come as a surprise since the γ value corresponding to this speed, mode and acceleration triplet was approximately 0.08, which implies an 8% variation in speed EVERY cycle of vibration.

In stark contrast with the above case, the response between the 6.8-7 second marks has a γ value of 0.03 which corresponds to a 3% variation in speed every cycle. Figure 8-14 compares the data extracted from the ramp over 5 cycles centered at ~ 7 seconds with the response envelopes from the steady speed or conventional tests. The agreement is good which should further emphasize the importance of the unsteady flow parameter, γ, in dictating whether ramp extracted results (i.e., unsteady or time-varying flow) are similar to the response observed at steady speeds.

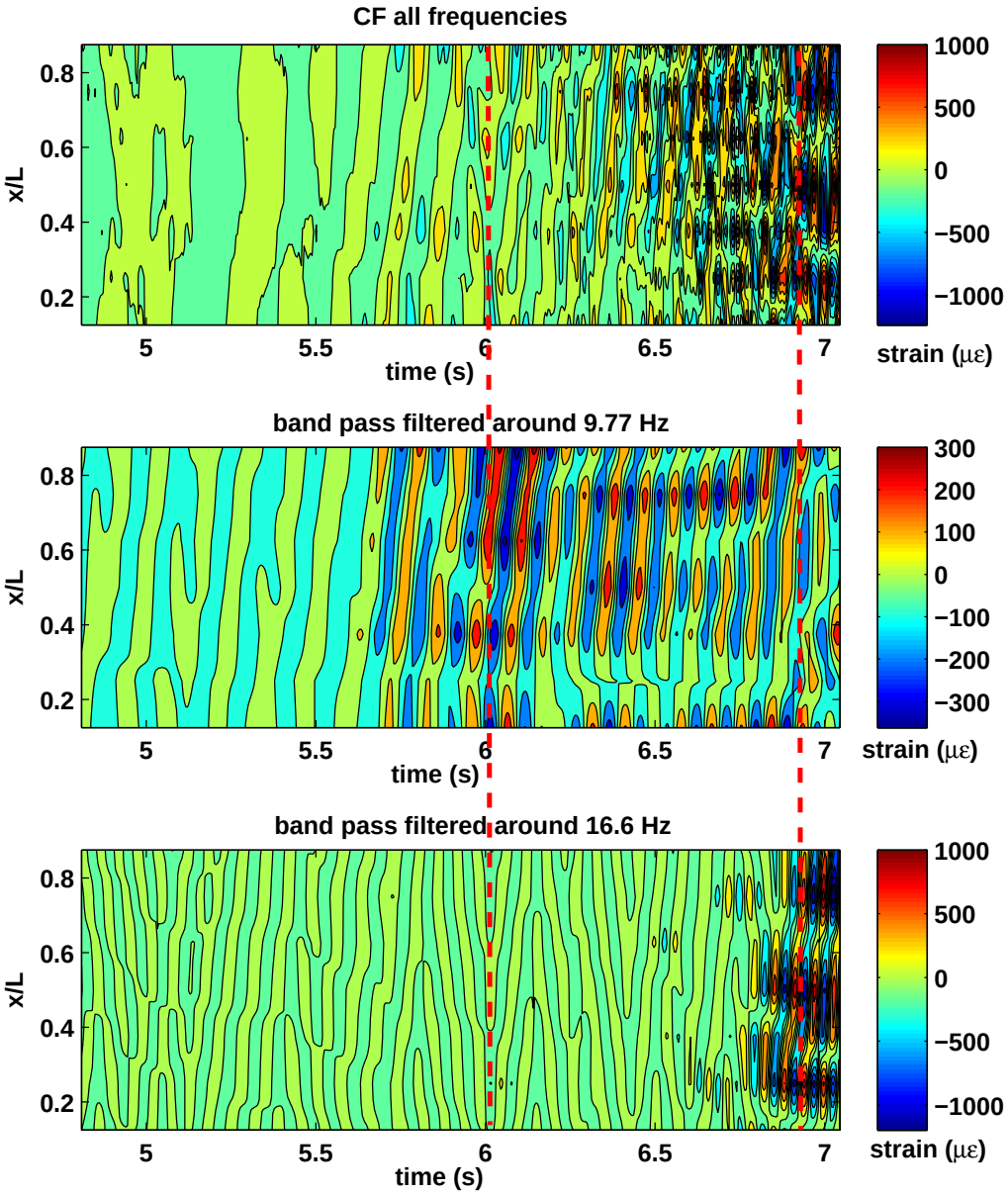

Figure 8-12: CF strain ($\mu\varepsilon$) along the cylinder span (x/L) as a function of time (s) for Test-1a. **Top:** No filtering **Middle:** band-pass filtered around 9.77Hz **Bottom:** band-pass filtered around 16.6Hz

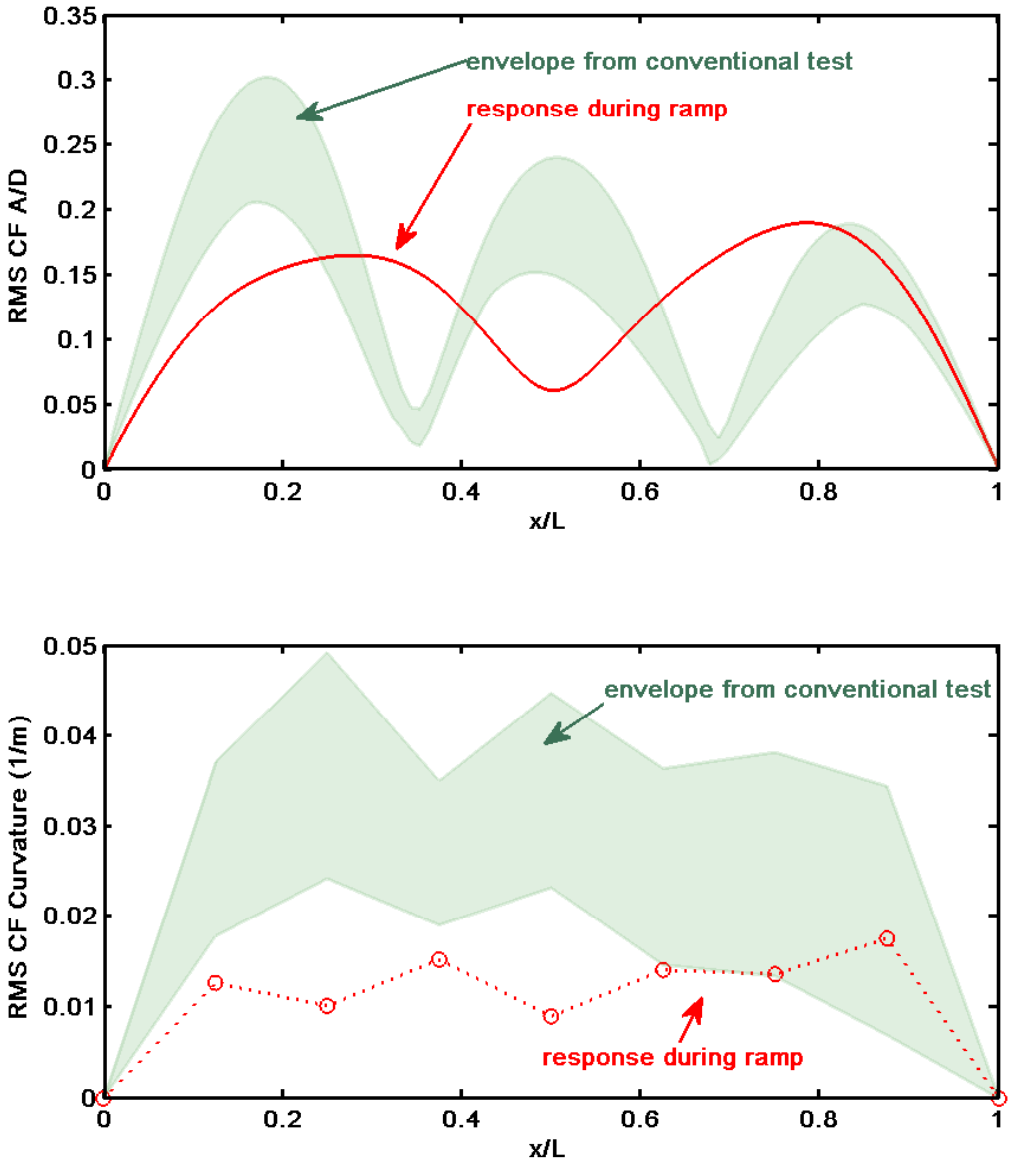

Figure 8-13: Comparison of data extracted from ramp Test-1a with the steady state values. Mode with excitation frequency of 9.77Hz (or $1.4m/s$) and $\gamma \sim 0.08$
Red lines: ramp results **Gray areas:** RMS response envelopes from constant speed tests

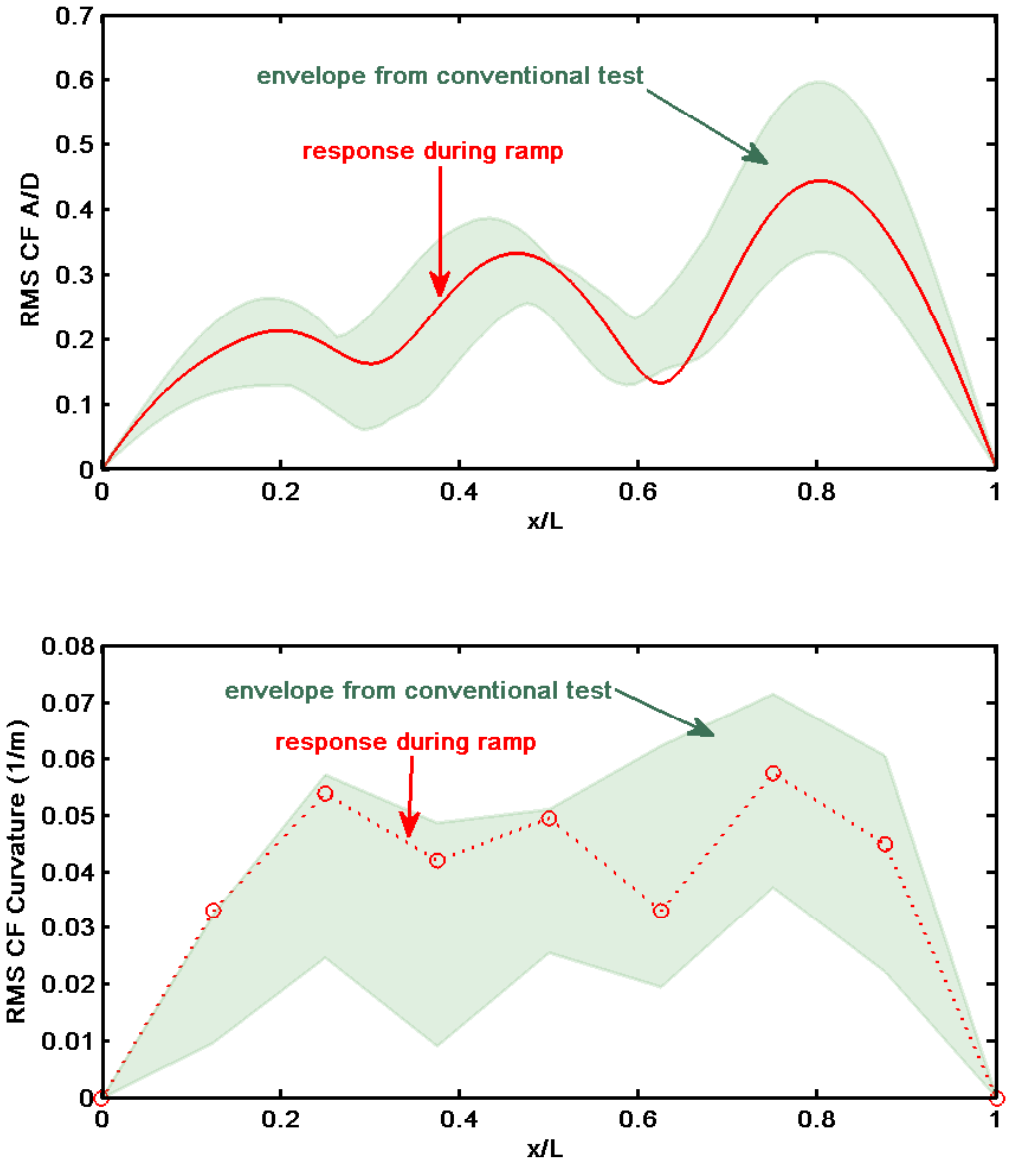

Figure 8-14: Comparison of data extracted from ramp Test-1a with the steady state values. Mode with excitation frequency of 16.6Hz (or $\sim 2.3m/s$) and $\gamma \sim 0.03$
Red lines: ramp results **Gray areas:** RMS response envelopes from constant speed tests

8.4 Summary of All Ramp Tests Conducted at SJTU

Up to this point, it has been shown that in some time-varying cases the VIV response observed can be very similar to the VIV response at steady flows or constant towing speeds. This section compares the response at various values of γ with the steady speed results in order to determine if there is a threshold γ value below which the response in unsteady conditions is virtually indistinguishable from a steady state test.

Before presenting the results from the entire SJTU dataset, it is very important to emphasize that due to the stochastic nature of VIV, even a steady speed test, if repeated would not always yield identical results. Furthermore, during the duration of each such test the response amplitude and the strain will vary as the pipe transitions from single frequency sinusoidal response, when most quantities are statistically stationary, to a strongly chaotic response typical of broadband excitation (see Appendix A). The variability observed in the response of a steady speed or conventional test is demonstrated in Figure 8-15, where instead of showing a single line, an envelope that includes all possible RMS responses observed is utilized. The RMS A/D value was ~ 0.25 at position $x/L \sim 0.2$ and during the test this varied between $0.18 < A/D < 0.38$.

Figure 8-16 shows the maximum RMS A/D response –anywhere along the cylinder's span– as well as the spanwise mean RMS A/D response as a function of the γ value of the ramp from which the data was extracted. These are compared with the results from the constant speed tests (steady flows), with the dashed lines indicating plus or minus one standard deviation around the average value from the repeated steady speed tests. In a similar manner, Figure 8-17 compares the constant speed values with the maximum and mean RMS strain along the span obtained from all the ramp tests.

From both of these figures, it can be seen that at values of γ smaller than ~ 0.02 the response from the unsteady speed tests agrees well with the steady state values. In fact the extracted results tend to be larger than the values observed during steady speed tests. This is consistent with the fact that the pipe was free to respond at the

exact speed which caused the greatest VIV response instead of being limited to a set of predetermined flow speeds which could easily lie to the left (lower V_r) or to the right (higher V_r) of the reduced velocity that would cause the greatest response, Vr_{crit}. In essence, because a ramp test will pass through a given mode's entire synchronization region it is guaranteed to excite the cylinder at the Vr_{crit} that will lead to the largest possible response.

The threshold limits on γ are determined by identifying below which γ value the unsteady results presented in Figures 8-14 and 8-15 are consistently higher or similar to the steady flow results. For the time-varying tests around $1.4m/s$ this value is found to be $\gamma \sim 0.02$.

Figures 8-18 & 8-19 compare the steady speed results with the ramp extracted results around speeds of $2.3m/s$. Once again, as a ramp's γ value decreases, the results that it provides are increasingly similar to the steady flow results. There appears to be a range of γ values between 0.02 and 0.1 where the response is erratic. In a few tests, the response observed was very similar to the steady speed response whereas, for other tests in the same range of γ values the response was consistently smaller than the steady speed tests.

There is clear need to further investigate the γ parameter space in the region 0.02 and 0.1 much more carefully in order to determine a more precise threshold on γ, below which a ramp result will always agree with or exceed the steady flow results. This would require further experimental testing and it will be important to investigate the effect of the moving operator length (5, 10, 15 cycles, etc) on the threshold. This is discussed at this point because the threshold is determined by the γ value above which the unsteady results are consistently smaller than the steady speed results. As such, it is important to know whether the observed cylinder response is 'small' because it did not have enough time to reach its maximum vibration amplitude due to the flow changing too rapidly and quickly exiting the synchronization region or because the large amplitude response only lasted 3 cycles yet the RMS calculation was performed over 5 cycles.

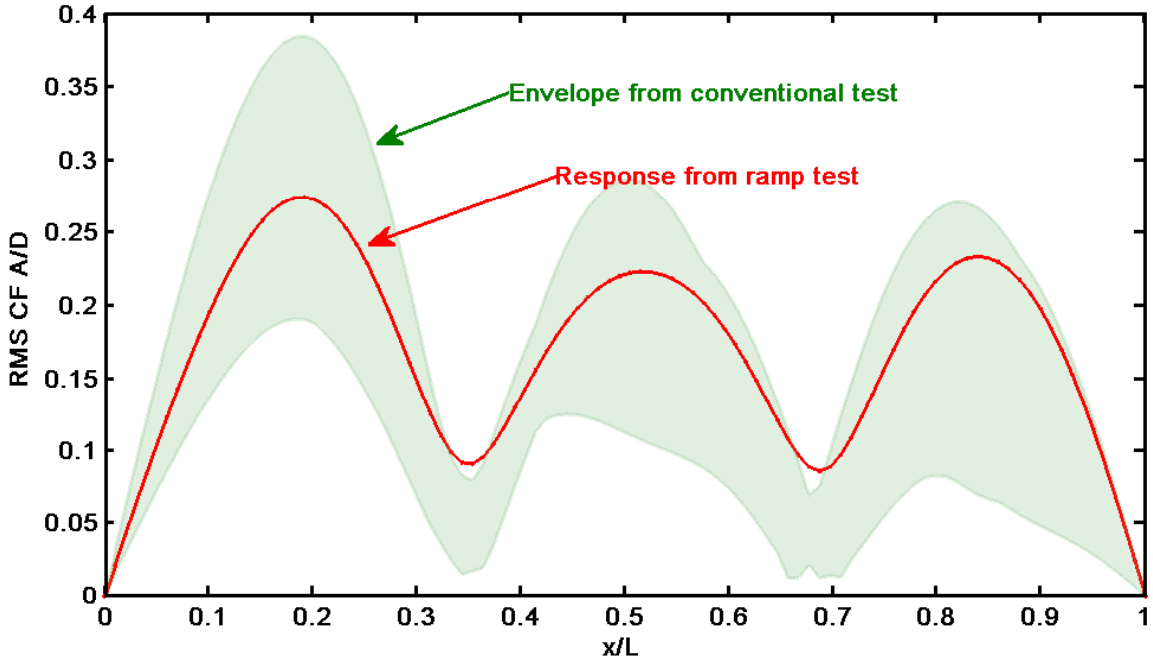

Figure 8-15: CF RMS amplitude vs. axial position. Shaded gray area is the RMS response envelope from a steady speed test. Red line is a 'ramp extracted' result

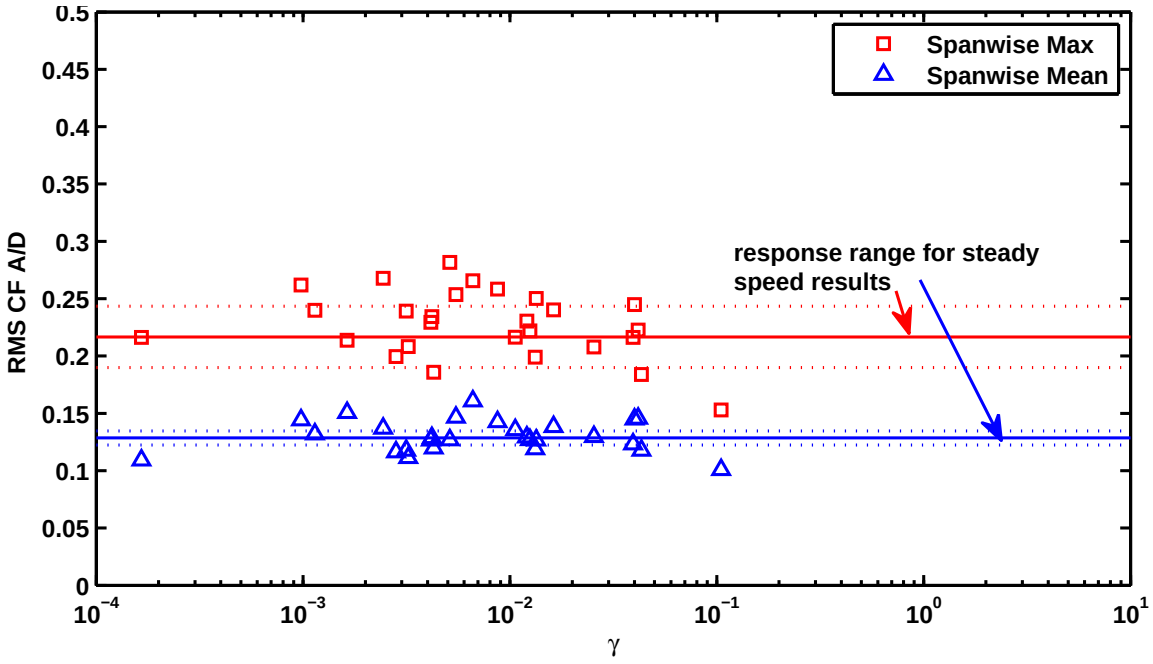

Figure 8-16: Response amplitude vs. γ around $1.4m/s$

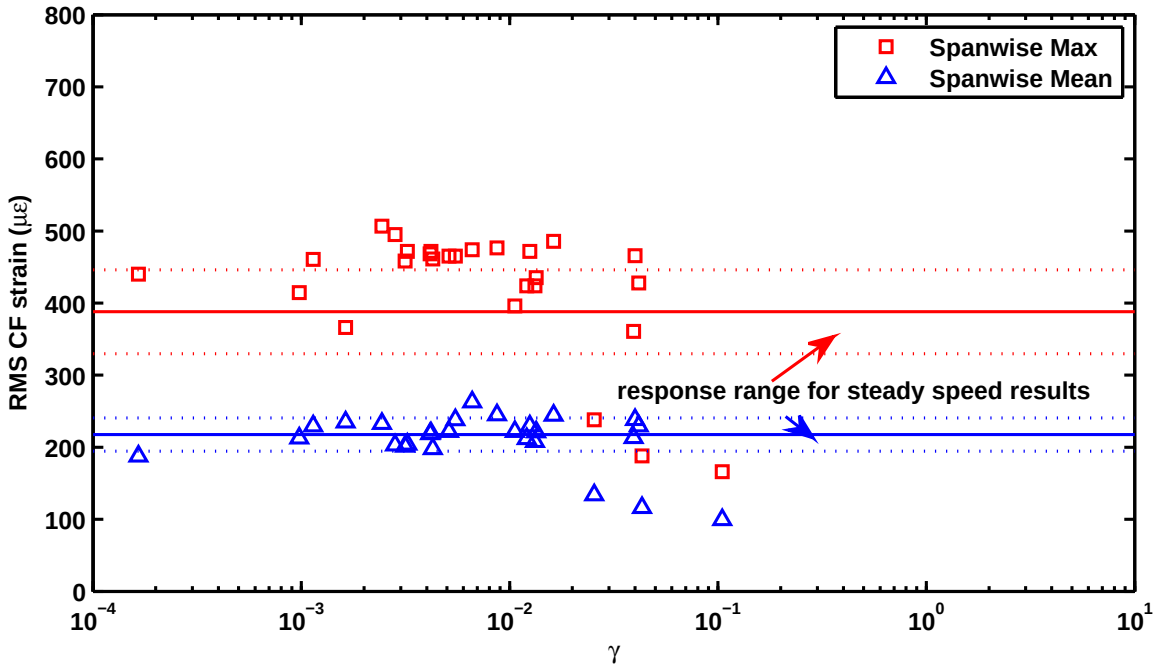

Figure 8-17: Strain ($\mu\varepsilon$) vs. γ around $1.4m/s$

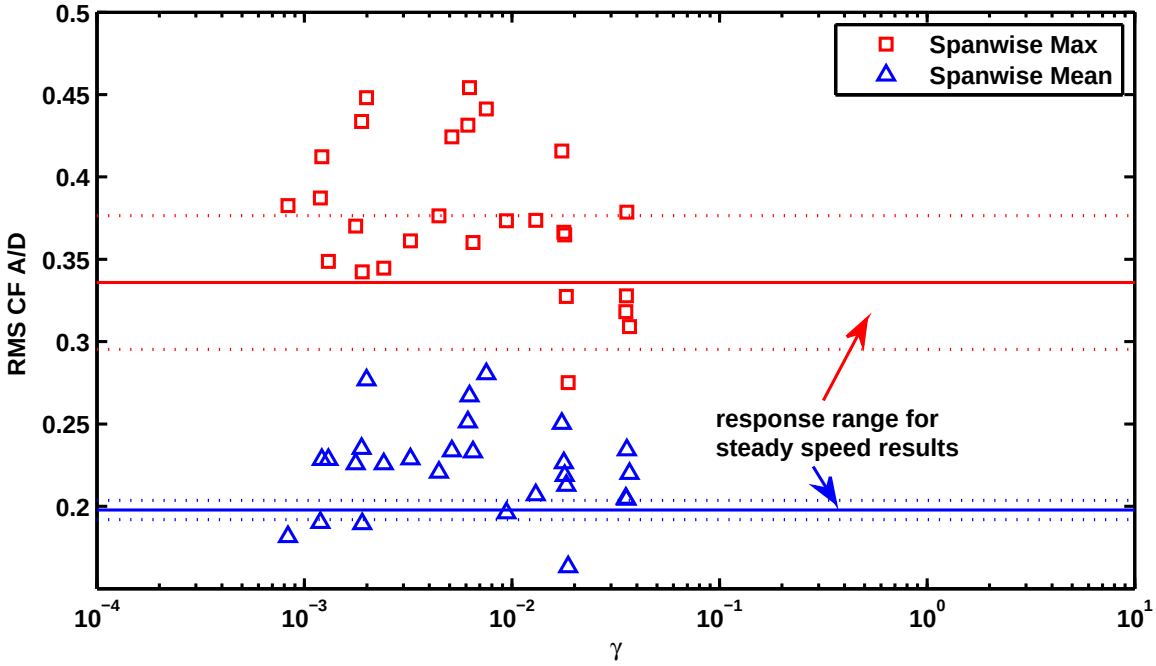

Figure 8-18: Response amplitude vs. γ around $2.3m/s$

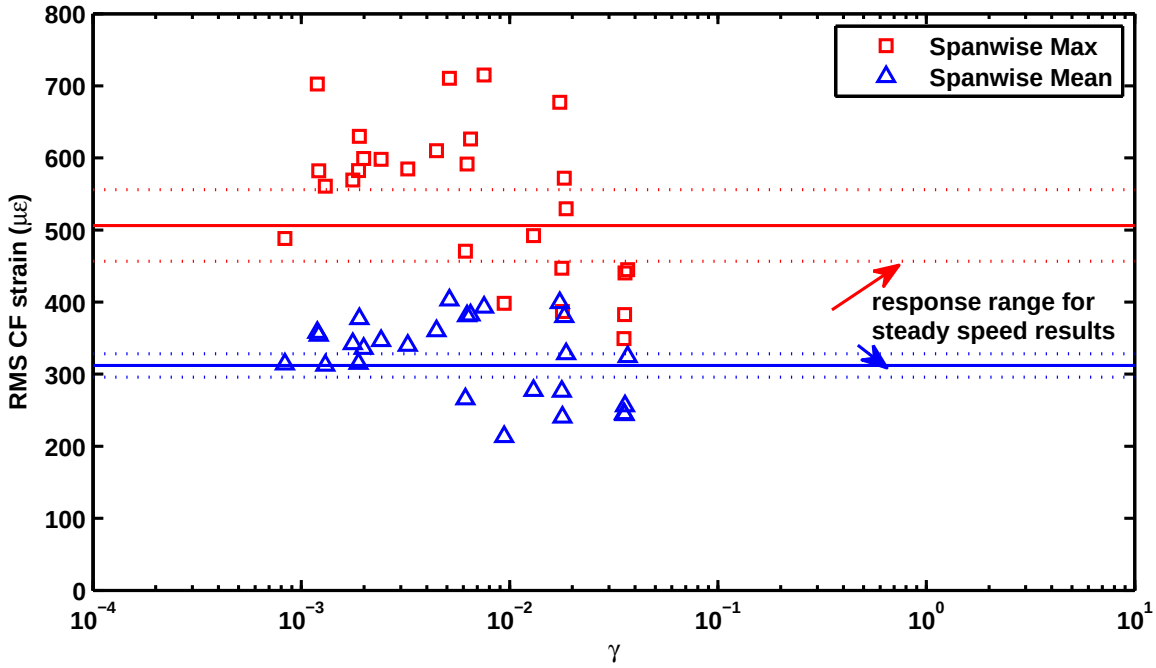

Figure 8-19: Strain ($\mu\varepsilon$) vs. γ around $2.3m/s$

8.5 Chapter Summary

This chapter showed that even in a time-varying flow, flexible cylinders are still susceptible to VIV and this can be as damaging as the VIV experienced in steady flows. Note, that in an unsteady flow even though the vibrations will only last for a short time (while the reduced velocity is in the synchronization region) the response can easily be larger than what is observed under steady flows. This happens because in a ramp test the pipe traverses the entire synchronization region and is 'free' to choose the conditions the will result in the largest VIV response.

The unsteady flow parameter, γ, which was introduced in this thesis was shown to be useful in predicting whether VIV will be an issue in time-varying flows. The reader is reminded that the physical meaning of this dimensionless parameter is simply the change in current or towing speed in one cycle of cylinder vibration.

$$\gamma = \frac{\frac{\partial U}{\partial t}}{U} T_n$$

Based on the experimental results presented in this chapter, a preliminary classification of the VIV response of low mass ratio flexible cylinders in time-varying flows based on the γ value would be:

- **For $\gamma < 0.02$ VIV very similar to what is observed in steady speed tests**

  The results suggest that unsteady tests with corresponding γ values smaller than 0.02 will show a response that is similar both in magnitude and responding mode number to the response observed in conventional VIV tests. This was not apparent *a priori* but is a reasonable conclusion seeing how a γ value of 0.02 corresponds to a speed change only of 2% per cycle.

- **For $0.02 < \gamma < 0.1$ VIV may be observed but response is not always similar to steady speed VIV** Tests with γ values corresponding to $0.02-0.1$ show much more erratic behavior and the response often did not agree well with the steady speed results. This is most likely related to structure's response time

and the limited duration of the excitation force. This is best explained with an example: imagine a ramp with a γ value of 0.1 which means that in every vibration cycle the speed is changing by 10% and it would only take 4 cycles to completely traverse the V_r-bandwidth or synchronization region.

- **And for $\gamma > 0.1$ No observable VIV** On ramps with γ values larger than 0.1 it was extremely hard to even identify whether the cylinder vibrated for a single cycle and as such the result extraction process is not possible.

Chapter 9

Results From the Time-Varying $38m$ Shell Tests

This chapter presents the results from the time-varying flow tests conducted while carrying out the test matrix for the $38m$ SHELL tests at MARINTEK. The SHELL ramps tests were experiments of opportunity added to the test matrix at the last minute. The SHELL tests predated the SJTU tests and, at the time, it was not known what the test range of accelerations should be. A few values were chosen to see what might be learned. Nonetheless, the SHELL ramp tests are extremely interesting because they were performed at a very large ocean basin under moderate accelerations which meant that during a single test many modes could be excited consecutively while the towing speed was continuously changing.

The main objectives of this chapter are:

- To demonstrate that the γ dependence that was identified in the SJTU data is not unique to that specific situation but instead it is a general property of low mass ratio cylinders vibrating in unsteady flows. This is done by demonstrating how the unsteady flow parameter, γ, can be used to analyze 'ramp data' from an entirely different dataset performed at a very different experimental facility.

- To show that a single 'ramp test' can provide similar, if not better, data describing the response of a flexible cylinder undergoing VIV than many constant

speed tests (conventional tests).

- To demonstrate the effects that increasing or decreasing speed (i.e., the sign of $\frac{\partial U}{\partial t}$) can have on the observed VIV response of a flexible cylinder in time-varying flows.

Early on in the thesis, it was stated that one of the motivating reasons for studying VIV in unsteady flows was the desire to improve on current model testing practices by drastically reducing the number of runs necessary to cover a test matrix. This would result in a steep reduction in 'tank time' and associated costs. However, simply performing the experiment faster is meaningless unless it can be shown that the 'ramp tests' are also capable of meeting the test objectives. A free vibration VIV test may have objectives that vary based on the specific problems being investigated (e.g., evaluation of suppression devices, buoyancy distribution, etc.) but it invariably involves measuring the cylinder's response at many different towing speeds. For rigid elastically mounted cylinders this is done in order to span the entire V_r range (i.e., synchronization region) whereas on flexible cylinders one wants to characterize the response of many different modes over a range of speeds. This chapter shows some results from 'ramp tests' that will support the claim that not only can 'ramp tests' be used to meet the typical objectives of a VIV model test but they can go one step further by actually obtaining the response information at the most damaging external conditions that are easy to miss on a grid-like test matrix used in conventional tests.

9.1 A Ramp From the SHELL Dataset

Figure 9-1 shows the towing speed as a function of time for a ramp test on the $30mm$ diameter cylinder (Pipe 2). The acceleration was held constant until the carriage reached a speed of $1.4m/s$ at which point the carriage started decelerating. The same figure has superimposed on it, lines showing the speeds which we would expect to excite modes 1 through 8, assuming a 'Strouhal' value of 0.15. Each towing speed and mode number combination has an associated γ value based on the natural period

of the corresponding mode and the acceleration which is common to all potentially excited modes in this specific ramp test.

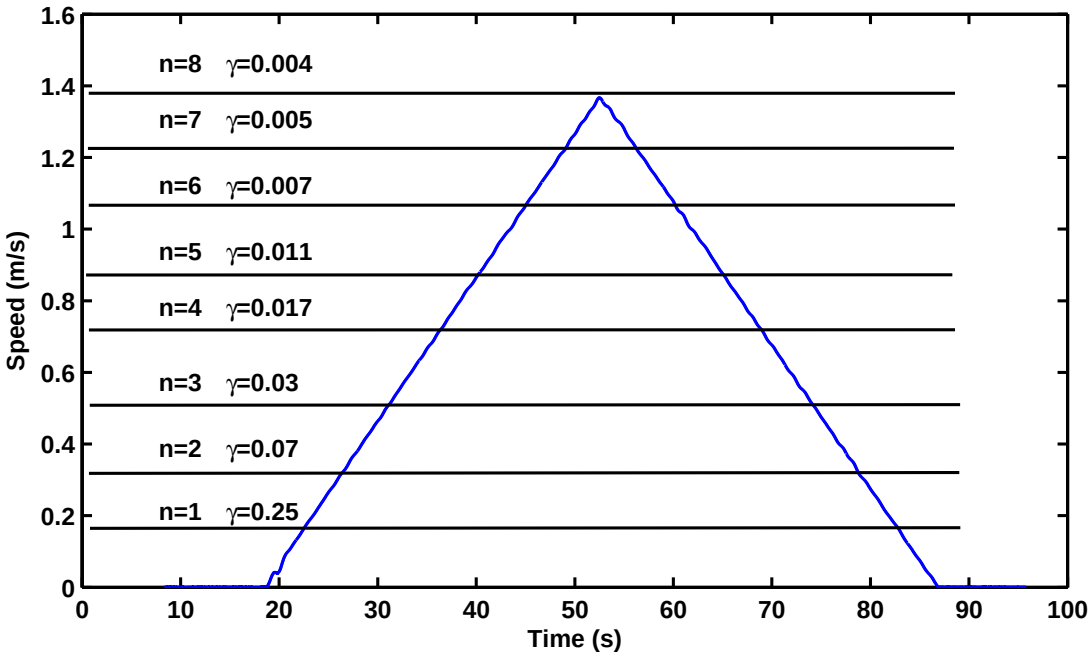

Figure 9-1: Towing speed vs. time ('ramp test': Test 3023)

Based on the results from the previous chapter, one would expect modes with an associated γ value of 0.02 or smaller to be excited. Hence, one would expect to see the cylinder responding in modes 4 or higher starting around the 35^{th} second. Mode 3 has a γ value of approximately 0.03 which is in the range where the response can be erratic; sometimes it might be excited but other times it might not. Modes 1 and 2 have γ values of 0.25 and 0.07 respectively, which implies that the speed will be changing by 25% or 7% every cycle; which is quite high and thus modes 1 and 2 are unlikely to be excited.

Figure 9-2 shows how the response frequency, measured from all CF curvature sensors, varied during the ramp. The 1X CF frequency is clearly visible in dark red color, and the general trend of increasing and decreasing frequency is entirely consistent with the increasing and decreasing towing speed. On the same plot the 3X and 5X response frequencies can be seen to have a slope 3 or 5 times larger than the slope of the 1X response frequency.

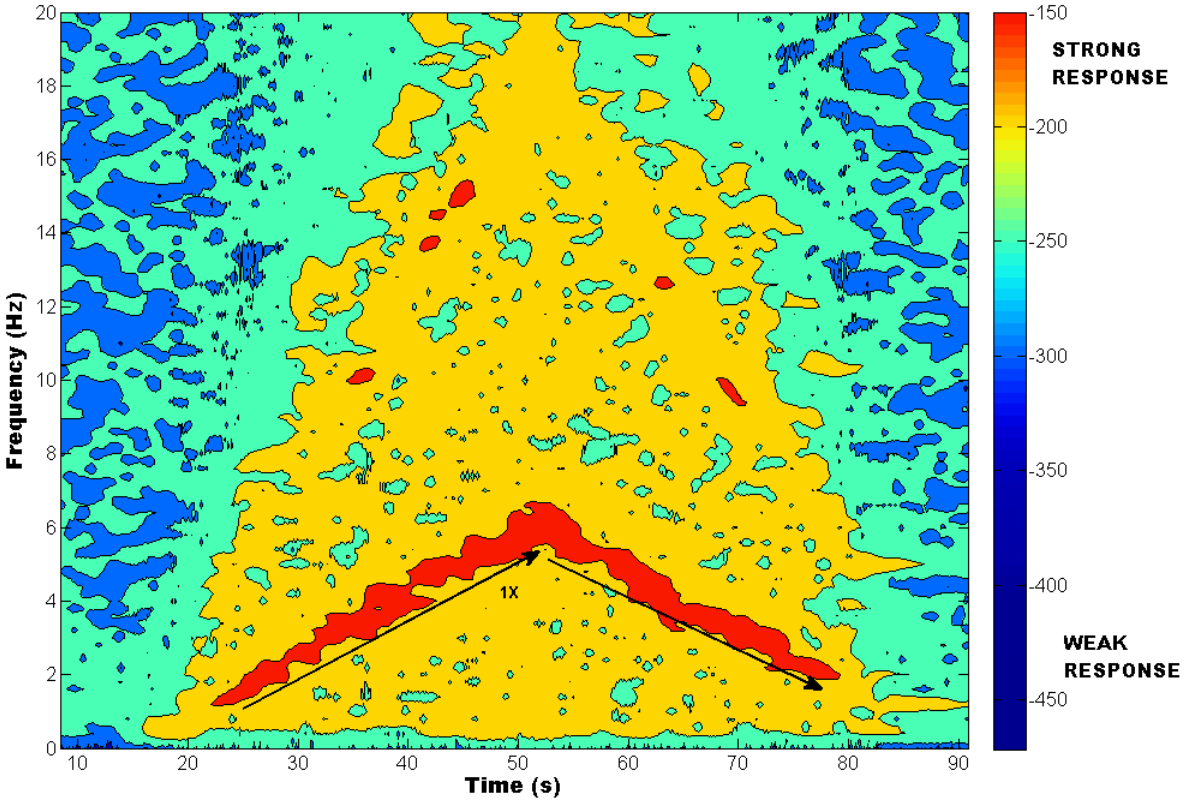

Figure 9-2: Response Frequency (Hz) vs. Time (s)

Figure 9-3 shows the spanwise averaged CF RMS curvature as a function time for the same test. All RMS calculations are actually 'moving RMS' calculations using a time window corresponding to an estimated 10 cycles (see Equation 8.2). Since the vortex shedding frequency and presumably the response frequency depend on the flow speed, one vortex shedding period will be much longer at the beginning of the ramp than at the peak flow speed. Therefore, even though size of the time window that was used for all operators (moving mean, moving RMS, etc.) is of a fixed length in terms of cycles its actual duration when measured in seconds (or discrete samples) at low speeds will be much larger than the time window at high speeds.

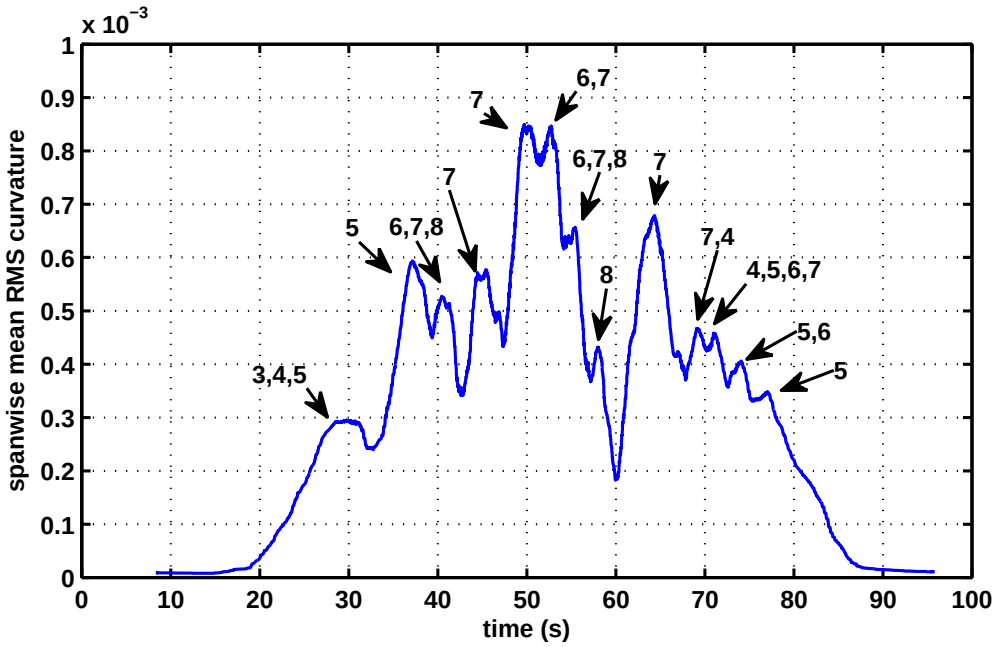

Figure 9-3: Moving RMS curvature vs. Time (Test 3023)

The local maxima that are easily identifiable on the plotted curvature signal are indicators of VIV lock-in at different modes. In order to understand why this is so, it would be useful to describe and explain some of the main features of Figure 9-3 and how these relate to cylinder response:

The overall trend of increasing (and later decreasing) curvature is associated with the general vortex shedding off of the cylinder which induces forces along its length. As the towing speed or the incident current increases, there is more energy in the flow and therefore the induced strains are larger.

Only when the flow speed is within the narrow band necessary to excite a mode will lock-in occur (assuming the speed doesn't change too rapidly). At lock-in the response amplitudes will be larger and approaching their limit cycles, these larger amplitudes induce considerably larger curvatures compared to those induced outside the lock-in band and are responsible for the local maxima clearly visible in Figure 9-3.

Therefore the local maxima are primarily associated with VIV lock-in, as such the local maxima indicate the time(s) when the largest response occurred. The increasing

and decreasing curvature around each one the identified maxima is consistent with traversing the synchronization region of a given mode, this is readily visible for the maxima labeled $n = 5$.

The double peak at 50 seconds is most likely due to a temporary change in the response behavior: while the cylinder is vibrating at mode 7, the second peak is due to a return of the 6^{th} mode that was absent at the first peak. Appendix A shows an example of this.

Figure 9-4 shows the reconstructed mode weights as function of time which should reinforce the above observations. The plot shows the contributions of modes 3 through 8 to the total structural response during this ramp test. The 3^{rd} mode is the first to show a significant contribution, and this is quickly followed by the 4^{th} and 5^{th} modes and later by the 6^{th} and 7^{th} modes. The mode 8 response between 40 and 50 seconds is a 'non-resonant' contribution to the total structural response that at the time is being dominated by modes 6 and 7. The 8^{th} mode doesn't become dominant until the 57^{th} second until the 60^{th} second at which point the 7^{th} mode is contributing as a non-resonant mode.

It is important to note that care should be taken when choosing which signals to plot as a function of time, because on flexible cylinders with many distributed sensors there is always the chance that a randomly chosen sensor is located close to a specific mode's nodal point (node) which will have very small motions and strains that could easily be overlooked. A safer approach that was used in this thesis, would be to use spanwise averaged quantities or at the very least several time traces from neighboring sensors. Once the local maxima have been identified it is fairly straightforward to isolate a small portion of the time history corresponding to that maxima and to proceed with modal reconstructions, drag calculations and any other analysis one would perform on the data collected during a VIV test. The entire process is summarized in the flowchart in Figure 9-5.

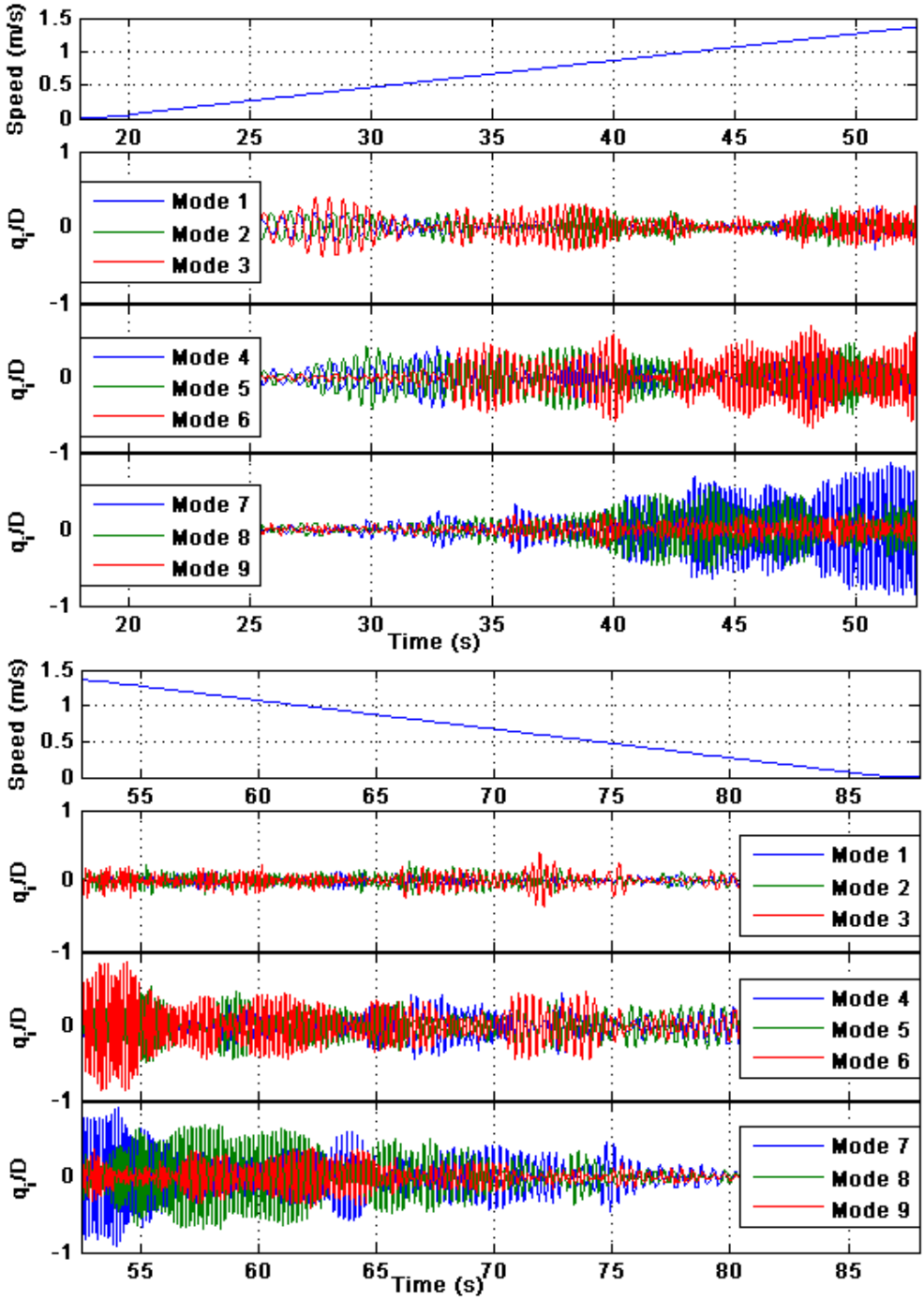

Figure 9-4: Mode Weights, q_i/D, as a function of time for Test 3023

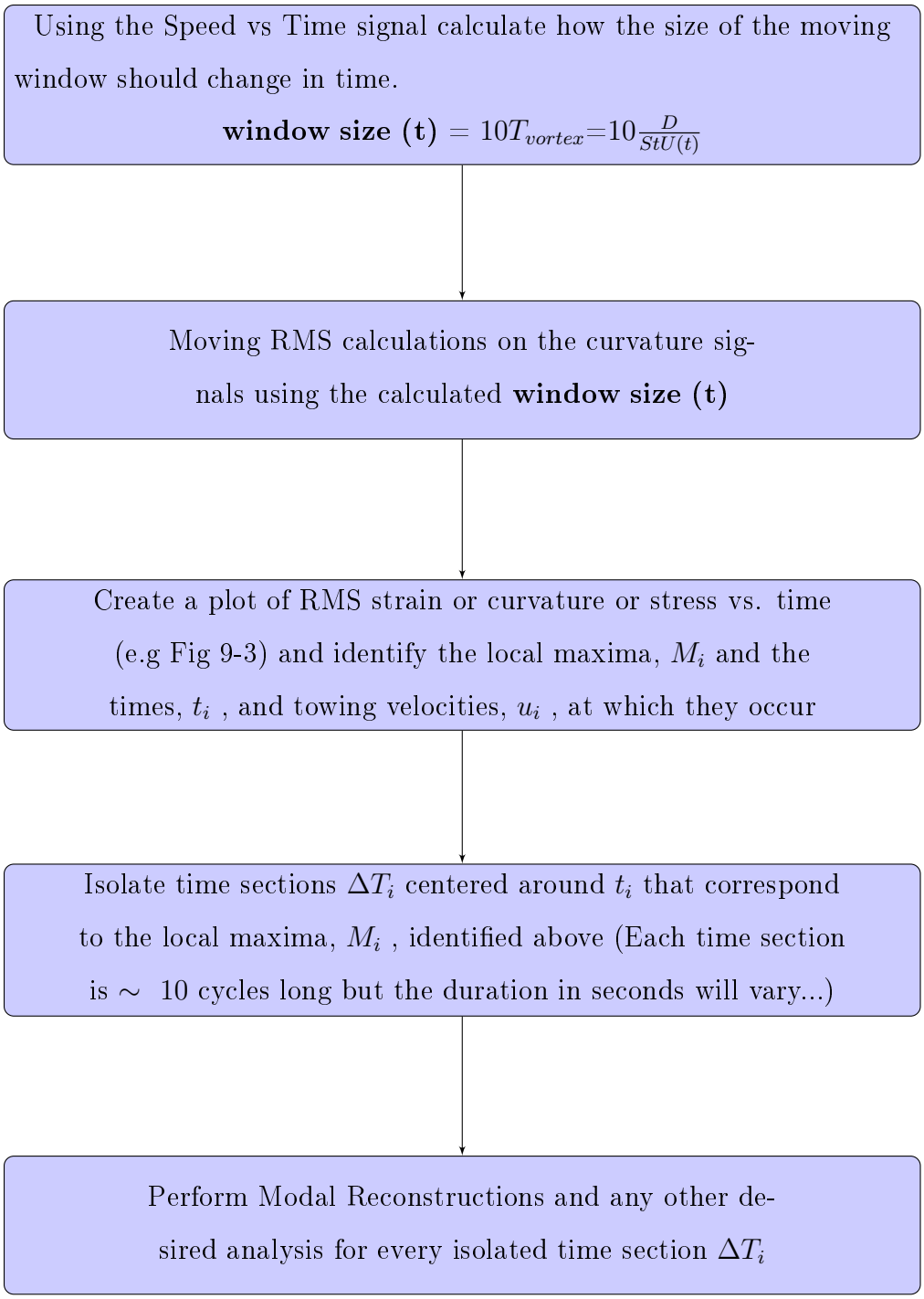

Figure 9-5: Flow chart summarizing data analysis procedure for each 'ramp test'. Procedure was used to obtain datapoints shown in Figures 9-6 through 9-10

Figures 9-6 & 9-7 compare the spanwise variation of the response observed during a ramp test with the response during a steady speed test. This is done to confirm that the two types of responses (i.e. steady speed test and ramp test) are in fact similar and it is not simply by chance that the spatial maxima and mean values agree since it is well known that more than one type of distribution (here spatial) can share the same maximum and mean values. Furthermore, because the response at steady speeds is not in fact stationary but varies in time (discussed in Appendix A) instead of presenting a single result for the response, the author believes that presenting an envelope of all possible response states is indeed much more representative of the VIV response in steady flows.

Figure 9-6 compares the ramp response at $\sim$ 55.4 seconds with the response envelope from the conventional Test 3009 which responded in the same mode number. The upper plot shows the CF RMS response amplitude (A/D) along the cylinder whereas the lower plot compares the CF RMS curvatures. The extracted ramp result is shown with a solid black and is based on a reconstruction using signals that lasted $\sim$ 10 cycles. Similarly, the response envelope for the conventional speed tests is created after processing the test data using a similar 10 cycle moving operator. The shaded blue regions show the upper and lower limits of the cylinder's RMS response during the constant speed Test 3009, whereas the solid red line is the RMS response observed if the entire time signal was used.

In a similar manner, Figure 9-7 compares the ramp result at approximately 74.1 seconds with the response envelopes from the conventional Test 3003, at the same speed of $0.5m/s$.

In both comparisons shown, (i.e., Figures 9-6 & 9-7) the ramp extracted results are in good agreement with the steady flow results. In both cases, the maximum CF amplitude and curvature along the span are larger than those for the steady speed tests if the analysis had been performed on the entire time signal (solid red lines).

Figures 9-8 through 9-10 compare all the results extracted from two almost identical ramp tests with the $30mm$ diameter cylinder. The two ramp tests, #3023 and #3031, had identical acceleration and deceleration rates and maximum speeds. The

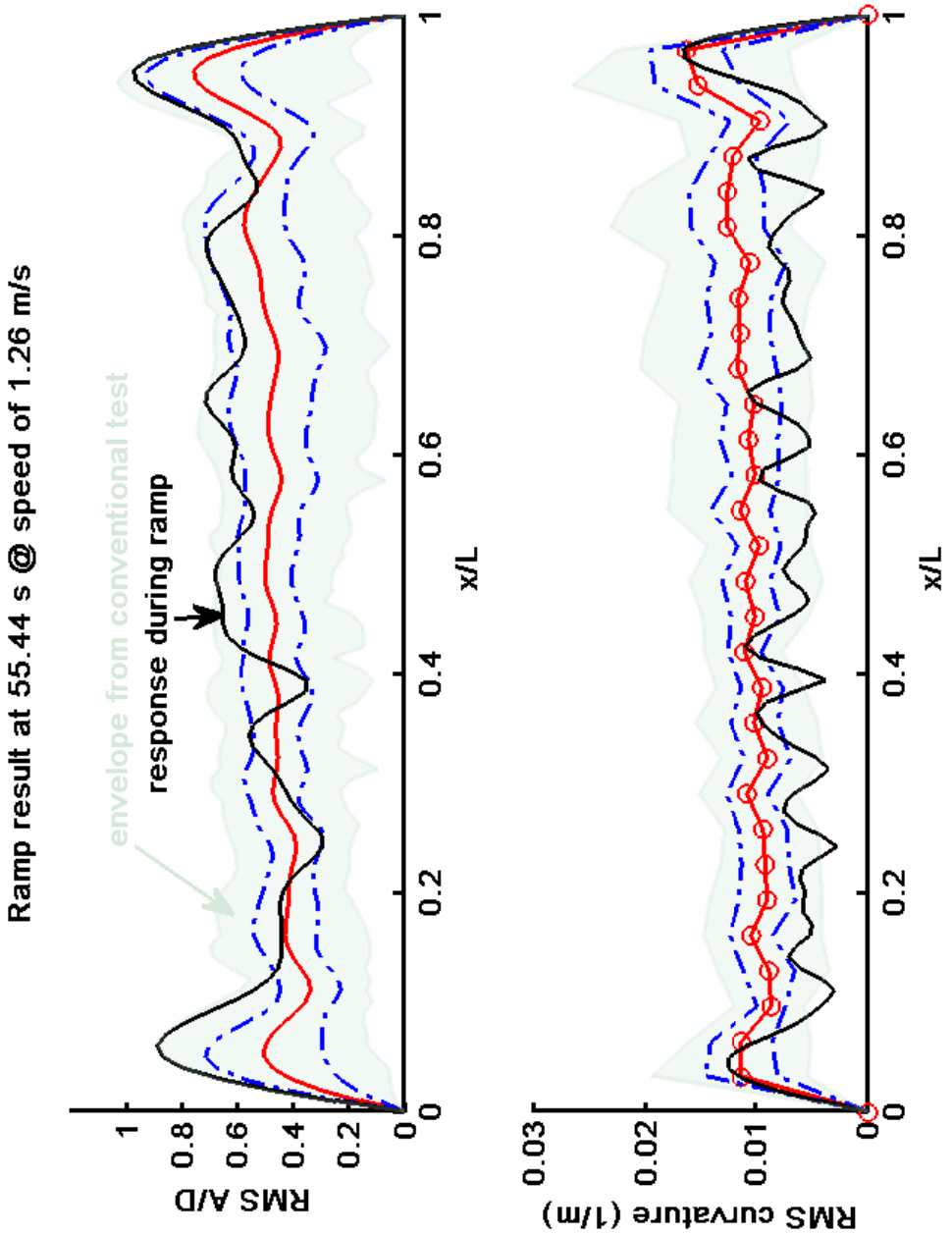

Figure 9-6: Comparison of ramp extracted result with RMS response envelope from a steady flow. **Green-gray:** the RMS response envelope for the conventional Test 3009, **Solid Red:** The RMS response for the conv. test using the whole time series, **Dashed blue line:** +- 1 stand. deviation around the RMS response (conv. test). **Solid black:** The ramp result from ramp 3023 at a $\gamma \sim 0.005$ (or 0.5% variation per cycle)

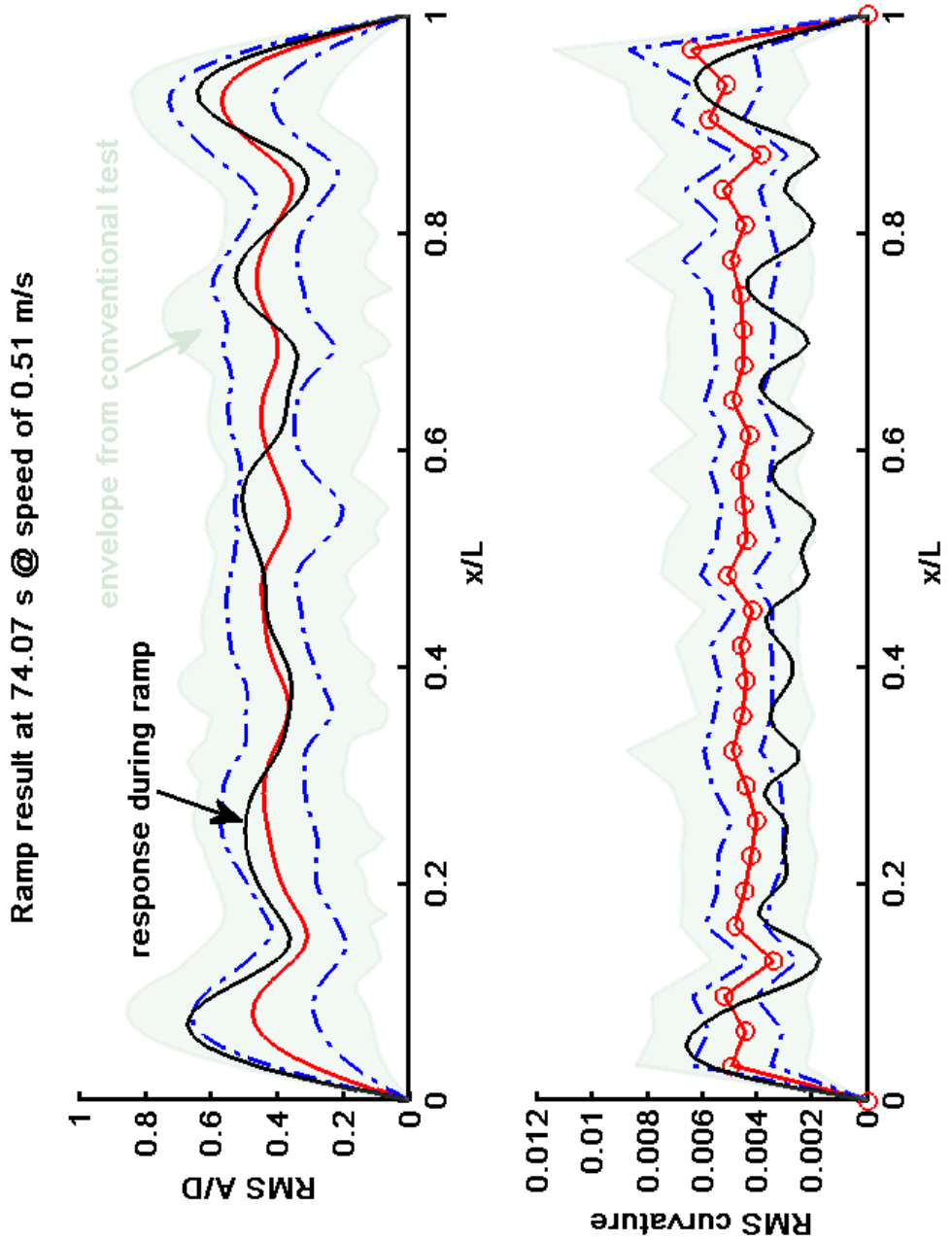

Figure 9-7: Comparison of ramp extracted result with RMS response envelope from a steady flow. **Green-gray:** the RMS response envelope for the conventional Test 3003, **Solid Red:** The RMS response for the conv. test using the whole time section, **Dashed blue line:** +- 1 stand. deviation around the RMS response (conv. test). **Solid black:** The ramp result from ramp 3023 at a $\gamma \sim 0.03$ (or 3% variation per cycle)

only difference being the magnitude of the initially applied pretension. Figure 9-8 reveals the difference in the mean tensions during these two ramp and compares these tensions with the values recorder during the steady flow (conventional) tests. The examination of the following figures will reveal what effect this had on the extracted results.

Figure 9-9 compares the CF spanwise mean and maximum response amplitudes as a function of towing speed for the ramp tests and the conventional tests. It is interesting to note that in most cases the response amplitude from the ramp tests is larger than that of the conventional tests at similar towing speeds. This can be explained because the data extracted from the ramp tests essentially correspond to the velocities associated with the ideal reduced velocity for maximum response for a given mode (i.e., the 'sweet spot'). This is in contrast to the conventional speed tests which are at specific pre-defined speeds which do not necessarily excite the pipe at the critical reduced velocity since the variability in the dimensionless response frequency (equiv. Strouhal number) makes it impossible to choose such a test matrix *a priori*.

At very low speeds ($\sim 0.4m/s$) the ramp results yield response amplitudes slightly smaller than the conventional tests. This happens because these modes had moderate γ values ~ 0.05 (between 0.07 and 0.03, see Figure 9-1) and examination of the kurtosis for the data extracted suggests a behavior closer to Gaussian excitation (mean values of 2.8, 2.5, 2.4) contrary to most of the other data points that had kurtosis values much closer to sinusoidal excitation (mean values ~ 1.8). This is a further indicator that results extracted at $\gamma \sim 0.05$ can be erratic and should be avoided if possible.

Figure 9-10 compares the CF spanwise mean and maximum RMS curvatures as a function of towing speed for the ramp tests and the conventional tests. Once again, for ramp #3023 the maximum spanwise curvatures are larger than those recorded during the conventional tests. This is entirely consistent with the larger amplitudes shown in Figure 9-9, since:
$\kappa = k^2 A$ where κ is the curvature, k is the wavenumber and A is the response amplitude.

Note how the ramp #3031 results are consistently larger than both the ramp #3023 and the conventional test results. This is due to the smaller initial pretension on the pipe at the beginning of ramp #3031. A smaller pre-tension will result in a lower fundamental frequency $\sqrt{\frac{Tension}{mass}}$ which means that at a given current velocity the excited mode number will be higher than that of a pipe with a larger tension. So even though the amplitudes are similar between the two ramp tests, a higher excited mode number will always result in larger curvature.

Alternatively, the wave propagation speed is $c = \sqrt{\frac{T}{m}}$
And the response frequency is primarily governed by the shedding frequency:

$$2\pi f_{shed} = 2\pi St\frac{U}{D} \approx \omega = ck = c\sqrt{\frac{\kappa}{A}}$$

Which can be rewritten as $\kappa = \frac{\omega^2}{c^2}A$ and it can easily be shown that a cylinder with a low wave propagation speed, c, will have a larger curvature, κ, than a cylinder with a high wave propagation speed at the same response amplitude, A and same frequency ω or towing speed, U.

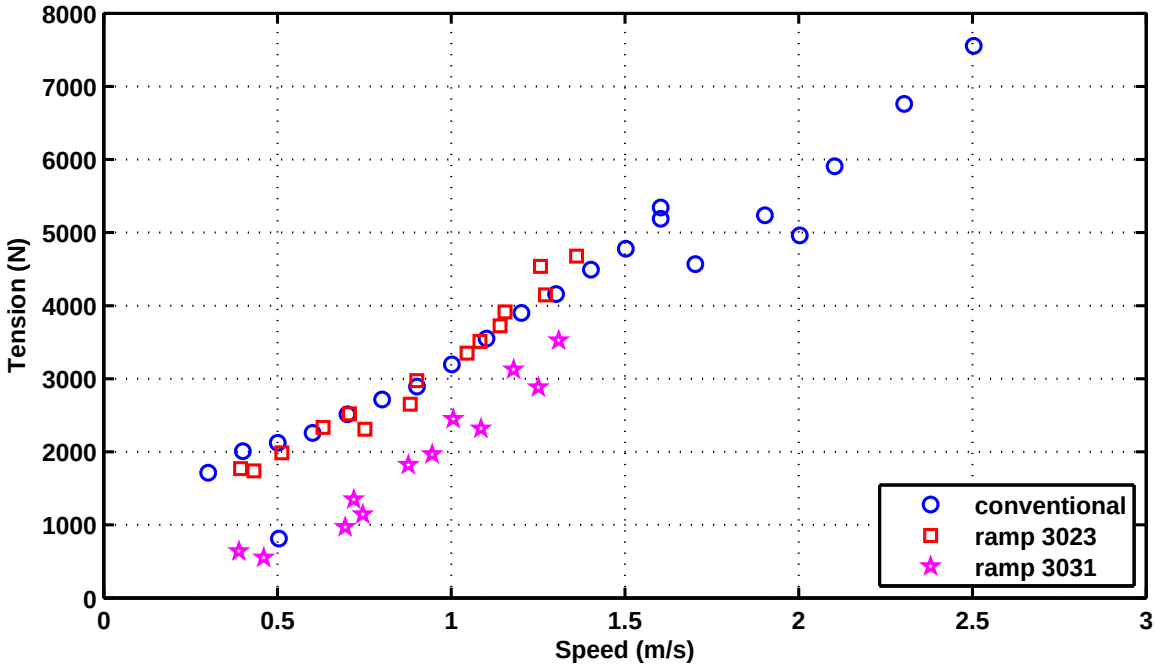

Figure 9-8: Tension vs. Speed for conventional and ramp tests (Pipe 2)

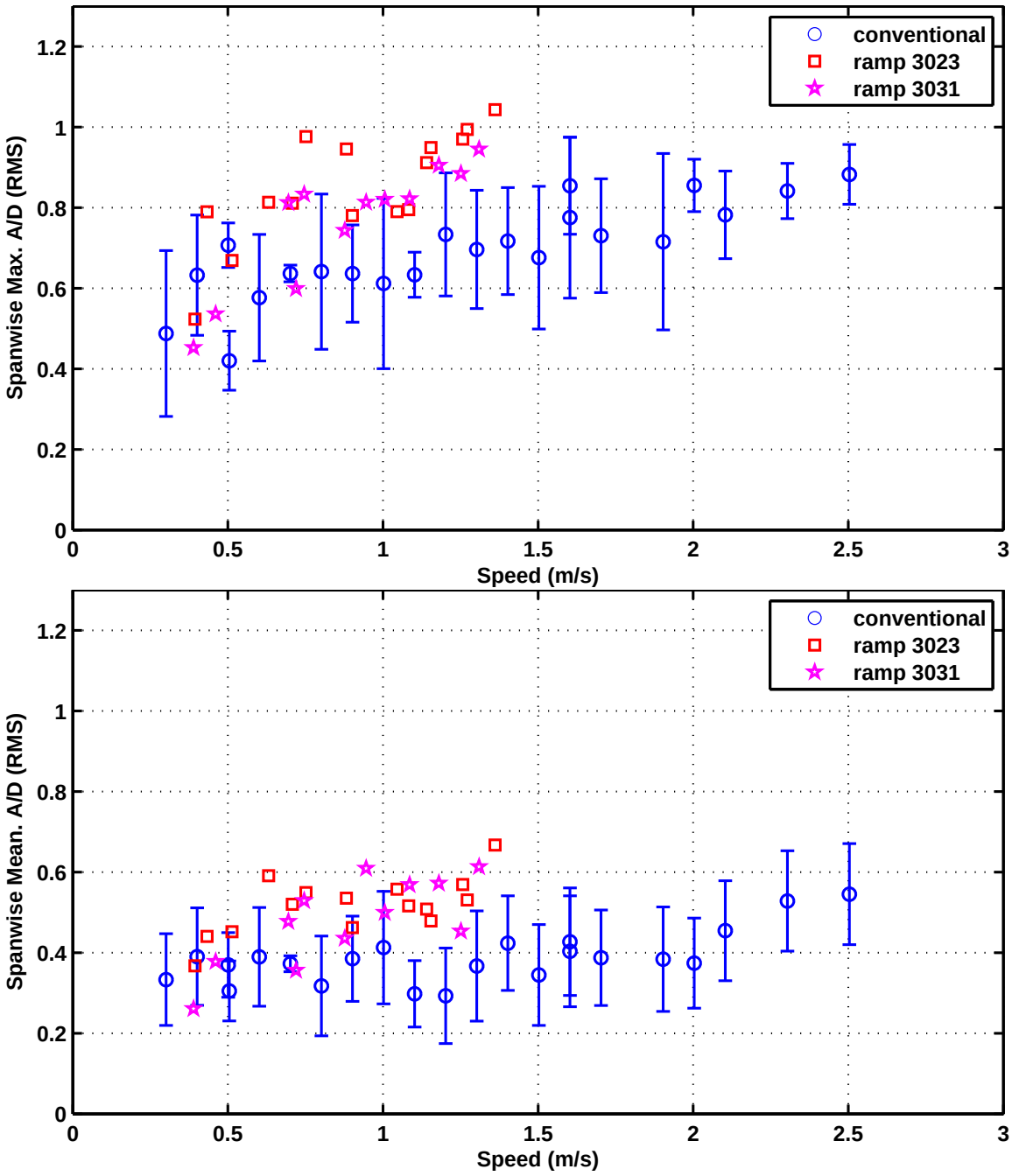

Figure 9-9: CF Response amplitude vs. Towing speed for conventional and ramp tests (Pipe 2)

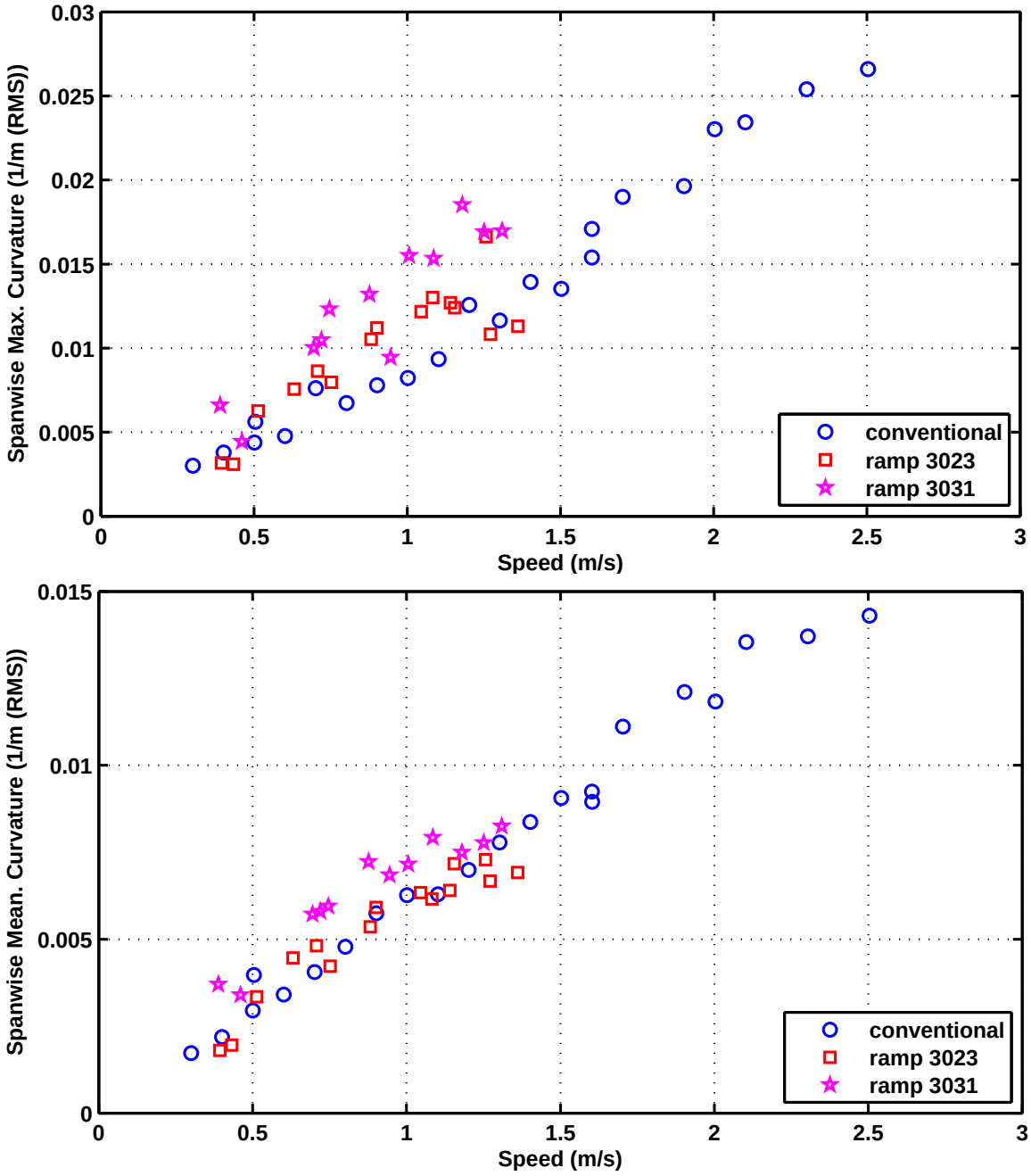

Figure 9-10: CF Curvature vs. Towing speed for conventional and ramp tests (Pipe 2)

9.2 Effects of Increasing or Decreasing Speed on the Response of Flexible Cylinders

The final pieces of evidence that will be presented to support the claim that lock-in is possible even in time varying flows comes from ramp tests performed using the $12mm$ diameter cylinder. Because of its smaller size compared to the $30mm$ and $80mm$ cylinders it will respond at much higher mode numbers. Since the cylinder is responding at much higher mode numbers, mode overlap becomes increasingly important and is believed to be responsible for the interesting phenomena observed. Namely, that the cylinder shows a distinct preference to respond at a lower mode number when the flow speed is increasing slowly and a preference to respond at a higher mode number when the speed is decreasing when compared to the response observed during steady speed test.

Figures 9-11 through 9-14 show 4 different ramp tests #2117, #2118, #2129 and #2130 that will be the main topic of discussion in this section. The four ramps shown covered a large range of velocities and both positive and negative accelerations. The figures include estimates of the γ parameter at certain speeds that have been calculated after approximating: $T_n = T_{vortex}$ and $St = 0.16$ which leads to:

$$\gamma_{estimate} = \frac{\frac{dU}{dt}}{U} T_n \approx \frac{\frac{dU}{dt}}{U} T_{vortex} = \frac{dU}{dt}\frac{D}{StU^2} = \frac{\frac{dU}{dt}}{U^2}\frac{1}{13.33}$$

Based on these calculations, in ramp #2118 one would not expect to see much, if any, response at speeds smaller than $0.5m/s$. For ramps #2129 and #2130 one would not expect to see a significant response at speeds lower than $1m/s$. At speeds higher than these one would expect to see considerable response due to VIV that is qualitatively very similar to what would be observed in a steady speed test.

In every one of the ramps shown, the local maxima in the moving RMS curvature signals (lower plots) indicate instances in time when the pipe locked-in. Time sections that are approximately 10 cycles in duration are then isolated for every one of these time instances, and subsequent analysis is performed on each one of the isolated short

time sections.

The keen observer will notice that these local maxima also appear in the 'steady' portions of the ramps, a nice example of this is in Figure 9-14 between 43 and 47 seconds. When these local maxima appear during a steady flow (constant speed) they are often due to mode switching and are a result of the variability in VIV response observed even when the flow speed is constant. This is discussed in Appendix A.

Figure 9-15 compares the results that were extracted from the time-varying portions of these four ramps and compares them with the conventional test results. The plot shows the spanwise averaged RMS curvature versus towing speed. Unlike the first example shown in Section 9.1 which only covered modes $3 \sim 8$, these four ramp tests, which are primarily exciting higher modes $10 \sim 25$, clearly demonstrated the difference that increasing (accelerating) and decreasing (decelerating) speed have on the observed VIV response at the same speed.

There is a clear difference in the observed response depending on whether the flow speed was increasing or decreasing. The difference is believed to be the result of mode overlap and VIV lock-in: When the towing speed is continuously changing, the pipe 'lags behind' responding in the last excited mode for as long as possible. This means that when the speed is increasing the response 'lags' in a lower mode than what would be excited during a constant speed test. Similarly, when the speed is decreasing the observed response tends to 'lag behind' in a higher mode than a conventional speed test.

This difference in responding mode number between a conventional test and a ramp test is shown Figure 9-15 which has a number next to every datapoint shown. The numbers correspond to the dominant mode identified through modal reconstructions on the ramp extracted data (or time series) and are color coded to match the ramp or test they refer to.

For the sake of clarity the figure does not list the γ values for each one of the extracted results. Figures 9-11 through 9-14 showed that these were relatively large at the beginning and ending of a ramp and can be very small ($\gamma \sim 0.0025$) near the ramp's peak. This, in turn, is responsible for the larger difference between ramp re-

sults and conventional tests at the beginning and ending of the ramps when compared to the difference between the ramp results and conventional tests for data extracted near the peak of the ramp where the γ values were very small. This is clearly seen with ramps #2117 and #2118 and is not surprising since a small γ value implies a very small change in velocity for every cycle of vibration as such the test is essentially quasi-steady and the results should be very close to the conventional tests or steady flow results.

The implication of this observed phenomenon when performing model testing using 'ramp tests' is that, if the towing velocities are large and high mode numbers are excited, then there will be a systematic bias in comparisons of stresses, strains or curvatures between conventional tests and ramp tests.

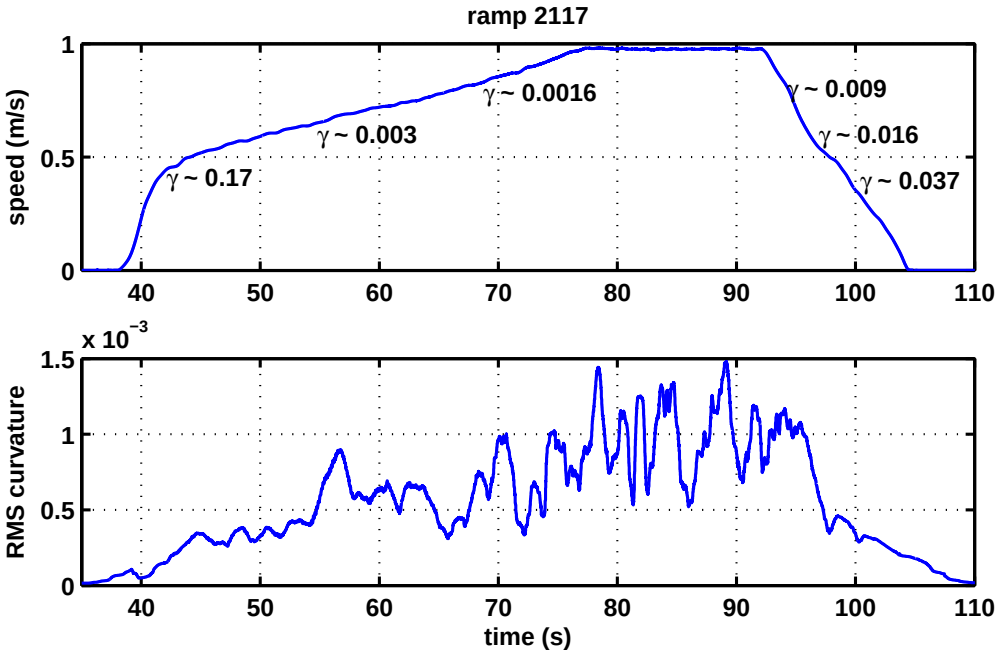

Figure 9-11: Ramp test #2117 with the 12mm diameter cylinder

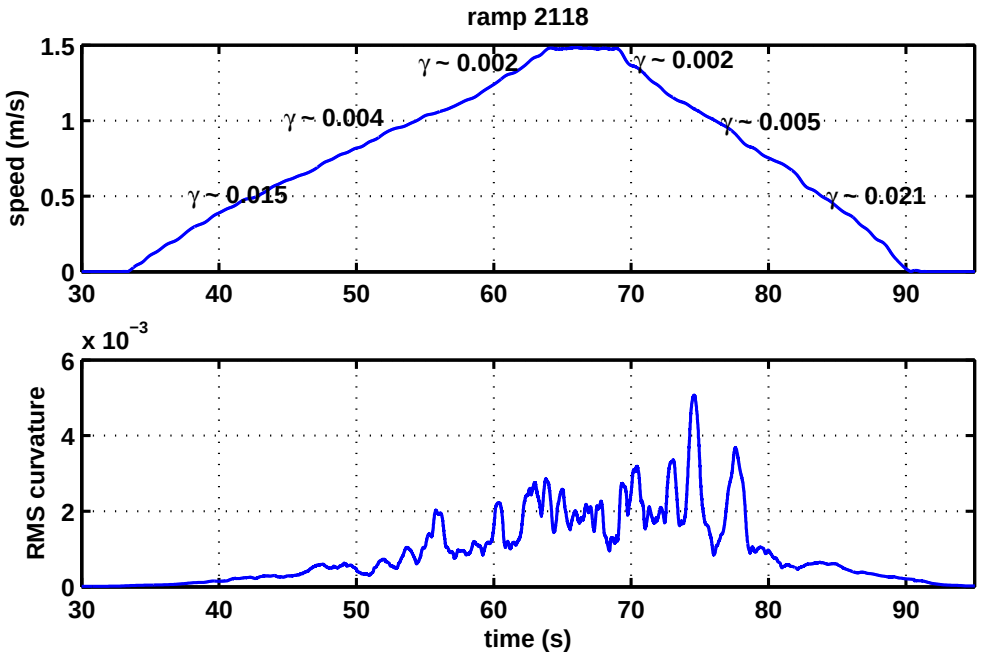

Figure 9-12: Ramp test #2118 with the 12mm diameter cylinder

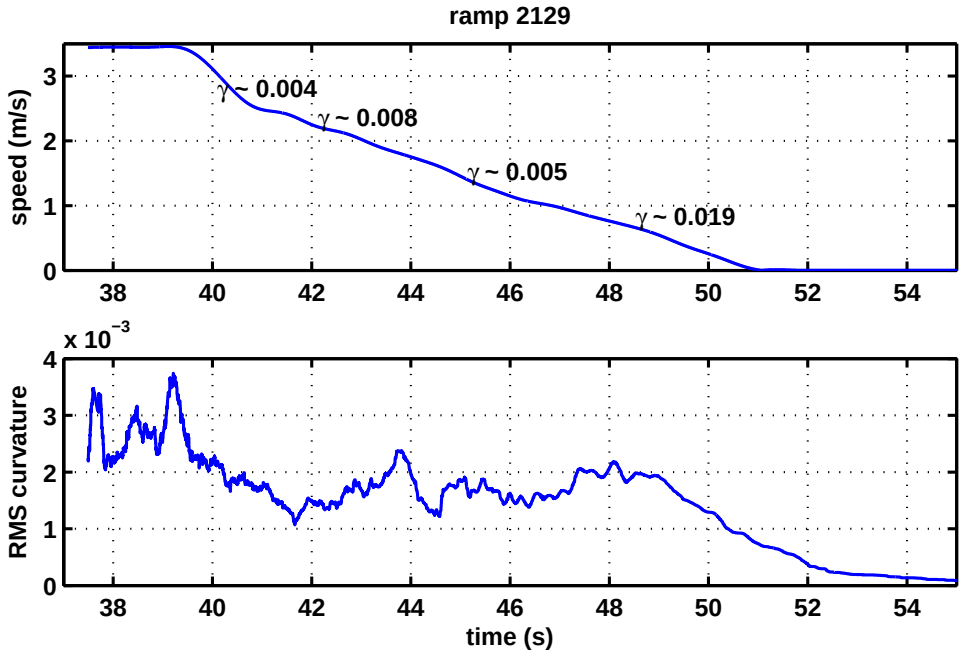

Figure 9-13: Ramp test #2129 with the 12mm diameter cylinder

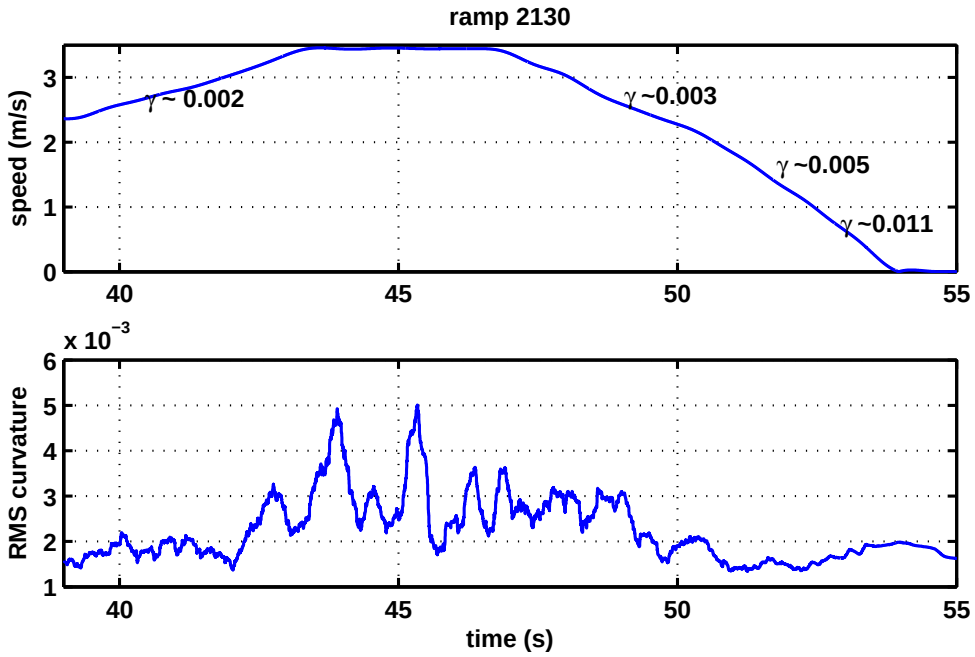

Figure 9-14: Ramp test #2130 with the 12mm diameter cylinder

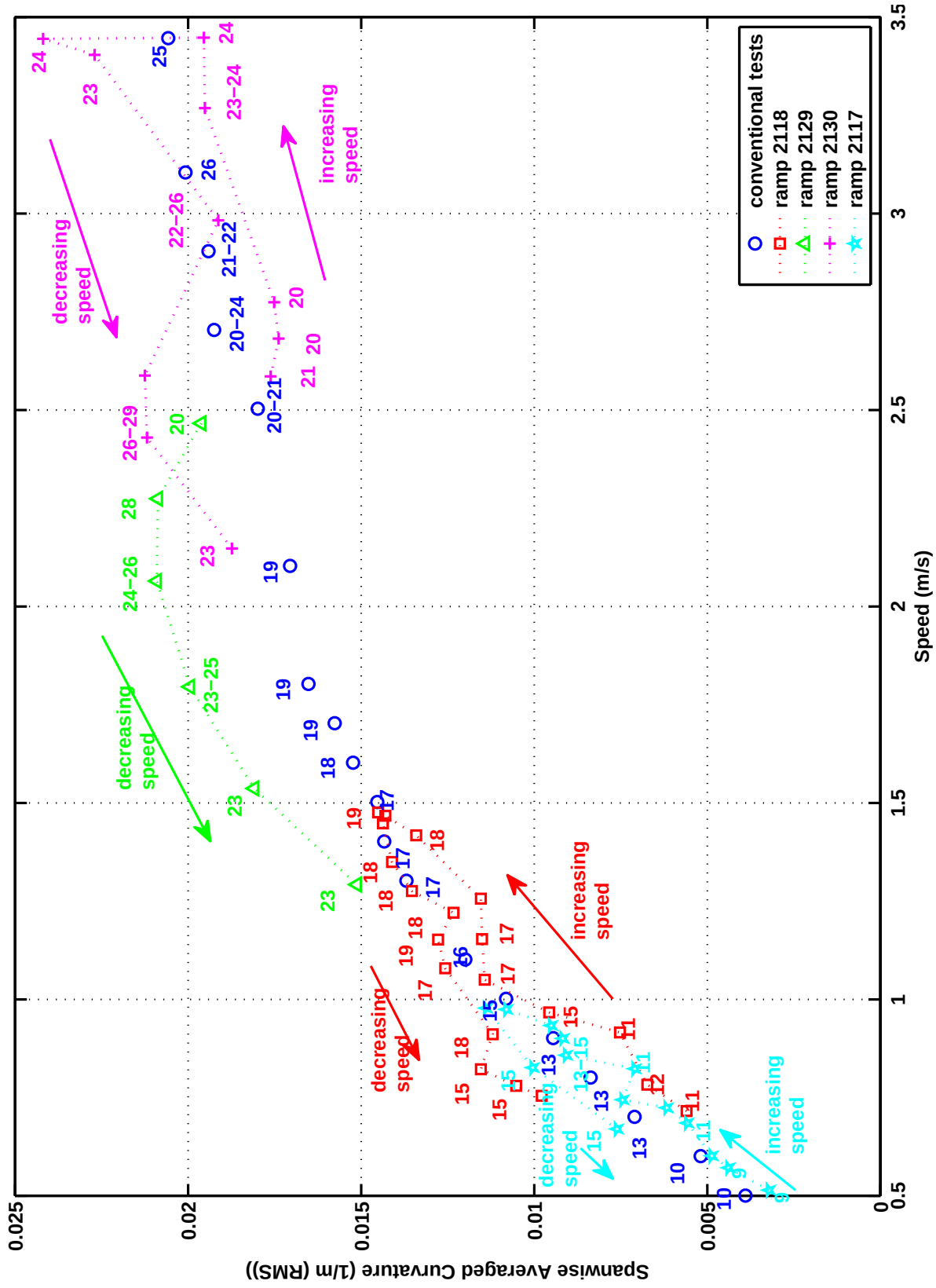

Figure 9-15: Comparison of ramp tests with conventional tests for the 12mm diameter cylinder (Pipe 1)

9.3 Chapter Summary

This chapter demonstrated that the γ dependence that was identified in the SJTU data is not unique to those specific tests but instead it is a general property of vibrating, low mass ratio, cylinders in time-varying flows. This was done by demonstrating how the unsteady flow parameter, γ, can be used to analyze 'ramp data' from an entirely different dataset performed at a different experimental facility with three cylinders that were much longer than what was used at SJTU.

It was shown that a single 'ramp test' can provide similar, if not better, data describing the response of a flexible cylinder undergoing VIV than what could be collected with many conventional tests at constant towing speeds. When designing a test matrix for the conventional testing of flexible cylinders, one has no other choice but to choose a few speeds and start testing but there is no guarantee that the test points chosen *a priori* will actually correspond to the conditions that will cause the most damaging response (i.e., Vr_{crit} or the 'sweet spot'). This is where a ramp test can prove to be extremely useful; because the towing speed is continuously changing, as long as this change in speed is slow (say $\gamma < 0.02$), the cylinder will 'choose' the speed (or conditions) at which it wants to respond most vigorously. This means that is easy to identify the most damaging current or towing speeds when post processing the results.

Finally, by comparing results from tests on flexible cylinders responding at high mode numbers (10-25) it was possible to reveal the effects that increasing or decreasing speed (i.e. the sign of $\frac{dU}{dt}$) can have on the observed response of a flexible cylinder. It was quite clear that once the cylinder locked-in, it wanted to continue to vibrate at that specific mode for as long as possible. This, in turn, means that the cylinder tends to 'lag behind' in response and the implication is that the cylinder will tend to respond at lower mode numbers when the flow speed is increasing and at higher mode numbers when the flow speed is decreasing when compared to the response in an steady flow. Both situations lead to a 'hysteresis' effect.

Chapter 10

Proposed Method for Model Testing With Ramps of Constant γ

The linearly accelerating and decelerating ramps that were presented in the previous sections all have in common, that the acceleration remains (mostly) constant during the ramping-up and down processes. A constant acceleration test will have very large γ values for the low modes at the beginning of the ramp and very small γ values for the higher modes excited at the peak of the ramp. This means that the response at low mode numbers (if excited) will not be equivalent to response in steady flows and conversely the higher modes will be responding for much longer than is actually necessary to obtain meaningful statistics.

This section will demonstrate what the *speed* vs. *time* profile would look like if one attempted to keep γ constant for every potentially excited mode in a ramp. This will be done by creating an example 'ramp test' that would be capable of capturing the VIV response of multiple modes of the $80mm$ diameter cylinder (Pipe 3) used in the SHELL experiments at MARINTEK.

Table 10.1 lists the natural frequencies and velocities that would excite modes 3 through 10 after assuming a $St = 0.16$. The last row in the table lists the acceleration through each 'target velocity' to ensure that $\gamma \sim 0.02$. This specific value of γ was chosen since the experimental results presented in the previous sections suggest that for γ values smaller than 0.02 the VIV response is very similar to a steady flow test.

Table 10.1: Kinematic Constraints for γ=0.02 ramp

Mode Number (n)	3	4	5	6	7	8	9	10
F_n (Hz)	1.36	1.81	2.27	2.72	3.18	3.65	4.11	4.59
T_n (s)	0.74	0.55	0.44	0.37	0.31	0.27	0.24	0.22
U_{excite} (m/s)	0.68	0.91	1.13	1.36	1.59	1.82	2.06	2.29
Accel for $\gamma = 0.02$ (m/s^2)	0.018	0.033	0.051	0.074	0.101	0.133	0.170	0.211

The information presented in the last two rows of table 10.1 will determine what the *acceleration* vs. *time*, *speed* vs. *time* and *distance traveled* vs. *time* plots will look like. These are shown in Figure 10-1. On the carriage acceleration vs. time plot, the red circles identify the accelerations necessary to excite modes 3 through 10 with a γ value of 0.02. The *speed* vs. *time* plot has a set of red lines superimposed onto it, the intersection of each red line with the green curve represents the expected time at which each mode will be excited. Finally, the last plot of distance traveled vs. time is necessary to ensure that the test being designed can actually 'fit' in the experimental facility in question.

Now that the *speed* vs. *time* profile has been determined, it is interesting to estimate how much time is available for each mode to respond (i.e., the duration of excitation). This can be approximated by assuming that the width of the lock-in band is $\pm 20\%$ of the critical reduced velocity and then examining the appropriate portion of the *speed* vs. *time* plot for each mode of interest.

This is shown in Figure 10-2 for modes 3 and 4, where the dotted lines correspond to the critical reduced velocity and the dash-dot lines form the boundaries of the lock-in bands. In a similar manner, Figure 10-3 shows the duration of the lock-in band for modes 9 and 10. The results are summarized in Table 10.2.

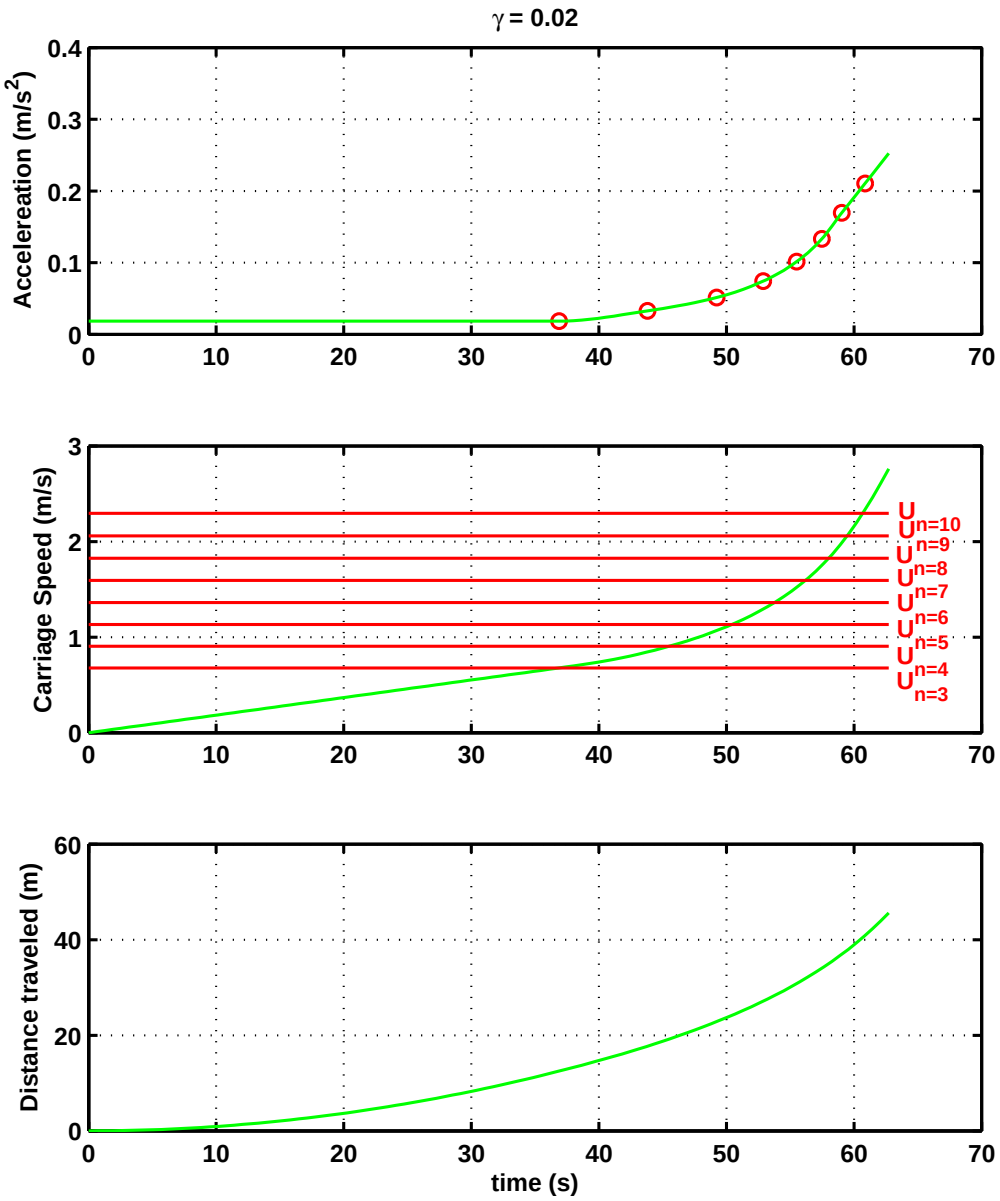

Figure 10-1: Constant $\gamma = 0.02$ test

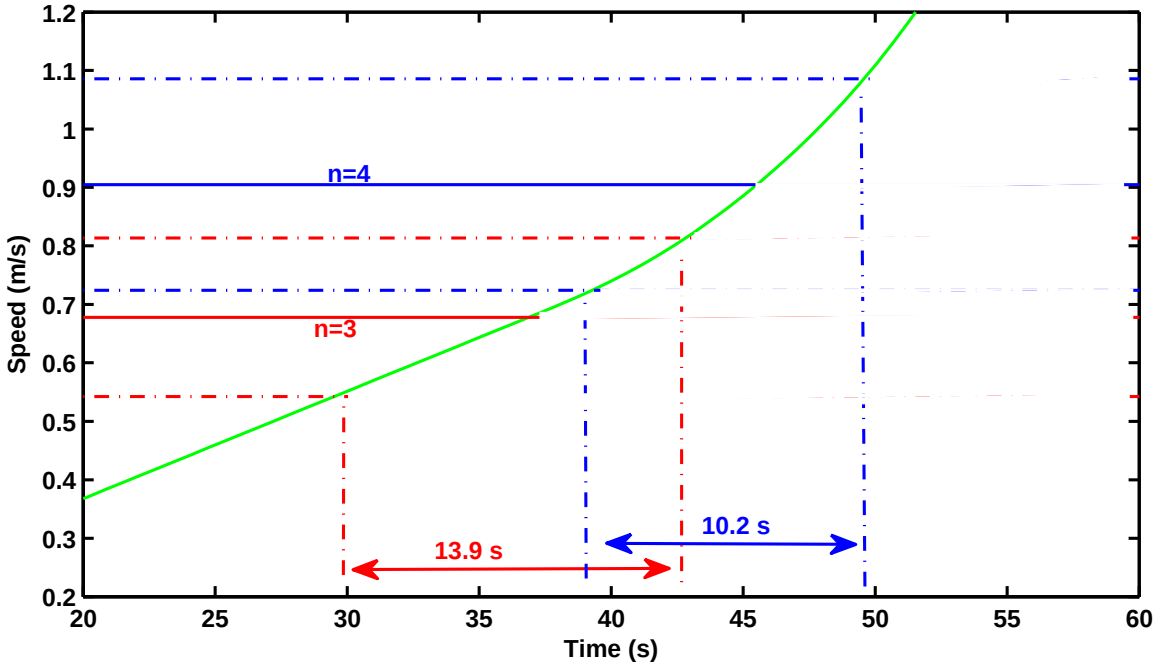

Figure 10-2: Duration of lock-in for modes 3 and 4 and possible overlap

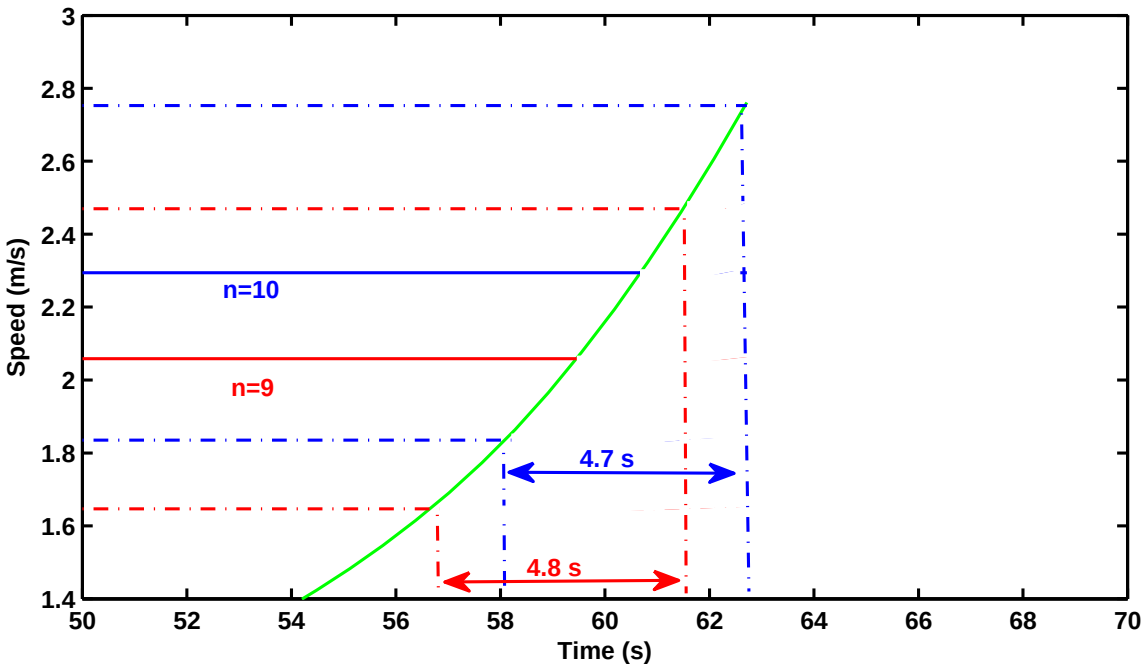

Figure 10-3: Duration of lock-in for modes 9 and 10 and overlap due to closely spaced natural frequencies

Table 10.2: Estimates of Mode Overlap

Mode Number (n)	3	4	5	6	7	8	9	10
F_n (Hz)	1.36	1.81	2.27	2.72	3.18	3.65	4.11	4.59
T_n (s)	0.74	0.55	0.44	0.37	0.31	0.27	0.24	0.22
Lock-in duration (s)	13.9	10.2	8.2	7.1	6.0	5.2	4.8	4.7
Lock-in duration (cycles)	~ 19	~ 19	~ 19	~ 19	~ 19	~ 19	~ 20	~ 20
Overlap with prev. mode(% of time)	N.A.	$\sim 36\%$	$\sim 48\%$	$\sim 62\%$	$\sim 65\%$	$\sim 69\%$	$\sim 73\%$	$\sim 75\%$

Figures 10-2 & 10-3 are instructive because they demonstrate the concept of mode overlap (i.e., the fact that on flexible cylinders the lock-in bands of neighboring modes tend to overlap). This effect becomes more pronounced at higher mode numbers since the separation of natural frequencies of cables or tension dominated beams tends to follow $1/n$. This is shown in the last row of Table 10.2 where the overlap is increasing as the mode number increases. The existence of overlap will tend to lead to mode-switching or mode jumping e.g., there is the possibility that the response will jump from mode 3 to mode 4 even though the speed has not moved out of the mode 3 lock-in band. The exact details of how mode overlap can affect the response of flexible cylinders are not clearly understood and there is definitely room for more research on this topic through carefully designed experiments. Even though the mechanism may not be clearly understood the existence of mode overlap could lead to two possible alternatives:

The first point of view would require the cylinder to pass through every single mode and jump from one mode to the next as soon as the reduced velocity is favorable (i.e., as soon as the overlap starts; in Figure 10-2 this would occur at $\sim 39s$)

The second point of view would require the cylinder to continue to vibrate for as long as possible at the mode number at which it is currently responding or locked-in and only jump to the next mode when it has moved outside the current excitation region (in the example in Figure 10-2 this would occur at $\sim 42.5s$). At high mode

numbers ($n \sim 20$), where the excitation regions of many modes overlap where the natural frequencies are separated by only $\sim$1/20 Hz the 40% wide synchronization region of several modes would almost completely overlap. This scenario would lead to mode-jumping that could easily skip a mode (i.e., jump from mode 20 to 22, without ever responding in mode 21).

Nature is rarely so 'black and white' and reality probably lies somewhere in between the two opposing scenarios presented. The differences in responding mode number during the 'accelerating' and 'decelerating' branches of the ramps shown in Section 10.3 seems to support the second point of view. [1]

The effect of the overlapping lock-in bands and the possibility of mode switching means that even though the lock-in duration has been estimated (listed in Table 10.2) it is highly unlikely that one would ever observe the full 19-20 cycles of vibration at a given mode since at the low modes the response could jump to the next higher one at $\sim 2/3$ (i.e., 1-0.36) of the way through the lock-in band and at higher modes it could jump to the next mode as early as 1/4 (i.e. 1-0.75) through the lock-in band. Recall, that at least 4-5 cycles are necessary for VIV to reach its steady-state or maximum amplitude and by the time one accounts for some lost cycles due to mode-switching it should be clear that at $\gamma \sim$0.02 one would be left with less than 10 cycles to extract the response data of interest.

Now that it has been shown that mode-overlap might prevent one from observing enough cycles to obtain meaningful statistics, one could attempt to design an experiment with a slightly different constraint. Instead of starting the design by specifying a (specific) value for γ, which will be kept constant throughout the test, we could impose a different restriction:

We want to observe a minimum number of cycles within a very small band inside the lock-in region; tightly centered around the critical reduced velocity.

[1] At this point it would be wise to discuss the effects that the cylinder's mass ratio will have on the preceding discussion. Govardhan & Williamson (2002) showed that that the synchronization region of an elastically mounted cylinder tends to increase as the mass ratio decreases until the critical mass ratio of 0.54 is reached at which point the synchronization region extends indefinitely. If the synchronization regions of flexible cylinders are similarly affected by the mass ratio, issues related to mode overlap and mode switching should be more pronounced on flexible cylinders with low mass ratio compared to high mass ratio cylinders.

For example consider the following requirements:

observe at least 10 cycles, within a band $\pm 5\%$ of the critical reduced velocity

These two requirements in association with the initial conditions uniquely define the kinematics and as such the acceleration (and hence γ) with which the carriage should traverse a specific mode will be given by:

$$accel_n = \frac{1.05U_n - 0.95U_n}{10T_n}$$

And the corresponding γ value would be:

$$\gamma_n = \frac{accel_n}{U_{excite\,n}} T_n$$

The acceleration and associated γ values imposed by the above requirements are listed in Table 10.3.

The carriage acceleration, speed and distance traveled vs time for the aforementioned conditions are shown in Figure 10-4. Note that since γ is half as large as the initial example, this test would need to travel a distance twice as large.

Table 10.3: Kinematic Constraints Required to Observe 10 Cycles

Mode Number (n)	3	4	5	6	7	8	9	10
F_n (Hz)	1.36	1.81	2.27	2.72	3.18	3.65	4.11	4.59
T_n (s)	0.74	0.55	0.44	0.37	0.31	0.27	0.24	0.22
U_{excite} (m/s)	0.68	0.91	1.13	1.36	1.59	1.82	2.06	2.29
Accel (m/s^2)	0.009	0.016	0.026	0.037	0.051	0.67	0.085	0.105
γ	0.01	0.01	0.01	0.01	0.01	0.01	0.01	0.01

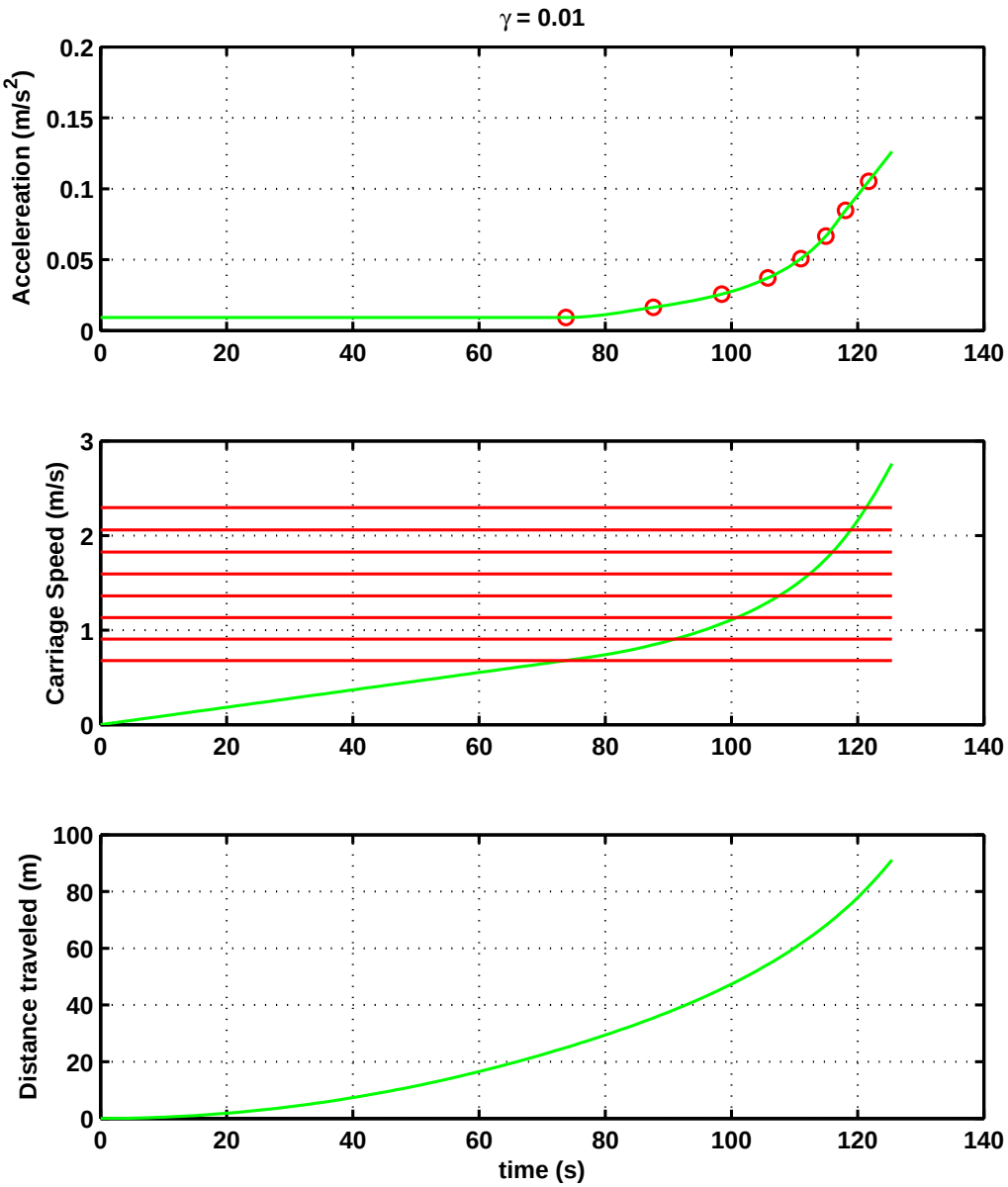

Figure 10-4: Constant $\gamma = 0.01$ test

Chapter 11

Conclusions and Proposed Future Work

11.1 Conclusions

This thesis looks at two aspects of Vortex-Induced Vibrations on long flexible cylinders. The work is split into a minor and major part. The minor part addresses the effect of Reynolds number on flexible cylinder VIV. The major contribution addresses the prediction of VIV under unsteady current excitation or time-varying flows.
The study on the effect of Reynolds number makes extensive use of a recent set of experiments performed by MARINTEK on behalf of SHELL Exploration and Production. Three $38m$ long cylinders of different diameters were towed through the ocean basin over a wide range of Reynolds numbers in both uniform and sheared flows.

The experimental data revealed that the response amplitudes and dimensionless response frequency were strongly influenced by the Reynolds number. Both of these Reynolds effects should be of interest to riser designers that traditionally rely or make use of experimental data obtained at much lower Reynolds numbers. The effect of Reynolds number on the response amplitude could be explained through the influence of the Reynolds number on the lift coefficient. Identifying the Reynolds number effects on the response of flexible cylinders in steady flows proved critical to explaining other

details that were observed in the cylinder response. This was necessary before even attempting to compare these results with the cylinder's response to VIV that was observed in unsteady flows.

One of the key findings from the analysis of the steady flow experiments was that the VIV response amplitude will vary considerably throughout the duration of the test. This has serious implications when choosing the time-section or time-record for further analysis, since it is shown that using the entire time-section or attempting to use a statistically stationary time portion will not reveal or does not necessarily coincide with the largest VIV response and most damaging conditions.

The final finding from the analysis of the $38m$ SHELL experiments shows that the Cross-Flow and In-Line damage rates are always of the same order of magnitude and that the most damaging location on the circumference of the cross-section usually coincides with the Cross-Flow direction.

In this thesis, I propose a dimensionless parameter, γ, that governs whether lock-in under unsteady flow conditions is possible and show that it is useful for determining *a priori* whether the response under unsteady conditions will be similar to the response under steady flows. The unsteady flow parameter, γ, is a dimensionless parameter that describes the change in flow speed in a single cycle of cylinder vibration. The experimental data necessary to support this work is taken from a set of experiments performed at the State Key Laboratory of Ocean Engineering at Shanghai Jiao Tong University (SJTU), where a $4m$ long flexible cylinder was towed through an ocean basin under carefully selected amounts of acceleration/deceleration. Further evidence is drawn from a subset of the aforementioned SHELL tests which shows how a single ramp test can be used to extract data equivalent to ten or more individual tests at constant speeds.

The SJTU test included runs with slowly and quickly accelerating flows and it was found that as long as the current or towing speed is within a specific band (synchronization region), the response can typically be divided into three regimes based on the acceleration or γ value:

- For very quickly accelerating flows ($\gamma > 0.1$ i.e., greater than 10% variation in

speed per cycle) the cylinder cannot react quickly enough and **at most** a couple of cycles of small amplitude vibration will be observed.

- For moderately accelerating flows ($0.02< \gamma <0.1$) the cylinder will typically start vibrating and can build up a significant response however most of the time the flow will have exited the required synchronization region before the cylinder manages to reach the maximum amplitudes observed in steady flows.

- For very slowly accelerating flows ($\gamma <0.02$ i.e., less than 2% variation in speed per cycle) the flow is changing considerably slower than the cylinder's reaction time and thus the cylinder has more than enough time build up its response.

This thesis shows that the VIV response in time-varying flows is qualitatively similar to the response of flexible cylinders in steady flows and can often be larger than what is observed in a typical VIV test matrix where cylinders are tested at predetermined speeds believed to be close to the speed that will cause the greatest response. The larger response amplitudes observed in slowly time-varying flows are the result of allowing the cylinder to choose the speed at which it will respond the most vigorously instead of limiting it to a few specific speeds. This, in turn, is one of the most compelling reasons to use 'ramp tests' or slowly-varying flows for future VIV model testing. Designers are typically interested in the most damaging response not one that is believed to be close to the most damaging. Another reason to introduce 'ramps' in VIV model testing is the ability to excite multiple modes in a single run through the basin or towing tank.

This thesis shows how a single 'ramp test' may be used to obtain the same information as ten constant speed tests. This can and will significantly reduce the number of runs necessary to completely characterize the VIV response of flexible cylinders and will translate into large cost savings in the future. The thesis closes by describing the differences observed in the VIV response at high mode numbers depending on whether the time-varying flow was accelerating or decelerating. In both situations a 'hysteresis' effect is noted, where the cylinder is found to 'lag behind' preferring to vibrate in the previously excited mode as a result of cylinder lock-in. In accelerating

flows, this means that the cylinder will typically be responding (at least) one mode number lower than it would have in a steady flow. In decelerating flows the same 'lag' will cause the cylinder to respond (at least) one mode number higher than it would have in a steady flow.

The rise time of the cylinder's response and the transient behavior of the lift force are very important when trying to explain why it is possible to excite and observe Vortex-Induced Vibrations in time-varying flows.

11.2 Future Work

The experiments described in this thesis succeeded in answering many of the original research questions and met the test objectives but as is typical with experimental work, the analysis of the results identified several new issues or topics for further investigation.

In steady flows, there is a great need to extended VIV model testing to the critical and supercritical Reynolds number regime, because it is highly unlikely that the Reynolds number dependence that was identified in this thesis will continue to hold outside the sub-critical regime. Another topic that needs to be addressed is the large variability in the VIV response of flexible cylinders. It is definitely worthwhile to try and identify the causes of this variability in future model testing, some of these are addressed in Appendix A.

In time-varying flows it would be very interesting to continue experimenting with 'ramp tests' but using cylinders of different mass ratios and under varying amounts of damping. Both mass ratio and damping can affect the size of the synchronization region and it would be interesting to see if, at high mass ratio and higher damping levels when the synchronization region is smaller, it is harder to observe a VIV response.

These should be investigated independently since Appendix C shows that cylinders with larger mass ratios will have a longer 'rise time' than their low mass ratio counterparts, and the length of the rise time is important to explaining why VIV is

possible in time-varying flows. Studying the effects of both of these parameters would greatly help understand the threshold γ values that were identified in this thesis.

In conclusion, one of the motivations for studying VIV in time varying flows was to be able to predict what will happen in an oscillatory flow that has a non-zero mean flow. Appendix B sets out to explain how the lessons learned from this thesis could be used to create a screening tool for predicting whether or not VIV will be in an issue in a non-zero mean oscillatory flow, but obviously its applicability would need to be confirmed with further model testing. The examples given in Appendix B would be ideal scenarios around which to design a new unsteady flow experiment.

THIS PAGE INTENTIONALLY LEFT BLANK

Appendix A

Variability in VIV Response in Steady Flows

The main objective of this appendix is to demonstrate that the VIV response amplitude of flexible cylinders can show considerable variation even in steady flows. This is usually not addressed in the literature and currently there is no framework or 'best-practice' in the VIV community that can address statistically non-stationary data. This variation in response can take two forms:

- In the first case, all sensor locations on the flexible cylinder have the same dynamic response but this can vary in time (i.e., non-stationary)

- In the second case, different portions of the flexible cylinder show very different response characteristics at the same instance in time.

This has serious implications when choosing the time-section or time-record for further analysis, since it is shown that using the entire time-section or attempting to use a statistically stationary time portion will not reveal or does not necessarily coincide with the largest VIV response and most damaging conditions. This appendix proposes a novel way to plot the VIV response of a flexible cylinder by making use of the 'RMS response envelope' which is capable of revealing the variability in the response.

VIV is by its own nature a stochastic problem and treating it deterministically will inevitably mask many interesting and fascinating features. This section will investigate some aspects of this behavior by presenting some brief statistics concerning the observed VIV response. This is done in order to increase the reader's confidence in the Reynolds number trends identified earlier in Chapter 4 in light of the relatively large amount of scatter in the data.

Mandel (1984) offers a very convincing argument for the statistical analysis of experimental data. His opinion is that the purpose of the analysis is to confirm the presumed linearity (or other underlying trend) of an identified relationship and obtain the best values for the parameters characterizing the relationship by investigating this lack of definitiveness and thus ascertain the limits of validity of the conclusions drawn from the experiment.

Additionally, having a range of possible response quantities for a given test will provide some leeway when comparisons with the unsteady data are made later on. Essentially this will mean that instead of comparing a ramp result with a single value from the conventional tests, we will have the ability to compare the ramp result with a range of values characterizing the VIV response in steady flows. Finally, statistical analysis should be useful as a diagnostic tool. Causality is hard to determine, but from a practical standpoint one could start asking whether the variability in the response will get smaller if:

- The signals appear to be stationary in time
- The test is conducted at the exact V_r that results in maximum response (i.e Vr_{crit})
- There is no mode-switching
- There are no fluctuations in velocity
- There is little or no turbulence in the mean flow

Eliminating each one of the above would potentially decrease the size of the error bands until they reach the point that they are entirely due to the stochastic nature

of VIV and nothing else. The experimentalist often has little control over some of the factors listed above and therefore it is not easy or straightforward to address all of them. In this section the first three are addressed.

Modarres-Sadeghi et al. (2011) looked at the VIV response of flexible cylinders and concluded that the response can usually be classified as type-1 or type-2 based on the observed response. VIV response which is (almost) monochromatic and periodic is classified type-1 (or quasi-periodic) whereas VIV which shows strong narrow-banded response is termed type-2 (or chaotic). The authors observed three types of behavior:

- cases where the entire signal is mostly type-1
- cases dominated by type-1 response with occasional bursts of type-2 response
- cases entirely dominated by type-2 response where it is impossible/or very hard to even identify a small time section with type-1 response.

Test 3002 involved towing the $30mm$ diameter cylinder (Pipe 2) in a uniform flow of $0.4m/s$. Figure A-1 shows some displacement time histories at 6 different accelerometer locations; the top three plots correspond to neighboring accelerometers near one end of the flexible pipe whereas the lower three plots correspond to three neighboring accelerometers on the other end. The phase plane corresponding to each time history is shown next to it. The displacements and velocities shown have been obtained by integrating the accelerometer signals in the frequency domain.

Modarres-Sadeghi et al. used the phase-plane (among other tools) to identify whether an observed VIV response is best classified as type-1 or type-2. The blue line in the phase plane corresponds to the entire time signal of the test, whereas the red line corresponds to the time sections shown in red. Just by observing the time-histories colored in red one could conclude that the data looks very periodic and stationary, but this is further reinforced by the neat phase shown planes in red. One would expect a constant amplitude sinusoidal signal to have a phase plane that looks like a circle or an ellipse depending on the scaling. The additional kinks present in the red ellipses are due to the 3X and 5X contributions, i.e. the higher harmonics.

For the time section identified in red color between 62 and 79 seconds, one can easily conclude that the VIV response is dominated by type-1 or quasi-periodic behavior.

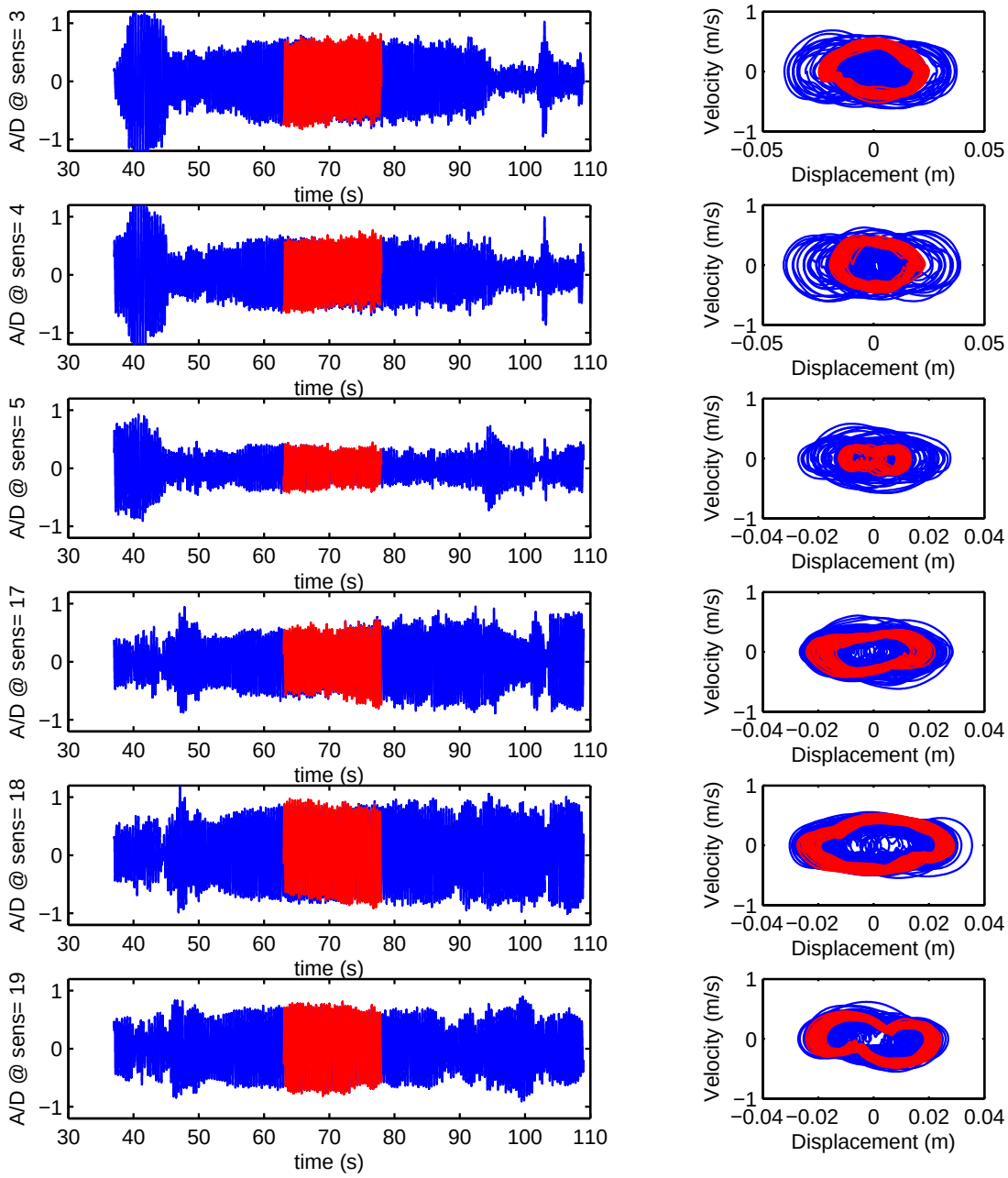

Figure A-1: Time-histories and phase planes for Test 3002

Test 3002 is an example of VIV response where one can indeed identify a statistically stationary time section which could then be used for further analysis. However, it will be shown that this type of response where every point of the entire structure is behaving in a very specific manner is definitely the exception and not the norm when analyzing the $38m$ long SHELL dataset.

Test 3003, shown in Figure A-2, is much more typical of the behavior observed in the SHELL dataset. The testing conditions for Test 3003 were very similar to Test 3002, with the only difference being a slightly higher towing speed of $0.5m/s$, yet by observing the time histories in Figure A-2, it is very difficult to determine a time section where all points along the flexible model behave in a similar manner.

Specifically, the time section identified in red color would appear to be a good time section to use for analysis for one end of the pipe (sensors 17, 18 & 19) with the response characterized by constant amplitude periodic oscillations. At the same time though, it should be clear that the time section identified in red color is characteristic of chaotic response for the other end of the cylinder (top three plots).

Figure A-3, once again shows the displacement time-histories from Test 3003, but now a time-section characterized by type-1 (quasi-periodic) oscillations is chosen for the opposite end of the pipe which had previously been characterized by a strong chaotic response.

The behavior identified in Test 3003 is very typical of what is seen in the Shell dataset, i.e., different parts of the riser model can have very different response characteristics at the same instance in time. This fact makes identifying suitable stationary time sections very hard or impossible and a different approach might be more suitable.

Many of the tools used to analyze the unsteady data (non-stationary data) can also be applied for the analysis of steady speed tests (conventional tests). The moving-RMS calculation proved especially useful in this situation. The moving RMS is calculated according to Equation 8.2 with a window length corresponding to ~ 5 vortex shedding periods. For Test 3002 at a speed of $0.5m/s$ the window length would be:

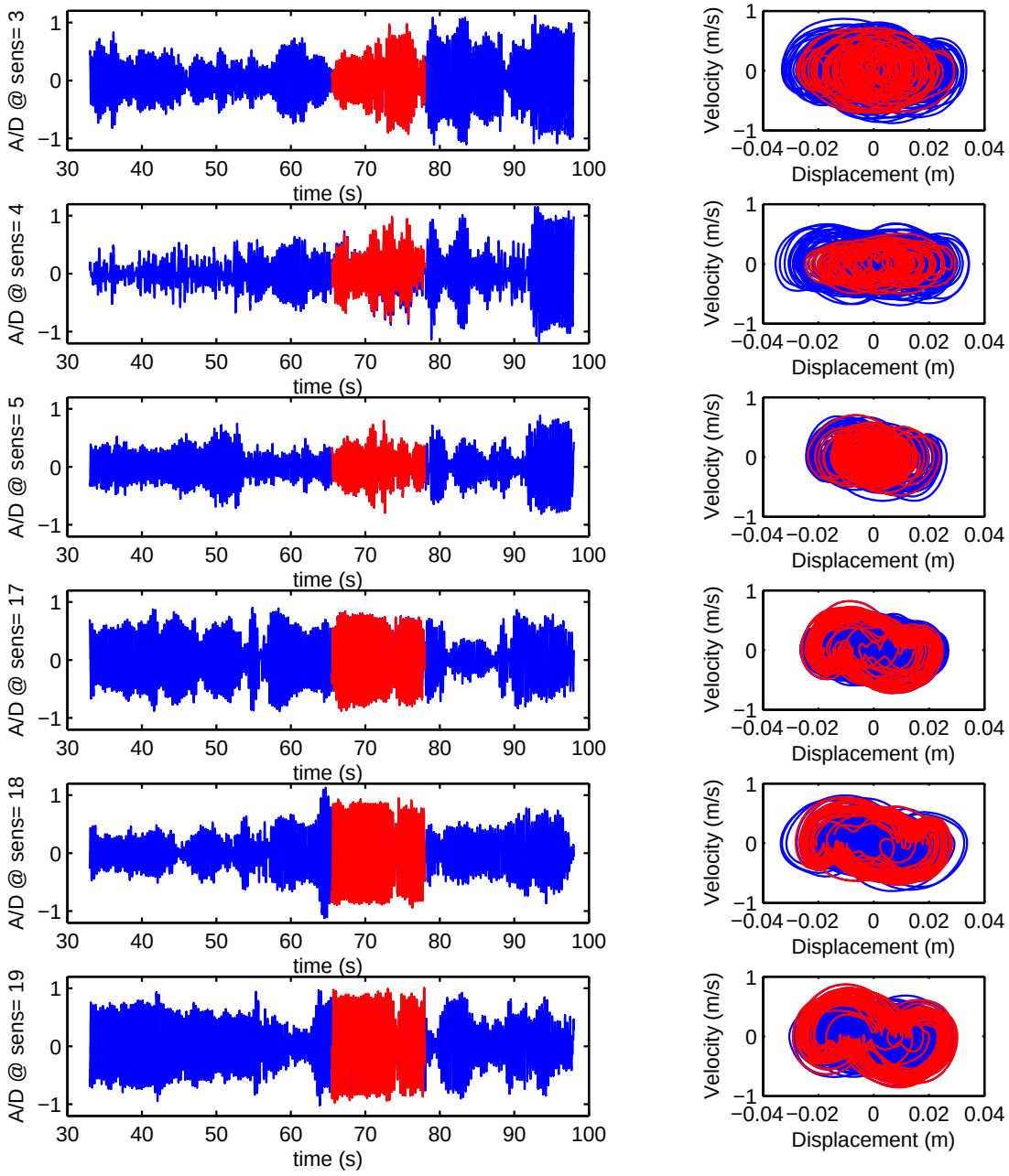

Figure A-2: Time-histories and phase planes for Test 3003

$$\text{window length} = 5T_{vortex} = 5(\frac{D}{0.15U})$$

Figure A-4, shows how the mean (spanwise) CF RMS curvature varied with time for Test 3002. The stationary time-section between 60 and 80 seconds, identified earlier in Figure A-1, results in a constant curvature of $\sim 3.5 \times 10^{-4}(1/m)$ for the same time section. It is interesting to note that the large variations in the curvature at the beginning and end of the time record are associated with large changes in the modal weights whereas for the stationary time section the mode weights remain almost constant.

Figure A-5 is a novel way of presenting VIV response data and this single figure includes all the VIV responses observed during Test 3002. It is created in the following way: The grey-green envelopes shown are created by identifying the largest and smallest RMS response after passing through all the data using a moving-RMS operator. This envelope of RMS response does not include any information relating to the time instance when the largest or smallest RMS response occurred but it brackets every response calculated during the ∼72 second test. The red line is the RMS response using the ENTIRE time section instead of a moving 5 second window; this is what would be typically shown in the literature as the response for a given test. The dashed lines correspond to the result displayed by the red line plus or minus one standard deviation as calculated at every point. This is best explained using Figure A-6, which shows a histogram of the RMS amplitude calculated at the position of maximum response ($x/L = 0.91$). Examining this figure indicates that for a large portion of time, at this specific position along the span, the RMS amplitude was approximately $0.63A/D$, but it in fact it varied anywhere between $\sim 0.48A/D$ and $\sim 0.8A/D$.

For completeness, the response during the short stationary time-section identified in Figure A-1 between the 62^{nd} and 79^{th} second is shown in Figure A-8. Notice how much 'tighter' the response envelope (shaded green) and the plus or minus 1 standard deviation lines (dashed blue) are in Figure A-8 compared to Figure A-5. Also

note, how much narrower the band of possible RMS amplitudes is in Figure A-7 when compared to Figure A-6.

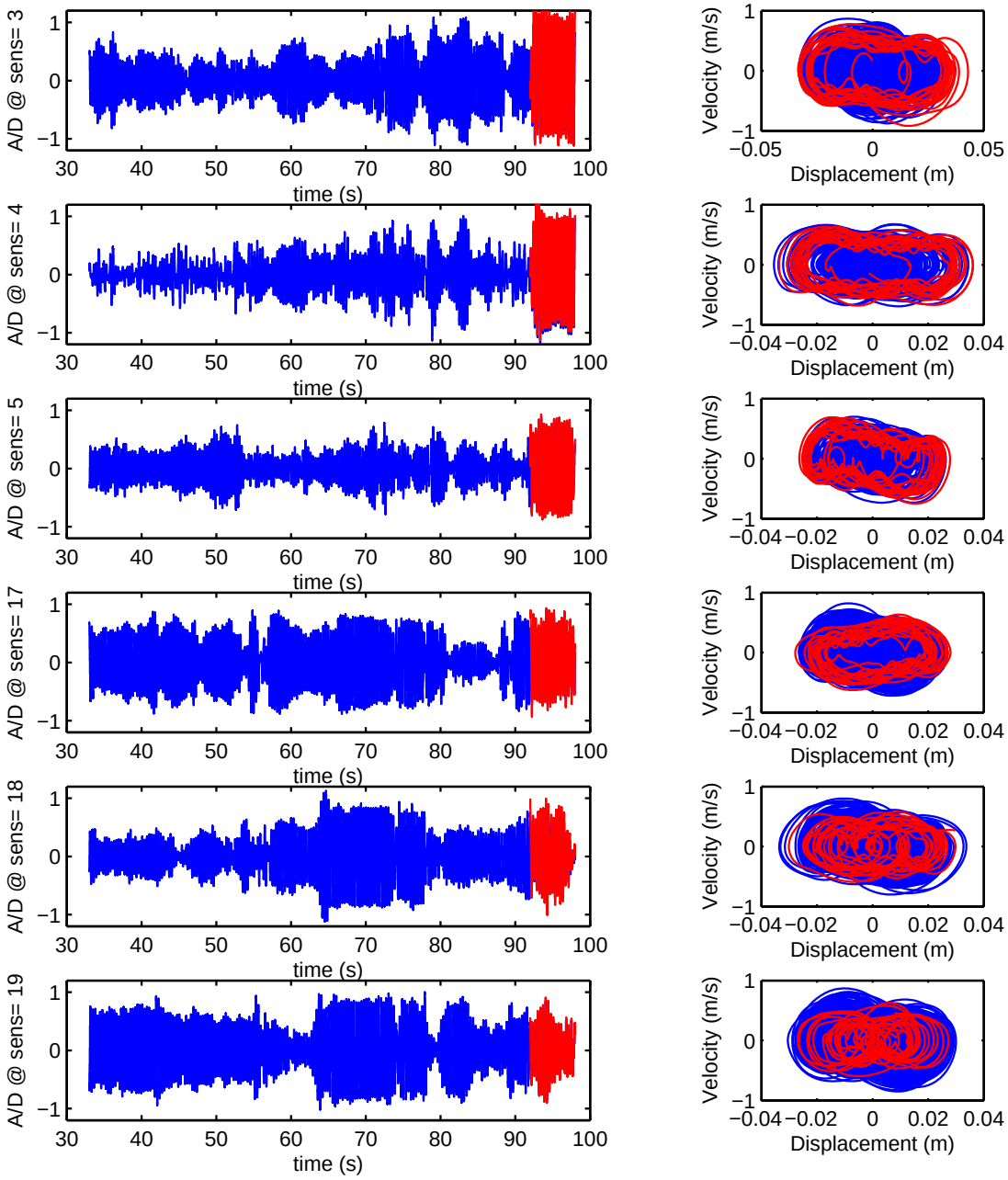

Figure A-3: Time-histories and phase planes for Test 3003

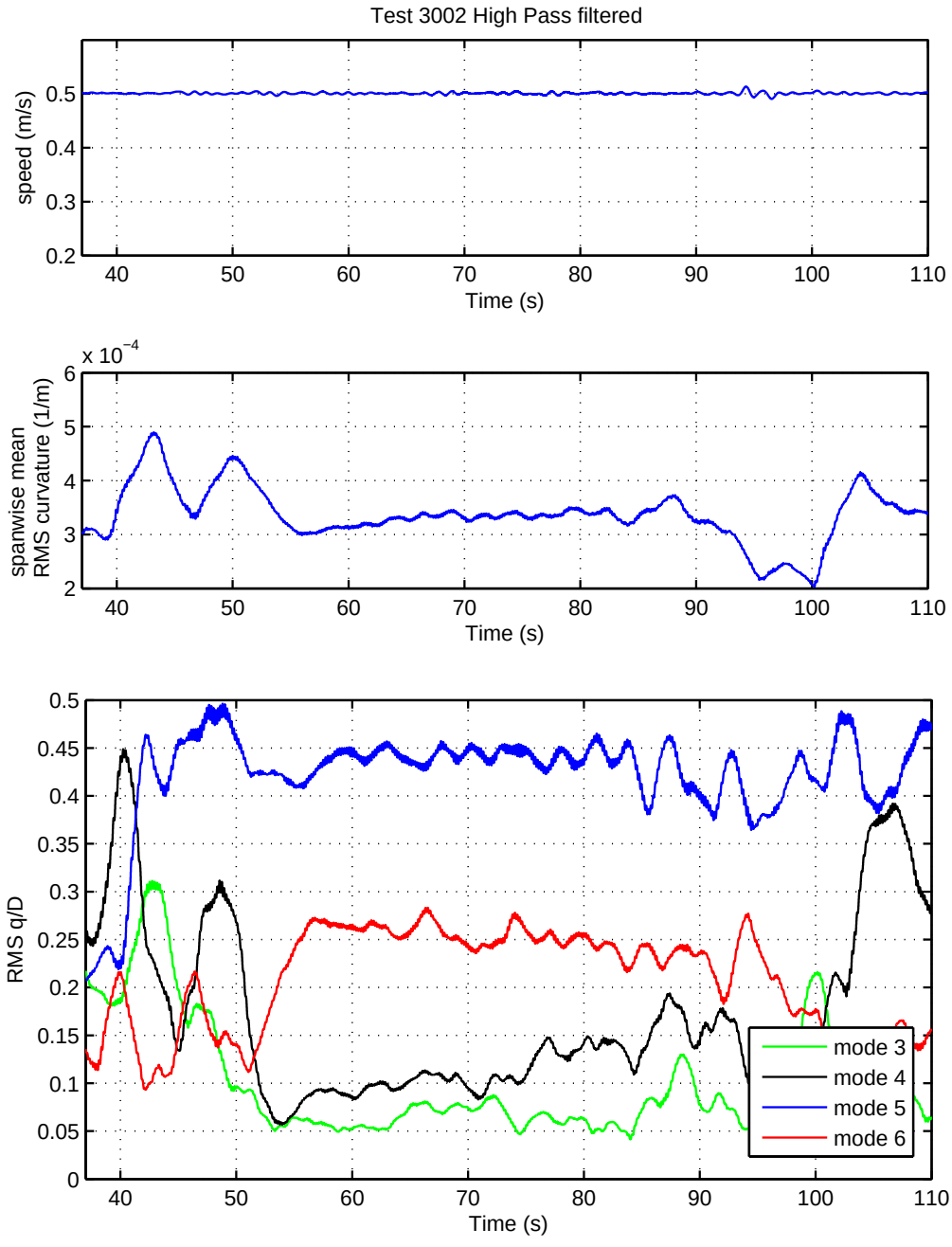

Figure A-4: Moving RMS curvature $(1/m)$ and modal weights vs. time (s) for Test 3002

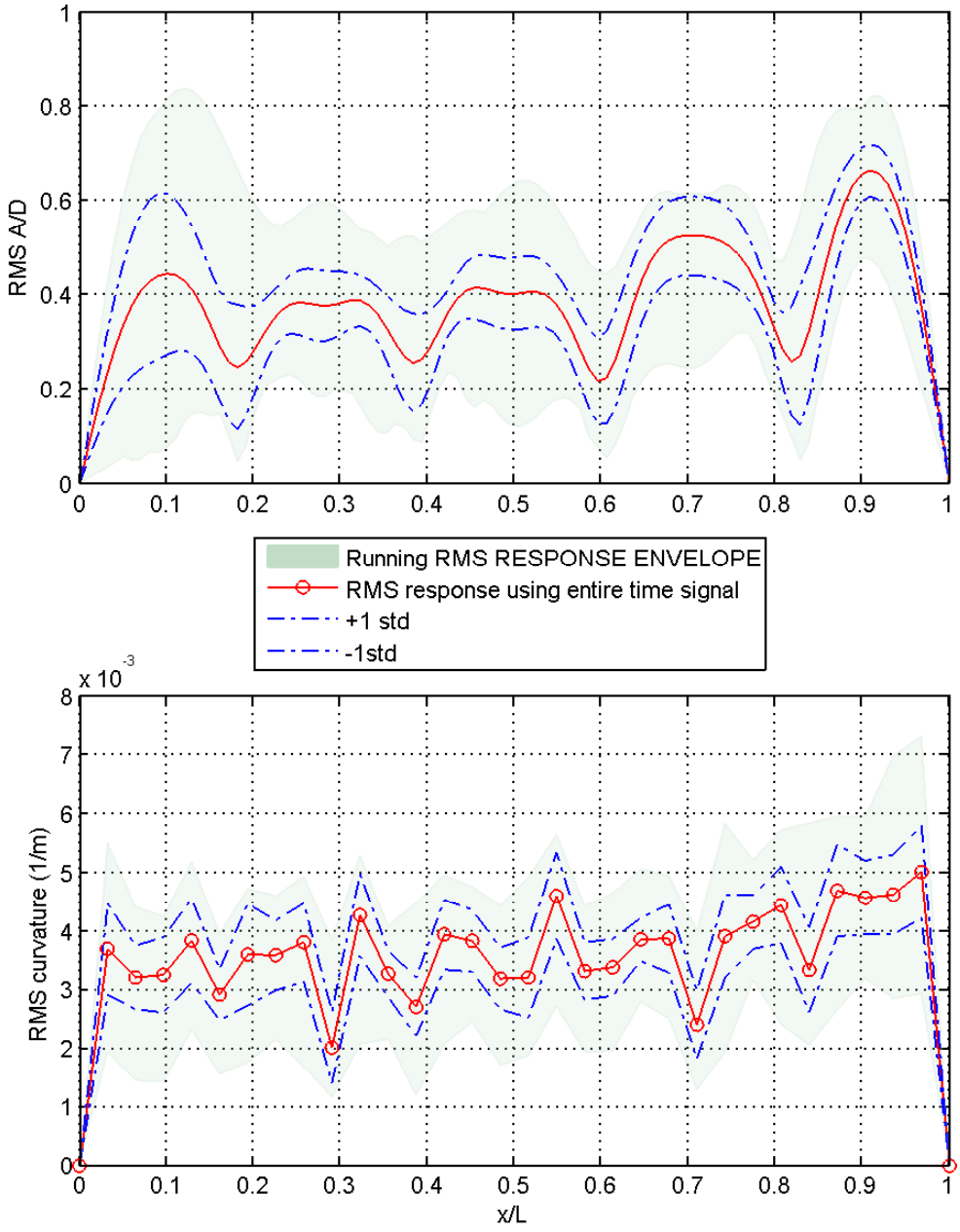

Figure A-5: CF RMS A/D and Curvature $(1/m)$ as calculated using a moving RMS for Test 3002

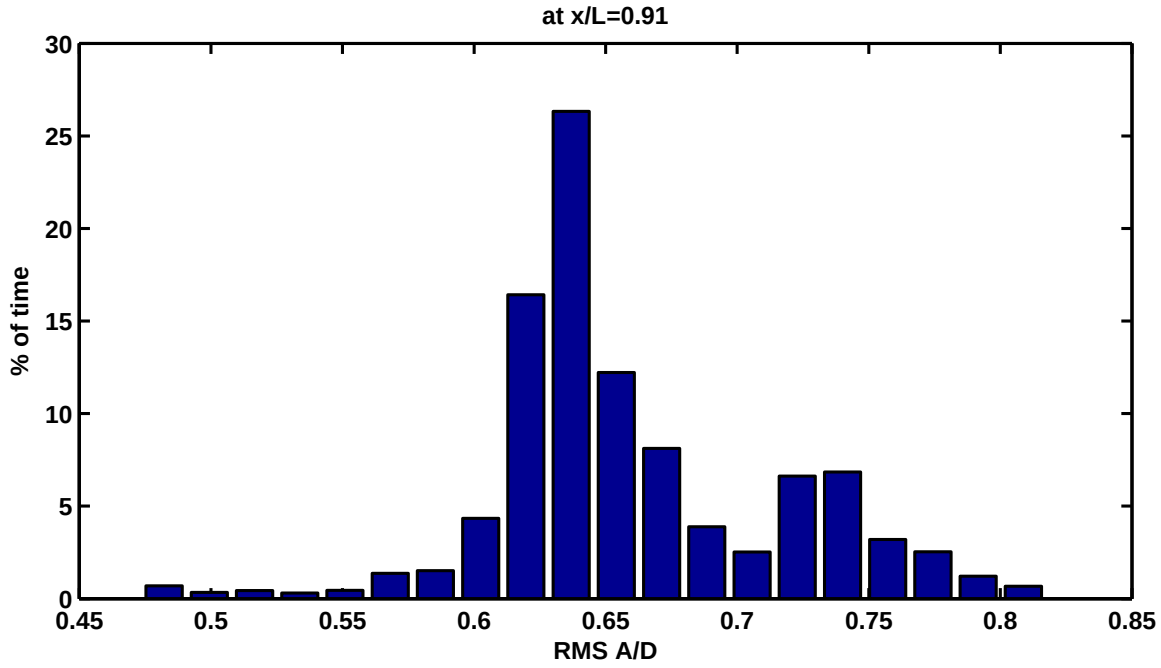

Figure A-6: Variation in the RMS response at $x/L \sim 0.91$ for Test 3002

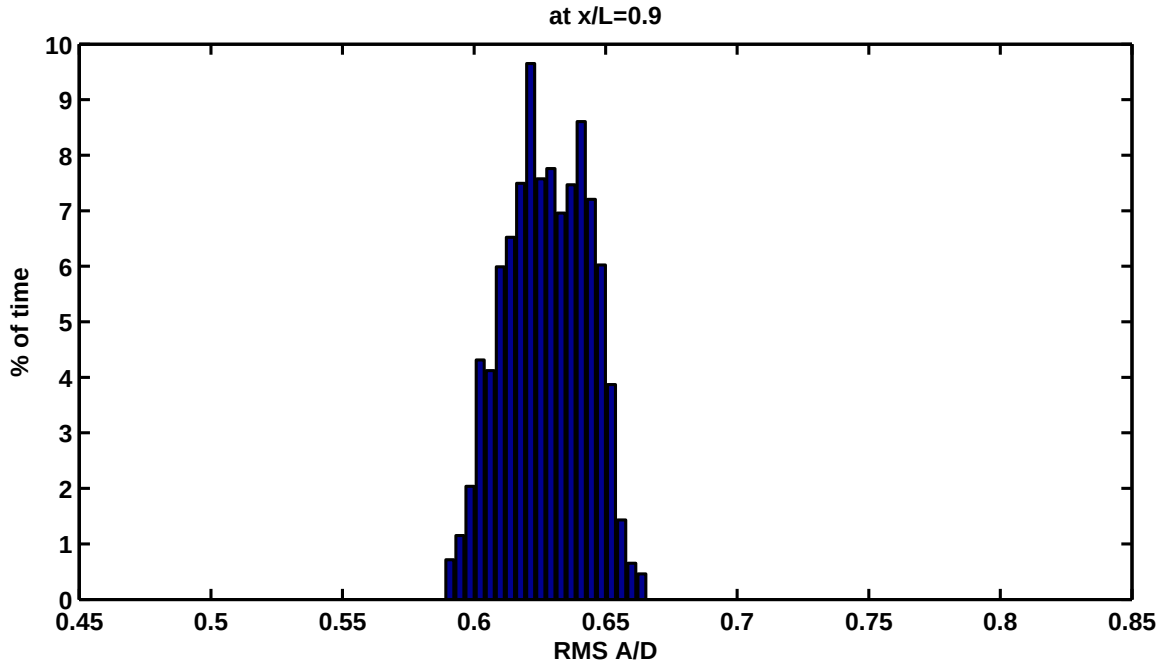

Figure A-7: Variation in the RMS response at $x/L \sim 0.9$ for **a short stationary time section** identified in Test 3002

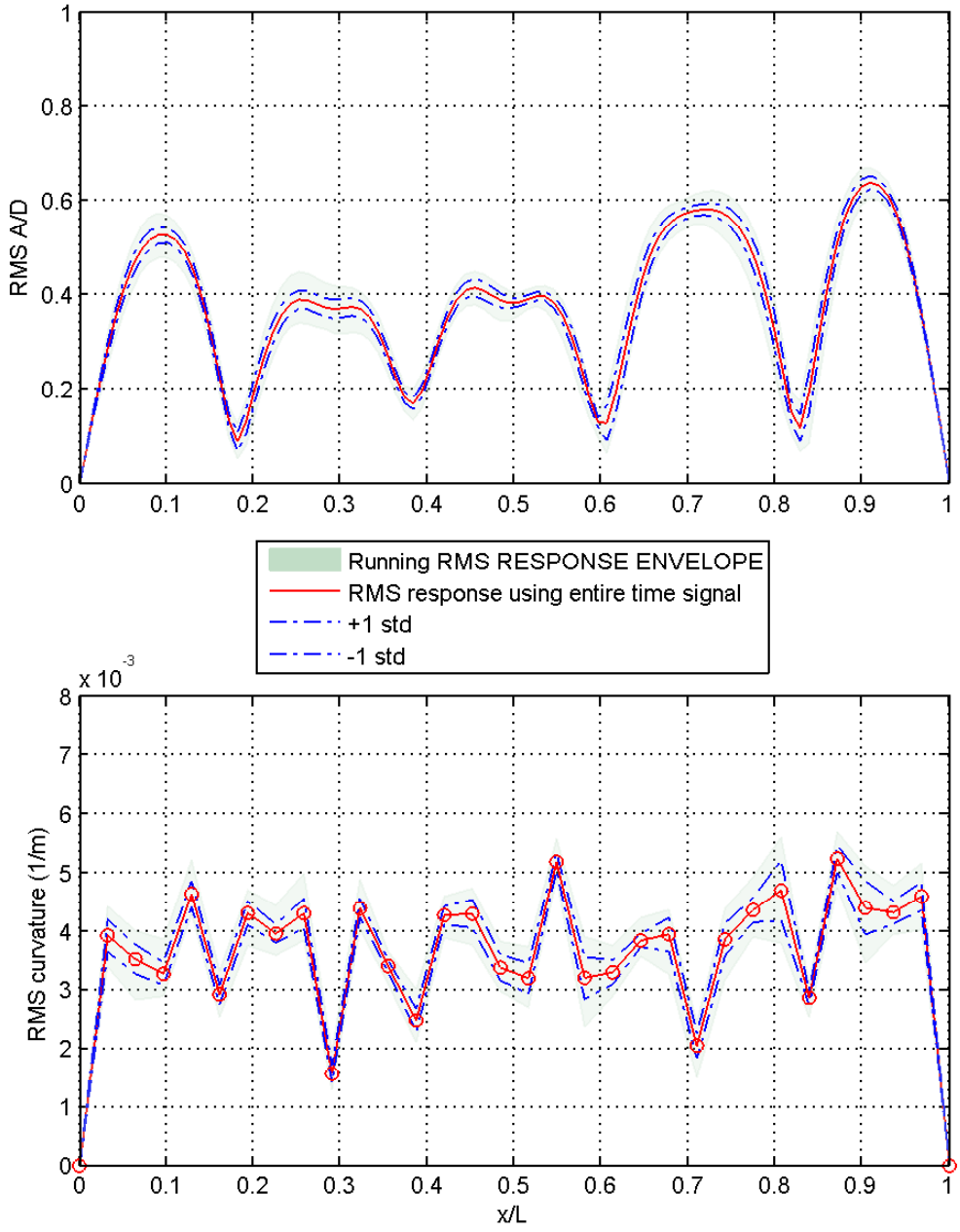

Figure A-8: CF RMS A/D and Curvature $(1/m)$ as calculated using a moving RMS for **a short stationary time-section** identified in Test 3002

Repeating this analysis for every test case in the SHELL dataset allows the calculation of 'error bars' as shown in Figures A-9 and A-10. Calling these error bars is not entirely appropriate because they are not associated with experimental or data-processing errors but instead they are indicators of the inherent variability in the VIV response of flexible cylinders.

Examination of the uniform flow results shown in Figures A-9 and A-10 confirms that the Reynolds number dependence of the VIV amplitudes shown in Chapter 4 persists even after taking into account the random variations in the response amplitudes and curvatures of a steady speed test.

The most important conclusion of this appendix is the fact that the VIV response of flexible cylinder in steady flows (i.e. constant towing speed) is anything but steady and deterministic.

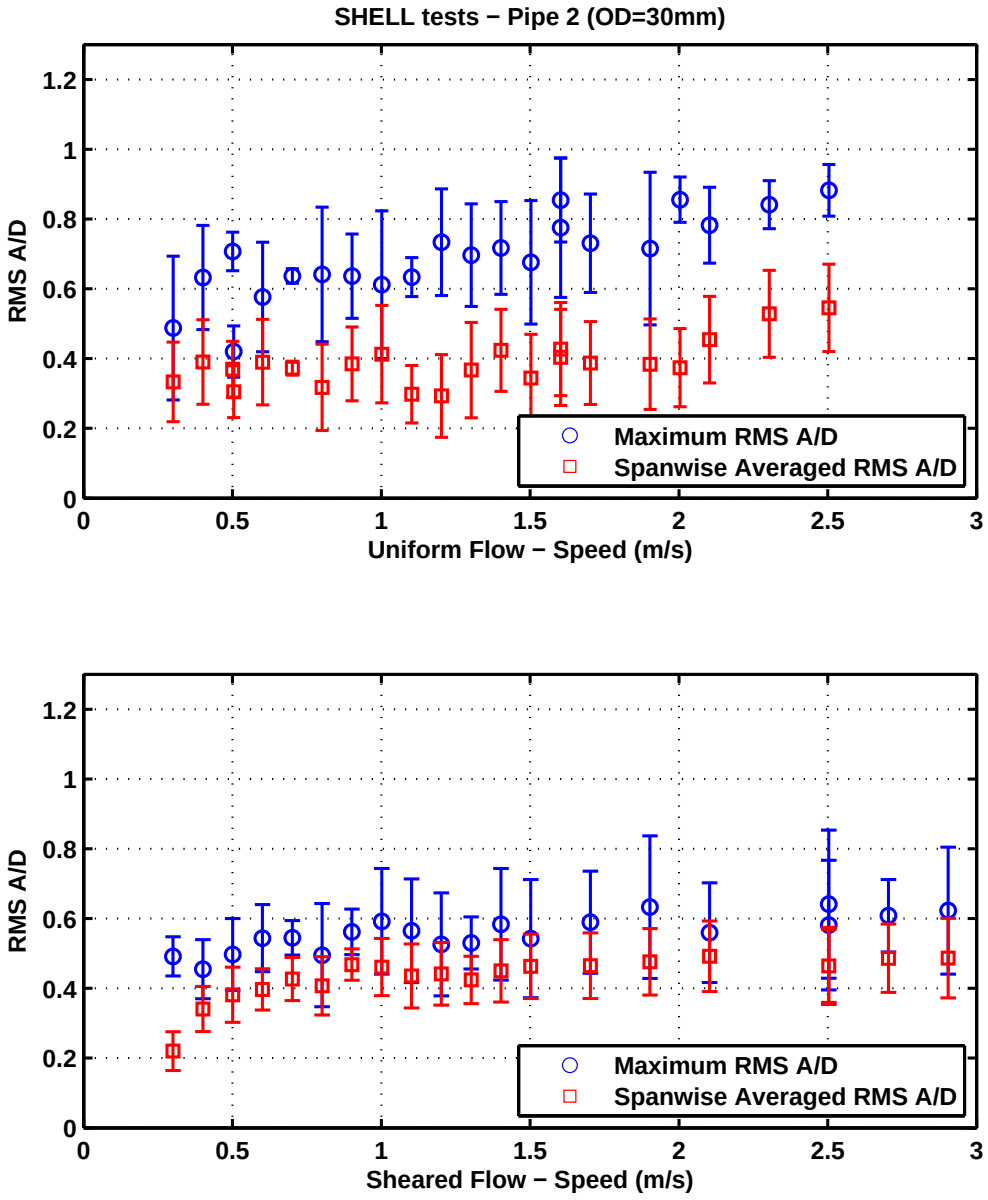

Figure A-9: CF RMS A/D vs. towing speed for the $30mm$ diameter cylinder (Pipe 2)

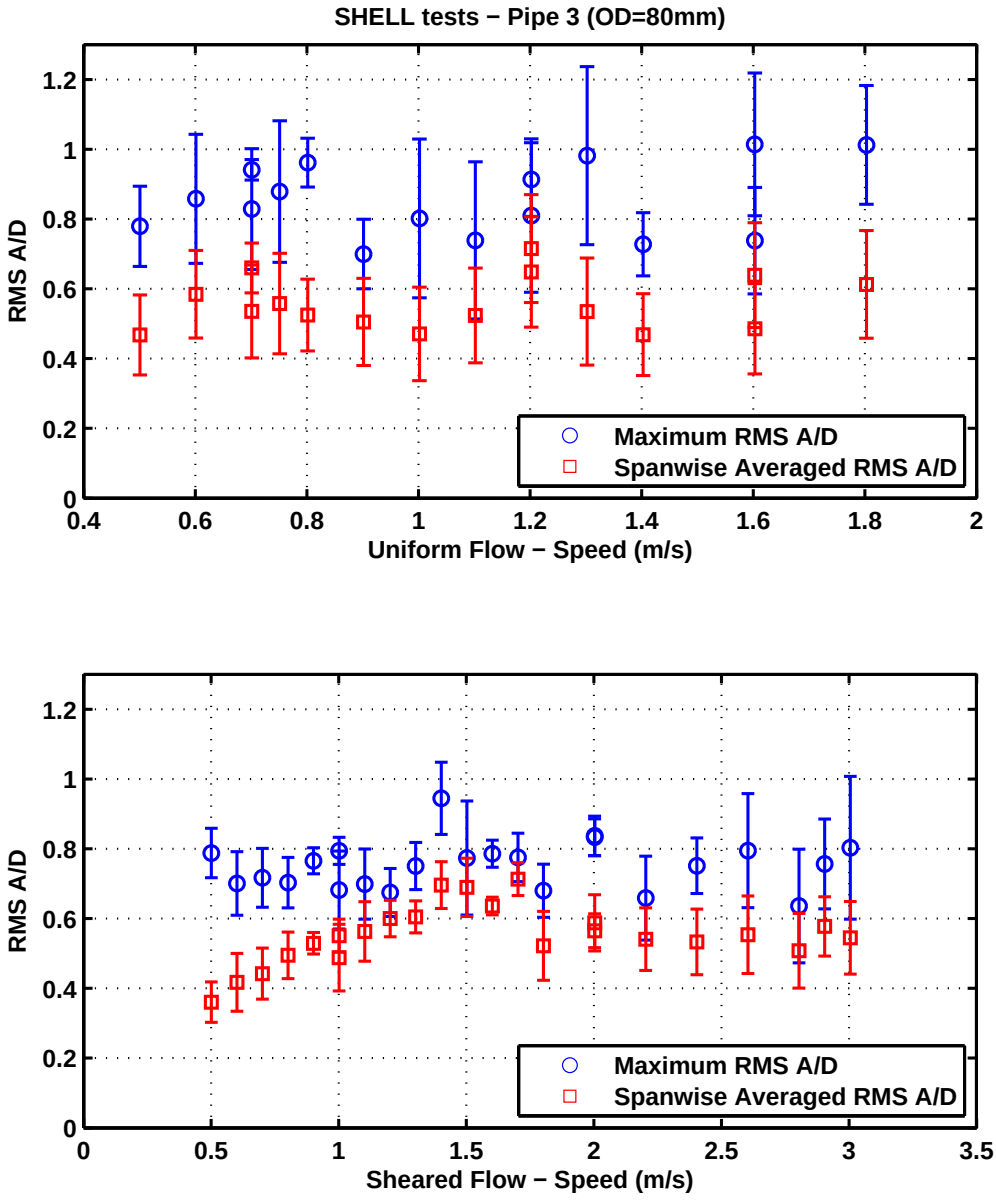

Figure A-10: CF RMS A/D vs. towing speed for the $80mm$ diameter cylinder (Pipe 3)

THIS PAGE INTENTIONALLY LEFT BLANK

Appendix B

Oscillatory Flow Examples - The Parameter as a Screening Tool

Up to this point we have only encountered the unsteady flow parameter, γ, in the context of linearly (or almost linearly) accelerating and decelerating flows. As discussed in the introduction, one of the motivating reasons for studying VIV in unsteady flows was the possibility of cylinder or riser lock-in in time varying flows created by the combined effects of steady currents and surface waves or platform motions. This sections decribes how the unsteady flow parameter could be used as a screening tool to assess whether VIV and lock-in are possible under such conditions. This will be done by presenting to the reader three different examples of oscillatory flow with non-zero mean flows. In all three examples shown, the current speed vs time history could be due to oscillatory flow superimposed on top of a steady flow or it could be the incident current on a section of a riser in a steady flow with 'global' motion that is prescribed by the platform motion far way from the section of interest for example.

For each example we will be assessing whether lock-in is possible for the 4^{th} mode of the 80mm diameter Shell cylinder. The fourth mode had a natural freq. approximately equal to 1.81 Hz.

The screening process can be outlined as following:

1. Check to see which modes are excited by the range of velocities in the current time-history

2. Calculate the unsteady flow parameter, γ, for each one of these modes

3. Identify the regions where **both** the reduced velocity and the γ parameter are within the limits necessary for lock-in

4. Determine the length of these regions in terms of vibration cycles, and then dismiss regions that are too short in duration and do not allow enough time to build up to large amplitude VIV.

The screening process presented above is based entirely on what has been learned about VIV in time-varying flows presented earlier in this thesis, as such extensive model testing would have to be carried out in order to confirm its applicability. In any case the examples presented below could serve as the basis for the design of future model testing experiments.

B.1 1^{st} Example (Small KC Number)

The first current is created by combining a steady flow of $0.77m/s$ with an oscillating flow of amplitude $0.136m/s$ and return period of $T_w = 5$ seconds.

$$U(t) = 0.77 + 0.136 \sin \frac{2\pi t}{5}$$

The oscillating portion of the current would have a KC number of:

$$KC = \frac{0.136 \times 5}{0.080} \approx 8.5$$

The screening process described above will be demonstrated with the help of Figure B-1. The top row shows how the incident current speed varies with time. The second

row shows variation in reduced velocity with time that is a direct result of the varying speed. The reduced velocity has been calculated as:

$$Vr_{n=4} = \frac{U(t)}{DF_{n=4}}$$

The second row also contains lines indicating the critical reduced velocity as calculated assuming a $St = 0.16$ and the reduced velocity bands for a reduced velocity bandwidth of 0.4 ($U_n \pm 20\%$). These lines are helpful because any portion of the time history that falls within this reduced velocity band could be potentially excited assuming that the flow acceleration and deceleration were not too large, i.e., that γ is below a certain value.

The next step is to identify the portions of the time history that lie within the reduced velocity band and have a γ value that will favor/allow VIV lock-in. Here the unsteady flow parameter has been calculated with the following formulation:

$$\gamma(t) = \frac{\frac{dU}{dt}}{U(t)} T_{n=4}$$

as such the γ values will vary due to the oscillatory nature of the acceleration time-history. The third row in Figure B-1, shows how the unsteady flow parameter varies with time. On this figure we have drawn a line corresponding to $\gamma = 0.05$ which we will take as the limiting γ value based on the linear acceleration results presented earlier (Recall that γ=0.05 lies half-way through the region of γ values where VIV response is observed but can be erratic).

The green rectangles superimposed on the figure identify the time sections where both the V_r and γ requirements are satisfied. The final step is to try and identify the duration of these sections in terms of vibration cycles. This is done because it has already been shown that VIV needs between 4-5 cycles to reach its steady state amplitudes. Examining figure G1 we can conclude that each green rectangle is only 1.5-2 cycles in duration. The conclusions that we can draw from this example is that even though the flow is varying slowly enough to shed a couple of vortex pairs at frequencies close to the resonant frequency there simply isn't enough time available

for the structure to build up its response before the flow conditions change and the structure finds itself in a "power-out" situation where any vibrations will decay due to the increased hydrodynamic damping (or negative lift coefficient) present outside the synchronization region.

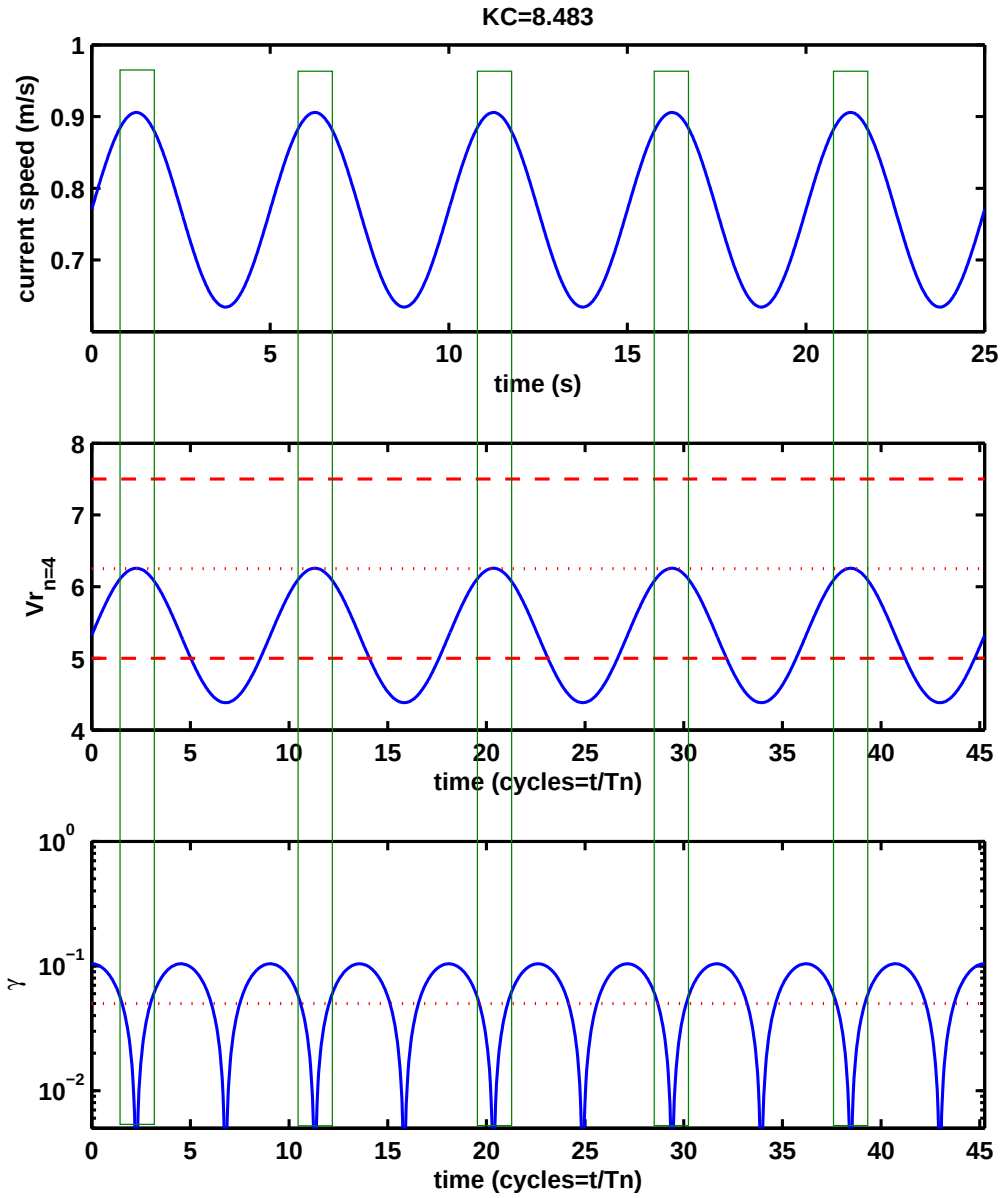

Figure B-1: Oscillatory flow example 1

B.2 2^{nd} Example (Large KC Number)

The second example has been chosen in such a way that the range of reduced velocities excited is identical to the first but now the oscillatory component of the flow will have a much larger period of $T_w = 25s$. The much larger period of the flow implies much smaller accelerations in the flow field and as such the computed $\gamma(t)$ values will be much smaller and time sections where both the V_r and γ requirements are met will include many more vibration cycles.

Figure B-2 demonstrates this graphically. Note how the width of the green rectangles which indicate time sections where both V_r and γ requirements are being met now has a length of approximately 29 vibration cycles. This is more than enough time for VIV to build up and reach its steady state values and we would expect the VIV response inside the green rectangle to closely resemble the VIV response in a steady flow exciting the 4^{th} mode. During the time that is outside of the green rectangle (i.e between 14 and 23 seconds) we would expect the vibrations to start decaying due to the increased hydrodynamic damping until the ~ 23 second mark where excitation is again possible.

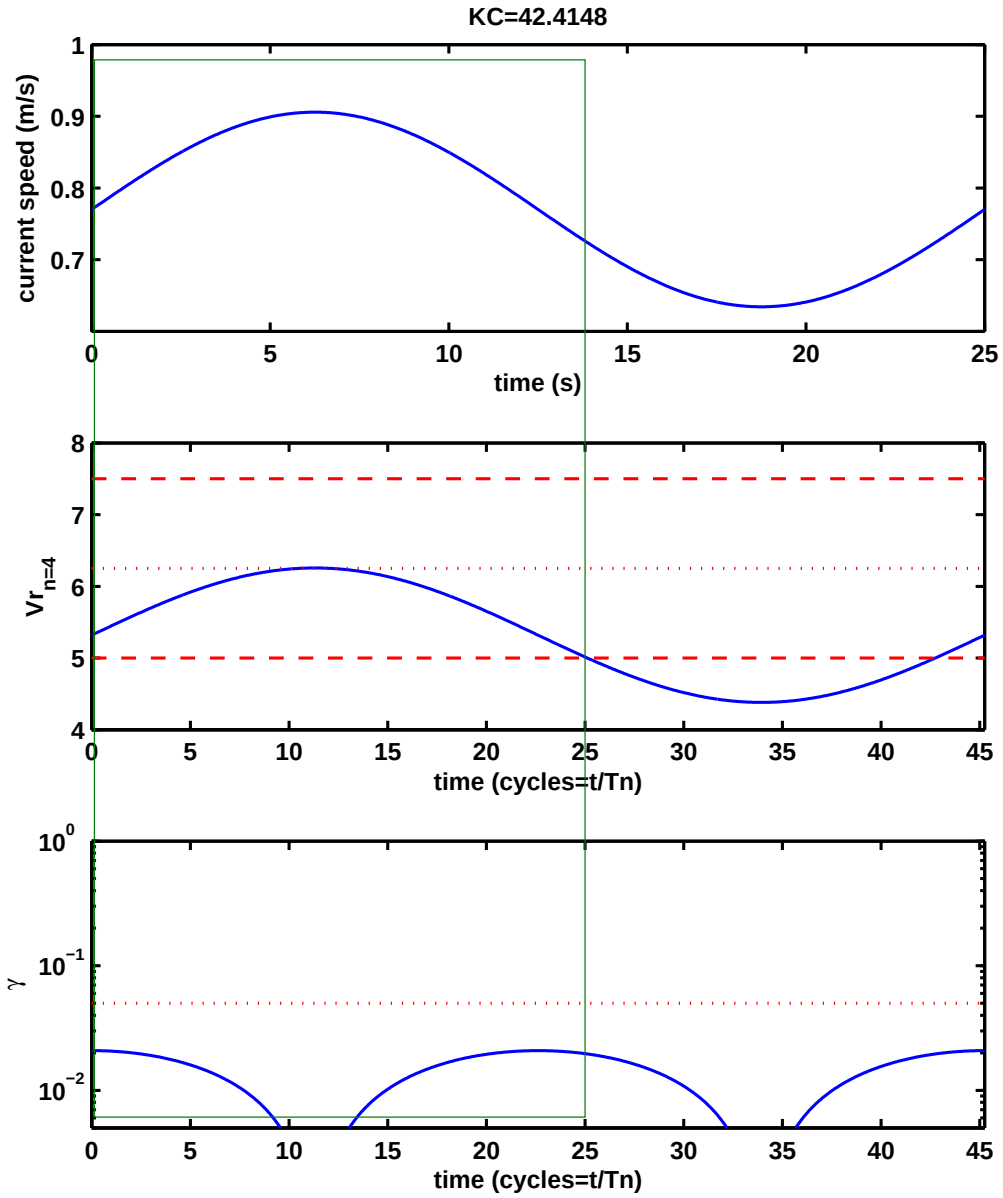

Figure B-2: Oscillatory flow example 2

B.3 3^{rd} Example

The third and final example case that will be discussed pertains to an oscillatory flow that is always within the V_r bands with the velocity time history given by:

$$U(t) = 0.905 + 0.136 \sin \frac{2\pi t}{5}$$

$U(t)$ is shown in the top plot of Figure B-3. This is an interesting case because even though the accelerations are large and the corresponding γ values can be above the threshold limit of $\gamma \sim 0.05$, the flow always remains within the V_r band. Because the structure will be vibrating at its resonant frequency for the entire time, as such the γ value will not affect whether or not lock-in is possible. The unsteady flow parameter, γ, is relevant only when the flow moves into or out of the V_r bands that can excite the structure.

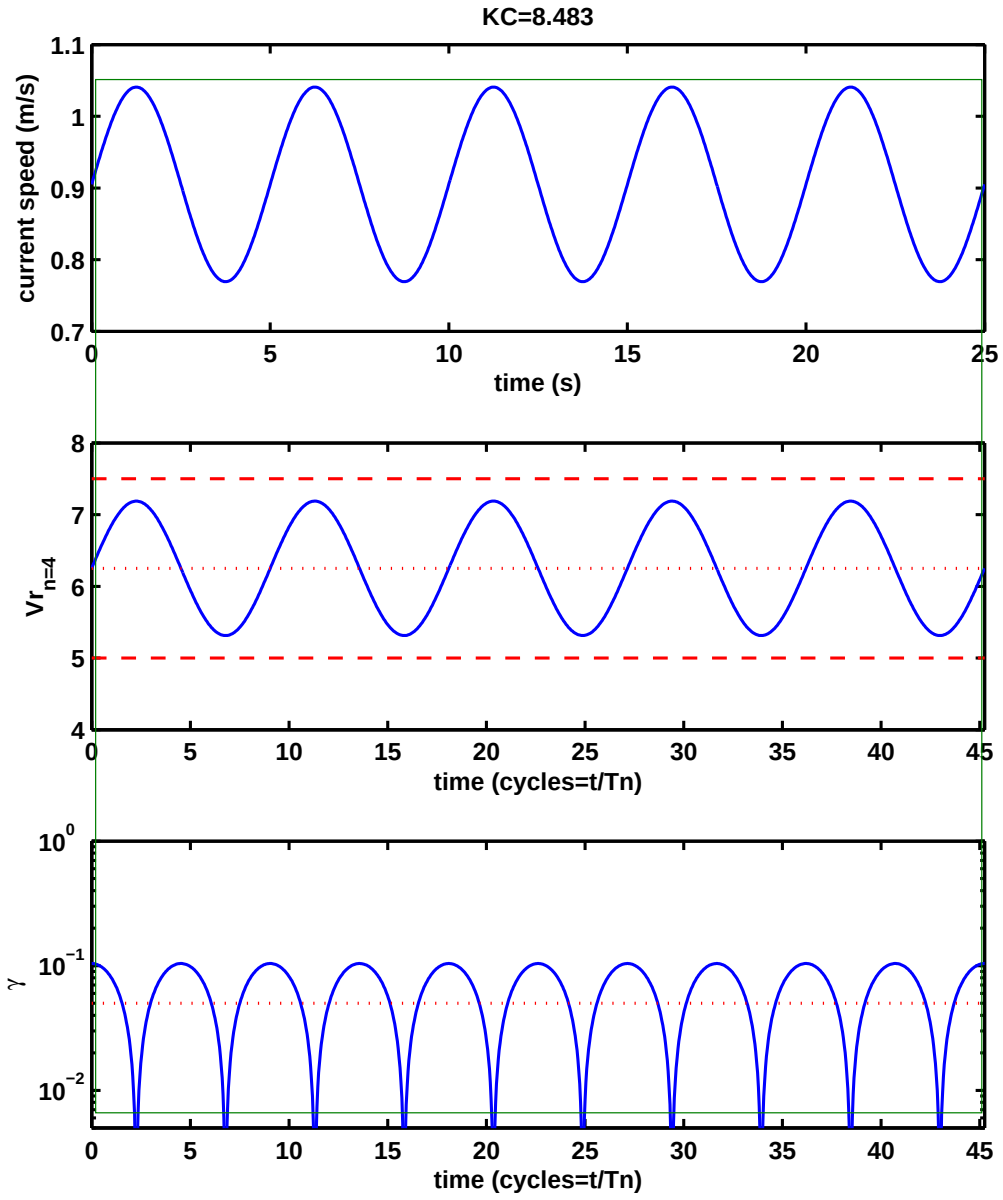

Figure B-3: Oscillatory flow example 3

Appendix C

Transient Behavior of the Lift Force (or Excitation Force)

It has already been shown that under certain situations flexible cylinders exposed to unsteady currents can lock-in and exhibit VIV responses very similar to steady state VIV. This section attempts to explain why it is possible to observe a typical VIV response even if the external forcing conditions are changing (i.e., the flow speed is changing). The main goal is to study the transient portion of the structural response and to determine the excitation that could have caused the observed behavior. Emphasis is placed on how quickly the VIV response can build up and the implications that this must have for the excitation force.

The unsteady flow parameter can also be thought of as the ratio of two time scales:

$$\gamma = \frac{\frac{dU}{dt}}{U}\tau \tag{C.1}$$

$U/\frac{dU}{dt}$ is the timescale over which the excitation (or forcing) changes and τ is the timescale at which the structure can respond (either the 'rise time' or T_n). Then, at small γ, the structural timescale is much smaller than the timescale characterizing the change in excitation force and hence the structure has time to respond to changes in the excitation.

C.1 VIV Response Build-Up (the 'Rise Time')

Studying what the excitation (or lift force) looks like when it first starts acting on the cylinder and how it evolves with time should help shed some light on the problem at hand. The transient behavior is often overlooked in the literature simply because the beginning and ending of any time-record is usually dismissed and excluded from the analysis because researchers prefer to deal with 'steady-state' or 'time-invariant values'. Instead of dismissing the beginning of the VIV response record one can obtain great insight by taking a closer look. Figure C-1, shows the CF strain at a single sensor location for a steady speed test. It is very impressive how the measured strain on the cylinder reaches its maximum value within a matter of 4 to 5 cycles after the towing speed has reached its steady value.

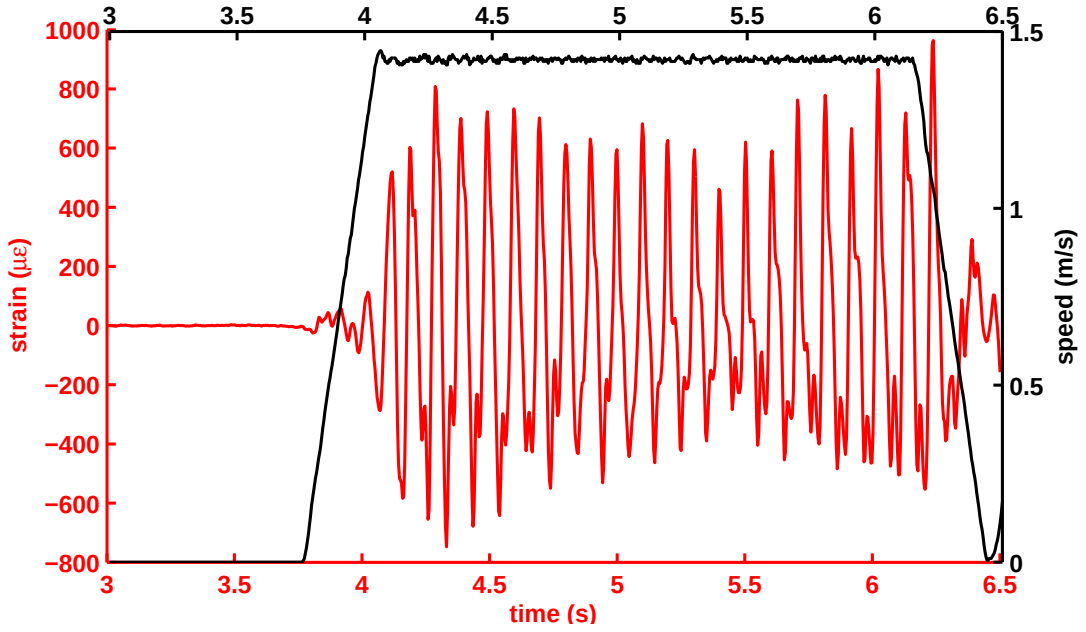

Figure C-1: Typical CF strain sensor time history from a constant speed test.

It should be noted here, that this very rapid rise time, is not unique to the SJTU dataset but has been observed in many low mass ratio tests on single-degree-of-freedom cylinders, also on flexible cylinders responding at high mode numbers, such as the Miami 2 tests and the SHELL dataset as well as tests on joints from full scale drilling risers. This rapid 'rise time' of the VIV response, usually in a matter of a

few cycles is essential to explaining why cylinders are able to adapt rapidly to time-varying flows. Consider first the response of a single DOF linear oscillator, consisting of a lumped mass, a spring and a linear damper.

For linear systems excited by sinusoidal forces of constant amplitude, the rise time is closely related to the damping present, specifically:

$$x(t) = (1 - e^{\zeta\omega_n t})A\sin\omega_d + \phi$$

and the response envelope is described by: $(1 - e^{\zeta\omega_n t})$
So, for small amounts of damping the rise time to say 95% of the steady-state or maximum amplitude would be:

$$\frac{x(t)}{x_{max}} = 0.95 = (1 - e^{\zeta\omega_n t})$$
$$0.05 = e^{\zeta\omega_n t}$$
$$\zeta\omega_n t \approx 3$$

The rise time in (seconds) is

$$t = \frac{3}{\zeta\omega_n} = \frac{3(2m\omega_n)}{c\omega_n} = 3\frac{2m}{c} \tag{C.2}$$

The rise time expressed in cycles is

$$\frac{t}{T_n} \approx \frac{3}{2\pi\zeta} \approx \frac{1}{2\zeta}$$

The cylinders used for VIV testing typically have very small amounts of structural damping; the SJTU test cylinder had a measured structural damping ratio, around 1.5% of critical. This means that if the system had been excited by a constant amplitude sinusoidal force it would have taken on the order of 30 cycles to approach the steady state or maximum amplitude. As noted earlier, in Figure C-1 , the rise time was 4-5 cycles which reveals that something different is going on here: It is

well known that the hydrodynamic lift force is periodic and that the structure's dynamic properties are constant. This implies that the only way that a response with a rise time of 4-5 cycles could be achieved would be if the amplitude of the periodic excitation force was heavily modulated in the beginning.

Figure C-2 shows the amplitude modulation on the lift force for a spring mounted rigid cylinder with little damping, calculated by Ravi et al. (2013). The rise time of approximately 10 cycles, is slightly larger than what was shown in Figure C-1, and is due to cylinder's much larger mass ratio (10 vs. $\sim$1.5 for the SJTU cylinder). The amplitude modulation which occurs during the first few cycles of vibration is entirely consistent with our knowledge of how the lift coefficient depends on the response amplitude, shown in Figure C-3. Specifically, the lift coefficient starts with a finite value at zero or small amplitudes and grows larger with increasing response amplitude until a certain point after which it starts decreasing as the amplitude grows larger. After reaching the maximum response amplitude (which will be a function of the Re, V_r and damping present) the amplitude of the lift coefficient will remain constant at a value that satisfies the equilibrium requirements.

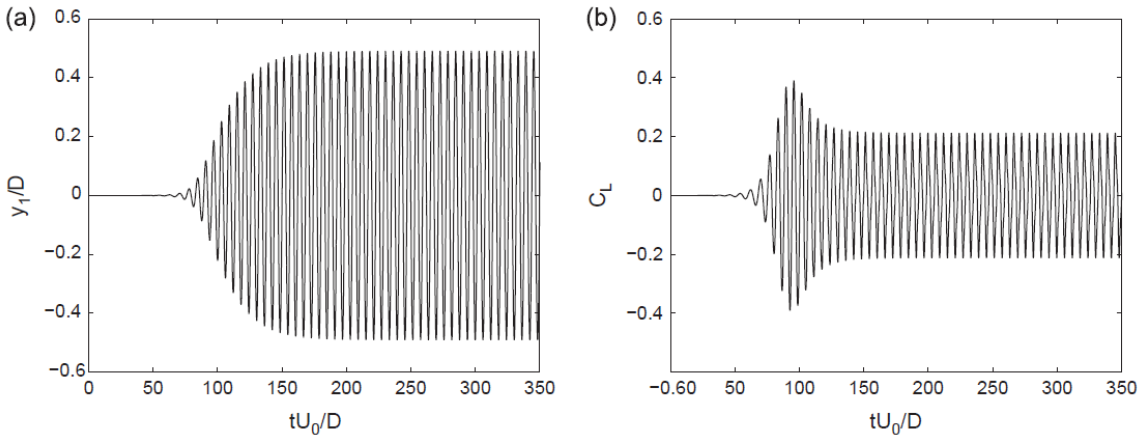

Figure C-2: Rise time and amplitude modulated force from CFD (Ravi et al, 2013)

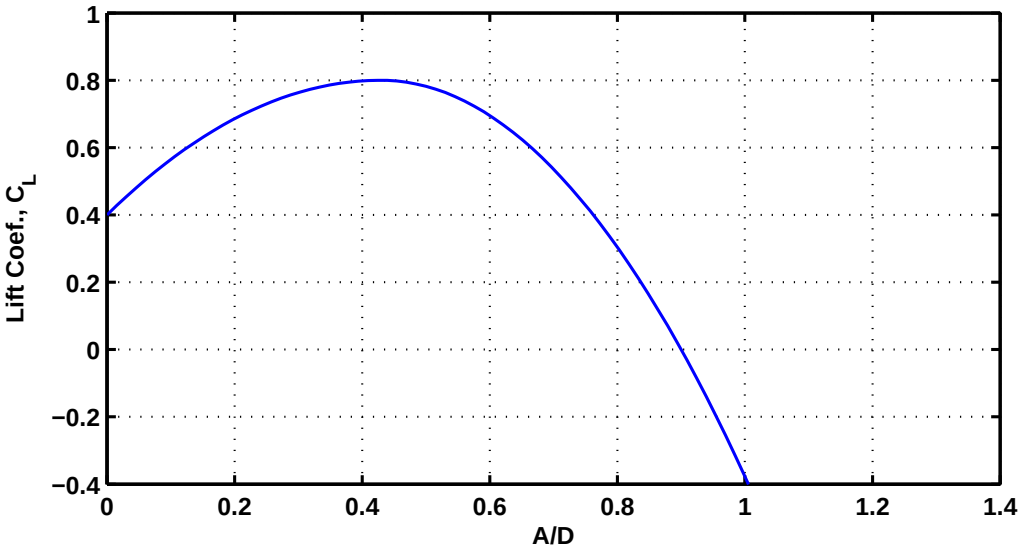

Figure C-3: C_L vs. A/D at a specific V_r

C.2 Deconvolution

Figure C-2 demonstrated what the excitation force would have to look like in order for the system to build-up its response rapidly. It would be extremely insightful if we could observe what the excitation force actually looks like for the SJTU model. As mentioned earlier, since in these tests only the structural response was measured we will have to come up with a method to infer what the excitation force might have actually looked like. The fundamental idea of modal analysis is that the complicated response of a continuous system to an arbitrary forcing can be analyzed/understood as the linear superposition of the responses of many individual SDOF systems, each one representing a given mode, to the same force. The response $x(t)$ of a linear system to any arbitrary time dependent force $F(t)$ is given by the convolution or *Duhammel integral*:

$$x(t) = \int h(\tau)F(t-\tau)d\tau$$

Where $h(t)$ is the impulsive response function:

$$h(t) = \frac{1}{m\omega_n\sqrt{1-\zeta^2}} e^{-\zeta\omega_n t} \sin(\sqrt{1-\zeta^2}\omega_n t)$$

In free vibration VIV tests the system response, $x(t)$, is the primary quantity of interest and is typically recorded. If $h(t)$ is known, then a numerical deconvolution will yield the unknown forcing, $F(t)$.

In the SJTU dataset, as noted earlier in Chapter 8, a modal analysis was performed for each test, yielding the modal contributions, $x_n(t)$ to the total response. For each one of the modes we can define a corresponding impulsive response function, $h_n(t)$, where the main assumption is that the added mass coefficient is equal to 1 and is not time dependent.

Figure C-3 shows the modal amplitude for the 3^{rd} mode, $x_3(t)$ that was obtained from the modal analysis of Test-8a. For the 3^{rd} mode the impulsive response function can be approximated as:

$$h_3(t) = \frac{1}{m\omega_3\sqrt{1-\zeta^2}} e^{-\zeta\omega_3 t} \sin\sqrt{1-\zeta^2}\omega_3 t$$

Figure C-4, shows the result of the numerical deconvolution, of $x_3(t)$ with $h_3(t)$ which will yield the modal force. The amplitude modulation of the modal force from 4 to 4.5 seconds is very similar to the amplitude modulation of the lift coefficient in the first few cycles shown in Figure C-2.

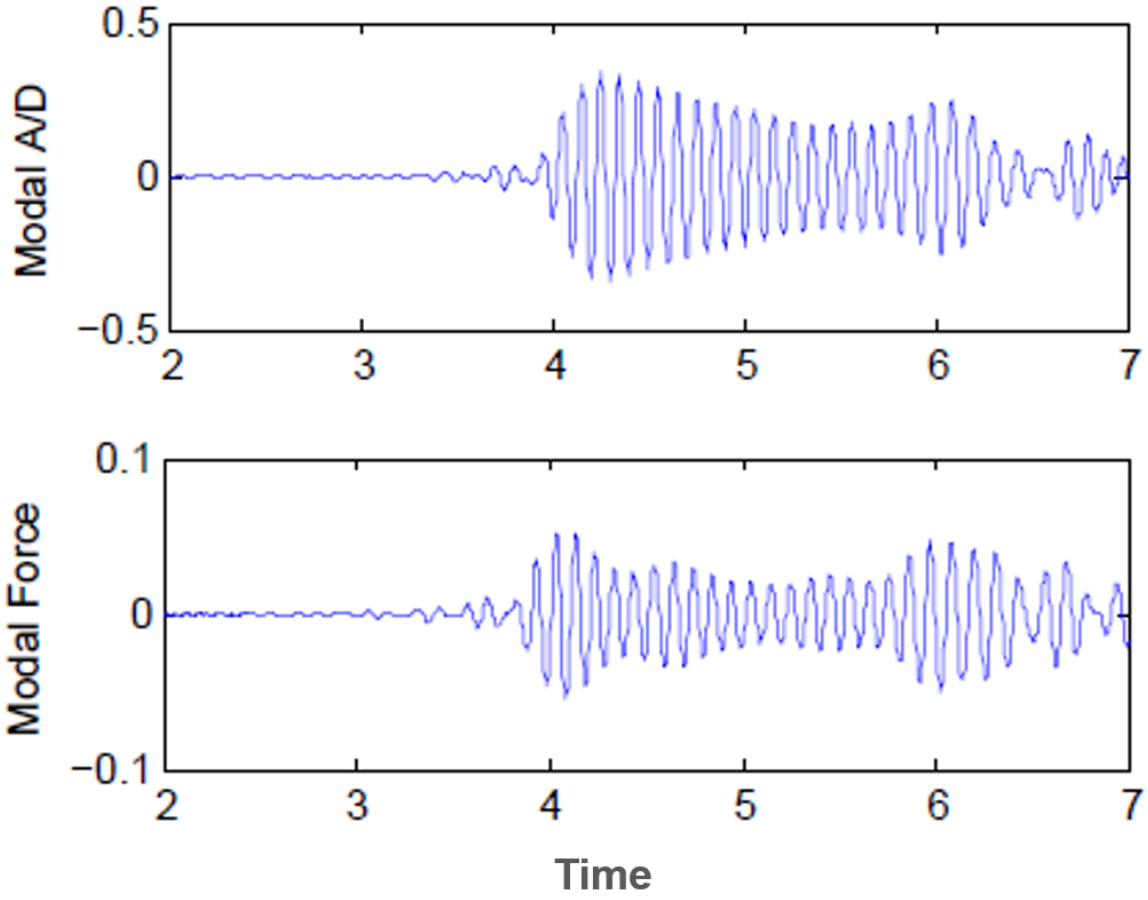

Figure C-4: Mode 3 modal amplitude and modal force for Test-8a

The experimental evidence supports the conclusion that the excitation force is amplitude modulated during the initial cycles of vibration while the VIV response is still building-up. What is even more reassuring is that such an amplitude modulated force is entirely consistent with our knowledge of how the lift coefficient varies with the response amplitude.

C.3 Effects of Mass Ratio and Damping

Unfortunately, because it was shown that the lift force is heavily modulated during the first few cycles of the response, the rise time cannot be predicted or computed directly from Equation C.2. Nonetheless, Equation C.2 stills provides a lot of information about the effects of mass and damping on the rise time.

Specifically, it can be shown that as the system's mass increases the rise time will also increase, since energy is supplied by the flow or force at a finite rate and the heavier (or more massive) system will have a large potential and kinetic energy at steady state amplitudes.

The opposite is true for the amount of damping present: As damping is increased the rise time to steady state or maximum response amplitude will be smaller because the final or steady state amplitude at these conditions (high damping) is much smaller than the steady state amplitude at small or zero damping and thus it will be reached sooner.

Understanding the effects of mass (or mass ratio) and damping on the 'rise time' means that one can make an educated estimate of how these two parameters will affect the γ behavior that was identified in this thesis for cylinders with mass ratios between 1-2 and small amounts of damping (less than 1.5% of critical). For the cylinders tested it was found that as long as γ was less than 0.02 (i.e., a change in speed is less than 2% per cycle of vibration) it was possible to observe a VIV response similar to what is observed in steady flows.

If cylinders with larger mass ratios (>2) were exposed to an unsteady flow they would have to be subjected to a smaller change in speed per cycle (the γ threshold would be lower) if one still wanted to observe a steady like response. This is because the rise time will be greater and therefore the duration of the excitation force would need to be longer.

If cylinders with much larger amounts of damping were exposed to an unsteady flow, the change in speed per cycle could be greater (larger γ) and one would still be able to observe a large amplitude VIV response similar to what is observed in steady flows. Now the rise time will be smaller and thus the duration of the excitation force can be shorter.

Table C.1 summarizes how the two threshold values on γ that were identified in these model tests would change due to the effects of mass and damping on the rise time. Recall that for $\gamma < 0.02$ the response is similar to steady flows and for $\gamma > 0.1$ there was no observable VIV.

Table C.1: Effect of m^* and ζ on Rise Time and γ Threshold

	Rise Time	γ Identified Threshold
Larger mass ratios ($m^* > [1-2]$)	INCREASES	DECREASES
Smaller mass ratios ($m^* < [1-2]$)	DECREASES	INCREASES
Larger damping ($\zeta > [0.7-1.5\%]$)	DECREASES	INCREASES
Smaller damping ($\zeta < [0.7-1.5\%]$)	INCREASES	DECREASES

The mass ratio and to a lesser extent the damping ratio, have also been shown to influence the size of the lock-in band or synchronization region. This too will influence the γ threshold, since larger synchronization regions imply that the excitation duration will be longer and hence there is more time available for the cylinder to build up its response. The size of the synchronization region becomes less important as mode number increases, since the closely spaced natural frequencies will have increasingly larger overlap in their synchronization regions.

THIS PAGE INTENTIONALLY LEFT BLANK

Appendix D

Determining the Axial and Bending Stiffness of the SJTU Riser Model

The riser model tested at SJTU had an elaborate construction and therefore its mechanical properties were determined by subjecting a small section of the cylinder to tensile testing and three-point bending tests. All tests were conducted by the personnel at the State Key Laboratory at SJTU. Figures D-1 and D-4 are photographs of the riser model while it is being tested. Figure D-2 shows the *Force* vs. *Strain* plot used to calculate the axial stiffness of $6.66 \times 10^5 N$. Figure D-4 shows the *Bending Moment* vs. *Strain* plot that was used to calculate the bending stiffness of $10.52 N/m$.

Figure D-1: Tensile test for determining axial stiffness, EA

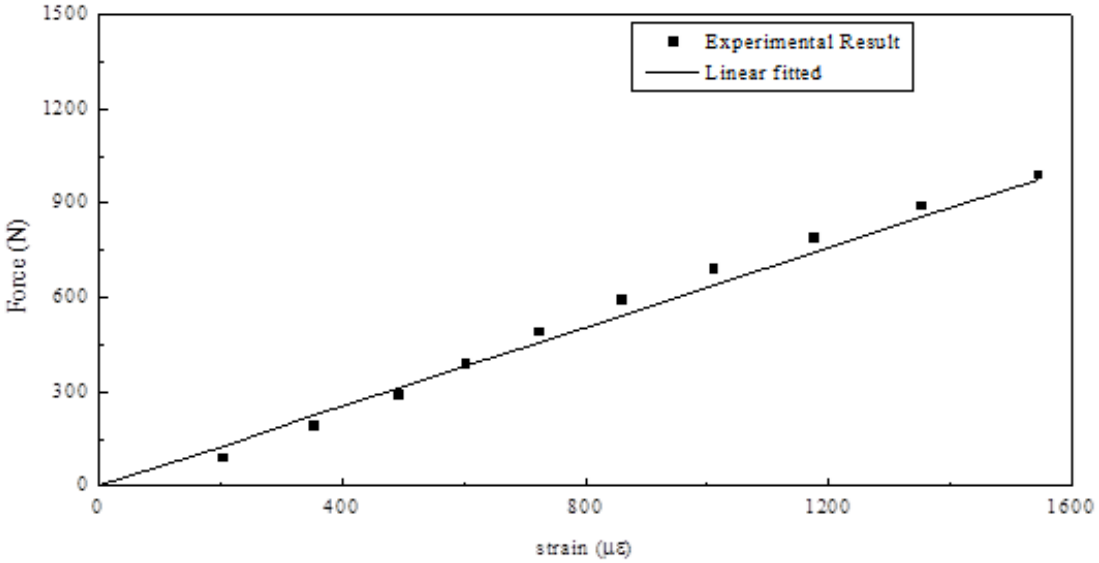

Figure D-2: Measured axial stiffness, $EA = 6.659 \times 10^5 N$

Figure D-3: Three-point-bending test for determining bending stiffness, EI

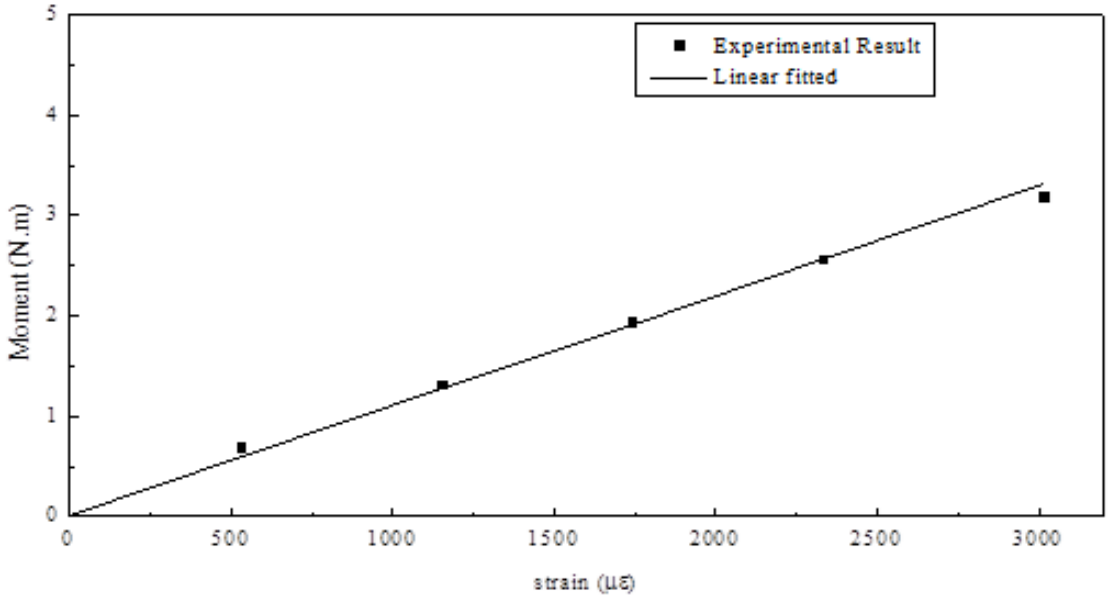

Figure D-4: Measured bending stiffness, $EI = 10.522 Nm^2$

THIS PAGE INTENTIONALLY LEFT BLANK

Appendix E

Transverse Vibrations of Tensioned Beams

This appendix presents the governing equations for the transverse vibration of a tensioned beam and the procedure to calculate the beam's natural frequencies in bending. The material is often covered in textbooks on the mechanical vibrations of continuous systems or structural dynamics. The derivation that follows is based on the analysis presented in Rao (2011).

Figure E-1 shows a beam in bending and a free body diagram for a small differential element from this beam. V is the shear force, M is the bending moment, P is the applied tension and f is a force per unit length.

Force equilibrium in the *z-direction* requires that,

$$-(V - dV) + f(x,t)dx + V + (P + dP)(sin\theta + d\theta) - P\sin\theta = \rho A(x)dx\frac{\partial^2 w}{\partial t^2}$$

Similarly, Moment equilibrium about point O requires that,

$$(M + dM) - (V - dV)dx + f(x,t)dx\frac{dx}{2} - M = 0$$

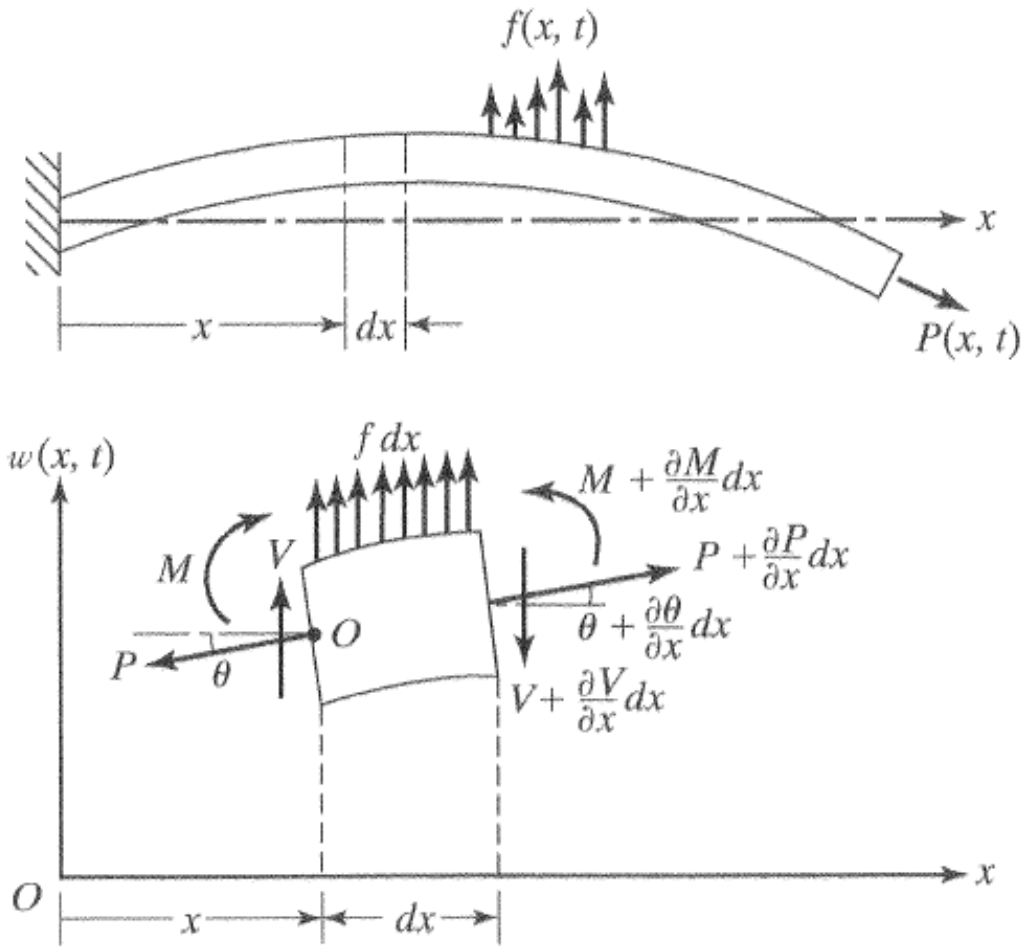

Figure E-1: Transverse vibration of a tensioned beam (Rao, 2011)

For small deflections

$$sin\theta + d\theta \approx \theta + d\theta = \theta + \frac{\partial \theta}{\partial x}dx = \frac{\partial w}{\partial x} + \frac{\partial^2 w}{\partial x^2}dx$$

and recalling that $M(x,t) = EI(x)\frac{\partial^2 w}{\partial x^2}(x,t)$ The equilibrium equations can be rewritten as

$$\frac{\partial^2}{\partial x^2}(EI\frac{\partial^2 w}{\partial x^2}) + \rho A\frac{\partial^2 w}{\partial t^2} - P\frac{\partial^2 w}{\partial x^2} = f$$

If the beam has a uniform cross-section and the mechanical properties remain constant along the length, EI can be moved outside of the first differentiation term. Since we are interested in the natural frequencies of the system, the free vibration equation

becomes

$$EI\frac{\partial^4 w}{\partial x^4} + \rho A\frac{\partial^2 w}{\partial t^2} - P\frac{\partial^2 w}{\partial x^2} = 0 \tag{E.1}$$

The above partial differential equation can be solved by separating variables using, $w(x,t) = W(x)(A\cos\omega t + B\sin\omega t)$ where the constants A and B are found from the initial conditions. Substituting $w(x,t)$ in Equation E.1 leads to

$$EI\frac{d^4 W}{dx^4} - \rho A\omega^2 W - P\frac{d^2 W}{dx^2} = 0$$

If the solution $W(x)$ is a normal function $W(x) = Ce^{sx}$, substitution into Equation E yields the auxiliary equation

$$s^4 - \frac{P}{EI}s^2 - \frac{\rho A\omega^2}{EI} = 0$$

whose roots are

$$s_1^2, s_2^2 = \frac{P}{2EI} \pm \sqrt{\frac{P^2}{4E^2I^2} + \frac{\rho A\omega^2}{EI}} \tag{E.2}$$

And the solution can be rewritten in the form of a transcendental equation

$$W(x) = C_1\cosh s_1 x + C_2\sinh s_1 x + C_3\cos s_2 x + C_4\sin s_2 x$$

Where the constants $C_1, C_2, C_3 \text{and} C_4$ are determined by the boundary conditions. For a pinned-pinned beam $W(0) = \frac{d^2W}{dx^2}(0) = W(L) = \frac{d^2W}{dx^2}(L) = 0$ which leads to

$$\sinh(s_1 l)\sin(s_2 l) = 0$$

which requires that

$$s_2 = n\pi \text{ for } n = 0, 1, 2, 3\ldots$$

Rearranging Equation E.2 yields the natural frequencies of vibration now that s_2 is known

$$\omega_n = \frac{\pi^2}{L^2}\sqrt{\frac{EI}{\rho A}}\sqrt{n^4 + \frac{n^2 P L^2}{\pi^2 EI}} \qquad n = 1, 2, 3, \ldots$$

Appendix F

Ramp Test with the 80mm Diameter Cylinder with Surface Roughness

This appendix presents the results from 'ramp test' using the 80mm diameter flexible cylinder when it was covered with P80 sandpaper to increase the surface roughness. The results from the ramp test will be compared with the conventional test result that where part of the SHELL 38m experiments at MARINTEK.

Figure F-1 shows the towing speed as a function of time for a ramp test on the roughened 80mm diameter cylinder. The plot has lines superimposed on it indicating the speed to excite specific modes and the associated γ values based on the constant acceleration of $0.04m/s^2$.

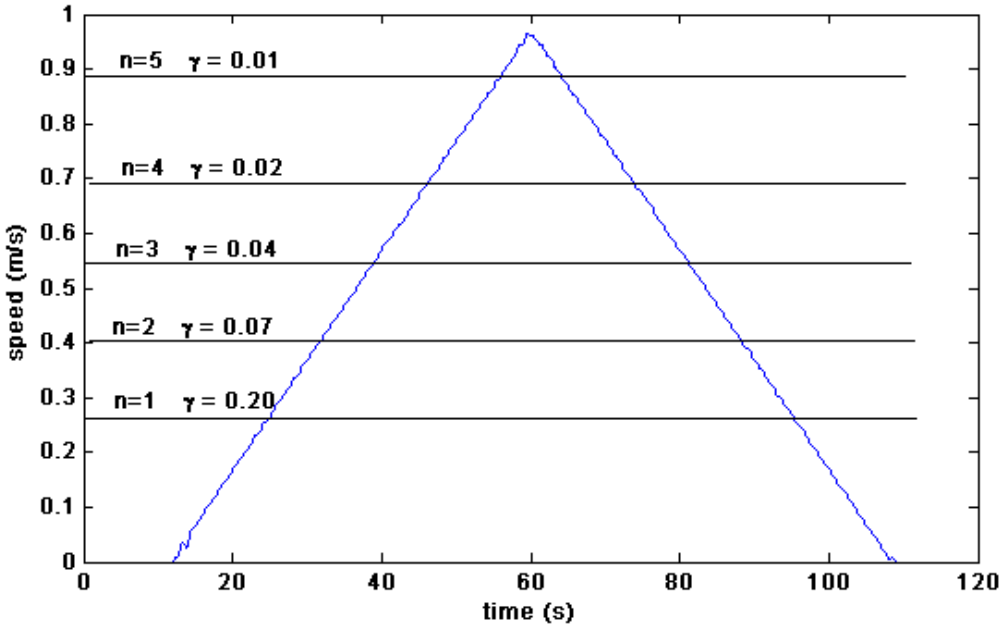

Figure F-1: Speed vs. Time for ramp test 7045

Figure F-2 is a plot of spanwise averaged RMS strain as a function of time. The figure clearly shows the local maxima associated with the pipe going into lock-in for modes 2, 4, 5 and 3 as indicated on the figure. The 1^{st} mode is not excited since it has a γ value of 0.20 which implies a 20% speed change per cycle. Figure F-3 shows the reconstructed mode weights as a function of time for the same ramp test. The mode weights clearly show that the 2^{nd} mode is the first to be excited, followed by the 3^{rd} mode. The 3^{rd} mode is followed by a strong response of the 5^{th} mode with the 4^{th} mode being skipped on the accelerating branch an only appearing during the decelerating portion of the ramp after the 60^{th} second.

Inspection of Figure F-4 reveals that the tensions for ramp test 7045 are very similar to the tensions of the conventional tests which means that the ramp results are directly comparable to the conventional test results. Figures F-4 and F-5 are such comparisons of the dimensionless response amplitudes and the curvatures respectively.

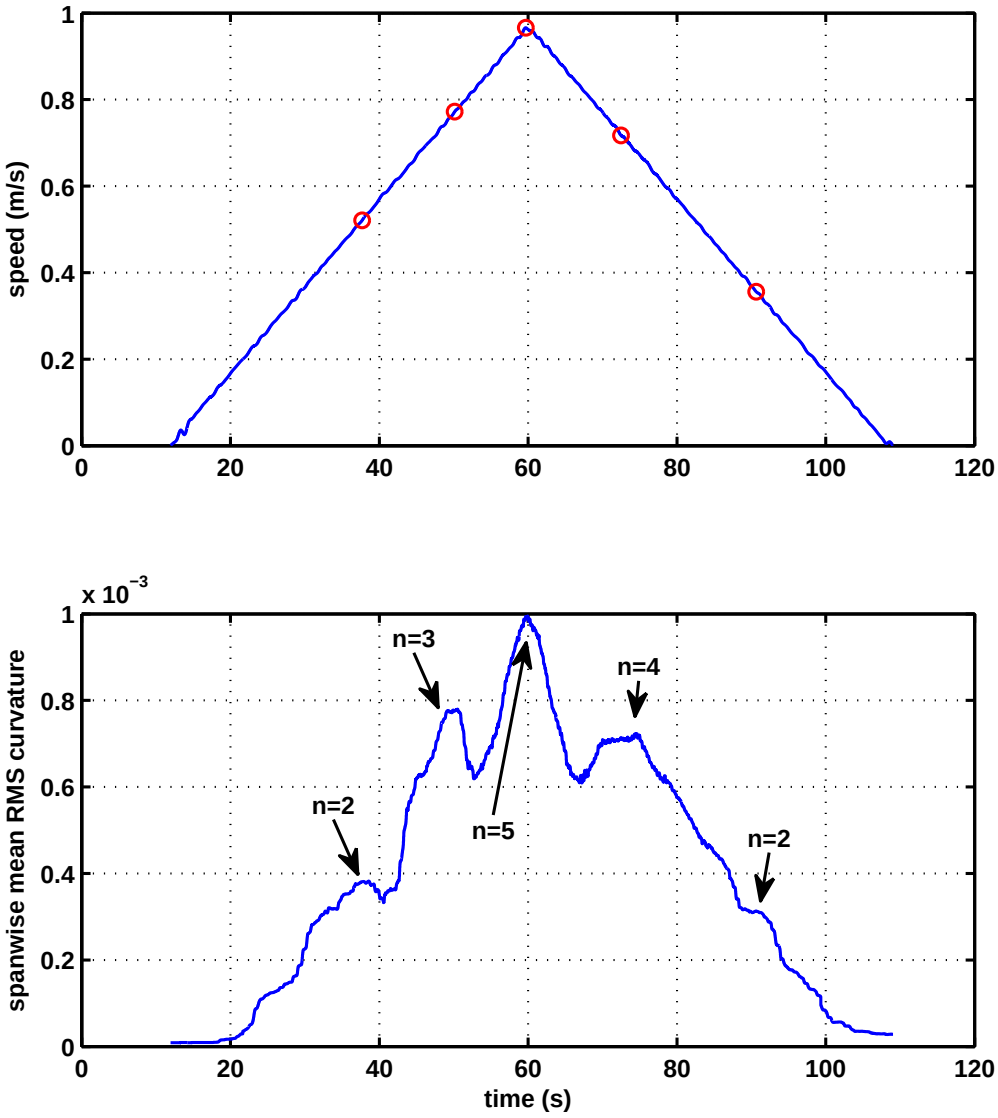

Figure F-2: Moving RMS strain vs. time for ramp test 7045 and dominant excited mode for each local maximum.

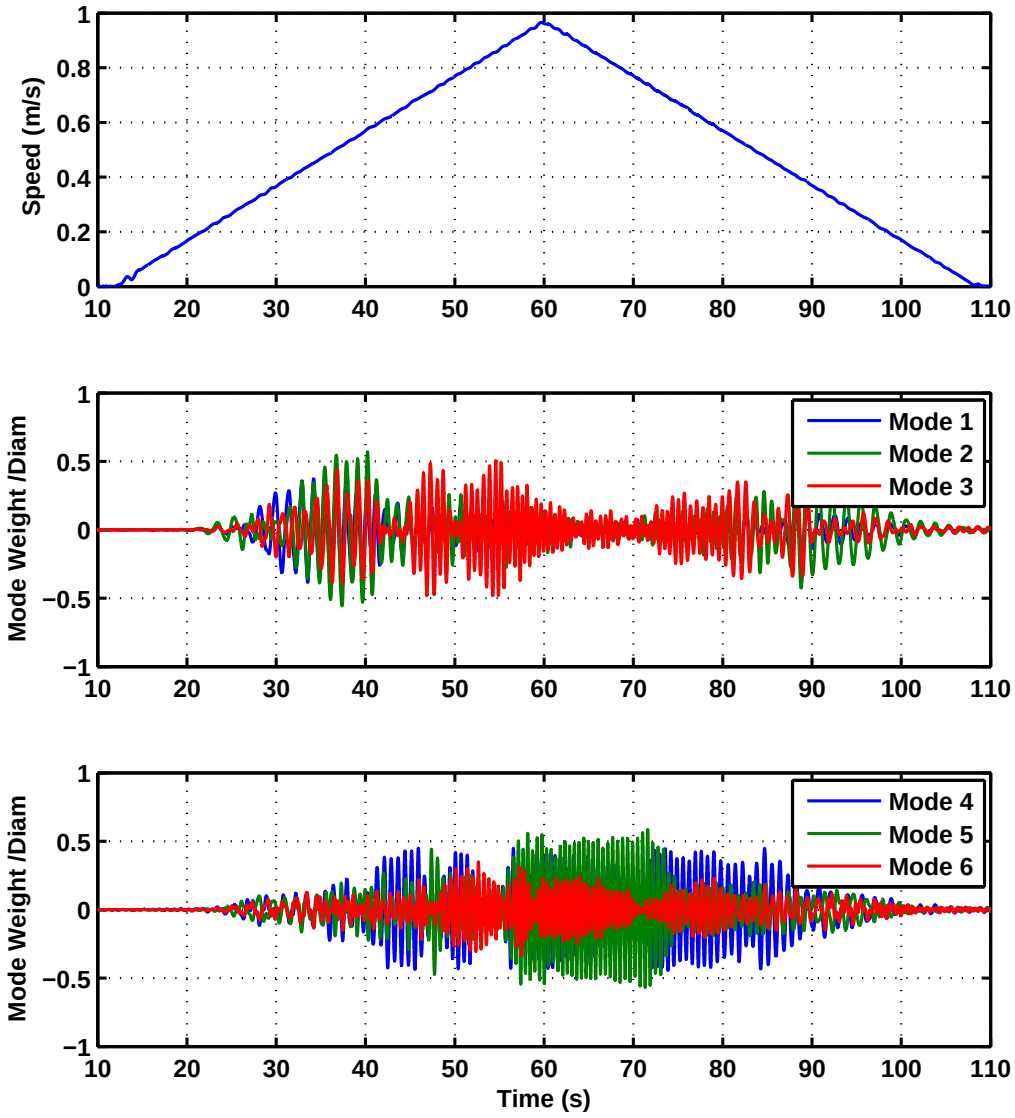

Figure F-3: Mode Weights/Diameter for ramp test 7045

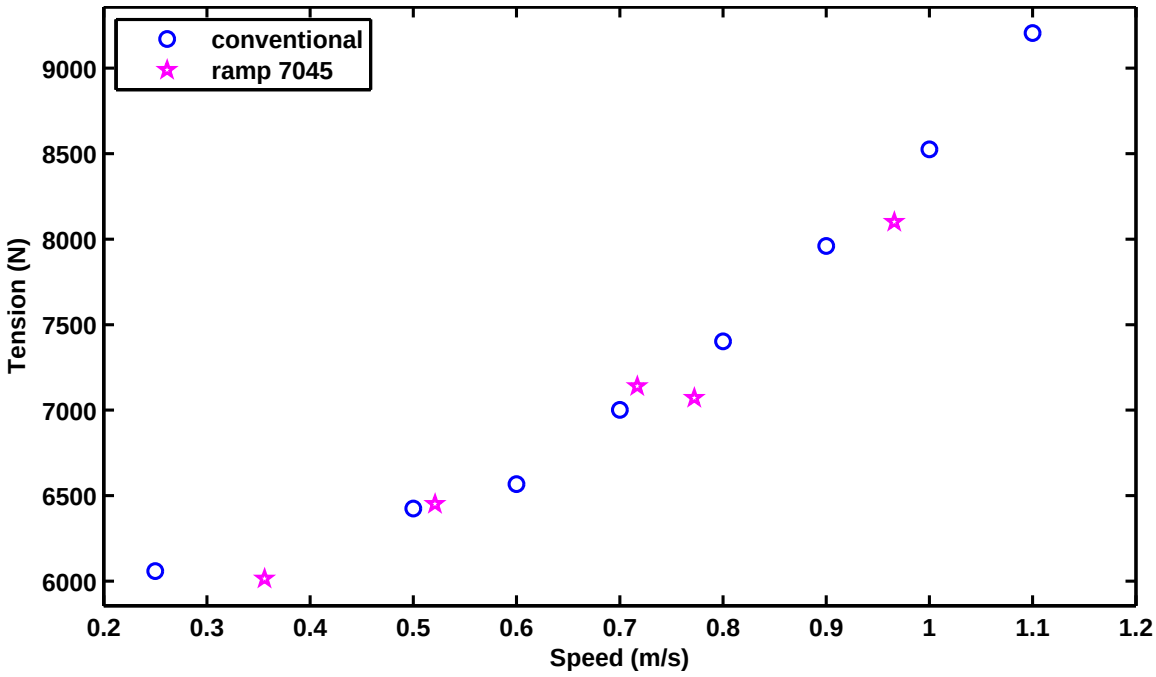

Figure F-4: Comparison of tensions during ramp test 7045 with the tensions recorded in the conventional tests

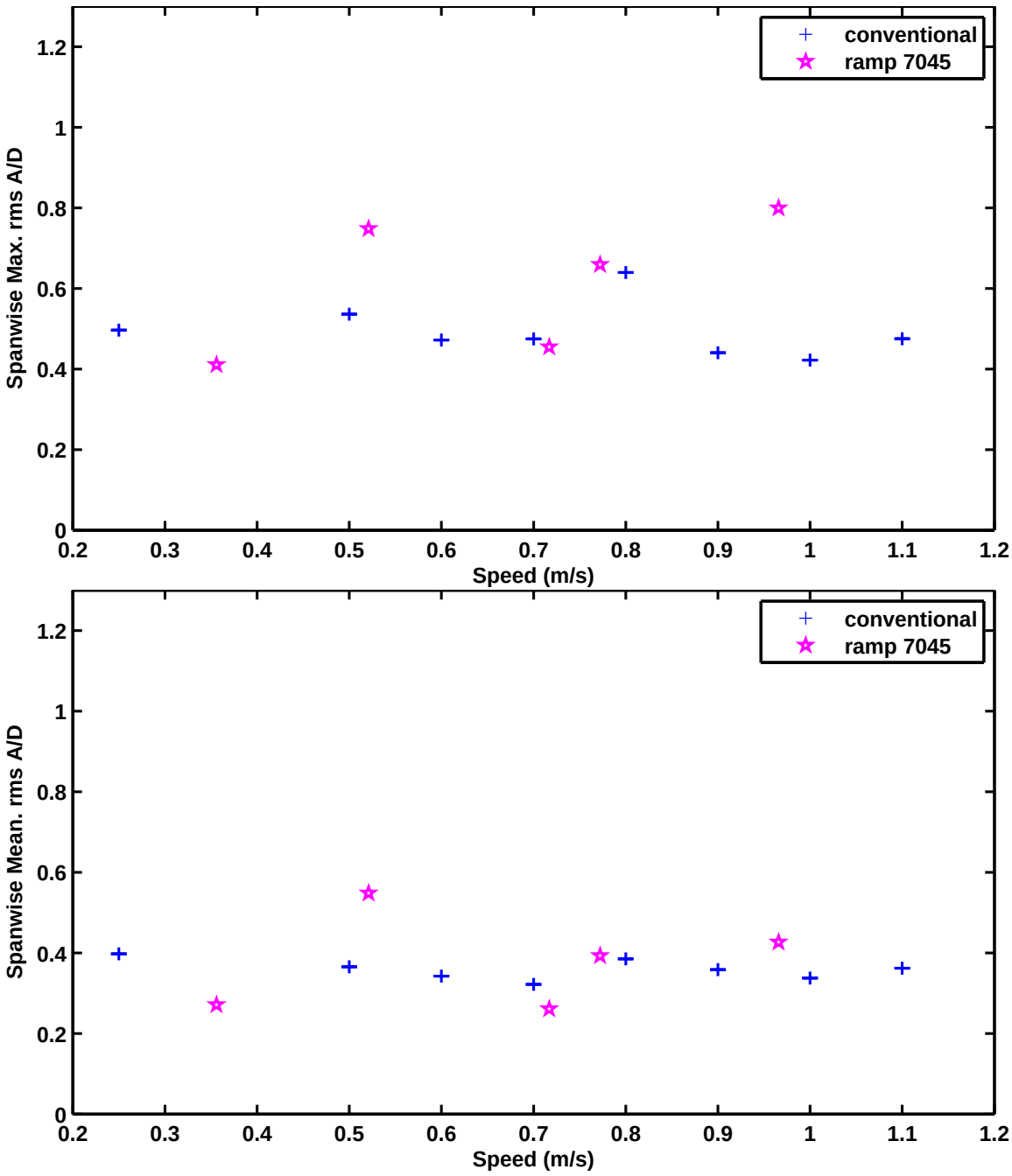

Figure F-5: Comparison of maximum and mean CF response amplitude from ramp test 7045 with the conventional tests

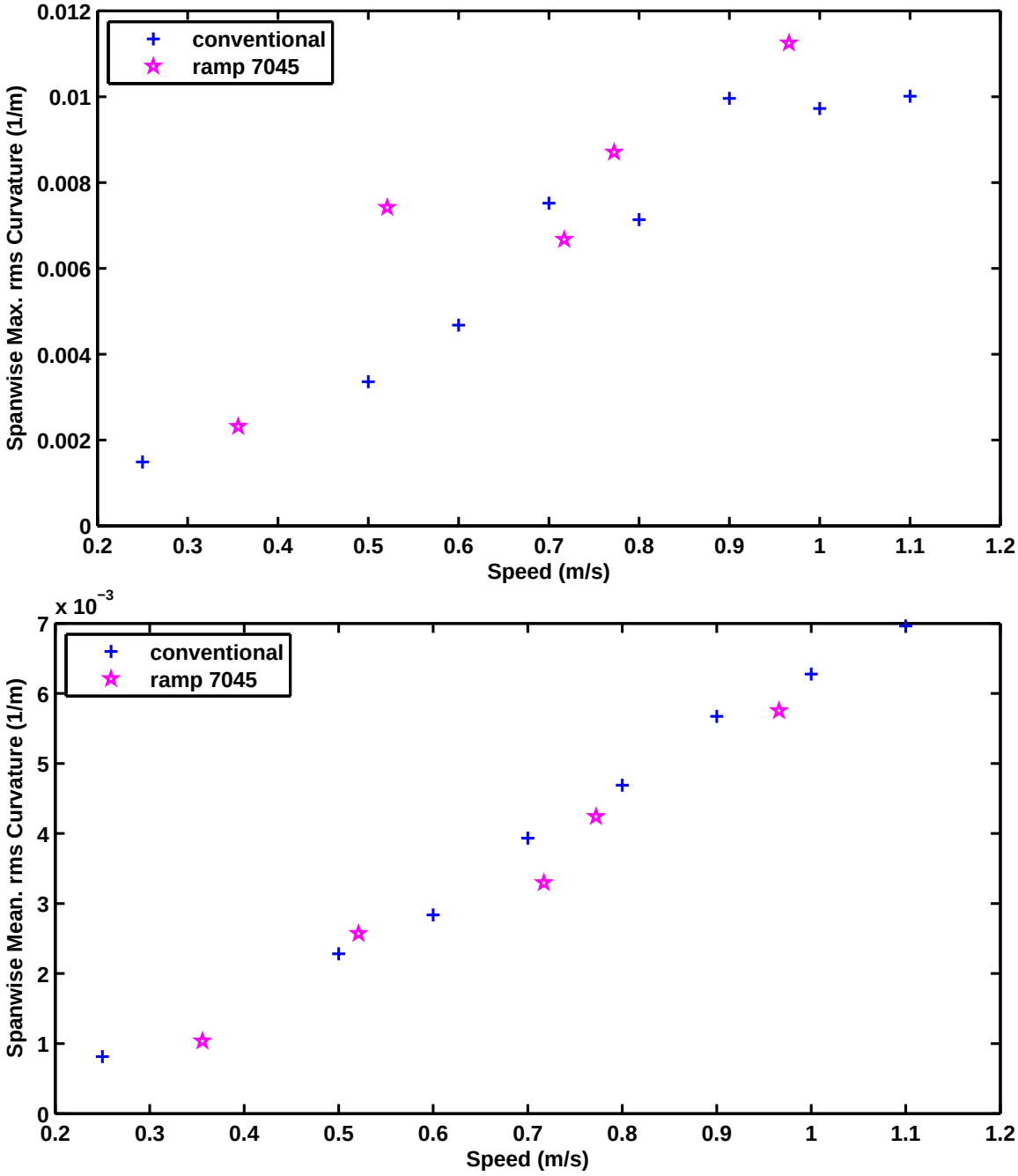

Figure F-6: Comparison of maximum and mean CF curvature from ramp test 7045 with the conventional tests

THIS PAGE INTENTIONALLY LEFT BLANK

Appendix G

Example .DAT File for SHEAR7v4.6

Figure G-1 shows a typical SHEAR7 .DAT file (input file) used for the SHEAR7 predictions shown in Chapter 6. When modelling each case from the 38m SHELL experiments, the .DAT file was updated with the appropriate tension, current speed, Strouhal number for each test case. The updated C_L curves that take into account the Reynolds number effects where provided in a separate .CL file.

```
                                                  test4019
Data file for testing the 38m-SHELL riser (SI units) for SHEAR7v4.6
Template File Name: SHELL-BARE.dat
*** BLOCK 1. unit system ***
         0                flag for units
*** BLOCK 2. structural and hydrodynamic data ***
        11                flag for structural model
        38.0              total length of the structure (m)
        1000              number of spatial segments
        1000              volume weight of the fluid (kg/m**3)
        1.1E-06           kinematic viscosity of the fluid (m**2/s)
        0.00300           structural damping coefficient:
        10295.6           effective tension at origin (N)
        1                 no. of zones to define sectional property
        0.0    1.0        zone start and end point in x/L
        0.080   0.027    0.021          hydro strength inside diameter(in)
        1.65405E-08     1.088   0.0     inertia(m^4) mass(kg/m) sbmg wt(kg/m)
        3.46E+10        1               modulus of elasticity (N/m**2), S-N Curve I.D. No.
        0.4      0.18   1   1           bandwidth, St code, Cl reduction factor, zoneCLtype
        1.000   0.2     0.18    0.2     Ca, DampCoeff1, DampCoeff2, DampCoeff3
*** BLOCK 3. current data ***
        2         1.00     4019         no. of profile data pts probability profile ID
        0.000     1.600
        1.000     1.600
*** BLOCK 4. s-n and scf data ***
        1                              No. of S-N curves defined
        1       1                      S-N curve I.D., No. of S-N curve segments
        0.0000                         cut-off stress range (N/m**2)
        1.62e+07   1.00E+08            stress range (Pa) cycles to failure
        3.49E+08   1.00E+04            stress range (Pa) cycles to failure
        1.000                          global stress concentration factor
        0                              no. of local stress concentration positions
*** BLOCK 5. computation/output option ***
      1                                calculation option
      0.00  1.00  0.1                  response location definition
      0.0                              gravitational acceleration
      0.05  0.3                        power cutoff, primary zone amplitude limit
      1                                power value exponent
      0                                flag for importing nodal effective tension and mass
      0                                flag for MATLAB animation data output (1=yes;0=no)
      0                                flag for generating *.scr file, (1=yes;0=no)
      0                                flag for generating *.dmg file, (1=yes;0=no)
      0                                flag for generating *.fat file, (1=yes;0=no)
      0                                flag for generating *.out1 file, (1=yes;0=no)
*** BLOCK 6. supplemental data ***
```

Figure G-1: Example .DAT File for SHEAR7v4.6 for Chapter 6

Bibliography

Beards, C. F. (1996). *Structural Vibration: Analysis and Damping*. Butterworth Heineman, Oxford, UK.

Bearman, P. W. (1984). Vortex shedding from oscillating bluff bodies. *Annual Review of Fluid Mechanics*, 16:195–222.

Bearman, P. W. and Obasaju, E. D. (1982). An experimental-study of pressure fluctuations on fixed and oscillating square-section cylinders,. *Journal of Fluid Mechanics*, 119:297–321.

Bendat, J. S. and Piersol, A. G. (1980). *Engineering Applications of Correlation and Spectral Analysis*. John Wiley & Sons, New York.

Bendat, J. S. and Piersol, A. G. (2010). *Random Data: Analysis and Measurement Procedures*. John Wiley & Sons, New York, 4^{th} edition.

Blevins, R. D. (1986). *Flow-Induced Vibration*. Robert E. Krieger Publishing Co, Florida.

Campbell, B. and Slocum, S. (2013). Prediction of VIV for risers with effective strakes. In *Proc. ASME* 32^{nd} *International Conference on Offshore Mechanics and Arctic Engineering*, number 2013-11413 in OMAE, Nantes, France.

Chen, S. S. and Chun, H. (1976). Design guide for calculating hydrodynamic mass, part i: Circular cylindrical structures. Technical Report ANL-CT-76-45, Argonne national Laboratory, Argonne, IL.

Crandall, S. H. (1963). Zero crossings, peaks and other statistical measures of random responses. *The Journal of the Acoustical Society of America*, 35(11):1693–1699.

Crandall, S. H. and Mark, W. D. (1963). *Random Vibration in Mechanical Systems*. Academic Press Inc., New York.

Dahl, J. M. (2008). *Vortex-Induced Vibration of a Cylinder With Combined In-Line and Cross-Flow Motion*. PhD thesis, Dept. of Mechanical Eng, MIT, Cambridge, MA.

Dahl, J. M. et al. (2010). Dual resonance in vortex-induced vibrations at subcritical and supercritical reynolds numbers. *Journal of Fluid Mechanics*, 643:395–424.

Den Hartog, J. P. (1985). *Mechanical Vibrations*. Dover Publications, New York, 4^{th} edition.

Det Norske Veritas (2010). Recommended practice: Fatigue design of offshore structures. Recommended Practice DNV-RP-C203, Det Norske Veritas.

Fei, C. and Vandiver, J. K. (1995). A gaussian model for predicting the effect of unsteady windspeed on the vortex-induced vibration response of structural members. In *Proc. ASME* 14^{th} *International Conference on Offshore Mechanics and Arctic Engineering*, OMAE, Copenhage, Denmark.

Fei, C. Y. (1995). *Vortex-Induced Vibration of Structural Members in Natural Winds*. PhD thesis, Dept. of Ocean Eng., MIT, Cambridge, MA.

Fontaine, E. et al. (2011). Reliability based factors of safety for VIV fatigue using NDP riser high mode VIV tests. In *Proc. ASME* 30^{th} *International Conference on Offshore Mechanics and Arctic Engineering*, number 2011-49820 in OMAE, Rotterdam, Netherlands.

Fontaine, E. R. et al. (2013). Using model test data to assess VIV factor of safety for SCR and TTR in GOM. In *Proc. ASME* 32^{nd} *International Conference on Offshore Mechanics and Arctic Engineering*, number OMAE2013-10984 in OMAE, Nantes, France.

Frank, W. R. et al. (2004). Flow-induced vibration of a long, flexible, straked cylinder in uniform and linearly sheared currents. In *Proc. 2004 Offshore Technology Conference*, number 16340 in OTC.

Fu, S. et al. (2013). VIV of flexible cylinder in oscillatory flow. In *Proc. ASME* 32^{nd} *International Conference on Offshore Mechanics and Arctic Engineering*, number 2013-10348 in OMAE, Nantes, France.

Fu, S. et al. (2014). Features of vortex-induced vibration in oscillatory flow. *Journal of Offshore Mechanics and Arctic Engineering*, 136.

Gopalkrishnan, R. (1993). *Vortex Induced Forces on Oscillating Bluff Cylinders,*. PhD thesis, Dept. of Ocean Engineering, MIT, Cambridge, MA.

Govardhan, R. and Williamson, C. H. K. (2002). Resonance forever: Existence of a critical mass and an infinite regime of resonance in vortex-induced vibrations. *Journal of Fluid Mechanics*, 473:146–166.

Govardhan, R. N. and Williamson, C. H. K. (2006). , defining the modified griffin plot in vortex-induced vibration: Revealing the effect of reynolds number using controlled damping. *Journal of Fluid Mechanics*, 561:147–180.

Jhingran, V., Jaiswal, V., and Vandiver, J. K. (2008). Spatial variation of drag on long cylinders in sheared flow. In *Proc. ASME* 27^{th} *International Conference on Offshore Mechanics and Arctic Engineering*, number 2008-57803 in OMAE, Estoril, Portugal.

Jhingran, V. and Vogiatzis, J. (2010). Lift coefficient curves for predicting response using shear7. In *Proc. ASME* 29^{th} *International Conference on Offshore Mechanics and Arctic Engineering*, number 2010-20597 in OMAE, Shanghai, China.

Kaasen, K. E. et al. (2000). Norwegian deepwater program: Analysis of vortex-induced vibrations of marine risers based on full-scale measurements. In *Proc. 2000 Offshore Technology Conference*, number 11997 in OTC, Houston, TX.

Kim, Y. H., Vandiver, J. K., and Holler, R. (1985). Vortex-induced vibration and drag coefficients of long cable subject to sheared flow. In *Proc. ASME* 4^{th} *International Conference on Offshore Mechanics and Arctic Engineering*, OMAE, pages 584–592, Dallas, TX.

Kim, Y. H., Vandiver, J. K., and Holler, R. (1986). Vortex-induced vibration and drag coefficients of long cables subject to sheared flow. *ASME Journal of Energy Resources Technology*, 108:73–83.

Klamo, J. T., Leonard, A., and Roshko, A. (2005). On the maximum amplitude of a freely vibrating cylinder in cross-flow. *Journal of Fluids and Structures*, 21:429–434.

Kosakiewicz, A., Sumer, B., and Fredsoe, J. (1992). Spanwise correlation on vibrating cylinder near a wall in oscillatory flows. *Journal of Fluids and Structures*, 6:371–392.

Kosakiewicz, A., Sumer, B., and Fredsoe, J. (1994). Cross-flow vibrations of cylinder in irregular oscillatory flow. *Journal Waterway, Port, Coastal, Ocean Engineering*, 120:515–534.

Lague, F. and Laneville, A. (2002). Vortex-induced vibrations of a flexible cylinder in a slowly varying flow: Experimental results. In *Proc. 2002 ASME IMECE*, number 2002-32167 in IMECE, New Orleans, LA.

Liao, J. C. (2002). *Vortex-Induced Vibration of Slender Structures in Unsteady Flow*. PhD thesis, Dept. of Ocean Eng., MIT, Cambridge, MA.

Lie, H. et al. (2012). Comprehensive riser VIV model tests in uniform and sheared flow. In *Proc. ASME* 31^{st} *International Conference on Offshore Mechanics and Arctic Engineering*, number 2012-84055 in OMAE, Rio de Janeiro, Brazil.

Lie, H. and Kaasen, K. (2006). Modal analysis of measurements from a large scale VIV model of a riser in a linearly sheared flow. *Journal of Fluids and Structures*, 22:557–575.

Mandel, J. (1984). *The Statistical Analysis of Experimental Data*. Dover Publications, New York.

Marcollo, H. et al. (2007). Phenomena observed in VIV bare riser field tests. In *Proc. ASME* 26^{th} *International Conference on Offshore Mechanics and Arctic Engineering*, number 2007-29562 in OMAE, San Diego, CA.

MARINTEK (2011). Shell riser VIV tests main report. Technical Report 580233.00.01, MARINTEK, Trondheim, Norway.

MARINTEK (2012). NDP analysis of shell riser VIV tests. Technical Report 580439.00.01, MARINTEK, Trondheim, Norway.

Modarres-Sadeghi, Y. et al. (2011). Chaotic response is a generic feature of vortex-induced vibrations of flexible risers. *Journal of Sound and Vibration*, 330:2565–2579.

Mukundan, H. et al. (2010). Optimal lift force coefficient databases from riser experiments. *Journal of Fluids and Structures*, 26:160–175.

Norberg, C. (2003). Fluctuating lift on a circular cylinder: Review and new measurements. *Journal of Fluids and Structures*, 17:57–96.

Proakis, J. G. and Manolakis, D. G. (2007). *Digital Signal Processing*. Prentice-Hall, New Jersey, 4^{th} edition.

Rao, S. S. (2011). *Mechanical Vibrations*. Prentice Hall, Upper Saddle River, NJ, 5^{th} edition.

Ravi, K. R. T. et al. (2013). Computational study of vortex-induced vibration of a sprung rigid circular cylinder with a strongly non-linear attachment. *Journal of Fluids and Structures*, 40:214–232.

Resvanis, T. L. and Vandiver, J. K. (2011). Modelling risers with partial strake coverage. In *Proc. ASME* 30^{th} *International Conference on Offshore Mechanics and Arctic Engineering*, number 2011-49817 in OMAE, Rotterdam, Netherlands.

Resvanis, T. L. and Vandiver, J. K. (2012). Reynolds number effects on the vortex-induced vibration of flexible marine rise. In *Proc. ASME* 31^{st} *International Conference on Offshore Mechanics and Arctic Engineering*, number 2012-83565 in OMAE, Rio de Janeiro, Brazil.

Rigzone.com (accessed on May, 2014). http://www.rigzone.com/training/insight.asp?insight_id=308c_id=17.

Sarpkaya, T. (1978). Fluid forces on oscillating cylinders. *Journal of the Waterway, Port, Coastal and Ocean Division*, pages 275–290.

Sarpkaya, T. (1979). Dynamic response of piles to vortex shedding in oscillating flows. In *Proc. 1979 Offshore Technology Conference*, number 3647 in OTC.

Sarpkaya, T. (1986). Force on a circular cylinder in viscous oscillatory flow at low keulegan-carpenter numbers. *Journal of Fluid Mechanics*, 165:61–71.

Sarpkaya, T. (2004). A critical review of the intrinsic nature of vortex-induced vibrations. *Journal of Fluids and Structures*, 19:389–447.

Scruton, C. (1955). Wind-excited oscillations of tall stacks. *Engineer*, 199:806–808.

Sumer, B. and Fredsoe, J. (1988). Transverse vibrations of an elastically mounted cylinder exposed to an oscillating flow. *Journal of Offshore Mechanics and Arctic Engineering*, 110:387–394.

Sumer, B. and Fredsoe, J. (1989). Effect of reynolds number on vibrations of cylinders. *Journal of Offshore Mechanics and Arctic Engineering*, 111:131–137.

Sumer, B. M. and Fredsoe, J. (2006). *Hydrodynamics around Cylindrical Structures*, volume 26 of *Adv. Series on Ocean Eng.* World Scientific, New Jersey.

Swithenbank, S. B. (2007). *Dynamics of Long Flexible Cylinders at High-Mode Number in Uniform and Sheared Flows*. PhD thesis, Dept. of Mechanical Eng., MIT, Cambridge, MA.

Swithenbank, S. B. et al. (2008). Reynolds number dependence of flexible cylinder VIV response data. In *Proc. ASME* 27^{th} *International Conference on Offshore Mechanics and Arctic Engineering*, number 2008-57045 in OMAE, Estoril, Portugal.

Thomson, W. T. (1988). *Theory of Vibration with Applications*. Prentice-Hall, New Jersey, 3^{rd} edition.

Tognarelli, M. A. et al. (2004). VIV response of a long flexible cylinder in uniform and linearly sheared currents. In *Proc. 2004 Offshore Technology Conference*, number 16338 in OTC.

Tognarelli, M. A. et al. (2013). VIV safety factors for drilling risers: Propagating model uncertainty in a long-term reliability analysis. In *Proc. ASME* 32^{nd} *International Conference on Offshore Mechanics and Arctic Engineering*, number 2013-10738 in OMAE, Nantes, France.

Triantafyllou, M. S. et al. (2003). Vortex-induced vibrations of slender structures in shear flow. In *Proc. of IUTAM*, New Brunsewick, NJ.

Van Dyke, M. (1982). *An Album of Fluid Motion*. The Parabolic Press, Stanford, California.

Vandiver, J. (1993). Dimensionless parameters important to the prediction of vortex-induced vibration of long, flexible cylinders in ocean currents. *Journal of Fluids and Structures*, 7:423–455.

Vandiver, J. et al. (2009). Insights on vortex-induced, traveling waves on long risers. *Journal of fluids and structures*, 25:641–653.

Vandiver, J., Resvanis, T., and Marcollo, H. (2012). *User Guide for SHEAR7 v4.7*. SHEAR7, Cambridge, MA.

Vandiver, J. K. (1983). Drag coefficients of long flexible cylinders. In *Proc. 1983 Offshore Technology Conference*, number 4490 in OTC.

Vandiver, J. K. (1985). The prediction of lockin vibration on flexible cylinders in a sheared flow. In *Proc. 1985 Offshore Technology Conference*, number 5006 in OTC.

Vandiver, J. K. (2012). A damping parameter for flow induced vibration. *Journal of Fluids and Structures*, 35:105–119.

Vandiver, J. K. and Chung, T. Y. (1987). Hydrodynamic damping on flexible cylinders in sheared flow. In *Proc. 1987 Offshore Technology Conference*, number 5524 in OTC.

Vandiver, J. K. et al. (2006). Fatigue damage from high mode number vortex-induced vibration. In *Proc. ASME* 25^{th} *International Conference on Offshore Mechanics and Arctic Engineering*, number 2006-9240 in OMAE, Hamburg, Germany.

WAFO-group (2006). *WAFO -A Matlab Toolbox for Analysis of Random Waves and Loads - A Tutorial*. Math. Stat., Center for Math Sci., Lund Univ., Lund, Sweden. http://www.maths.lth.se/mathstat/wafo.

Williamson, C. H. K. and Govardhan, R. (2004). Vortex-induced vibrations. *Annual Review of Fluid Mechanics*, 36:413–455.

Williamson, C. H. K. and Govardhan, R. (2008). A brief review of recent results in vortex-induced vibrations. *Journal of Wind Engineering and Industrial Aerodynamics*, 97:713–735.